2009

Study on Regional Responses of Pan-Arctic Terrestrial Ecosystems to Recent Climate Variability Using Satellite Remote Sensing

Ke Zhang
The University of Montana

STUDY ON REGIONAL RESPONSES OF PAN-ARCTIC TERRESTRIAL ECOSYSTEMS TO RECENT CLIMATE VARIABILITY USING SATELLITE REMOTE SENSING

By

Ke Zhang

B. Eng, Hohai University, Nanjing, China, 2002
M. Eng, Hohai University, Nanjing, China, 2005

Dissertation

presented in partial fulfillment of the requirements
for the degree of

Doctor of Philosophy
in Organismal Biology and Ecology

The University of Montana
Missoula, MT

Spring 2009

Approved by:

Dr. Perry Brown, Associate Provost for Graduate Education
Graduate School

Dr. John S. Kimball, Chair
Flathead Lake Biological Station
Division of Biological Sciences

Dr. Steven W. Running
Department of Ecosystem and Conservation Sciences

Dr. Ragan M. Callaway
Division of Biological Sciences

Dr. Anna Sala
Division of Biological Sciences

Dr. Jack A. Stanford
Flathead Lake Biological Station
Division of Biological Sciences

Zhang, Ke, Ph.D., Spring 2009 Organismal Biology and Ecology

Study on Regional Responses of Pan-Arctic Terrestrial Ecosystems to Recent Climate Variability Using Satellite Remote Sensing

Chairperson: Dr. John S. Kimball

ABSTARCT

I applied a satellite remote sensing based production efficiency model (PEM) using an integrated AVHRR and MODIS FPAR/LAI time series with a regionally corrected NCEP/NCAR reanalysis surface meteorology and NASA/GEWEX shortwave solar radiation inputs to assess annual terrestrial net primary productivity (NPP) for the pan-Arctic basin and Alaska from 1983 to 2005. I developed a satellite remote sensing based evapotranspiration (ET) algorithm using GIMMS NDVI with the above meteorology inputs to assess spatial patterns and temporal trends in ET over the pan-Arctic region. I then analyzed associated changes in the regional water balance defined as the difference between precipitation (P) and ET. I finally analyzed the effects of regional climate oscillations on vegetation productivity and the regional water balance.

The results show that low temperature constraints on Boreal-Arctic NPP are decreasing by 0.43% per year ($P < 0.001$), whereas a positive trend in vegetation moisture constraints of 0.49% per year ($P = 0.04$) are offsetting the potential benefits of longer growing seasons and contributing to recent drought related disturbances in NPP. The PEM simulations of NPP seasonality, annual anomalies and trends are similar to stand inventory network measurements of boreal aspen stem growth ($r = 0.56$; $P = 0.007$) and atmospheric CO_2 measurement based estimates of the timing of growing season onset ($r = 0.78$; $P < 0.001$).

The simulated monthly ET results agree well (RMSE=8.3 mm $month^{-1}$; R^2=0.89) with tower measurements for regionally dominant land cover types. Generally positive trends in ET, precipitation and available river discharge measurements imply that the pan-Arctic terrestrial water cycle is intensifying. Increasing water deficits occurred in some boreal and temperate grassland regions, which agree with regional drought records and recent satellite observations of vegetation browning and productivity decreases.

Climate oscillations including Arctic Oscillation and Pacific Decadal Oscillation influence NPP by regulating seasonal patterns of low temperature and moisture constraints to photosynthesis.

The pan-Arctic water balance is changing in complex ways in response to climate change and variability, with direct linkages to terrestrial carbon and energy cycles. Consequently, drought induced NPP decreases may become more frequent and widespread, though the occurrence and severity of drought events will depend on future water cycle patterns.

ACKNOWLEDGEMENTS

This investigation was carried out at the University of Montana and at the Jet Propulsion Laboratory (JPL), California Institute of Technology, under contract to the National Aeronautics and Space Administration (NASA). This work was supported by NASA Earth and Space Science Fellowship award NNX07AN78H, NASA Earth Science Enterprise grants NNG04GJ44G and NNX08AG13G, and NSF OPP grants 3702AP15297803211 and 0732954.

I would like to thank my advisor, Dr. John S. Kimball, for his great patience, wonderful guidance and large inspiration to me. Many thanks to other committee members, Drs. Steve Running, Ray Callaway, Anna Sala, and Jack Stanford, for their advice and encouragement and their interest in my work. I thank Dr. Maosheng Zhao of the Numerical Terradynamic Simulation Group (NTSG) for help in processing the meteorological data and MODIS data. The work of Lucas Jones, Dr. Qiaozhen Mu and Dr. Faith Ann Heinsch of NTSG for obtaining and processing flux tower data is appreciated. Dr. Kyle McDonald of JPL and Dr. Youngwook Kim of Flathead Lake Biological Station (FLBS) kindly provided the SSM/I freeze-thaw data. I thank the principal investigators and their research teams of the flux tower sites and the CIPHA study for providing data for this study, including Steve Wofsy, Allison Dunn, T. Andy Black, Alan Barr, Lawrence Flanagan, Yoshinobu Harazono, Walter C. Oechel and E.H. Hogg. I thank NASA, NCEP/NCAR, NOAA, ECMWF, NCDC, ArcticRIMS, Water Survey of Canada and GRDC for providing additional data. I would like to acknowledge the administrative and technical support provided by FLBS and NTSG. Thanks to my friends and fellow graduate students for their sincerely help and support. Finally, I thank my family for their constant love, support and patience, which made this whole journey possible.

TABLE OF CONTENTS

LIST OF TABLES

LIST OF FIGURES

CHAPTER 1: INTRODUCTION

1.1. Importance of Pan-Arctic Terrestrial Ecosystems

1.1.1. Geography and Climate

The Pan-Arctic terrestrial ecosystems cover the Pan-Arctic basin and Alaska including all land areas draining into the Arctic Ocean, Hudson Bay, James Bay, Hudson Strait and the Bering Sea (Figure 1-1). The Pan-Arctic region spans a latitudinal range from 45.35 °N to 83.62 °N and encompass approximately 25 million km^2 of the northern high (>50°N) latitudes and 30% of the combined North American and Eurasian landmass (Kimball *et al.*, 2006b). It includes the entire arctic tundra biome, most of the boreal forest biome and a small portion of the northern temperate grassland biome.

The NASA International Geosphere-Biosphere Programme (IGBP) 17-class Moderate Resolution Imaging Spectroradiometer (MODIS) Type 1 global land cover classification (Friedl *et al.*, 2002) distinguishes 9 general land cover categories within this region at 1-km spatial resolution, including open shrubland, savanna, grassland, cropland, woody savanna, evergreen needleleaf forest, deciduous needleleaf forest, mixed forest and barren (Figure 1-1(a)) . Vegetated areas in this region can be aggregated into three major biome types, i.e. the arctic tundra, boreal forest and northern temperate grassland biomes (Figure 1-1(b)). The climate for Arctic tundra has a mean temperature below 0 °C and a growing season of less than 50 days. During the winter it is very cold and dark, with average temperature around -30 °C, sometimes dipping as low as -50 °C (Woodward, 2003). During the summer, temperatures rise somewhat and daytime

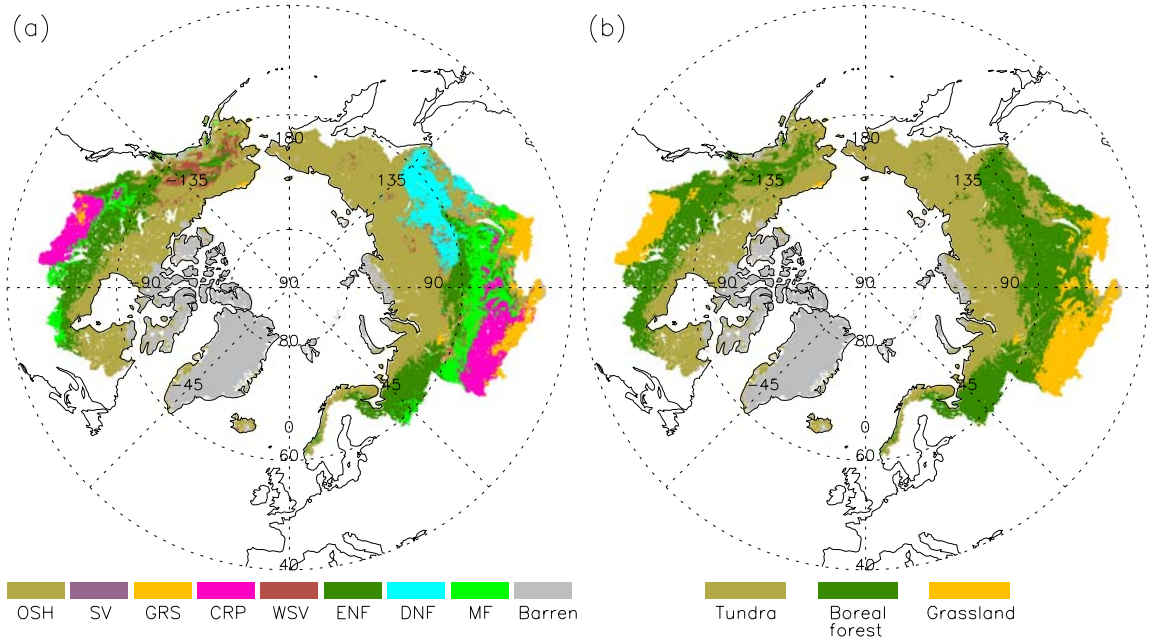

Figure 1-1: Maps of (a) land cover derived from the NASA IGBP-MODIS global land cover classification (Friedl *et al.*, 2002) and (b) corresponding aggregated major biome types for the Pan-Arctic basin and Alaska domain, including OSH: open shrubland; SV: savanna; GRS: grassland; CRP: cropland; WSV: woody savanna; ENF: evergreen needleleaf forest; DNF: deciduous needleleaf forest; MF: mixed forest; Barren: barren or sparsely vegetated cover types. Areas in white represent open water and other areas outside the study domain.

temperatures generally can rise to about 12 °C but often drop to 3 °C or even below freezing. The year-round cold temperatures permanently freeze the tundra subsoil below 25-90 cm termed permafrost. Annual precipitation averages about 150-500 mm and usually occurs as snow (Whitney, 2002; Woodward, 2003).

Boreal forests, or taiga, have higher annual average temperature but larger variations in extreme temperatures than arctic tundra. Temperatures vary from -50 °C to 30 °C throughout the whole year, with eight or more months of temperatures averaging below 10 °C (Arno & Hammerly, 1984). The greatest range in mean monthly temperatures (56 °C) occurs in eastern Siberia; in North America, the maximum range of mean monthly temperature (44 °C) occurs in interior Alaska (Bonan, 2008; Bonan &

Shugart, 1989).Winters are typically long and severely cold, with up to six months having an average temperature at or below freezing. Summers are short and cool to warm. Only 50 to 100 days may be frost free. Mean annual precipitation is 200-750 mm, primarily as rain during the summer months, but also as fog and snow; as evaporation is also low for most of the year, precipitation exceeds evaporation and is sufficient to support relatively dense vegetation growth (Sayre, 1994; Woodward, 2003).

1.1.2. Ecological, Climatic and Social Significance

Pan-Arctic terrestrial ecosystems have extraordinary biological and ecological value and represent interrelated habitats made up of forests, lakes, wetlands, rivers, grasslands and tundra. The vegetation in arctic tundra is composed of dwarf shrubs, sedges and grasses, mosses, and lichens, while the boreal forest region is dominated by spruces, pines, firs, larches, birches and aspens or poplar (Woodward, 2003). Although there are less species and lower biodiversity in arctic tundra and boreal forests than temperate forests and tropical rain forests, arctic tundra and boreal forests are wildlife habitats of international significance, especially for caribou, polar bears, musk ox, grizzly bears, migratory birds, etc. Boreal forests are home to the world's largest population of wolves, lynx, black and grizzly bears, and even the threatened woodland caribou. The lakes of the boreal region are teeming with some of the world's largest trout, bass, perch and whitefish. Many species from around the world depend on summer breeding and feeding grounds in this region.

Arctic tundra and Boreal forest play vital roles in the global climate system and impact climate through three major mechanisms, or so-called "feedbacks", including

surface reflectivity, greenhouse gas storage and emission, and ocean circulation (ACIA, 2004; Hassol *et al.*, 2004). The first feedback involves changes in the reflectivity of the surface as snow and ice melt and vegetation cover changes, the second involves changes in the amounts of greenhouse gases emitted to the atmosphere from the land as warming progresses, and the third involves changes to ocean circulation as arctic ice melts, adding freshwater to the oceans.

The high latitudes of the pan-Arctic region receive less solar radiation relative to tropical and subtropical regions on an annual basis. Many areas of the pan-Arctic are covered with snow and ice so a larger fraction of incoming solar energy is reflected back to space than at lower latitudes. As a result, this region represents an energy sink in the global climate system and acts as a global refrigerator by attracting heat from the lower latitudes. If not for the atmosphere and oceans moving energy from the tropics to the poles, the tropics would overheat and the polar regions would be much colder than thy currently are.

The icy temperatures and permafrost of the pan-Arctic region slow plant litter decomposition, resulting in a build-up of soil organic matter and thus slowing the release of carbon dioxide, one of the most important green-house gases to the atmosphere. Arctic tundra ecosystems currently store approximately 14% of the Earth's terrestrial carbon (Oberbauer *et al.*, 1991) and over the past 10,000 years climatic conditions have favored carbon sequestration in the Arctic (Gorham, 1991). The boreal forest region covers just under 15% of the global land surface, but contains over 30% of all carbon contained in the terrestrial biome (Table 1-1) (Kasischke, 2000). Together, the whole Pan-Arctic

Table 1-1. Comparison of carbon storage in world major biomes based on the estimation from Kasischke (2000).

Biome	Area ($\times 10^6$ ha)	Soil Carbon ($\times 10^{15}$ g)	Plant Biomass Carbon ($\times 10^{15}$ g)	Total Carbon ($\times 10^{15}$ g)
Arctic Tundra	890	180	<<1	~181
Boreal Forests	1,509	625	78	703
Temperate Forests	1,040	100	21	121
Tropical Forests	1,756	216	159	375

region contains up to 40% of the global terrestrial carbon reservoir (Lal & Kimble, 2000; Saugier *et al.*, 2001). The accelerated release of this carbon in the form of carbon dioxide and methane would greatly enhance global warming.

The pan-Arctic region also plays a key role in global oceanic circulations, especially thermohaline circulation (Broecker, 1997; Levermann *et al.*, 2007; Rahmstorf, 2006). One of the ways the sun's energy is transported from the equator toward the poles is through the globally interconnected movement of ocean waters primarily driven by differences in heat and salt content, known as the thermohaline circulation, or the great ocean conveyor ("thermo" for heat and "haline" for salt) (Broecker, 1991; Broecker & Denton, 1990). At present, the northward extension of the warm Gulf Stream current in the North Atlantic Ocean warms the surrounding atmosphere and provides much of the moisture that falls as precipitation over northwestern Europe. As the waters move northward, they become cooler and denser, until they are heavier than the waters below and sink deep into the ocean at high latitudes to form the North Atlantic Deep Water. The formation of sea ice at high latitudes also makes the near-surface water saltier and denser as salt is rejected from the ice. This sinking dense seawater flows over the continental

shelves into the deep ocean basin, contributing to deep-water formation and the further drawing northward of heat from the tropics (Broecker, 1991; Rahmstorf, 2006). This process is delicately balanced; if the waters are made less salty by an increase in freshwater runoff, precipitation or glacial melt, or because temperatures are not sufficiently cold to form sea ice, the formation rate of deep water will decrease and less heat from the tropical regions will be pulled northward by the ocean.

The pan-Arctic region encompasses part of all the territories of eleven nations: Norway, Sweden, Finland, Denmark, Iceland, Mongolia, Kazakhstan, Canada, China, Russia, and the United States, as well as the homelands of dozens of indigenous groups that encompass distinct sub-groups and communities. There are abundant natural resources in this region including oil, natural gas, minerals, fish, timber, etc.

1.2. Evidence of Changes in Pan-Arctic Terrestrial Ecosystems

1.2.1. Pan-Arctic Climate Change

Northern latitudes (45° to 90°N), encompassing Arctic tundra and boreal forest regions, experienced the greatest regional warming on earth in recent decades. Annual average temperatures in some regions, especially the arctic, have increased at almost twice the rate as that of the rest of the world over the past few decades (ACIA, 2004, 2005). Average annual temperatures in northern high latitudes (60° to 90°N) have risen by about 2 to 3 °C since the 1950s and in winter by up to 4 °C (Trenberth *et al.*, 2007) (see also Figures 1-2 (a) and 1-3), while the larger region from 45° to 90°N and global

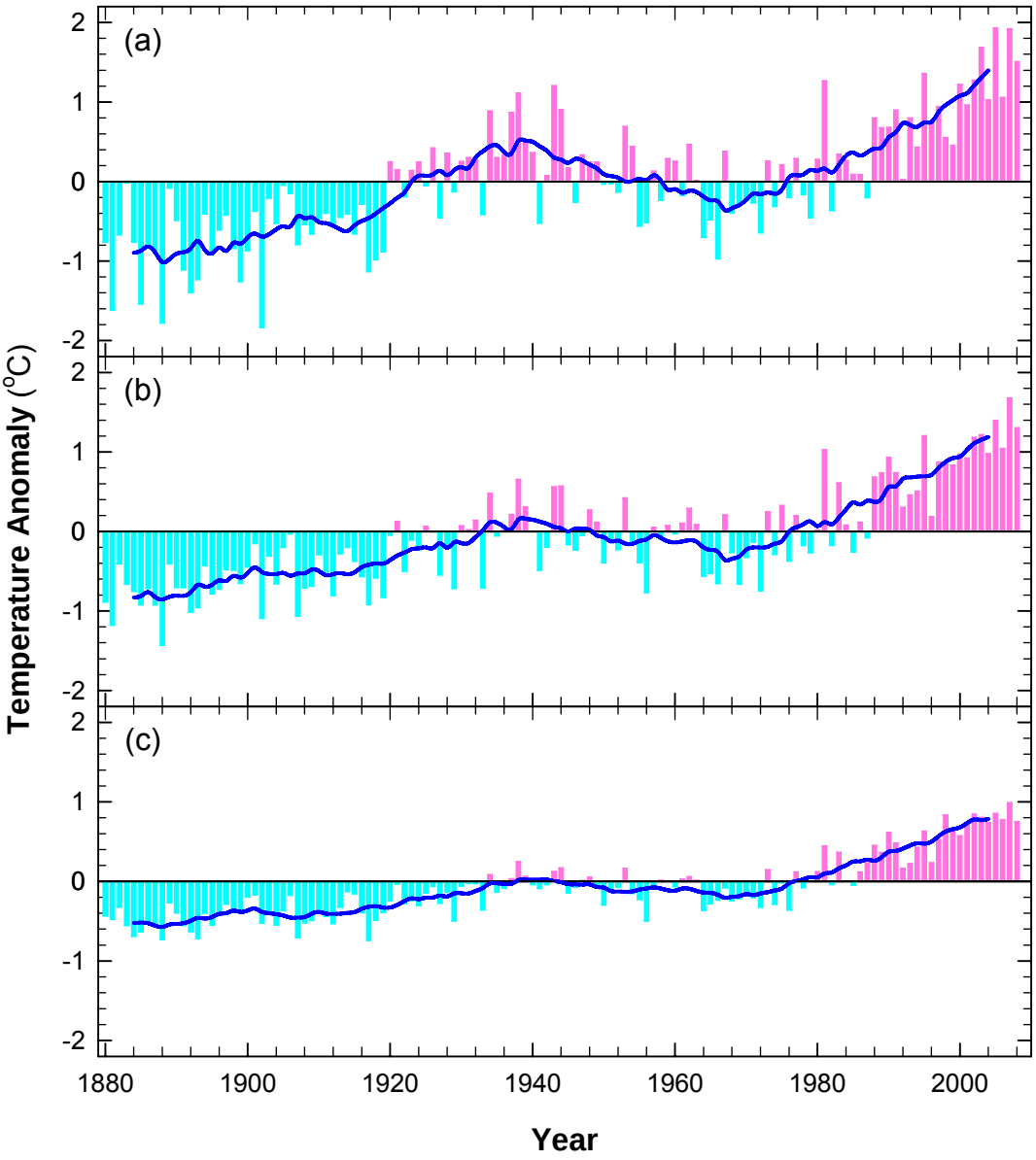

Figure 1-2: Annual anomalies of land-surface air temperature in (a) the northern high latitudes (65° to 90°N), (b) the region from 45° to 90°N and (c) the globe for the 1880-2008 period using station observations from the Global Historical Climatology Network (GHCN) data (updated from Peterson & Vose (1997)). Anomalies are calculated relative to the 1961-1990 average. The smoothed curves were created using a 10-year running mean.

average temperatures have increased by about 1.5 °C and 1 °C, respectively (Figures 1-2(b) and (c)). Although cooling has occurred in some areas like southern Greenland, Davis Strait and eastern Canada, warming in most areas has resulted in extensive melting

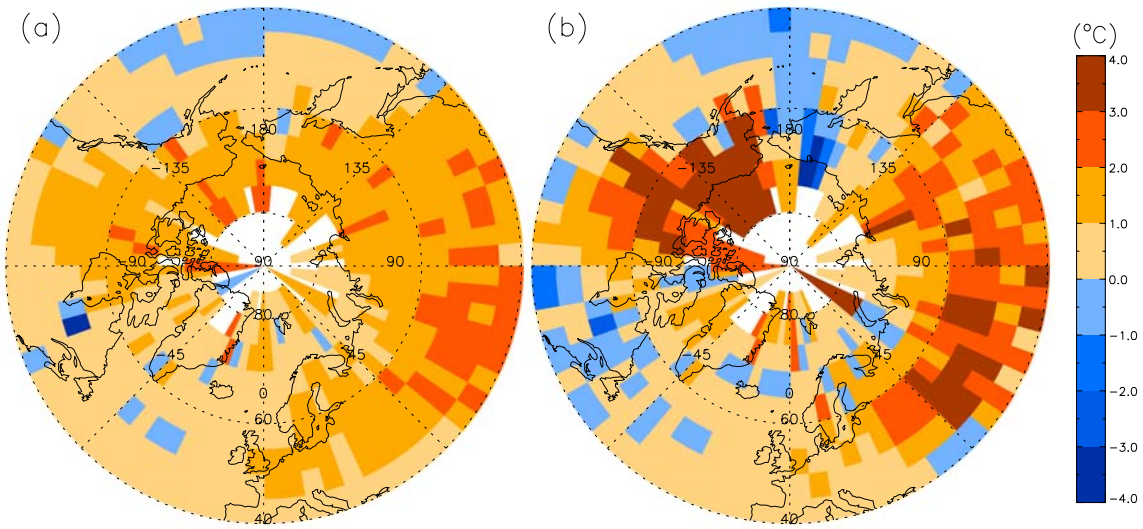

Figure 1-3: Change in observed land and marine temperatures between 1950s (1950-1959) and 2000s (2000-2008) for the region from 40° to 90°N: (a) annual mean; (b) winter (data from Climatic Research Unit (CRU) HadCRUT3v at 5°×5° spatial resolution (Rayner *et al.*, 2006)).

of glaciers (Sapiano *et al.*, 1998), thawing of permafrost (Osterkamp & Romanovsky, 1999), and reductions in sea ice in the Arctic Ocean (Rothrock *et al.*, 1999; Vinnikov *et al.*, 1999). The warming has generally been accompanied by increases in precipitation, but a decrease in the duration of snow cover (ACIA, 2005; Trenberth *et al.*, 2007). Rainfall (liquid precipitation) has increased during the past 50 years over western portions of North American and Eurasia north of 50°N by about 6% (Trenberth *et al.*, 2007). The rainfall season has become longer by up to three weeks in some regions of the boreal high latitudes over the last 50 years (Groisman *et al.*, 2005; Groisman *et al.*, 2007) owing, in particular, to an earlier onset of spring. Therefore, in some regions (southern Canada and western Russia), snow has provided a declining fraction of total annual precipitation (Groisman *et al.*, 2005; Groisman *et al.*, 2007).

Climate projections suggest an amplified warming trend at high latitudes resulting from positive feedbacks involving snow and sea ice, and other processes (IPCC, 2001;

Meehl *et al.*, 2007). The warming is particularly large in autumn and early winter (Holland & Bitz, 2003; Masson-Delmotte *et al.*, 2006). Five Arctic Climate Impact Assessment (ACIA) designated general circulation models project additional warming in the annual mean air temperature of approximately 1°C by 2020, 2 to 3°C by 2050, and 4 to 5°C by 2080 in northern high latitudes under the B2 emissions scenario used by the Intergovernmental Panel on Climate Change (IPCC) (ACIA, 2005).

1.2.2. Ecosystem Responses to Climate Changes

The pan-Arctic region is currently undergoing significant change coinciding with recent and persistent climatic warming (Comiso, 2003; Serreze *et al.*, 2000). Recent climate change in this region is not only linked with global warming but also to changes in large-scale atmospheric (Wallace & Thompson, 2002) and ocean (Siedler *et al.*, 2001) circulation patterns, i.e. oscillations, which is impacting ecological and hydrological processes directly or indirectly. Low temperature, cold-induced water stress and frozen ground (i.e. permafrost), and limited solar irradiance are the primary environmental constraints on vegetation activity and productivity in this domain (e.g. Chapin III *et al.*, 1986; Jolly *et al.*, 2005; Nemani *et al.*, 2003; Shaver & Chapin III, 1980). Low temperatures in this region depress soil microbial activities and correspondingly limit soil nutrient availability for plants (Chapin III *et al.*, 1986). A growing body of evidence indicates that a warming climate is adjusting the environmental constraints to plant phenology and productivity in pan-Arctic ecosystems. The low temperature constraint to photosynthesis and productivity is relaxing with recent climate change related warming of the region, resulting in thawing permafrost and increases in soil active layer depths

(Oelke *et al.*, 2004; Zhang *et al.*, 2005), and earlier and longer growing seasons (ACIA, 2004, 2005; IPCC, 2001; Kimball *et al.*, 2006a; McDonald *et al.*, 2004; Trenberth *et al.*, 2007). However, warmer temperatures have also coincided with increasing vegetation water stress in some regions (Angert *et al.*, 2005; Schindler & Donahue, 2006). Solar radiation can be influenced by cloud cover through a reduction of incident solar radiation (Nardino & Georgiadis, 2003). Wang & Key (2003) reported that the slightly increasing cloud amount in spring and summer in the Arctic may be damping the increase in surface temperature to some degree. Soil microbial activities and N mineralization are adjusted by climate change related changes in the state of soil thawing-freezing and the amount and duration of snow cover (Brooks & Williams, 1999).

Ecological and hydrological processes are strongly coupled in the Pan-Arctic domain. The processes of precipitation and snowmelt change soil moisture and water availability for plants, which directly impact the hydrological cycle through canopy transpiration and precipitation interception and evaporation. Ecological responses to these changes include earlier onset and lengthening growing seasons (Kimball *et al.*, 2006a; McDonald *et al.*, 2004; Sturm *et al.*, 2001), increased vegetation structure and growth (Lucht *et al.*, 2002; Sturm *et al.*, 2001), alteration of land-atmosphere CO_2 exchange (Oechel *et al.*, 2000; Oechel *et al.*, 1998; Serreze *et al.*, 2000), increased soil decomposition and soil carbon release (Chapin *et al.*, 1996; McKane *et al.*, 1997; Tarnocai, 2006), and alterations in ecosystem structure (Callaghan *et al.*, 2004b) as well as the biodiversity and distribution of species (Callaghan *et al.*, 2004a). Observed hydrological responses in arctic tundra and boreal forests include changes in seasonality and magnitude of river discharge (McClelland *et al.*, 2006), thawing and degradation of

permafrost (Oelke *et al.*, 2004; Zhang *et al.*, 2005) and associated rapid gains/losses in areal coverage of lakes and open water bodies (Smith *et al.*, 2005), increasing soil active layer depths (Overduin *et al.*, 2006; Zhang *et al.*, 2005), and receding glaciers (Hinzman *et al.*, 2005; White *et al.*, 2007).

Climatic change and corresponding ecosystem responses in the pan-Arctic domain have and/or will have worldwide physical, ecological, social and economic impacts and consequences (ACIA, 2004, 2005) including: (1) magnifying global warming by reducing surface reflectivity through melting of snow and ice and shifting of vegetation, interrupting ocean circulation through increasing freshwater supply to the ocean, and releasing greenhouse gases from soils and coastal oceans, (2) shifting vegetation zones and altering the function and structure of ecosystems and biodiversity, altering the distributions and adaptations of species, (3) increasing ecological disturbances such as insect outbreaks and forest fires, (4) exposing coastal communities and facilities to increasing storms, coastal erosion and flooding (5) disrupting transportation, buildings and other infrastructure by thawing ground, (6) impacting the economy and culture of indigenous communities, and (7) influencing marine transport through sea level rise and decreasing sea ice cover.

1.2.3. Recent and Ongoing Interdisciplinary Research within the Pan-Arctic Region

Many interdisciplinary research projects have been conducted within the Pan-Arctic region in recent years to assess climate change and to investigate northern ecosystem vulnerability and response to global warming. Some of these projects are still ongoing and vary at spatial scales ranging from local site to basin and region and at

temporal scales from years and decades to millennia. These projects include the Long Term Ecological Research (LTER) at the headwaters of the Kuparuk River Basin (ARC LTER; http://ecosystems.mbl.edu/ARC/) and Bonanza Creek (Bonanza Creek LTER; http://www.lternet.edu/sites/bnz/), the Land-Atmosphere-Ice Interactions (LAII; http://www.laii.uaf.edu/), the Boreal Ecosystem-Atmosphere Study (BOREAS; http://daac.ornl.gov/BOREAS/bhs/BOREAS_Home.html), the Arctic Transitions in the Land Atmosphere System (ATLAS; http://www.arts.monash.edu.au/ges/research/climate/atlas/), Paleoenvironmental ARCtic Sciences (PARCS; http://www.ncdc.noaa.gov/paleo/parcs/index.html), the Western Arctic Linkage Experiment (WALE; http://picea.sel.uaf.edu/projects/wale.html), Arctic Climate Impact Assessment (ACIA; http://www.acia.uaf.edu/), the International Polar Year (IPY) 2007-2008 (http://classic.ipy.org/index.php), Synthesis of Arctic System Science (SASS; http://www.arcus.org/arcss/sass/), and Study of the Northern Alaska Coastal System (SNACS; http://www.arcus.org/arcss/snacs/).

LTER: The Arctic LTER site (Hobbie *et al.*, 1995) is in the foothills region of the North Slope of Alaska and includes the entire Toolik Lake watershed and adjacent watershed of the upper Kuparuk River, down to the confluence of these two watersheds. The project started from 1980 and is ongoing. The goals are to understand the controls of arctic ecosystem structure and function and to predict the effect of environmental change through long-term monitoring and surveys of natural variation of ecosystem characteristics, through experimental manipulation of ecosystems for years and decades and through synthesis of results and predictive modeling at ecosystem and watershed scales. The Bonanza Creek LTER site (Chapin III *et al.*, 2006) is located in the boreal forest of interior Alaska, was established in 1987 and is in its third funding cycle. It

focuses on improving understanding of the long-term consequences of climate change and disturbance in the Alaskan boreal forest and documenting the major controls over forest dynamics, biogeochemistry, and disturbance and their interactions in the face of a changing climate.

LAII: The LAII flux study focused on studying processes controlling the fluxes of carbon dioxide, methane, water, energy, and nutrients between tundra ecosystems and the atmosphere and ocean in the Kuparuk River Basin (8,140 km^2) in northern Alaska and was conducted over a 4 year period (1993-1996) by a group of soil scientists, hydrologists, atmospheric scientists, biogeochemists, modeler, and ecosystem scientists mainly through the measurement of trace gas (CO_2 and CH_4) fluxes or the process and manipulation studies (Kane & Reeburgh, 1998).

BOREAS: The BOREAS project was initiated as a large-scale international investigation focused on improving understanding of the exchanges of radiative energy, sensible heat, water, CO_2, and other radiatively active trace gases between the boreal forest and the lower atmosphere (Sellers *et al.*, 1997). A primary objective of BOREAS was to collect the data needed to improve computer simulation models of the important processes controlling these exchanges so that scientists can anticipate the effects of global change, principally altered temperature and precipitation patterns, on the biome (Sellers *et al.*, 1997). The field phase of the experiment extended from 1993 to 1997 and included two series of intensive field campaigns in 1994 and 1996.

ATLAS: The ATLAS project succeeded the LAII Flux Study. The ATLAS project also concentrated on the exchange of mass and energy between terrestrial ecosystems in the Arctic and the atmosphere and ocean but expanded its spatial scope of

interest from a hydrologic basin to the Western Arctic region (i.e., Alaska and the Russian Far East) and to the circumpolar Arctic (McGuire *et al.*, 2003). Its key goal was to improve understanding of controls over spatial and temporal variability of terrestrial processes in the Arctic that have potential consequences for the climate system, i.e., processes that affect the exchange of water and energy with the atmosphere, the exchange of radiatively active gases with the atmosphere, and the delivery of freshwater to the Arctic Ocean (McGuire *et al.*, 2003).

PARCS: The PARCS program was a coordinated effort of the NSF Arctic System Science (ARCSS) and Earth System History (ESH) programs from 2000 – 2005 (PARCS, 1999). PARCS had two specific research goals: (1) to recover and synthesize a network of high-resolution (annual to decadal) Holocene paleoenvironmental records that span at least 2,000 years and extend through the 20^{th} century for addressing the periodicity and persistence of climatic states within the Arctic and their inter-relation with the global climate system and (2) to contribute to an understanding of a warmer Arctic by describing the state of marine, terrestrial, and biological systems during periods when the Arctic shifted toward and experienced warmer conditions in the past.

WALE: The WALE project lasted from 2002 to 2005 and was designed to assess the ability of models to simulate water/energy and CO_2 exchange with the atmosphere, and freshwater delivery to the ocean for the Alaskan region in the 1980s and 1990s. Its primary goal was to better understand uncertainties of simulated hydrologic and ecosystem dynamics of the western Arctic in the context of: (1) uncertainties in the data available to drive the models and (2) different approaches to simulating regional hydrology and ecosystem dynamics (McGuire *et al.*, 2008). The western Arctic was the

spatial domain and 1981-2000 was the temporal extent of this analysis to evaluate uncertainties in regional hydrology and carbon estimates associated with alternative driving datasets and simulation models.

ACIA: The ACIA is an international project of the Arctic Council and the International Arctic Science Committee (IASC) to evaluate and synthesize knowledge on climate variability, climate change, and increased ultraviolet radiation and their consequences. The results of this assessment were released at the ACIA International Scientific Symposium held in Reykjavik, Iceland in November 2004 (ACIA, 2004).

IPY 2007-2008: The International Council for Science (ICSU) and the World Meteorological Organization (WMO) sponsored the Fourth IPY (International Polar Year), i.e. the IPY 2007-2008. The concept of the IPY 2007-2008 is of an international programme of coordinated, interdisciplinary scientific research and observations in the Earth's Polar Regions to explore new scientific frontiers, deepen our understanding of polar processes and their global linkages, increase our ability to detect changes, attract and develop the next generation of polar scientists, engineers and logistics experts, and capture the interest of schoolchildren, the public and decision-makers (http://classic.ipy.org/).

SASS: The SASS is an ongoing effort of the NSF ARCSS Program and currently consists of 17 funded projects focused on advancing understanding of the arctic system by building on and integrating existing data and knowledge to advance understanding of linkages, interactions, and feedbacks among components of the arctic system

SNACS: The SNACS is another ongoing effort of the NSF ARCSS Program and is composed of two science plans: Land-Shelf Interactions (LSI) and Pan-Arctic Cycles,

Transitions, and Sustainability (PACTS). The LSI research effort is centered on the land-sea margin in the Arctic, focusing on the scientific challenges of environmental change on human and biological communities and related physical and chemical systems (Cooper, 2003). Its goal is to lay the groundwork for a coordinated, interdisciplinary research opportunity in the Arctic that would focus on the coastal zone, and would support land, river, and sea-based researchers. The PACTS research effort is focused on transition and changes in arctic biophysical, biogeochemical ad social systems (Sturm *et al.*, 2003). The focus of the research is the interaction of physical and living systems (e.g. the hydrological cycle and tundra ecosystems) rather than the individual systems themselves. It builds on ideas and research accomplishments from the LAII program, but represents a departure from previous plans by having a more explicit emphasis on biotic and abiotic interactions. Its scale and scope are larger as well, with a regional viewpoint that seeks to understand the Pan-Arctic as a large complex system (Sturm *et al.*, 2003).

The earlier projects were generally focused on monitoring changes at high latitudes, measuring the fluxes of carbon dioxide, methane, water, energy, and nutrients, inspecting the underlying mechanisms controlling arctic and boreal ecosystem structure and function, and evaluating the role of high latitudes, especially the Arctic, in the global system through *in situ* measurements and experimental manipulations at the site or basin level. These precedent scientific efforts provided a large amount of data and knowledge to understand the effects of global environmental and climatic changes in the high latitudes and a solid scientific basis for further research and the prediction of future global climate change. However, these efforts largely consisted of detailed site level studies or involved relatively small areas within the larger Arctic and Boreal region. Most

of these projects were also limited to a few years. Although these projects had a multi-disciplinary focus, detailed analyses of linkages and interactions between ecological and hydrological processes at regional scales were lacking. In view of the tremendous spatial and temporal variability of boreal and Arctic biomes, there is a need to examine the integrative effects of these processes across the entire pan-Arctic in order to determine the net response of the region to recent climate change and potential trajectories of change under future warming. Therefore, the following scientific projects have expanded to encompass regional and even continent scale process. The study technology has also moved from site-level experiments to modeling and satellite remote sensing.

1.3. Importance of Satellite Remote Sensing Approaches and Ecological Modeling

Due to the remoteness and climatic challenges of Arctic and boreal regions, small-scale vegetation studies may be ideal, but are not always feasible (Jacobsen & Hansen, 1999; Stow *et al.*, 1993), nor necessarily useful in extrapolating to broader expanses of land (Davidson & Csillag, 2001; Dungan, 1995; Hope *et al.*, 1995; Lobo *et al.*, 1998). Remote sensing from airborne and satellite platforms can provide spatially-contiguous data on vegetation and geomorphic patterns and characterize surface variables that control carbon and water fluxes over landscapes and regions, which can be utilized to estimate patterns of carbon and water fluxes from plot to regional scales (Hope *et al.*, 1995; Stow *et al.*, 1998). This capability is especially important in arctic and boreal environments where it is difficult to move across the landscape on foot or by vehicle, and the remoteness of study sites often limits the opportunity and period for field campaigns as a function of accessibility, financial cost, and extreme weather conditions (Jacobsen &

Hansen, 1999; Lévesque, 1996; Shippert *et al.*, 1995; Stow *et al.*, 1993). Previous integrative regional scientific studies such as LTER, LAII, BOREAS, and ATLAS acquired the data needed to improve ecological and hydrological models and to improve our understanding of the dependence of biophysical processes on physical climate variations within the Pan-Arctic region. These studies show that remote sensing based approaches are effective and necessary for studying biophysical processes and environmental changes in remote, extensive arctic and boreal ecosystems.

In addition, the application of process-based ecosystem models provides an effective supplement to remote sensing since these models account for underlying processes and detailed coupling between ecological and hydrologic processes, which can be used to compare against remote sensing based observations of vegetation patterns and comparatively simple models of productivity, carbon and water exchange. Ecosystem process models also represent an efficient approach to test hypotheses and extend limited observations in space and time. Conversely, remote sensing can be used with relatively sparse surface biophysical network measurements to validate ecosystem models.

The early development of remote sensing as a scientific field is closely tied to developments in photography (Elachi & van Zyl, 2006). The first recorded aerial photographs were taken from an airplane piloted by Wilbur Wright in 1909 over Centocelli, Italy. During World War II, research was conducted on the spectral reflectance properties of natural terrain and the availability of photographic emulsions for aerial color infrared photography. In 1956, Colwell performed some of the early experiments on the use of special-purpose aerial photography for the classification and recognition of vegetation types and the detection of diseased and damaged vegetation.

Beginning in the mid-1960s, a large number of studies on the application of color infrared and multispectral photography were undertaken under the sponsorship of NASA, leading to the launch of multispectral imagers on the Landsat satellites in the 1970s. The Landsat program provides the longest continuous remote sensing data series for monitoring and managing Earth's resources. The later NOAA series of satellites carrying the Advanced Very High Resolution Radiometer (AVHRR) instruments were launched since 1978. The AVHRR instruments were originally used to monitor clouds and to measure thermal emissions, but the Normalized Difference Vegetation Index (NDVI) calculated from the spectral reflectance measurements acquired in the red and near-infrared regions by the NOAA AVHRR instruments were found to be highly related to vegetation photosynthetic capacity and sensitive to vegetation structure (Tucker, 1979). At the same time, the Scanning Multichannel Microwave Radiometer (SMMR) instruments onboard the Seasat and Nimbus 7 satellites measured dual-polarized microwave brightness temperatures, at 6.63, 10.69, 18.0, 21.0 and 37.0 GHz frequencies, from the Earth's atmosphere and surface since 1978, resulting in the creation of an areal sea-ice climatology for the Arctic and Antarctic. Its successor, the Special Sensor Microwave/Imager (SSM/I) provides similar microwave radiometric observations at 19.35, 22.235, 37.0 and 85.5 GHz since 1987. Passive microwave observations at certain frequencies from SMMR and SSM/I are sensitive to a variety of land surface features including fractional open water, vegetation biomass, freeze-thaw state, sea ice and snow cover.

The latest generation of NASA's Earth Observing System (EOS) satellites provide continuous satellite remote sensing based global observations and an

unprecedented array of global daily monitoring capabilities at moderate spatial resolution, including multi-band optical-infrared and passive microwave based measurements from the MODerate-resolution Imaging Spectroradiometer (MODIS), Advanced Space-borne Thermal Emission and Reflection Radiometer (ASTER) and Advanced Microwave Scanning Radiometer for EOS (AMSR-E).

1.4. Objectives and Hypotheses

This investigation is supported by the NSF's Office of Polar Programs as part of the PACTS plan of the SNACS project (grant numbers 3702AP15297803211 and 0732954), the NASA Earth Science Enterprise Program (NNG04GJ44G) and the NASA Earth and Space Science Fellowship Program (NNX07AN78H). It is focused on spatial patterns and temporal dynamics of carbon flux, water flux, energy balance, vegetation changes and disturbances induced by climate change in Pan-Arctic ecosystems. To this end, satellite remote sensing observations and process-based ecosystem modeling are used. Therefore, the objectives of this dissertation are to:

1. Determine uncertainties in model reanalyses based surface meteorology for the pan-Arctic domain and associated impacts of these uncertainties on regional satellite remote sensing based vegetation productivity simulation; correct the reanalysis based meteorology inputs using available weather station network observations to reduce uncertainties regarding vegetation productivity simulation;

2. Quantify the spatial patterns, temporal anomalies and recent trends in annual growing seasons and vegetation productivity in the pan-Arctic domain and associated environmental constraints to these processes by combining NOAA AVHRR and NASA

MODIS satellite sensor time series (1982 onward) derived measures of vegetation structure (LAI) and productivity (GPP, NPP) and land cover, with SSM/I time-series (1988 onward) brightness temperature derived measurements of the timing and length of annual frozen and non-frozen seasons;

3. Develop satellite remote sensing based methods to quantify spatial patterns and recent changes in evapotranspiration (ET) and the terrestrial water balance under recent climate warming, and associated changes to vegetation structure, productivity, and water use efficiency over the domain;

4. Assess the impacts of large-scale atmospheric and ocean circulation patterns (i.e. teleconnections) on satellite remote sensing based measures of vegetation productivity and freeze-thaw dynamics, and determine linkages between these patterns and temporal anomalies in northern atmospheric CO_2 concentrations;

5. Validate the results of satellite remote sensing based approaches using biophysical measurements from regional eddy covariance flux tower and stand inventory networks.

I base this effort on four primary hypotheses:

1. Persistent warming of boreal forest and tundra ecosystems over the last two decades has promoted a general increase in vegetation productivity through the gradual release of low temperature constraints to photosynthesis and lengthening vegetation growing seasons.

2. Warming-induced advances in the timing of spring thaw and increased length of the non-frozen season are promoting drier conditions through increasing water losses

such as increasing evapotranspiration (ET), permafrost thaw and associated increases in soil active layer depths, and earlier snowmelt;

3. Increasing drought stress is counteracting the positive productivity effects of longer growing seasons and reduced low temperature stress.

4. Large-scale atmospheric and ocean oscillations (i.e. teleconnections) contribute to variation in northern atmospheric CO_2 anomalies by regulating spatial patterns and temporal anomalies in vegetation productivity.

1.5. Dissertation Structure

This dissertation consists of six chapters. In Chapter 1, I introduce the background for this investigation involving climatic change and associated ecosystems responses in the pan-Arctic region, the science rationale, objectives and hypotheses for this investigation.

In Chapter 2, I focus on the uncertainty analysis of general circulation model (GCM) based meteorology reanalyses, and the corresponding sensitivity of satellite remote sensing based vegetation productivity estimates to these uncertainties. Moreover, I introduce a regional meteorology correction scheme using observations from the regional weather station network to reduce uncertainty in the GCM based meteorology reanalyses and corresponding satellite remote sensing based vegetation productivity estimates. A condensed version of this chapter was published in the Journal of Geophysical Research-Biosciences in 2007 (Zhang *et al.*, 2007a).

In Chapter3, I analyze changes in vegetation productivity and phenology (e.g. growing season onset and end), and landscape seasonal freeze-thaw derived from satellite

remote sensing observations during the recent decades. I also validate the satellite derived results using available ground observations, quantify the climatic drivers of recent vegetation changes, and evaluate linkages between vegetation productivity and seasonal freeze-thaw timing. A condensed version of this chapter was published in the Journal of Geophysical Research-Biosciences in 2008 (Zhang *et al.*, 2008).

Chapter 4 is focused on the development of a satellite remote sensing based evapotranspiration algorithm and recent changes in ET and the associated water balance across the pan-Arctic study region. The results of the satellite-based ET algorithm are validated using the multi-year observations from regional eddy covariance flux tower sites within the study region. The work of this chapter was submitted to the Journal of Hydrology and is currently in review (Zhang *et al.*, in review).

Chapter 5 is aimed at quantifying teleconnections between large-scale atmospheric and oceanic oscillations and vegetation productivity within the pan-Arctic domain. I examine how these oscillations influence vegetation productivity by impacting the growing season and terrestrial water balance, resulting in better understanding of the connections between northern terrestrial ecosystems and the atmosphere and oceans under a warming climate. A condensed version of this chapter was published in the Geophysical Research Letters in 2007 (Zhang *et al.*, 2007b).

Chapter 6 summarizes the major conclusions of this dissertation, the broader implications of this research, and suggestions for future research in this field.

1.6. References Cited

ACIA (2004) *Impacts of a warming Arctic*. Cambridge University Press, Cambridge.

ACIA (2005) *Arctic climate impact assessment*. Cambridge University Press, Cambridge.

Angert, A., Biraud, S., Bonfils, C., Henning, C.C., Buermann, W., Pinzon, J., Tucker, C.J., & Fung, I. (2005) Drier summers cancel out the CO_2 uptake enhancement induced by warmer springs. *Proceedings of the National Academy of Sciences*, **102**, 10823-10827.

Arno, S.F. & Hammerly, R.P. (1984) *Timberline, mountain and arctic forest frontiers*. The Mountaineers, Seattle.

Bonan, G.B. (2008) Forests and climate change: Forcings, feedbacks, and the climate benefits of forests. *Science*, **320**, 1444-1449.

Bonan, G.B. & Shugart, H.H. (1989) Environmental factors and ecological processes in boreal forests. *Annual Review in Ecology and Systematics*, **20**, 128.

Broecker, W.S. (1991) The great ocean conveyor. *Oceanography*, **4**, 79-89.

Broecker, W.S. (1997) Thermohaline circulation, the Achilles heel of our climate system: Will man-made CO2 upset the current balance? *Science*, **278**, 1582-1588.

Broecker, W.S. & Denton, G.H. (1990) What Drives Glacial Cycles. *Scientific American*, **262**, 48-56.

Brooks, P.D. & Williams, M.W. (1999) Snowpack controls on nitrogen cycling and export in seasonally snow-covered catchments. *Hydrological Processes*, **13**, 2177-2190.

Callaghan, T.V., Bjorn, L.O., Chernov, Y., Chapin, T., Christensen, T.R., Huntley, B., Ims, R.A., Johansson, M., et al. (2004a) Biodiversity, distributions and adaptations of arctic species in the context of environmental change. *Ambio*, **33**, 404-417.

Callaghan, T.V., Bjorn, L.O., Chernov, Y., Chapin, T., Christensen, T.R., Huntley, B., Ims, R.A., Johansson, M., et al. (2004b) Effects on the structure of arctic ecosystems in the short- and long-term perspectives. *Ambio*, **33**, 436-447.

Chapin, F.S., Zimov, S.A., Shaver, G.R., & Hobbie, S.E. (1996) CO_2 fluctuation at high latitudes. *Nature*, **383**, 585-586.

Chapin III, F.S., McGuire, D., Ruess, R.W., Walker, M.W., Boone, R.D., Edwards, M.E., Finnery, B.P., Hinzman, L.D., et al. (2006). Summary and synthesis: Past and future changes in the Alaskan boreal forest. In *Alaska's changing Boreal Forest* (eds F.S. Chapin III, M.W. Oswood, K.V. Cleve, L.A. Viereck, D.L. Verbyla & M.C. Chapin). Oxford University Press, New York.

Chapin III, F.S., Shaver, G.R., & Kedrowski, R.A. (1986) Environmental Controls over Carbon, Nitrogen and Phosphorus Fractions in Eriophorum-Vaginatum in Alaskan Tussock Tundra. *Journal of Ecology*, **74**, 167-195.

Comiso, J. (2003) Warming trends in the Arctic from clear sky satellite observations. *Journal of Climate*, **16**, 3498-3510.

Cooper, L.W. (2003). Land-shelf interactions: A scientific initiative in the arctic near-shore. RAISE/LSI Project Management Office, University of Tennessee, 10515 Research Drive, Suite 100, Knoxville TN 37932, USA.

Davidson, A. & Csillag, F. (2001) The influence of vegetation index and spatial resolution on a two-date remote sensing-derived relation to C4 species coverage. *Remote Sensing of Environment*, **75**, 138-151.

Dungan, J.L. (1995) Geostatistical approaches for spatial estimation of vegetation quantities using ground and image data. In Remote Sensing in Action, Proceedings of the 21st Annual Conference, pp. 947-954. Remote Sensing Society 1995.

Elachi, C. & van Zyl, J. (2006) *Introduction to the physics and techniques of remote sensing*, 2nd edn. John Wiley & Sons, Inc., New Jersey.

Friedl, M.A., McIver, D.K., Hodges, J.C.F., Zhang, X.Y., Muchoney, D., Strahler, A.H., Woodcock, C.E., Gopal, S., et al. (2002) Global land cover mapping from MODIS: algorithms and early results. *Remote Sensing of Environment*, **83**, 287-302.

Gorham, E. (1991) Northern Peatlands - Role in the Carbon-Cycle and Probable Responses to Climatic Warming. *Ecological Applications*, **1**, 182-195.

Groisman, P.Y., Knight, R.W., Easterling, D.R., Karl, T.R., Hegerl, G.C., & Razuvaev, V.A.N. (2005) Trends in intense precipitation in the climate record. *Journal of Climate*, **18**, 1326-1350.

Groisman, P.Y., Sherstyukov, B.G., Razuvaev, V.N., Knight, R.W., Enloe, J.G., Stroumentova, N.S., Whitfield, P.H., Forland, E., et al. (2007) Potential forest fire danger over Northern Eurasia: Changes during the 20th century. *Global and Planetary Change*, **56**, 371-386.

Hassol, S.J., Berner, J., Callaghan, T.V., Fox, S., Furgal, C., Hoel, A.H., Instanes, A., Juday, G.P., et al. (2004) *Impacts of a warming Arctic*. Cambridge University Press, Cambridge.

Hinzman, L.D., Bettez, N.D., Bolton, W.R., Chapin, F.S., Dyurgerov, M.B., Fastie, C.L., Griffith, B., Hollister, R.D., et al. (2005) Evidence and implications of recent

climate change in northern Alaska and other arctic regions. *Climatic Change*, **72**, 251-298.

Hobbie, J.E., Deegan, L.A., Peterson, B.J., Rastetter, E.B., Shaver, G.R., Kling, G.W., O'Brien, W.J., Chapin, F.S.T., et al. (1995). Long-term measurements at the Arctic LTER site. In *Ecological Time Series* (eds T.M. Powell & J.H. Steele), pp. 391-409. Chapman and Hall, New York.

Holland, M.M. & Bitz, C.M. (2003) Polar amplification of climate change in coupled models. *Climate Dynamics*, **21**, 221-232.

Hope, A.S., Fleming, J.B., Vourlitis, G., Stow, D.A., Oechel, W.C., & Hack, T. (1995) Relating CO_2 fluxes to spectral vegetation indices in tundra landscape: importance of footprint definition. *Polar Record*, **31**, 245-250.

IPCC (2001). Climate change 2001: The scientific basis. In *Contribution of working group I to the third assessment report of the IPCC* (eds J.T. Houghton, Y. Ding, D.J. Griggs, M. Noguer, P.J. van der Linden & D. Su). Cambridge University Press, UK.

Jacobsen, A. & Hansen, B.U. (1999) Estimation of the soil heat flux net radiation ratio based on spectral vegetation indexes in high-latitude Arctic areas. *International Journal of Remote Sensing*, **20**, 445-461.

Jolly, W.M., Nemani, R., & Running, S.W. (2005) A generalized, bioclimatic index to predict foliar phenology in response to climate. *Global Change Biology*, **11**, 619-632.

Kane, D.L. & Reeburgh, W.S. (1998) Introduction to special section: Land-Air-Ice Interactions (LAII) Flux Study. *Journal of Geophysical Research-Atmospheres*, **103**, 28913-28915.

Kasischke, E.S. (2000). Boreal ecosystems in the global carbon cycle. In *Fire, Climate Change, and Carbon Cycling in the Boreal Forest* (eds E.S. Kasischke & B.J. Stocks), pp. 19-29. Springer-Verlag New York, Inc., New York.

Kimball, J.S., McDonald, K.C., & Zhao, M. (2006a) Spring thaw and its effect on terrestrial vegetation productivity in the Western Arctic observed from satellite microwave and optical remote sensing. *Earth Interactions*, **10**, 1-22.

Kimball, J.S., Zhao, M., McDonald, K.C., & Running, S.W. (2006b) Satellite remote sensing of terrestrial net primary production for the pan-Arctic basin and Alaska. *Mitigation and Adaptation Strategies for Global Change*, **11**, 782-804, doi:10.1007/s11027-005-9014-5.

Lal, R. & Kimble, J.M. (2000). Soil C pool and dynamics in cold ecoregions. In *Advances in soil science: Global climate change and cold regions ecosystems* (eds R. Lal, J.M. Kimble & B.A. Steward), pp. 3-28. Lewis Publishers, New York.

Levermann, A., Mignot, J., Nawrath, S., & Rahmstorf, S. (2007) The role of Northern sea ice cover for the weakening of the thermohaline circulation under global warming. *Journal of Climate*, **20**, 4160-4171.

Lévesque, E. (1996) Minimum area and cover-abundance scales as applied to polar desert vegetation. *Arctic and Alpine Research*, **28**, 156-162.

Lobo, A., Moloney, K., Chic, O., & Chiariello, N. (1998) Analysis of fine-scale spatial pattern of a grassland from remotely-sensed imagery and field collected data. *Landscape Ecology*, **13**, 111-131.

Lucht, W., Prentice, I.C., Myneni, R.B., Sitch, S., Friedlingstein, P., Cramer, W., Bousquet, P., Buermann, W., et al. (2002) Climatic control of the High-latitude vegetation greening trend and pinatubo effect. *Science*, **296**, 1687-1689.

Masson-Delmotte, V., Kageyama, M., Braconnot, P., Charbit, S., Krinner, G., Ritz, C., Guilyardi, E., Jouzel, J., et al. (2006) Past and future polar amplification of climate change: climate model intercomparisons and ice-core constraints (vol 26, pg 513, 2006). *Climate Dynamics*, **27**, 437-440.

McClelland, J.W., Déry, S.J., Peterson, B.J., Holmes, R.M., & Wood, E.F. (2006) A pan-arctic evaluation of changes in river discharge during the latter half of the 20th century. *Geophysical Research Letters*, **33**, L06715, doi:10.1029/2006GL025753.

McDonald, K.C., Kimball, J.S., Njoku, E., Zimmermann, R., & Zhao, M. (2004) Variability in springtime thaw in the terrestrial high latitudes: Monitoring a major control on the biospheric assimilation of atmospheric CO2 with spaceborne microwave remote sensing. *Earth Interactions*, **8**, 1-22.

McGuire, A.D., Sturm, M., & Chapin, F.S. (2003) Arctic transitions in the land-atmosphere system (ATLAS): Background, objectives, results, and future directions. *Journal of Geophysical Research-Atmospheres*, **D2**, 8166, doi:10.1029/2002JD002367.

McGuire, A.D., Walsh, J.E., Kimball, J.S., Clein, J.S., Euskirchen, S.E., Drobot, S., Herzfeld, U.C., Maslanik, J., et al. (2008) The western Arctic Linkage Experiment (WALE): Overview and synthesis. *Earth Interactions*, **12**, 1-13.

McKane, R.B., Rastetter, E.B., Shaver, G.R., Nadelhoffer, K.J., Giblin, A.E., Laundre, J.A., & Chapin, F.S. (1997) Climatic effects on tundra carbon storage inferred from experimental data and a model. *Ecology*, **78**, 1170-1187.

Meehl, G.A., Stocker, T.F., Collins, W.D., Friedlingstein, P., Gaye, A.T., Gregory, J.M., Kitoh, A., Knutti, R., et al. (2007). Global climate projections. In *Climate Change 2007: The Physical Science Basis* (eds S. Solomon, D. Qin, M. Manning, Z. Chen, M. Marquis, K.B. Averyt, M. Tignor & H.L. Miller). Cambridge University Press, Cambridge, United Kingdom and New York, NY, USA.

Nardino, M. & Georgiadis, T. (2003) Cloud type and cloud cover effects on the surface radiative balance at several Polar sites. *Theoretical and Applied Climatology*, **74**, 203-215.

Nemani, R.R., Keeling, C.D., Hashimoto, H., Jolly, W.M., Piper, S.C., Tucker, C.J., Myneni, R.B., & Running, S.W. (2003) Climate-driven increases in global terrestrial net primary production from 1982 to 1999. *Science*, **300**, 1560-1563.

Oberbauer, S.F., Tenhunen, J.D., & Reynolds, J.F. (1991) Environmental-Effects on CO_2 Efflux from Water Track and Tussock Tundra in Arctic Alaska, USA. *Arctic and Alpine Research*, **23**, 162-169.

Oechel, W.C., Vourlities, G.L., Hastings, S.J., Zulueta, R.M., Hinzman, L.D., & Kane, D.L. (2000) Acclimation of ecosystem CO_2 exchange in the Alaskan Arctic in response to decadal climatic warming. *Nature*, **406**, 978-981.

Oechel, W.C., Vourlitis, G.L., Hastings, S.J., Ault Jr., R.P., & Bryant, P. (1998) The effects of water table manipulation and elevated temperature on the net CO_2 flux of wet sedge tundra ecosystems. *Global Change Biology*, **4**, 77-90.

Oelke, C., Zhang, T., & Serreze, M.C. (2004) Modeling evidence for recent warming of the Arctic soil thermal regime. *Geophysical Research Letters*, **31**, L07208, doi:10.1029/2003GL019300.

Osterkamp, T.E. & Romanovsky, V.E. (1999) Evidence for warming and thawing of discontinuous permafrost in Alaska. *Permafrost and Periglacial Processes*, **10**, 17-37.

Overduin, P.P., Kane, D.L., & van Loon, W.K.P. (2006) Measuring thermal conductivity in freezing and thawing soil using the soil temperature response to heating. *Cold Regions Science and Technology*, **45**, 8-22.

PARCS (1999) *The arctic paleosciences in the context of global change research - PARCS, paleoenvironmental arctic sciences*. ESH Secretariat, AGU, Washington, D. C.

Peterson, T.C. & Vose, R.S. (1997) An overview of the global historical climatology network temperature database. *Bulletin of the American Meteorological Society*, **78**, 2837-2849.

Rahmstorf, S. (2006). Thermohaline ocean circulation. In *Encyclopedia of Quaternary Sciences* (ed S.A. Elias), pp. 739-750. Elsevier, Amsterdam.

Rayner, N.A., Brohan, P., Parker, D.E., Folland, C.K., Kennedy, J.J., Vanicek, M., Ansell, T.J., & Tett, S.F.B. (2006) Improved analyses of changes and uncertainties in sea surface temperature measured in situ since the mid-nineteenth century: The HadSST2 dataset. *Journal of Climate*, **19**, 446-469.

Rothrock, D.A., Yu, Y., & Maykut, G.A. (1999) Thinning of the Arctic sea-ice cover. *Geophysical Research Letters*, **26**, 3469-3472.

Sapiano, J.J., Harrison, W.D., & Echelmeyer, K.A. (1998) Elevation, volume and terminus changes of nine glaciers in North America. *Journal of Glaciology*, **44**, 119-135.

Saugier, B., Roy, J., & Mooney, H.A. (2001). Estimations of global terrestrial productivity: Coverging toward a single number? In *Terrestrial global productivity* (eds J. Roy, B. Saugier & H.A. Mooney), pp. 543-557. Academic Press, San Diego.

Sayre, A.P. (1994) *Taiga*. Twenty-First Century Books, New York.

Schindler, D.W. & Donahue, W.F. (2006) An impending water crisis in Canada's western prairie provinces. *Proceedings of the National Academy of Sciences*, **103**, 7210-7216.

Sellers, P.J., Hall, F.G., Kelly, R.D., Black, A., Baldocchi, D., Berry, J., Ryan, M., Ranson, K.J., et al. (1997) BOREAS in 1997: Experiment overview, scientific results, and future directions. *Journal of Geophysical Research-Atmospheres*, **102**, 28731-28769.

Serreze, M.C., Walsh, J.E., Chapin, F.S., Osterkamp, T., Dyurgerov, M., Romanovsky, V., Oechel, W.C., Morison, J., et al. (2000) Observational evidence of recent change in the northern high-latitude environment. *Climatic Change*, **46**, 159-207.

Shaver, G.R. & Chapin III, F.S. (1980) Response to fertilization by various plant growth forms in an Alaskan tundra: Nutrient accumulation and growth. *Ecology*, **61**, 662-675.

Shippert, M.M., Walker, D.A., Auerbach, N.A., & Lewis, B.E. (1995) Biomass and leaf-area index maps derived from SPOT images for Toolik Lake and Imnavait Creek areas, Alaska. *Polar Record*, **31**, 147-154.

Siedler, G., Church, J., & Gould, J. (2001) *Ocean circulation and climate: Observing and modelling the global ocean*. Academic Press, London.

Smith, L.C., Sheng, Y., MacDonald, G.M., & Hinzman, L.D. (2005) Disappearing Arctic lakes. *Science*, **308**, 1429-1429.

Stow, D., Hope, A., Boynton, W., Phinn, S., Walker, D., & Auerbach, N. (1998) Satellite-derived vegetation index and cover type maps for estimating carbon dioxide flux for arctic tundra regions. *Geomorphology*, **21**, 313-327.

Stow, D.A., Burns, B.H., & Hope, A.S. (1993) Spectral, Spatial and Temporal Characteristics of Arctic Tundra Reflectance. *International Journal of Remote Sensing*, **14**, 2445-2462.

Sturm, M., Chapin III, F.S., Edwards, M.E., Griffith, D.B., Huntington, H.P., Kofinas, G.P., Lloyd, A.H., Peterson, B.J., et al. (2003) PACTS (Pan-Arctic Cycles, Transitions, and Sustainability): A science plan. Land-Atmosphere-Ice Interactions Science Management Office, P.O. Box 757740, University of Alaska Fairbanks, Fairbanks, Alaska 99775-7740.

Sturm, M., Racine, C., & Tape, K. (2001) Increasing shrub abundance in the Arctic. *Nature*, **411**, 546-547.

Tarnocai, C. (2006) The effect of climate change on carbon in Canadian peatlands. *Global and Planetary Change*, **53**, 222-232.

Trenberth, K.E., Jones, P.D., Ambenje, P., Bojariu, R., Easterling, D., Klein Tank, A., Parker, D., Rahimzadeh, et al. (2007). Observations: surface and atmospheric climate change. In *Climate Change 2007: The Physical Science Basis* (eds S. Solomon, D. Qin, M. Manning, Z. Chen, M. Marquis, K.B. Averyt, M. Tignor & H.L. Miller). Cambridge University Press, Cambridge, United Kingdom and New York, NY, USA.

Tucker, C.J. (1979) Red and photographic infrared linear combinations for monitoring vegetation. *Remote Sensing of Environment*, **8**, 127-150.

Vinnikov, K.Y., Robock, A., Stouffer, R.J., Walsh, J.E., Parkinson, C.L., Cavalieri, D.J., Mitchell, J.F.B., Garrett, D., et al. (1999) Global warming and Northern Hemisphere sea ice extent. *Science*, **286**, 1934-1937.

Wallace, J.M. & Thompson, D.W.J. (2002) Annular modes and climate prediction. *Physics Today*, **55**, 28-33.

Wang, X. & Key, J.R. (2003) Recent trends in arctic surface, cloud, and radiation properties from space. *Science*, **299**, 1725-1728.

White, D., Hinzman, L., Alessa, L., Cassano, J., Chambers, M., Falkner, K., Francis, J., Gutowski Jr., W.J., et al. (2007) The arctic freshwater system: Changes and

impacts. *Journal of Geophysical Research*, **112**, G04S54, doi:10.1029/2006JG000353.

Whitney, S. (2002). *Tundra*, http://www.blueplanetbiomes.org/tundra_plant_page.htm. Last updated on 11/7/2006.

Woodward, S.L. (2003) *Biomes of earth: terrestrial, aquatic, and human-dominated*. Greenwood Press, Westport.

Zhang, T.J., Frauenfeld, O.W., Serreze, M.C., Etringer, A., Oelke, C., McCreight, J., Barry, R.G., Gilichinsky, D., et al. (2005) Spatial and temporal variability in active layer thickness over the Russian Arctic drainage basin. *Journal of Geophysical Research*, **110**, D16101, doi:10.1029/2004JD005642.

Zhang, K., Kimball, J.S., Hogg, E.H., Zhao, M., Oechel, W.C., Cassano, J.J., & Running, S.W. (2008) Satellite-based model detection of recent climate-driven changes in northern high-latitude vegetation productivity. *Journal of Geophysical Research*, **113**, G03033, doi:10.1029/2007JG000621.

Zhang, K., Kimball, J.S., Zhao, M., Oechel, W.C., Cassano, J., & Running, S.W. (2007a) Sensitivity of pan-Arctic terrestrial net primary productivity simulations to daily surface meteorology from NCEP-NCAR and ERA-40 reanalysis. *Journal of Geophysical Research*, **112**, G01011, doi:10.1029/2006JG000249.

Zhang, K., Kimball, J.S., McDonald, K.C., Cassano, J.J., & Running, S.W. (2007b) Impacts of large-scale oscillations on pan-Arctic terrestrial net primary production. *Geophysical Research Letters*, **34**, L21403, doi:10.1029/2007GL031605.

Zhang, K., Kimball, J.S., Mu, Q., Jones, L.A., Goetz, S.J., & Running, S.W. (2009) Satellite based analysis of northern ET trends and associated changes in the regional water balance from 1983 to 2005. *Journal of Hydrology*: in review.

CHAPTER 2: SENSITIVITY ANALYSIS OF SATELLITE-DERIVED VEGETATION PRODUCTIVITY TO METEOROLOGY REANALYSES AND REGIONAL CORRECTION OF METEOROLOGY REANALYSES

2.1. Meteorology Reanalyses

2.1.1. ERA-40

ERA-40 stands for the 45-year European Centre for Medium-range Weather Forecasts (ECMWF) Re-Analysis, and is a re-analysis of meteorological observations from September 1957 to August 2002 produced by the ECMWF in collaboration with many institutions (Uppala *et al.*, 2005). The ERA-40 product is a second-generation reanalysis carried out by ECMWF that benefits from many recent changes made to the operational ECMWF data assimilation system, and lessons learned from the earlier ERA-15 (15-year ECMWF Re-Analysis) reanalysis (Uppala *et al.*, 2005). The observing system changed considerably over this re-analysis period, with assimilable data provided by a succession of satellite-borne instruments from the 1970s onwards, supplemented by increasing numbers of ascents since the late 1980s. The observations used for ERA-40 include data from the operational archives of ECMWF supplemented by operational data archived by NCEP and the Japan Meteorological Agency. Data were also supplied to ECMWF by other institutions especially for use in the re-analysis. The ERA-40 uses a three-dimensional variational data assimilation system, including the spectral T159 model, with 60 hybrid sigma-pressure levels to produce the surface meteorology (Uppala *et al.*, 2005).

I used the ERA-40 Basic Atmospheric Data Sets product (http://www.ecmwf.int/products/data/archive/descriptions/e4/basic.html), which is produced with four times per day temporal repeat at $2.5° \times 2.5°$ spatial resolution globally. Surface downward solar shortwave radiation and 2-m air and dew point temperatures from the ERA-40 re-analysis were used to derive the daily downward solar shortwave radiation ($SW_{\downarrow}$: MJ m^{-2} d^{-1}), and daily minimum ($T_{\min}$: °C) and average (T_{avg} : °C) surface air temperatures for this investigation. Air vapor pressure (e_a : Pa) was calculated from the daily dew point (T_{dew} : °C), while daytime air vapor pressure deficit (VPD : Pa) was derived as the daily difference between e_a and the saturation vapor pressure (e_{sat} : Pa) of the mean daytime air temperature. These meteorology variables are used to drive the satellite remote sensing based vegetation productivity and surface evapotranspiration models.

2.1.2. NCEP/NCAR Re-analysis

The NCEP/NCAR Re-analysis or NNR is the National Centers for Environmental Prediction-National Center for Atmospheric Research (NCEP-NCAR) reanalysis (Kalnay *et al.*, 1996; Kistler *et al.*, 2001). The NNR is a first-generation reanalysis from 1948, which uses a frozen state-of-the-art analysis/forecast system and performs data assimilation using a variety of surface measurements to guide model simulations, including land surface, ship, rawinsonde, pibal, aircraft, satellite and other data (Kalnay *et al.*, 1996). The NNR is based on the NCEP global spectral model with 28 vertical "sigma" levels and a triangular truncation of 62 waves (T62), equivalent to about 210-km horizontal resolution (Kalnay *et al.*, 1996). The analysis scheme is a three-dimensional

variational scheme cast in spectral space denoted spectral statistical interpolation (Parrish & Derber, 1992). The reanalysis data assimilation system continues to be used with current data in real time (Climate Data Assimilation System or CDAS), so that its products are available from 1948 to the present.

In this study, I chose the NCEP/NCAR Reanalysis 1: Surface Flux product (http://www.cdc.noaa.gov/data/gridded/data.ncep.reanalysis.surfaceflux.html), which is provided four times per day in a global Gaussian grid (T62, 192×94 points) format with approximately $1.9° \times 1.875°$ spatial resolution. The surface downward solar shortwave radiation and surface air temperature data of the NNR were extracted to derive $SW_{\downarrow}$, $T_{\min}$ and T_{avg}. The e_a term used to derive daily VPD was calculated from NNR specific humidity and surface pressure information.

2.2. Validation and Inter-comparison of Meteorology Reanalyses

The reanalysis meteorological inputs for the satellite remote sensing based vegetation productivity model include $SW_{\downarrow}$, $T_{\min}$, T_{avg} and e_a (see section 2.3). I used daily minimum and average air temperatures and dew point from 1994-2000 for 1,122 World Meteorology Organization (WMO) stations (Figure 2-1) above 45°N to assess the relative accuracy of the reanalysis meteorological inputs across the pan-Arctic domain. These data were obtained from the National Climatic Data Center Climate Services Branch (NCDC CSB; http://www.ncdc.noaa.gov) Global Surface Summary of the Day. I also evaluated daily downward solar shortwave radiation inputs of the meteorology reanalyses using daily solar radiation data from 17 sites distributed across Alaska from

1982-1990, and available from the National Solar Radiation Data Base (NSRDB; http://rredc.nrel.gov/solar/old_data /nsrdb/). To compare the reanalysis data with the station observations, I applied Zhao *et al.*'s spatial interpolation method (2005, equations 3-5) to calculate the reanalysis values at the locations of the weather stations.

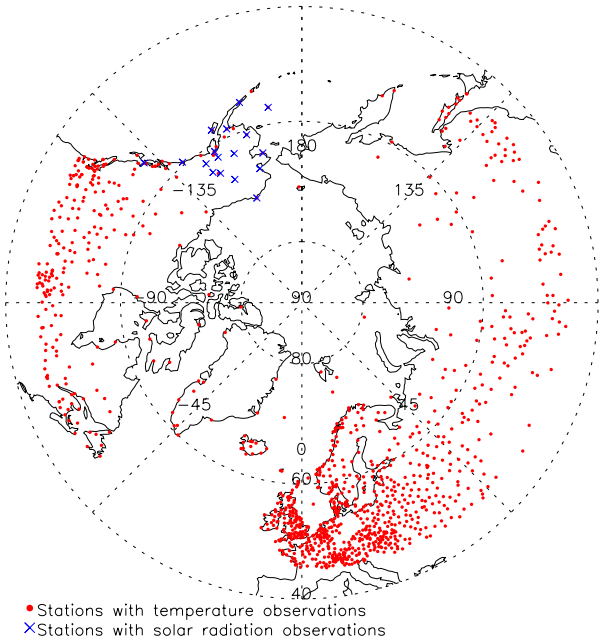

Figure 2-1: Distribution of WMO surface weather stations with daily temperature and dew point observations, and solar radiation observations above 45°N for the validation of meteorology reanalyses.

2.2.1. Validation Procedure

To validate the reanalysis meteorology data, I applied the following procedure. First, I calculated the residuals (ε) that are defined as the true values (x), namely the interpolated observations or measurements from the weather stations, minus the estimated values ($\hat{x}$), i.e. the data from the reanalyses. Analyses of error distribution, and the relative error (δ_ε), simple linear correlation coefficient (r) between the estimated

values and the true values, mean absolute error (MAE) and root mean square error (RMSE) parameters were then used to evaluate accuracy and uncertainty of the two reanalyses. The analysis of statistical error distribution includes the mean ($\bar{\varepsilon}$), median (M_{ε}), standard deviation (i.e. standard error, s_{ε}), first quartile (Q_{1st}), and third quartile (Q_{3rd}) of the residual distribution. The MAE and RMSE were calculated to describe the accuracy of the estimation. The δ_{ε}, defined as the ratio of the absolute value of the mean residual ($\left|\bar{\varepsilon}\right|$) to the mean of the absolute values of observations ($E(|x|)$), was used to show the relative magnitude of the errors, while the r parameter was used to evaluate the strength of the relationships between the estimations and the observations. I also analyzed the temporal and spatial patterns of the reanalysis meteorology error distribution.

2.2.2. Accuracy of Meteorology Reanalyses

Both reanalyses tend to underestimate T_{avg}, while ERA-40 has a smaller bias (i.e. the absolute value of $\bar{\varepsilon}$), a narrower error spread (i.e. higher precision) indicated by the box plot (Figure 2-2 (a)), a higher accuracy denoted by MAE and RMSE, and a higher correlation with surface observations than NNR (Table 2-1 and Figure 2-2 (a)). For T_{min}, ERA-40 has a positive bias whereas NNR has a negative bias with an absolute value. However, ERA-40 T_{min} has a narrower error spread, a higher correlation with the observations but a comparable accuracy relative to NNR T_{min} (Figure 2-2 (b) and Table 2-1). For e_{a}, ERA-40 has a much smaller bias, a much narrower error spread, a higher accuracy and a higher correlation with the observations than NNR, though both reanalyses have positive biases (Table 2-1 and Figure 2-2(c)). Though the magnitudes of

Table 2-1. Comparison of the error distribution, accuracy and correspondence of ERA-40 and NNR meteorological variables relative to the surface weather station observations.

		Error Distribution					Accuracy			
Variables		$\bar{\varepsilon}$	s_ε	Q_{1st}	M_ε	Q_{3rd}	MAE	RMSE	δ_ε	[e]r
[a]T_{avg} (°C)	[c]E	0.1	1.6	-0.4	0	0.6	0.9	1.6	2.0%	0.94***
	[d]N	1.2	2.1	0	0.9	2.2	1.7	2.4	17.9%	0.91***
[a]T_{min} (°C)	E	-1.6	1.7	-2.4	-1.6	-0.8	1.9	2.3	32.8%	0.95***
	N	0.9	2.5	-0.7	0.7	2.1	1.9	2.6	18.0%	0.90***
[a]e_a (Pa)	E	-4.3	77.7	-32.3	-7.6	21.7	46.9	75.1	0.5%	0.93***
	N	-65.5	93.0	-117.2	-74.1	-17.8	91.6	110.2	7.8%	0.90***
[b]$SW_\downarrow$	E	-1.4	1.2	-2.2	-1.2	-0.49	1.5	1.9	19.0%	-0.57**
(MJ m^{-2} d^{-1})	N	-4.9	0.8	-5.7	-5	-4.2	4.9	5.1	66.4%	0.52*

[a] The surface meteorological data are 7-year daily means over the 1994 to 2000 period; the observations come from 1122 weather stations across the domain.
[b] The solar radiation data are 9-year daily means over the 1982 to 1990 period; the observations come from 17 weather stations in Alaska.
[c,d] E and N denote ERA-40 and NNR, respectively.
[e]The significance levels of 0.1, 0.01 and 0.001 are indicated by *, **, and ***, respectively.

the biases for the temperature variables of the two reanalyses are small, the relative errors are still large due to the year-round low temperatures at high latitudes (Table 2-2). While instrumentation biases and inhomogeneities may exist in the weather station observational data, I chose a large station sample size (1,122 stations) to minimize the potential negative effects of individual station bias and compared these data with the interpolated reanalyses data.

Both reanalyses show relatively poor performance for the estimates of downward shortwave solar radiation and tend to overestimate it, though ERA-40 has a lower bias and higher accuracy than NNR. While both reanalyses consider cloud effects, generally poor reanalysis performance relative to surface observations likely reflects limitations in

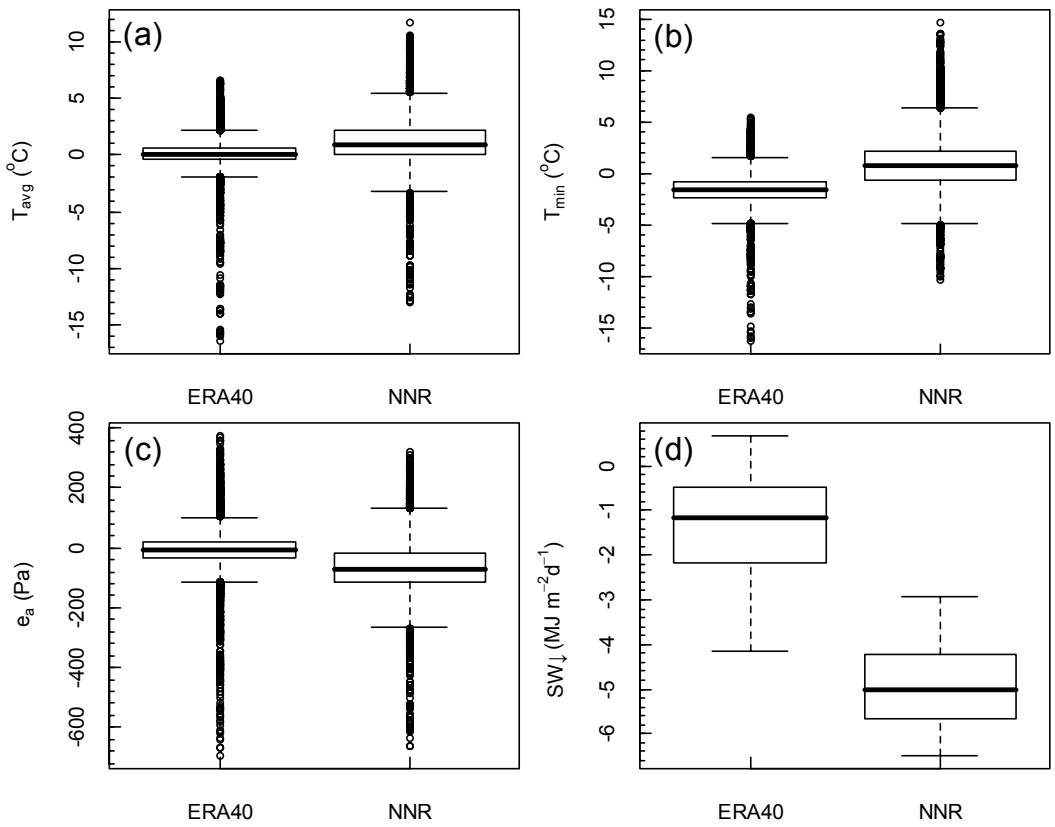

Figure 2-2: Box plots of the residuals in mean T_{avg}, T_{min}, e_a and $SW_{\downarrow}$ of the ERA-40 and NNR meteorology by comparing with the surface weather station observations.

the way the atmospheric models characterize cloud cover heterogeneity and atmospheric solar radiation transmittance. In ERA-40, cloud radiative properties relate more to model parameterization than to the quality of the basic reanalysis fields and are not well simulated, leading to relatively poor characterization of the all-sky radiation budget (Uppala *et al.*, 2005). The study of Yang *et al.* (1999) suggested that the NNR global data assimilation system (GDAS) contains shortcomings in the cloud/moisture parameterizations or deficiencies in the shortwave parameterizations, which lead to the large bias in solar radiation. In addition, while these results indicate generally poor model performance for solar radiation, they are based on comparisons with surface

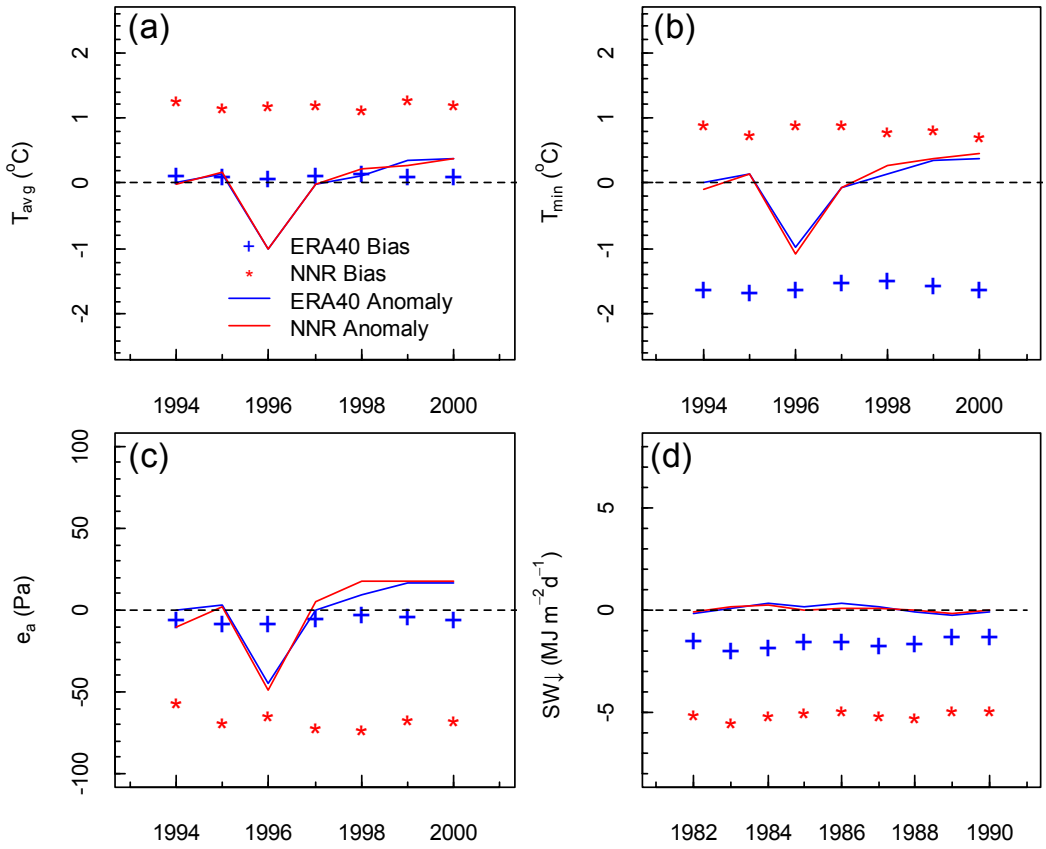

Figure 2-3: Temporal comparison of annual bias, namely mean error (reanalysis – observation), and annual anomalies of ERA-40 and NNR (a) T_{avg}, (b) T_{min}, (c) e_a, and (d) $SW_\downarrow$. Errors are calculated relative to observations from WMO and NSRDB station network.

observations from only 17 stations across Alaska. Model solar radiation performance is likely to vary across the larger pan-Arctic domain and may not be adequately defined from this limited observation network.

The four meteorological variables show no obvious temporal bias (relative to surface weather station observations), i.e. temporally independent for both reanalyses (Figure 2-3). The results of these comparisons indicate that ERA-40 is generally more accurate than NNR for surface air temperature and air vapor pressure, but both reanalyses show similar annual anomalies for the air temperatures, air vapor pressure and solar

radiation (Figure 2-3). These results are also consistent with previous studies (Simmons *et al.*, 2004; Zhao *et al.*, 2006).

Analysis of ERA-40 regional performance (Table 2-2) shows no obvious longitudinal pattern in temperature and e_a accuracies. However, ERA-40 temperatures and e_a show generally better performance in the Arctic relative to Boreal biomes. The NNR performance also showed no obvious longitudinal pattern, but showed higher e_a

Table 2-2. Regional comparison of annual means of daily air temperatures (T_{min} and T_{avg}) and daily mean atmospheric vapor pressure (e_a) from the two reanalyses relative to observed values across the pan-Arctic domain; the results are summarized for major sub-regions within the domain.

Region	[a]**Area (%)**		T_{min} (°C)			T_{avg} (°C)			e_a (Pa)		
			[b]r	$\bar{\varepsilon}$	RMSE	r	$\bar{\varepsilon}$	RMSE	r	$\bar{\varepsilon}$	RMSE
Pan-Arctic	100.0	[c]E	0.95	-1.6	2.3	0.94	0.1	1.6	0.93	-4.3	77.8
		[d]N	0.90	0.9	2.6	0.91	1.2	2.5	0.89	-65.5	113.7
North America	33.7	E	0.93	-1.3	2.4	0.95	0.7	1.8	0.90	26.1	81.4
		N	0.88	1.4	2.9	0.92	2.3	3.1	0.86	-56.8	110.1
Eurasia	66.3	E	0.94	-1.7	2.4	0.93	-0.1	1.7	0.91	-11.7	81.2
		N	0.88	1.0	2.6	0.89	1.1	2.4	0.86	-65.4	118.3
Boreal	39.0	E	0.93	-1.6	2.3	0.91	-0.1	1.6	0.90	-4.5	81.8
		N	0.87	0.8	2.6	0.86	1.2	2.4	0.85	-68.3	118.6
Arctic	33.2	E	0.96	-1.2	2.2	0.97	0.4	1.5	0.95	-3.3	47.9
		N	0.92	1.4	2.9	0.94	1.7	2.6	0.92	-49.5	80.0

[a] Proportional area represented within the entire 25 million km^2 study domain.
[b] All simple correlation coefficients are significant at the 0.001 significant level.
[c,d] E and N denote ERA-40 and NNR, respectively.

accuracy in the Arctic than in boreal regions. The relatively high temporal, spatial and anomaly correlation coefficients between the reanalyses and surface observations also indicate that both NNR and ERA-40 products capture the major climatic patterns and trends for surface air temperature.

To conclude, the ERA-40 surface air temperature, air vapor pressure and downward shortwave solar radiation data generally have higher accuracies and lower biases than the NNR counterpart. The biases and errors in the four meteorological variables of the two reanalyses don't show obvious temporal and spatial patterns in the modern satellite era (post 1978). Relative to air temperature and air vapor pressure, the solar radiation estimates in both reanalysis products have lower correlation with the observations. These results are also consistent with previous studies (Simmons *et al.*, 2004; Zhao *et al.*, 2006). Previous studies indicate a clear improvement of ERA-40 over the earlier NNR during the modern satellite era (post 1978) (Bromwich & Fogt, 2004; Uppala *et al.*, 2005). Bromwich and Fogt (2004) found that ERA-40 produced a generally improved simulation of mean sea level pressure fields after 1978 based on comparisons with Antarctic and southern hemisphere mid- to high-latitude station observations. Simmons *et al.* (2004) found that ERA-40 produced generally closer agreement for simulated surface air temperatures from 1979 onward based on comparisons with the Climatic Research Unit (CRU) CRUTEM2v data set, which is derived directly from monthly surface weather station observations. Bromwich and Wang (2005) also found that ERA-40 showed better overall performance in representing wind fields of the Arctic based on comparisons with rawinsonde data for two independent arctic field experiments.

2.3. Satellite-based Production Efficiency Model

A biome-specific Production Efficiency Model (PEM), i.e. MODIS MOD17A2/A3 algorithms (Heinsch *et al.*, 2003; Running *et al.*, 2004; Running *et al.*, 2000; Zhao *et al.*, 2008), was used to estimate vegetation gross primary production (GPP) and net primary production (NPP) for vegetated grid cells within the study domain using satellite-derived vegetation properties and model reanalysis based daily surface meteorology inputs. The PEM model is based on the original logic of Monteith (1972) and combined with climatic controls on GPP and NPP (Churkina & Running, 1998) and lessons learned from a general process-based ecosystem model, BIOME-BGC (Biome BioGeochemical Cycles) (Running & Hunt, 1993; Thornton & Running, 1999; White *et al.*, 2000). The model is driven by satellite-derived land cover, fractional photosynthetically active radiation (FPAR), leaf area index (LAI) and daily surface meteorology (Running *et al.*, 2000). The model has been successfully applied at global or regional scales (Kimball *et al.*, 2006; Nemani *et al.*, 2003; Zhao *et al.*, 2005; Zhao *et al.*, 2006) and has undergone several revisions in response to extensive, ongoing calibration and verification studies using biophysical information from regional station networks, including boreal and Arctic landscapes (Heinsch *et al.*, 2006; Turner *et al.*, 2003; Turner *et al.*, 2005; Zhao *et al.*, 2005; Zhao *et al.*, 2006).

GPP (g C m^{-2} d^{-1}) is derived on a daily basis as (Running *et al.*, 2000, 2004; Heinsch *et al.*, 2003; Zhao *et al.*, 2008):

$$GPP = \xi \cdot FPAR \cdot PAR \tag{2.1}$$

$$\xi = \xi_{\max} \cdot T_f \cdot VPD_f \tag{2.2}$$

where ξ is a light use efficiency parameter (g C MJ^{-1}) for the conversion of photosynthetically active radiation (PAR, MJ m^{-2} d^{-1}) to GPP, where PAR is assumed to represent 45% of downward solar shortwave radiation ($SW_{\downarrow}$); $\xi_{\max}$ is the potential maximum ξ under optimal conditions; T_f is a daily minimum temperature scalar that defines reductions in photosynthesis under low temperature conditions, while VPD_f is a vapor pressure deficit scalar that defines similar reductions under suboptimal surface air vapor pressure deficit and associated daytime water stress conditions. Both T_f and VPD_f are defined from $T_{\min}$ and VPD using simple photosynthetic response curves (Running *et al.*, 2000, 2004; Heinsch *et al.*, 2003; Zhao *et al.*, 2008).

Net primary production (NPP, g C m^{-2} yr^{-1}) is derived on an annual basis as the difference between the annual summation of daily net photosynthesis and autotrophic growth and maintenance respiration:

$$NPP = \sum_{1}^{365} (GPP - R_{m\_lr}) - (R_{m\_w} + R_g) \tag{2.3}$$

where R_{m_lr} (g C m^{-2} d^{-1}) is the daily maintenance respiration of leaves and fine roots; R_{m_w} (g C m^{-2} yr^{-1}) represents the annual maintenance respiration from live wood; and R_g (g C m^{-2} yr^{-1}) represents annual growth respiration. The characteristic response curves for calculating these parameters vary according to major biomes as defined by a Biome Properties Look-Up Table (BPLUT), which was developed from stand level ecophysiological studies (White *et al.*, 2000) and adjusted for the effects of regional meteorological and satellite-based FPAR/LAI data sets (Running *et al.*, 2000; Zhao *et al.*,

2005). $GPP - R_{m\_lr}$ is used as the approximation of daily NPP. To drive the model, satellite-derived land cover, FPAR and LAI data are required with observed or reanalysis daily surface meteorological data including incident $SW_{\downarrow}$, $T_{\min}$, T_{avg} and e_{a} to derive daily GPP and NPP.

2.4. Uncertainty and Sensitivity Analysis of PEM Output

2.4.1. Uncertainty and Sensitivity Analysis Scheme

I constructed the following experimental model and published it in Zhang *et al.* (2007) to determine the effects of ERA-40 and NNR reanalysis meteorological uncertainty on PEM based NPP calculations:

$$Y = f(\widetilde{d}_{SW_{\downarrow}}, \widetilde{\varepsilon}_{\text{T}_{\text{avg}}}, \widetilde{\varepsilon}_{\text{T}_{\min}}, \widetilde{\varepsilon}_{\text{e}_{\text{a}}}) \tag{2.4}$$

where $\widetilde{d}_{SW_{\downarrow}}$, $\widetilde{\varepsilon}_{\text{T}_{\text{avg}}}$, $\widetilde{\varepsilon}_{\text{T}_{\min}}$ and $\widetilde{\varepsilon}_{\text{e}_{\text{a}}}$ are the samples from $d_{SW_{\downarrow}}$, $\varepsilon_{\text{T}_{\text{avg}}}$, $\varepsilon_{\text{T}_{\min}}$ and $\varepsilon_{\text{e}_{\text{a}}}$ populations, respectively, which are defined as follows:

$$d_{SW_{\downarrow}} = \frac{SW_{\downarrow,\text{Obs}}}{SW_{\downarrow,\text{Res}}} \tag{2.5}$$

$$\varepsilon_{\text{T}_{\text{avg}}} = T_{\text{avg,Obs}} - T_{\text{avg,Res}} \tag{2.6}$$

$$\varepsilon_{T_{\min}} = T_{\text{min,Obs}} - T_{\text{min,Res}} \tag{2.7}$$

$$\varepsilon_{e_{\text{a}}} = e_{\text{a,Obs}} - e_{\text{a,Res}} \tag{2.8}$$

where *Obs* denotes the observed value and *Res* denotes the reanalysis value. $\varepsilon_{\text{T}_{\text{avg}}}$, $\varepsilon_{\text{T}_{\min}}$ and $\varepsilon_{\text{e}_{\text{a}}}$ are actually the residuals of T_{avg}, $T_{\min}$ and e_{a}, respectively. I multiplied

$SW_{\downarrow,\mathrm{Res}}$ by $\widetilde{d}_{SW_{\downarrow}}$, added $\widetilde{\varepsilon}_{\mathrm{T_{avg}}}$ to $T_{\mathrm{avg,Res}}$, added $\widetilde{\varepsilon}_{\mathrm{T_{min}}}$ to $T_{\mathrm{min,Res}}$ and added $\widetilde{\varepsilon}_{\mathrm{e_a}}$ to $e_{\mathrm{a,Res}}$ to produce the experimental input data. I used both reanalysis and experimental data with the PEM model to calculate NPP. Finally, I determined *Y* by subtracting the NPP driven by the original reanalysis data from the corresponding experimental input data based NPP results. This provided a relatively simple approach for quantifying PEM error due to input data uncertainty, since Y denotes NPP variability resulting from differences between surface observation and reanalysis meteorological inputs.

To quantify the uncertainty of reanalysis surface meteorology, I first constructed cumulative distribution functions (CDFs) of $d_{SW_{\downarrow}}$, $\varepsilon_{\mathrm{T_{avg}}}$, $\varepsilon_{\mathrm{T_{min}}}$ and $\varepsilon_{\mathrm{e_a}}$. Then, I used a Latin hypercube approach (Helton & Davis, 2003) to sample input variables of the experimental model by: (i) dividing the range of each variable into nS ($nS = 99$ in this experiment) disjoint intervals of equal probability and selecting one value randomly from each interval; (ii) pairing the nS values of $\widetilde{d}_{SW_{\downarrow}}$ randomly without replacement with the nS values for $\widetilde{\varepsilon}_{\mathrm{T_{avg}}}$ to produce nS pairs; (iii) combining the nS pairs randomly without replacement with the nS values for $\widetilde{\varepsilon}_{\mathrm{T_{min}}}$ to produce nS triples; (iv) combining the nS triples randomly without replacement with the nS values for $\widetilde{\varepsilon}_{\mathrm{e_a}}$ to produce nS quadruples.

To determine whether the distribution of points in the scatter plots is nonrandom, (i.e. the significance of $d_{SW_{\mathrm{rad}}}$, $\varepsilon_{\mathrm{T_{avg}}}$, $\varepsilon_{\mathrm{T_{min}}}$ and $\varepsilon_{\mathrm{e_a}}$ effects on Y), I used (i) statistical independence (SI) and (ii) entropy tests (Helton *et al.*, 2006). Both of these tests are based on a gridding method. In this study, I used a 5 by 5 grid. I (i) divided the range of

x ($d_{SW_{\downarrow}}$, $\varepsilon_{T_{avg}}$, $\varepsilon_{T_{min}}$ and ε_{e_a}) into n_x ($n_x = 5$) mutually exclusive and exhaustive subintervals containing equal numbers of sampled values, (ii) divided the range of y (i.e. Y) into n_y ($n_y = 5$) mutually exclusive and exhaustive subintervals containing equal numbers of sampled values, and (iii) counted the number of each cell nO_{rc} . The statistic in the SI test is defined as:

$$T = \sum_{c=1}^{n_x} \sum_{r=1}^{n_y} \left(nO_{rc} - nE_{rc} \right)^2 / nE_{rc} \tag{2.9}$$

where $nE_{rc} = nS / (n_x \cdot n_y)$ is an estimate of the expected number of observations that should fall in cell (r, c); and nS is the sample size. Asymptotically, T follows a χ^2 - distribution with $(n_x - 1)(n_y - 1)$ degrees of freedom when x and y are independent. Thus, $prob_{\chi^2}\left[\widetilde{T} > T \middle| (n_x - 1)(n_y - 1) \right]$ is the probability (i.e. p-value) of obtaining a value of $\widetilde{T}$ that exceeds T when x and y are independent. Measures of entropy provide another grid-based procedure to assess the strength of nonlinear relationships between x and y . The following quantities are defined as (Helton *et al.*, 2006):

$$H(y) = -\sum_{r=1}^{n_y} \left(n_{y_r} / nS \right) \ln\left(n_{y_r} / nS \right) \tag{2.10}$$

$$H(x) = -\sum_{c=1}^{n_x} \left(n_{x_c} / nS \right) \ln\left(n_{x_c} / nS \right) \tag{2.11}$$

$$H(y,x) = -\sum_{r=1}^{n_y} \sum_{c=1}^{n_x} \left(nO_{rc} / nS \right) \ln\left(nO_{rc} / nS \right) \tag{2.12}$$

$$U(y,x) = 2\left[H(y) + H(x) - H(y,x) \right] / \left[H(y) + H(x) \right] \tag{2.13}$$

where n_{x_c} is the number of points in column *c*; n_{y_r} is the number of points in row *r*; $H(y)$ and $H(x)$ are estimates of the entropy associated with y and x; and $U(y,x)$ is the entropy-based measure of the strength of the association between x and y.

2.4.2. Implementation of the Uncertainty and Sensitivity Analysis Schemes

In this part of the study, I used satellite-derived vegetation properties including monthly FPAR and LAI from the NOAA AVHRR Pathfinder (PAL) 16 km data set from 1982 to 2000 (Myneni *et al.*, 1997b). The LAI and FPAR data are based on a monthly maximum value compositing of AVHRR spectral reflectance data to mitigate cloud cover, smoke, and other atmospheric aerosol contamination effects. These data were reprojected to the 25-km polar EASE-grid format using a nearest-neighbor resampling scheme. The monthly LAI and FPAR data were then resampled to a daily time step by temporal linear interpolation of adjacent monthly values. The daily linear interpolation approach used for this investigation is a relatively simple, but effective means for producing a daily FPAR and LAI time-series for PEM simulations and has been used extensively for global vegetation analyses of the AVHRR Pathfinder series (Kimball *et al.*, 2006; Myneni *et al.*, 1997a; Nemani *et al.*, 2003).

In this study, VPD is calculated from daily average air temperature (T_{avg}) and mean daily atmospheric vapor pressure (e_{a}). Therefore, the actual PEM daily climate drivers include SW_{rad}, T_{min}, T_{avg} and e_{a}. I applied the above uncertainty and sensitivity analysis scheme (section 2.4.1) for the six general biome types defined by the regional land cover map, including evergreen needleleaf forest (ENF), deciduous needleleaf forest

(DNF), mixed forest (MF), open shrubland (OSH, i.e. tundra), grassland (GRS) and cropland (CRP), to evaluate the effects of uncertainties in the meteorology reanalyses on the satellite-derived NPP. I generated 99 samples from the cumulative distribution functions (CDFs) (Figure 2-4) of $\varepsilon_{T_{avg}}$, $\varepsilon_{T_{min}}$, ε_{e_a} and $d_{SW_{\downarrow}}$ to drive the experimental models and derived corresponding scatter plots (Figure 2-5) of Y against $d_{SW_{\downarrow}}$, $\varepsilon_{T_{avg}}$, $\varepsilon_{T_{min}}$ and ε_{e_a} for the six general biome types in the pan-Arctic region for both reanalyses.

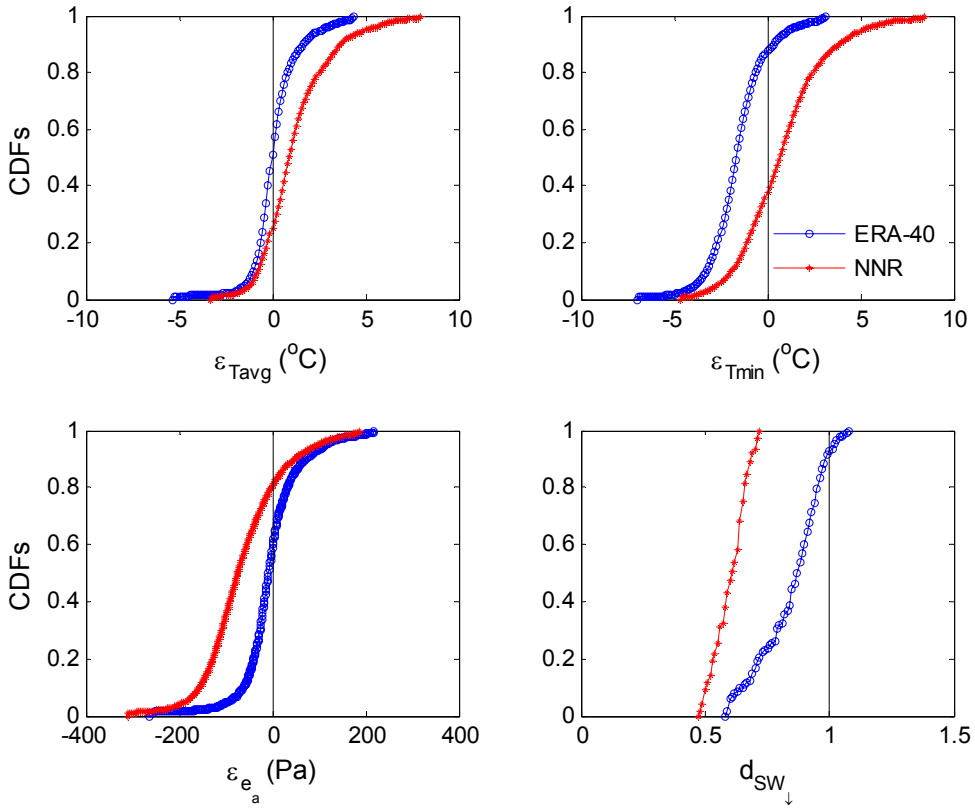

Figure 2-4: The cumulative distribution functions of ε_{Tavg}, ε_{Tmin}, ε_{ea} and $d_{SW\downarrow}$ from ERA-40 and NNR.

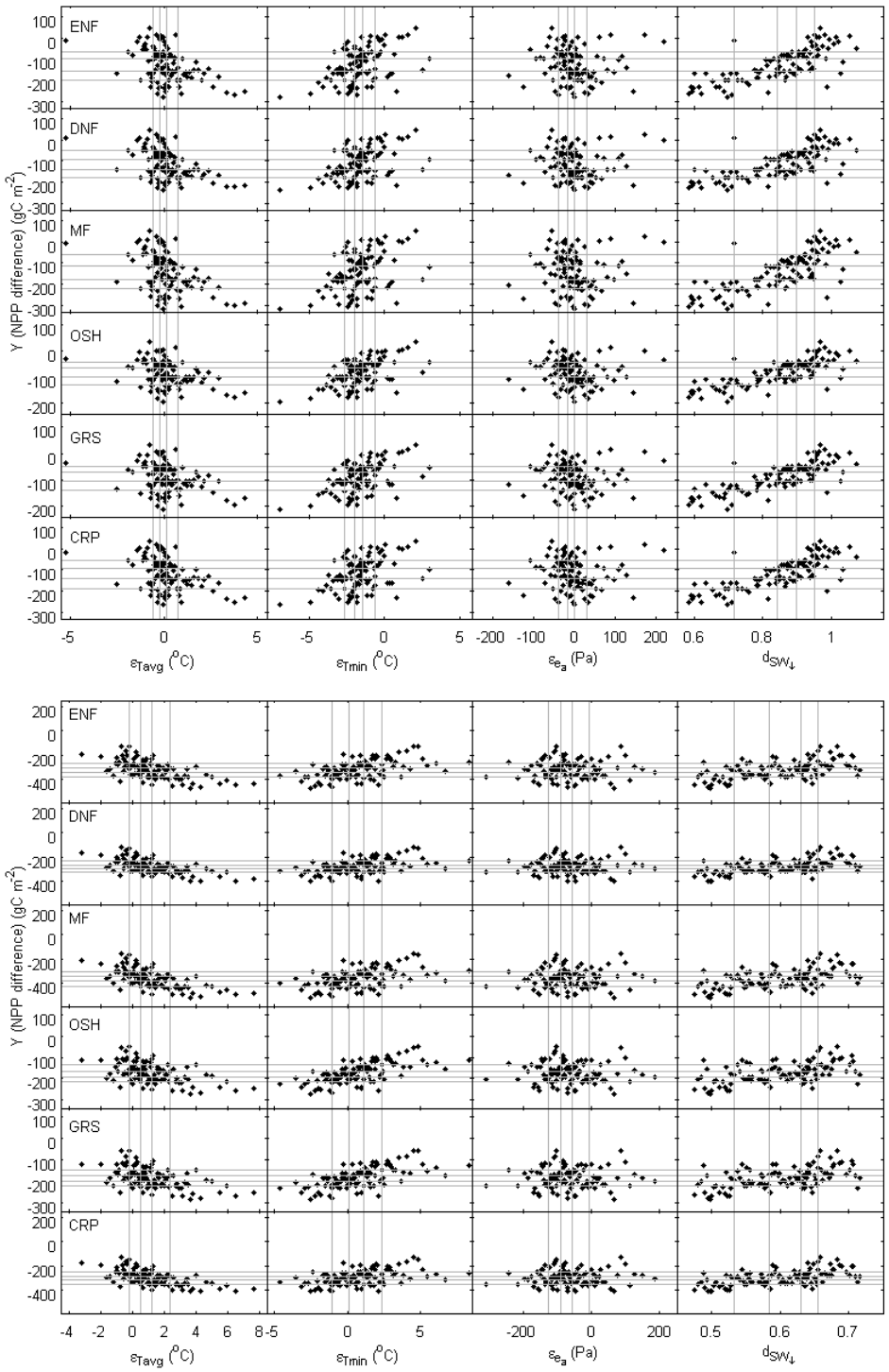

Figure 2-5: Scatter plots of Y vs. ε_{Tavg}, ε_{Tmin} , ε_{ea} and $d_{SW\downarrow}$ from ERA-40 (top) and NNR (bottom) for the six general biome types. The 5×5 grid for the SI and entropy tests is also shown in the graphs.

For the two meteorology reanalyses and the six vegetation types, the scatter plots of y vs. $d_{SW_{\downarrow}}$ show the most obvious non-random patterns followed by the scatter plots of y vs. temperature residuals ($\varepsilon_{T_{avg}}$ and $\varepsilon_{T_{min}}$) (Figure 2-5), while the patterns of y vs. ε_{e_a} are closest to the random pattern. The results of the SI and entropy tests are presented in Table 2-3. The higher values for χ^2 and $U(y,x)$ indicate that y is more sensitive to x. I also calculated the *P*-value for the χ^2 test (Table 2-3). These results are similar for both SI and entropy tests and indicate that PEM based NPP derived from ERA-40 is primarily sensitive to uncertainty in $SW_{\downarrow}$, followed by air temperature ($T_{\min}$ and T_{avg}) as a significant source of model uncertainty for all major biomes within the domain. However, the relative importance of $T_{\min}$ and T_{avg} to PEM based NPP varies for individual biome types. Though ERA-40 shows generally more accurate representation of T_{avg} than $T_{\min}$ (Figure 2-3; Table 2-1), the uncertainty in T_{avg} yields similar impacts on PEM based NPP as the uncertainty in $T_{\min}$. This response occurs because T_{avg} controls model calculations of VPD and vegetation autotrophic respiration. When T_{avg} is underestimated (Figure 2-3), both respiration and VPD are correspondingly underestimated. The latter result can also lead to overestimation of GPP. The coupled effects of these processes can therefore magnify model sensitivity to T_{avg} error. ERA-40 shows relatively accurate representation of e_a; relative to the above parameters, e_a uncertainty for this investigation does not have a significant impact on PEM based NPP results.

Table 2-3. Comparison of grid-based SI test and Entropy values between sensitivity experiment and ERA-40 and NNR uncertainty.

	ERA-40				NNR			
		[a]SI test		[a]Entropy		SI test		Entropy
	Variable	[b]χ^2	*P*-Value	$U(y,x)$	Variable	χ^2	*P*-Value	$U(y,x)$
ENF	$d_{SW_\downarrow}$	109.33	<0.0001	0.3814	$d_{SW_\downarrow}$	50.24	<0.0001	0.1580
	$\varepsilon_{T_{avg}}$	33.07	0.0072	0.1352	$\varepsilon_{T_{avg}}$	46.71	0.0001	0.1497
	$\varepsilon_{T_{min}}$	27.52	0.0361	0.0868	$\varepsilon_{T_{min}}$	31.56	0.0114	0.1174
	ε_{e_a}	15.90	0.4600	0.0514	ε_{e_a}	10.85	0.8186	0.0328
DNF	$d_{SW_\downarrow}$	108.83	<0.0001	0.3446	$d_{SW_\downarrow}$	57.31	<0.0001	0.1665
	$\varepsilon_{T_{avg}}$	41.66	0.0004	0.1608	$\varepsilon_{T_{avg}}$	41.15	0.0005	0.1367
	$\varepsilon_{T_{min}}$	30.04	0.0178	0.1005	$\varepsilon_{T_{min}}$	34.08	0.0053	0.1172
	ε_{e_a}	14.89	0.5327	0.0482	ε_{e_a}	12.36	0.7188	0.0359
MF	$d_{SW_\downarrow}$	120.44	<0.0001	0.3900	$d_{SW_\downarrow}$	53.78	<0.0001	0.1834
	$\varepsilon_{T_{avg}}$	36.61	0.0024	0.1448	$\varepsilon_{T_{avg}}$	38.63	0.0012	0.1247
	$\varepsilon_{T_{min}}$	32.57	0.0084	0.1198	$\varepsilon_{T_{min}}$	29.03	0.0237	0.1013
	ε_{e_a}	13.37	0.6455	0.0450	ε_{e_a}	8.32	0.9388	0.0252
OSH	$d_{SW_\downarrow}$	104.28	<0.0001	0.3599	$d_{SW_\downarrow}$	53.78	<0.0001	0.1866
	$\varepsilon_{T_{avg}}$	38.63	0.0012	0.1197	$\varepsilon_{T_{avg}}$	52.26	<0.0001	0.1576
	$\varepsilon_{T_{min}}$	21.96	0.1445	0.0825	$\varepsilon_{T_{min}}$	30.55	0.0154	0.1014
	ε_{e_a}	15.90	0.4600	0.0505	ε_{e_a}	11.35	0.7874	0.0389
GRS	$d_{SW_\downarrow}$	110.34	<0.0001	0.3785	$d_{SW_\downarrow}$	46.71	0.0001	0.1588
	$\varepsilon_{T_{avg}}$	37.62	0.0017	0.1137	$\varepsilon_{T_{avg}}$	44.69	0.0002	0.1362
	$\varepsilon_{T_{min}}$	26.00	0.0540	0.0953	$\varepsilon_{T_{min}}$	33.58	0.0062	0.1120
	ε_{e_a}	20.44	0.2011	0.0641	ε_{e_a}	9.84	0.8748	0.0314
CRP	$d_{SW_\downarrow}$	124.99	<0.0001	0.4087	$d_{SW_\downarrow}$	52.77	<0.0001	0.1684
	$\varepsilon_{T_{avg}}$	33.07	0.0072	0.1352	$\varepsilon_{T_{avg}}$	40.14	0.0007	0.1343
	$\varepsilon_{T_{min}}$	31.05	0.0133	0.1019	$\varepsilon_{T_{min}}$	23.98	0.0899	0.0771
	ε_{e_a}	13.37	0.6455	0.0641	ε_{e_a}	11.86	0.7536	0.0346

[a] Both SI test and entropy test were based on a 5×5 grid; [b] The degrees of freedom were 16.

Analyses of the PEM results derived from the NNR daily meteorology are similar to the ERA-40 based results and indicate that $SW_{\downarrow}$ and temperatures ($T_{\min}$ and T_{avg}) are the most important sources of model NPP uncertainty. Uncertainty in NNR e_a also had the lowest impact on PEM based NPP. The generally low accuracy of $SW_{\downarrow}$ and considerable biases in temperature inputs (Figure 2-1; Table 2-1; Table 2-2) relative to e_a uncertainty yield much larger negative impacts on PEM based NPP results.

Overall, these results show considerable uncertainties in both reanalyses, that significantly impact the spatial and temporal accuracy of PEM based NPP calculations. The ability of regional models to capture the magnitude and spatial and temporal variability in vegetation productivity for the region would be dramatically enhanced if future reanalyses can improve the representation of daily surface meteorology at northern latitudes.

2.4.3. Comparison between PEM NPP Results Driven by ERA-40 and NNR

The spatial distribution of PEM based mean annual NPP (g C m^{-2} yr^{-1}) derived from the two reanalyses for the 19-year (1982-2000) study period are shown in Figure 2-6. The respective mean annual NPP calculations over the entire vegetated area were 257.5 ± 103.9 g C m^2 yr^{-1} and 398.3 ± 172.0 g C m^2 yr^{-1} using ERA-40 and NNR inputs. Calculated mean annual NPP values for the major regional biomes are shown in Table 2-4. The NNR derived mean annual NPP is approximately 54.7% larger than the ERA-40 derived results. The primary reason for this discrepancy is that $SW_{\downarrow}$ from NNR is approximately 39.8% greater than ERA-40 radiation inputs for the region, while NNR

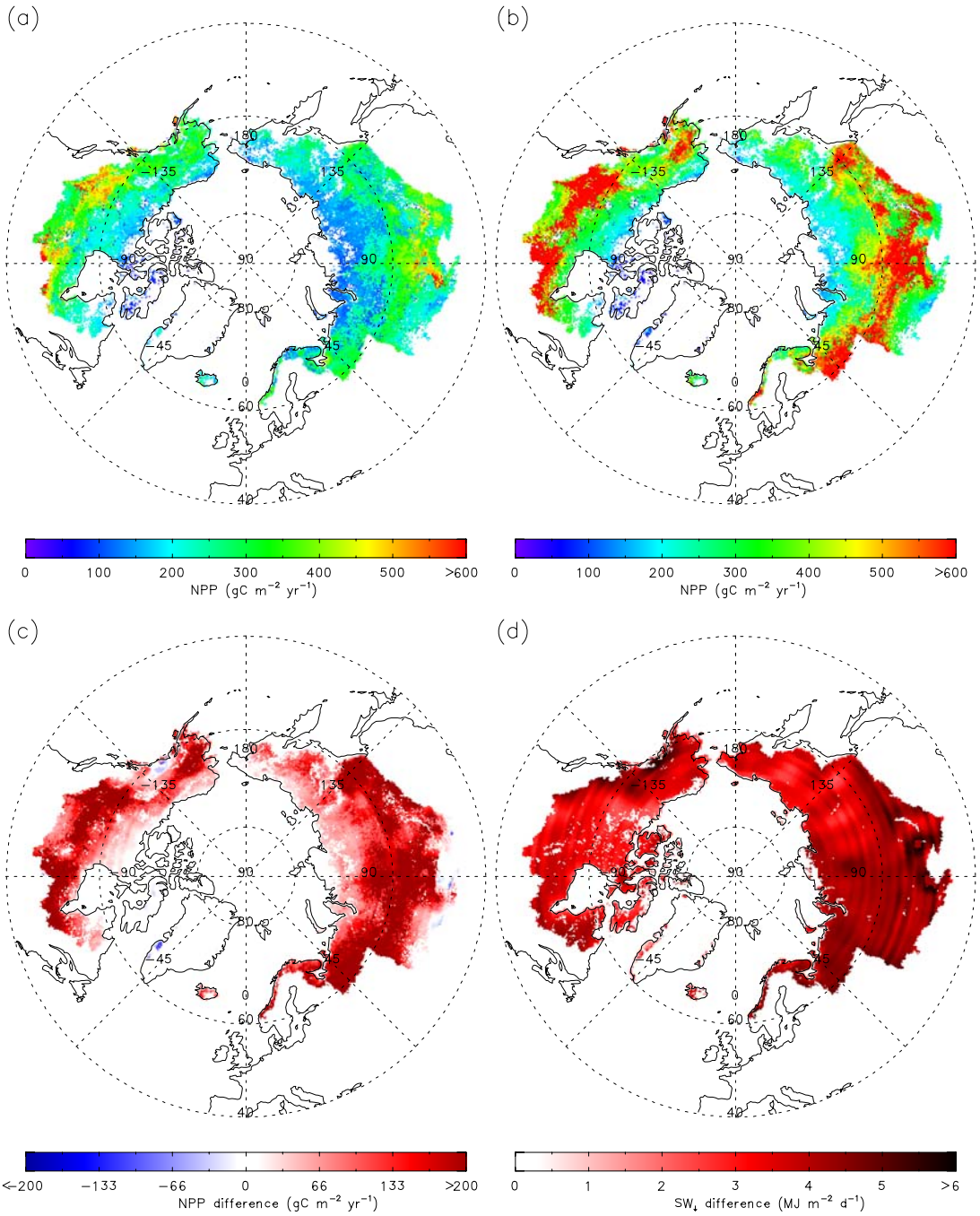

Figure 2-6: Mean annual NPP (g C m^{-2} yr^{-1}) derived from PEM calculations driven by ERA-40 (a) and NNR (b) over the pan-Arctic domain and 19-year (1982-2000) study period. The NPP (c) and $SW_{\downarrow}$ (d) difference maps refer to NNR less ERA-40 results.

Table 2-4. Comparison of PEM based NPP results derived from ERA-40 and NNR inputs for the major biomes within the study domain.

Veg. Type	PEM NPP driven by ERA-40 (g C m^{-2} yr^{-1})		PEM NPP driven by NNR (g C m^{-2} yr^{-1})		Observational Estimates (g C m^{-2} yr^{-1})
	[a]Uncorrected	[b]Corrected	Uncorrected	Corrected	
ENF	294.2 ± 99.4	167.0 ± 99.4	500.0 ± 149.9	178.8 ± 149.9	[c]123 ~ 460 for Siberian and European forests; [d]225 for Alaska Spruce; [e]226 ~ 478 in Central Canada.
DNF	248.8 ± 74.0	136.3 ± 74.0	438.1 ± 121.5	160.1 ± 121.5	
MF	344.2 ± 113.1	201.6 ± 113.1	552.6 ± 158.3	191.1 ± 158.3	
OSH	206.9 ± 75.1	123.0 ± 75.1	293.8 ± 114.8	120.4 ± 114.8	[f]70 ~ 500; mean: 90
GRS	248.6 ± 75.2	158.0 ± 75.2	312.9 ± 112.1	129.0 ± 112.1	[g]137-477
CRP	298.9 ± 99.0	181.3 ± 99.0	441.6 ± 152.8	144.6 ± 152.8	N/A

[a]Mean annual NPP ± standard deviations for 1982-2000 period.
[b]The average NPP difference from the sensitivity experiment was used as the error-correcting term.
[c]Values for Siberian and European forests (Schulze *et al.*, 1999).
[d]Values for mature spruce forests in central Alaska (Ruess *et al.*, 1996).
[e]Values for boreal forests in central Canada (Gower *et al.*, 1997b).
[f]From (Saugier *et al.*, 2001) and (Shaver & Jonasson, 2001).
[g]From (Olson *et al.*, 2001).

T_{avg} inputs were approximately 1.1 ^{o}C lower, on average, than ERA-40 temperatures. Higher $SW_{\downarrow}$ resulted in increases in PEM based GPP, while lower T_{avg} reduced calculated respiration rates; both of these factors resulted in relatively large increases in annual NPP calculations. A map of the mean $SW_{\downarrow}$ difference between the two reanalyses indicates that NNR solar radiation inputs exceeded the ERA-40 values over most of the domain (Figure 2-6). Based on comparisons of reanalysis and observed climate data, the ERA-40 surface meteorology appears to be relatively more reliable. Therefore, the generally lower NPP results derived from the ERA-40 reanalysis may be more realistic than the more productive results derived from NNR.

The Y parameter in Equation 2.4 (i.e., the difference between mean annual NPP values derived from experimental data and original reanalysis data) provides an error-correcting term for adjusting NPP calculations to better reflect surface meteorological observations. The adjusted NPP results are summarized in Table 2-4 for the major regional biomes. These results are quite similar to NPP values reported in the literature for major vegetation types within the domain. Annual NPP for Arctic tundra has been reported to range from approximately 70 g C m^{-2} yr^{-1} for low tundra shrub communities of the high Arctic up to 500 g C m^{-2} yr^{-1} for tall shrub communities for the low Arctic, with an average level of approximately 90 g C m^{-2} yr^{-1} for the global tundra biome (Saugier *et al.*, 2001; Shaver & Jonasson, 2001). Boreal NPP has been reported to range from 123 to 460 g C m^{-2} yr^{-1} for Siberian and European forests, respectively, based on chronosequence studies and national forestry statistics (Schulze *et al.*, 1999). NPP values for mature spruce forests in central Alaska were reported to be approximately 225 g C m^{-2} yr^{-1} (Ruess *et al.*, 1996), while values reported for boreal forests in central Canada range from 226 to 478 g C m^{-2} yr^{-1} (Gower *et al.*, 1997a). NPP observations for grasslands within the region range from 137 to 477 g C m^{-2} yr^{-1} and generally show intermediate levels of productivity between tundra and boreal forest biomes (Olson *et al.*, 2001).

Despite large differences in $SW_{\downarrow}$ between ERA-40 and NNR, both data sets generally capture the 19-year meteorological trend for the domain (see Section 2.2.2). Though the sensitivity analysis shows that uncertainty in temperature and $SW_{\downarrow}$ inputs had the largest impact on PEM based NPP for both reanalyses, the comparison of annual variability in the model results indicates that this uncertainty does not result in large

differences in NPP anomalies. The reason for this pattern is that $SW_{\downarrow}$ in both reanalyses shows only small and insignificant variability over the 19-year study period despite generally poor correspondence between reanalysis and observed $SW_{\downarrow}$ anomalies. In addition, reanalysis temperature anomalies were highly correlated with observed temperature anomalies. However, in some regions, e.g. Southern Alaska and Southern Eurasia, reanalysis over predictions of $SW_{\downarrow}$ exaggerated predicted NPP magnitudes and temporal anomalies.

Statistical analysis of these results indicated that annual NPP variability derived from both reanalyses was primarily driven by changes in terrestrial vegetation cover as detected by satellite LAI measurements ($r = 0.73$, $P < 0.001$ for PEM NPP driven by ERA-40; $r = 0.76$, $P < 0.001$ for PEM NPP driven by NNR) (Figure 2-7). The positive trend in LAI and NPP for the 19-year period has been attributed to earlier thawing and increasing growing season length with regional warming (Kimball *et al.*, 2006; Lucht *et al.*, 2002). Of the climatic variables, air temperature was the primary driver of annual NPP variability as derived from ERA-40 ($r = 0.22$, $P = 0.1840$) and NNR ($r = 0.45$, $P = 0.0264$) reanalysis climate drivers. The NPP response to air temperature was generally larger using NNR inputs relative to ERA-40, though calculated NPP anomalies and regional trends derived from both reanalyses were generally quite similar.

The calculated annual NPP anomalies derived from the two reanalyses for the pan-Arctic domain and 19-year study period are shown in Figure 2-7. Calculated mean

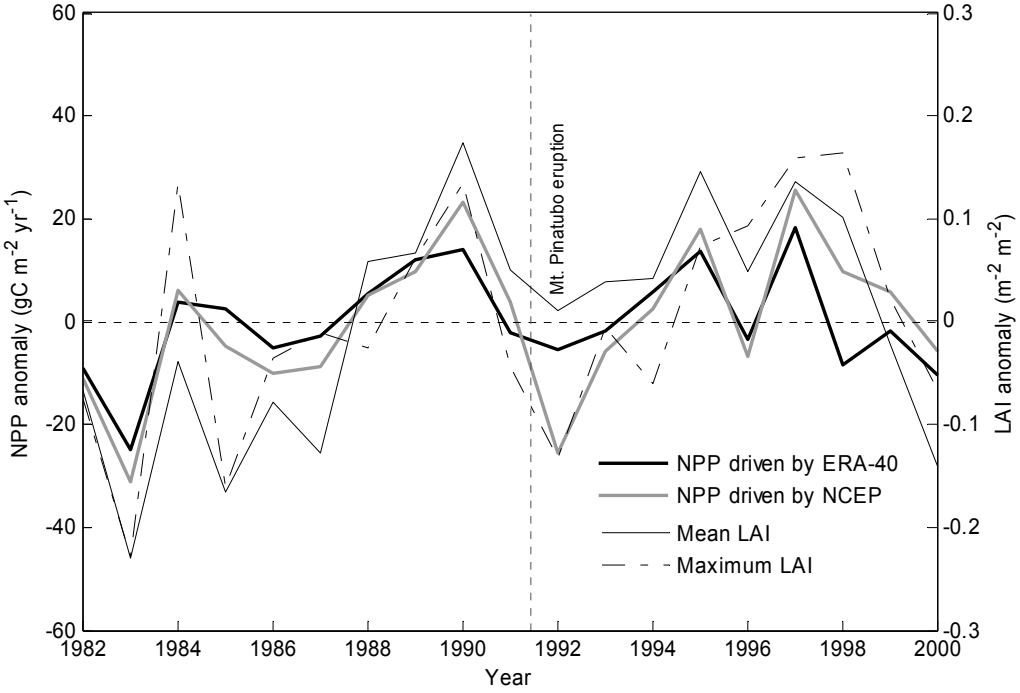

Figure 2-7: The calculated annual NPP anomalies for the pan-Arctic domain and 19-year study period using ERA-40 and NNR drivers for the PEM simulations; the AVHRR PAL derived mean and maximum annual LAI anomalies (relative to long-term mean) for the domain are also shown.

annual NPP for the entire vegetated domain increased by 0.372 g C m^{-2} $yr^{-1}$and 1.024 g C m^{-2} yr^{-1} over the 19-year period as derived from ERA-40 and NNR drivers, respectively. These regional trends are not statistically significant, though the temporal NPP trends for some regions were significant. Maps of the spatial pattern of the multi-year NPP trends are presented in Figure 2-8. The PEM results from the two reanalyses showed similar NPP trends for 74.7% of the vegetated study region (Figure 2-8). The latitudinal and longitudinal distributions of the multi-year NPP trends for the domain also showed generally similar patterns between ERA-40 and NNR results, though NNR results showed larger variations (Figure 2-9). In regions above 65° N, the multi-year NPP trends

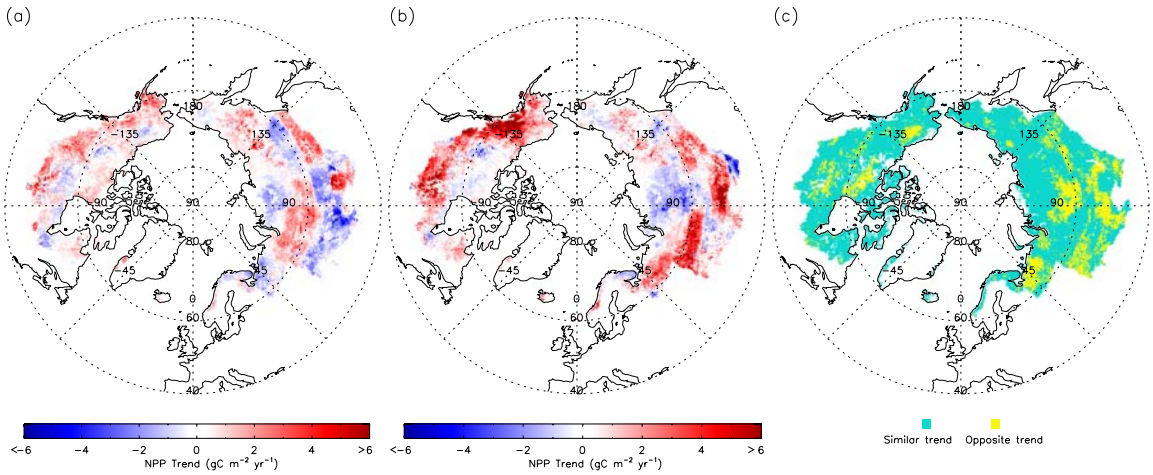

Figure 2-8: Spatial pattern of the multi-year trend in PEM based annual NPP (g C m^{-2} yr^{-1}) over the 19-year study period across the study domain excluding permanent ice and snow, open water and barren land as derived from ERA-40 (a) and NNR (b) inputs; a map of associated differences in NPP trends from these results is also shown (c).

showed similar patterns between ERA-40 and NNR results, while NNR results showed much larger NPP trends in regions between 46° N and 62° N. In regions between 160° W and 130° W and between 45 ° E and 90 ° E, NNR results also showed greatly exaggerated NPP trends relative to ERA-40 results. These latitudinal and longitudinal differences are largely due to over prediction of the NNR results across southern Alaska, and western and southern Eurasia relative to ERA-40 results (Figure 2-6). In this study, I only assessed the sensitivity and relative uncertainty of regional NPP simulations of the pan-Arctic basin and Alaska in response to uncertainties in surface meteorological inputs. However, model NPP results may also be negatively impacted by uncertainties in satellite remote sensing inputs including the PAL LAI/FPAR product, which incorporates uncertainties from dropped scan lines, navigation errors, data drop outs, edge-of-orbit composite discontinuities and other artifacts from the PAL NDVI (Tucker *et al.*, 2005). A NASA Global Inventory Modeling and Mapping Studies (NASA GIMMS) NDVI

product has attempted to correct most of the above problems and is currently available at ¼ degree resolution (Pinzon *et al.*, 2005). However, at the time of this investigation there was no alternative GIMMS LAI/FPAR product with similar spatial resolution to the 16 km PAL LAI/FPAR product.

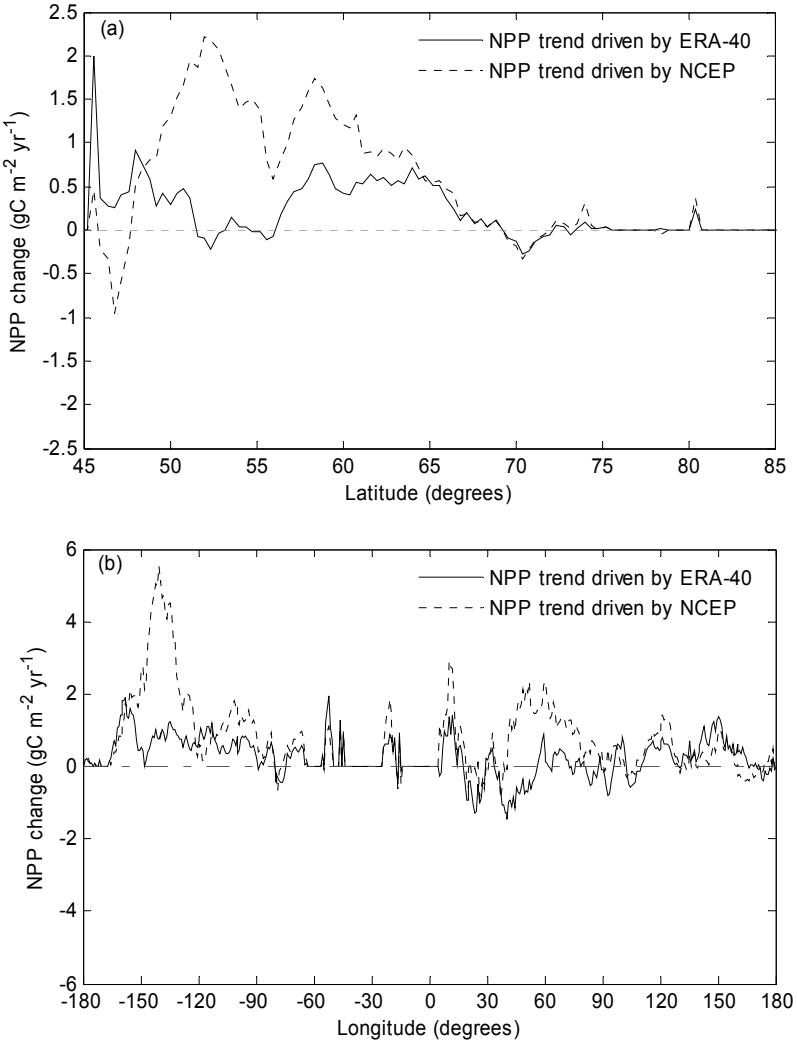

Figure 2-9: Mean latitudinal (a) and longitudinal (b) distributions of the 19-year trends in PEM based annual NPP (g C m^{-2} yr^{-1}) across the study domain as derived from the two reanalyses.

2.5. Regional Correction of Meteorology Reanalyses

2.5.1. Regional Correction Scheme

Section 2.4 shows that there are considerable uncertainties in both ERA-40 and NNR meteorology reanalyses, especially $SW_{\downarrow}$, $T_{\min}$ and T_{avg}, resulting in larger uncertainties in the satellite remote sensing based NPP estimates. Although the ERA-40 meteorology parameters generally show higher accuracies and lower biases than the NNR counterparts, the ERA-40 temporal coverage is confined between September 1957 and August 2002 (Uppala *et al.*, 2005). However, the NNR products are available from 1948 to the present. Therefore, I chose the NNR products as the meteorology inputs to extend the study period over the more recent record. Due to the large uncertainties in $SW_{\downarrow}$ from the NNR, I used $SW_{\downarrow}$ from the NASA World Climate Research Programme/Global Energy and Water-Cycle Experiment (WCRP/GEWEX) Surface Radiation Budget (SRB) Project (http://eosweb.larc.nasa.gov/PRODOCS/srb/table_srb.html) data set instead of the NNR counterpart. Due to the relative high quality of the SRB solar radiation product (Gupta *et al.*, 2001) and lack of direct solar radiation measurements in the region, I adopted the product without further corrections.

To reduce uncertainties in NNR inputs to the PEM, I applied a systematic correction of regional bias in the reanalysis daily surface meteorology through a local sample area correction method using surface observations of daily minimum and mean surface air temperatures and dew points from 1983–2005 for 6,164 weather stations distributed across the pan-Arctic domain following (Zhang *et al.*, 2007). The following

approach is used to correct NNR daily meteorological data ($T_{\min}$, T_{avg}, and e_a): (1) interpolate NNR daily meteorological data for each WMO ground station using an inverse distance squared method; (2) subtract the interpolated NNR data from corresponding surface observations for each station and define the differences as correction terms; (3) select the nearest four stations for each NNR pixel within the domain, calculate the mean correction terms using the inverse distance squared method, and add the correction terms to the original NNR meteorological data.

2.5.2. Validation of Corrected Meteorological Inputs

To verify the accuracy of the corrections, I calculated the interpolated meteorological variables for each station location using the corrected NNR. I then applied the same validation procedures in Section 2.2.1 to analyze the resulting meteorological error distributions. In addition, I analyzed both temporal and spatial distributions of errors in the corrected NNR daily meteorological inputs.

To verify the quality of solar radiation inputs, I compared both NNR and SRB solar radiation data with daily solar radiation observations from 17 sites distributed across Alaska from 1983–1990. These data were obtained from the National Solar Radiation Data Base (NSRDB; http://rredc.nrel.gov/solar/old_data/nsrdb/), whereas the same validation procedures in Section 2.2.1 were applied to assess product accuracy. Because of the extremely sparse regional observation network for solar radiation, I didn't inspect the spatial distribution of errors in the radiation products; instead, I analyzed the temporal variation of errors using a one-way ANOVA.

Table 2-5. Comparison of accuracy in the original and corrected NNR climate data, NNR solar radiation, and NASA SRB solar radiation.

Variables		Error Distribution					Accuracy			
		$\bar{\varepsilon}$	s_ε	Q_{1st}	M_ε	Q_{3rd}	MAE	RMSE	δ_ε	[e]r
T_{avg} (°C)	[a]O	1.2	2.0	0.1	1.0	2.0	1.6	2.3	31.6%	0.92
	[b]C	0.0	0.9	-0.3	0.0	0.3	0. 5	0.9	0.8%	0.99
T_{min} (°C)	O	0.6	2.4	-0.8	0.3	1.6	1.7	2.5	8.3%	0.89
	C	<0.1	1.1	-0.4	0.0	0.42	0.7	1.1	0.6%	0.98
e_a (Pa)	O	-93.5	72.9	-139.3	-98.9	-52.5	102.3	118.5	16.3%	0.88
	C	0.1	31. 8	-10.4	0.1	10.8	18.9	31.8	<0.1%	0.97
$SW_\downarrow$	[c]N	-3.6	4.2	-6.5	-2.4	-0.1	4.0	5.6	41.1%	0.91
(MJ m^{-2} d^{-1})	[d]S	-0.4	4. 6	-2.7	0.8	2.3	3.5	4.6	4.3%	0.84

[a,b] O and C indicate the original and corrected NNR reanalysis meteorology, respectively;
[c,d] N and S indicate the NNR reanalysis and NASA SRB;
[e]All correlation coefficients are significant at the level of 0.001.

The summary of error distributions for the original and corrected NNR meteorological inputs (T_{avg}, $T_{\min}$, and e_a) relative to daily surface weather station network observations are shown in Table 2-5. The error distributions of the NNR and SRB solar radiation products are also shown in Table 2-5. These results show considerable uncertainties in the original NNR meteorological data. The original NNR shows substantial bias in mean errors for all four variables. Both $T_{\min}$ and T_{avg} are generally underestimated for the original NNR, while e_a is greatly overestimated. The mean errors of the three variables in the corrected NNR are near zero indicating that the corrected NNR should impart minimal bias to the NPP calculations. The quartile and median error statistics indicate that errors for all the three variables are slightly skewed, whereas errors in the corrected NNR show a normal distribution. The standard and mean absolute errors of these results indicate that the error spreads are greatly reduced by the

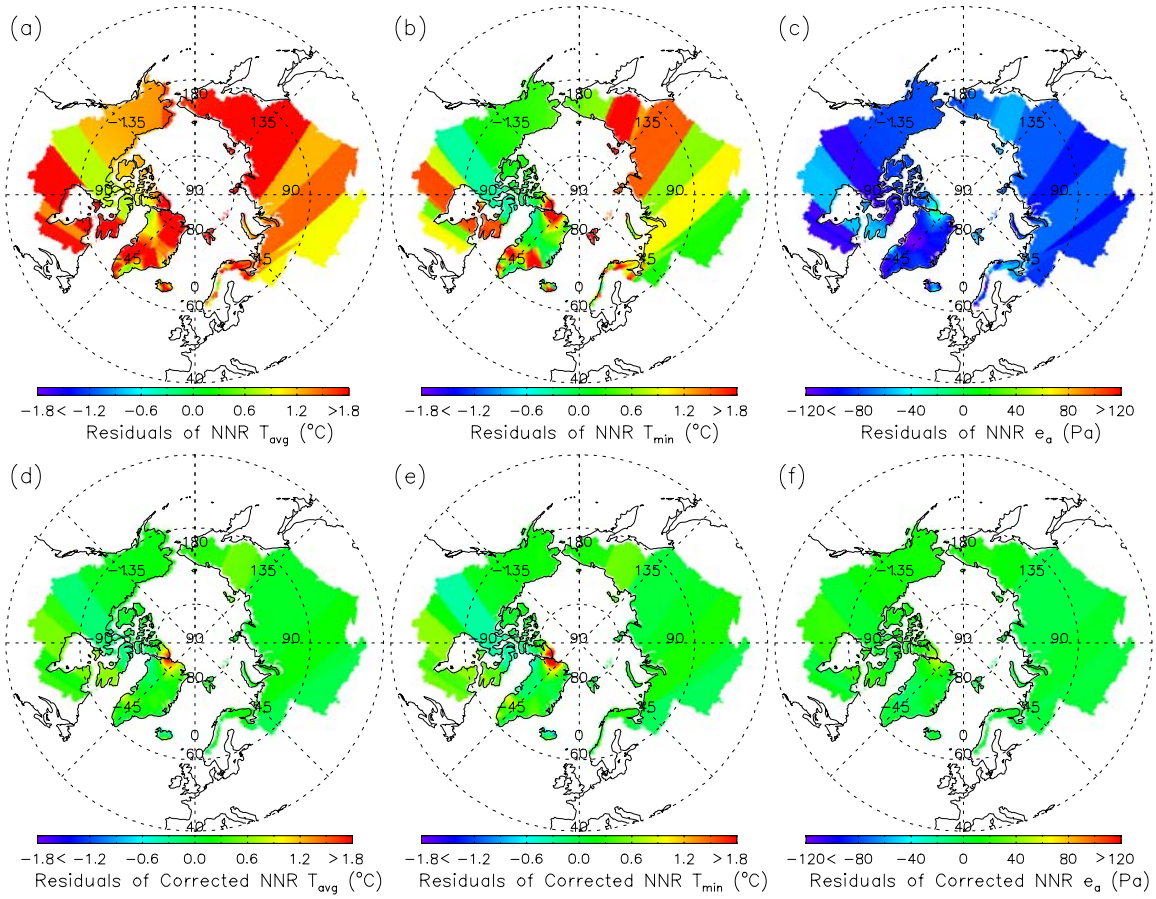

Figure 2-10: Maps of spatial error distributions of NNR T_{avg} (a), T_{min} (b), and e_a (c), and corrected NNR T_{avg} (d), T_{min} (e), and e_a (f). The errors were calculated as the average values of the differences between the reanalysis daily values (NNR or corrected NNR) and the daily observations (reanalysis - observations) from 1,644 WMO weather stations within the pan-Arctic region from 1983 to 2005.

corrections. Reductions in relative errors also indicate that the correction procedure greatly improves the accuracy of the NNR inputs. The correlation analysis also shows that correspondence between reanalysis and observations is greatly improved. These results indicate that the correction procedure effectively removed most uncertainties in NNR daily surface meteorological inputs relative to available surface weather station network observations.

The maps of error spatial distributions of both NNR and corrected NNR T_{avg}, $T_{\min}$ and e_a inputs (Figure 2-10) indicate that errors in the original NNR have significant spatial patterns, while errors in the corrected NNR meteorology are negligible and without strong spatial patterns. Analyses of error temporal variation also indicate that the errors are negligible and temporally independent in the corrected NNR (Figure 2-11).

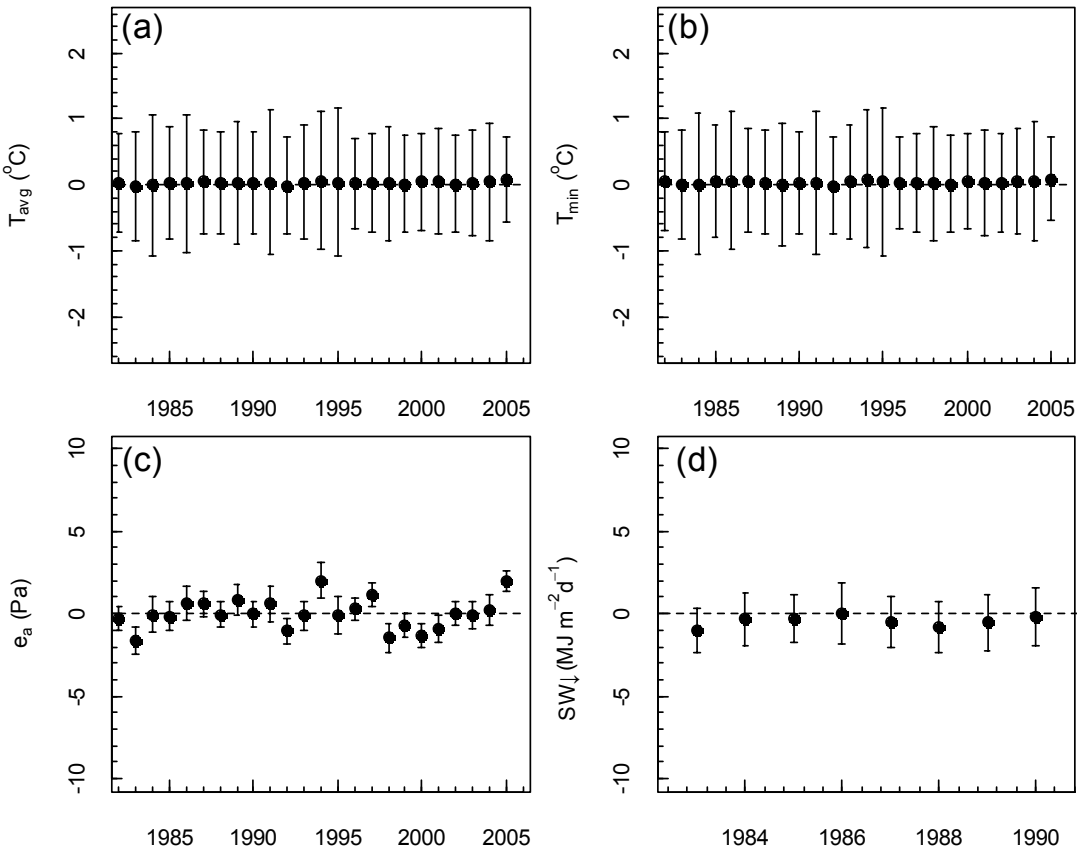

Figure 2-11: Temporal comparison of mean annual residuals (standard deviations indicated by the bars) in corrected NNR T_{avg} (a), $T_{\min}$ (b) and e_{a} (c), and NASA/GEWEX SRB $SW_{\downarrow}$ (d) estimated by comparing the observations from 1644 WMO weather stations from 1983 to 2005 and 17 NSRDB solar radiation stations from 1983 to 1990 within the pan-Arctic region. One-way ANOVA shows that the errors of corrected NNR T_{avg} ($P = 0.99$), $T_{\min}$ ($P > 0.99$), e_{a} ($P = 0.98$) and $SW_{\downarrow}$ ($P = 0.90$) are insignificantly temporally different, i.e. temporally independent.

Table 2-6. Comparison of estimated average errors of three PEM NPP series derived from the following meteorological inputs: 1) corrected NNR T_{avg}, T_{min} and e_a, and NASA SRB $SW_{\downarrow}$; 2) corrected NNR T_{avg}, T_{min} and e_a, and NNR $SW_{\downarrow}$; 3) NNR T_{avg}, T_{min}, e_a, and $SW_{\downarrow}$ using the uncertainty and sensitivity analysis procedure (Section 2.4.1). Different letters denote significant ($P < 0.05$, $n = 99$) differences between NPP errors derived from the different meteorology inputs according to the S-N-K ANOVA.

	Estimated Mean Residuals of PEM NPP (g C m^{-2} yr^{-1})		
Vegetation Type	Driven by Meteorology Inputs #1	Driven by Meteorology Inputs #2	Driven by Meteorology Inputs #3
Boreal Forest	-27.26[a]	-351.10[b]	-380.23[c]
Tundra	-14.60[a]	-171.58[c]	-152.20[b]

Although both NNR and SRB solar radiation data are overestimated relative to the 17 station observation series, the mean error of SRB solar radiation is near zero and much smaller than the NNR product. The SRB error distribution spread is also much smaller than the NNR product. Although the NNR solar radiation has a somewhat higher correlation with the observations than the SRB, both the relative error and error spread statistics indicate that the SRB is more accurate than the NNR solar radiation product for the study region. Temporal error analysis of SRB $SW_{\downarrow}$ (Figure 2-11) also indicates that the errors are small and temporally independent.

The sensitivity and error propagation analyses are consistent with previous findings that NNR solar radiation is the primary source of PEM-based NPP uncertainty for the pan-Arctic region (Table 2-6). The use of SRB $SW_{\downarrow}$ instead of NNR $SW_{\downarrow}$ significantly ($P < 0.05$) reduced associated NPP estimation uncertainty for the two main biomes (Table 2-6). The correction of NNR T_{avg}, T_{min} and e_a also significantly ($P < 0.05$) decreased uncertainty in PEM based NPP calculations for the two main biomes (Table 2-

6). Mean annual NPP for the region derived from corrected NNR and SRB inputs was overestimated by approximately 4.8%, which is much lower than relative error (61.6%) produced from NNR radiation inputs (Zhang *et al.*, 2007).

2.6. Summary

In this chapter, I applied the above statistical methods to validate the qualities of the widely used meteorology reanalysis products which are necessary for the satellite remote sensing based vegetation productivity retrievals. I also developed an uncertainty and sensitivity analysis scheme to quantify the effects of uncertainties in the meteorology reanalyses on the satellite remote sensing based vegetation productivity estimates. The study clearly points out that there are considerable uncertainties in the meteorology reanalyses, resulting in large uncertainties and biases in the corresponding vegetation productivity estimates.

To minimize the uncertainties in the meteorology reanalysis and maximize the quality of vegetation productivity estimates, I developed a regional meteorology correction scheme to correct the temperature and atmospheric water vapor pressure parameters in the NNR using the ground observation network and replaced the NNR solar radiation parameter with the satellite-derived NASA/GEWEX SRB solar radiation product.

Regional correction of the NNR surface meteorology and use of the NASA/GEWEX SRB solar radiation product substantially reduced uncertainties and biases in the meteorology inputs for the vegetation productivity estimates and

significantly improved the accuracy and reliability of the vegetation productivity estimates.

2.7. References Cited

Bromwich, D.H. & Fogt, R.L. (2004) Strong trends in the skill of the ERA-40 and NCEP-NCAR Reanalyses in the High and Mid-latitudes of the Southern Hemisphere, 1958-2001. *Journal of Climate*, **17**, 4603-4619.

Bromwich, D.H. & Wang, S.-H. (2005) Evaluation of the NCEP-NCAR and ECMWF 15- and 40-yr reanalyses using rawinsonde data from two independent arctic field experiments: Advances in high latitude numerical weather prediction. *Monthly Weather Review*, **133**, 3562-3578.

Churkina, G. & Running, S.W. (1998) Contrasting climatic controls on the estimated productivity of global terrestrial biomes. *Ecosystems*, **1**, 206-215.

Gower, S.T., Vogel, J.G., Norman, J.M., Kucharik, C.J., Steele, S.J., & Stow, T.K. (1997a) Carbon distribution and aboveground net primary production in aspen, jack pine, and black spruce stands in Saskatchewan and Manitoba, Canada. *Journal of Geophysical Research*, **102**, 290929-29041.

Gower, S.T., Vogel, J.G., Norman, J.M., Kucharik, C.J., Steele, S.J., & Stow, T.K. (1997b) Carbon distribution and aboveground net primary production in aspen, jack pine, and black spruce stands in Saskatchewan and Manitoba, Canada. *Journal of Geophysical Research-Atmospheres*, **102**, 29029-29041.

Gupta, S.K., Kratz, D.P., Stackhouse Jr., P.W., & Wilber, A.C. (2001). The Langley parameterized shortwave algorithm (LPSA) for surface radiation budget studies. TP-2001-211272. NASA.

Heinsch, F.A., Reeves, M., Votava, P., Kang, S., Milesi, C., Zhao, M., Glassy, J., Jolly, W.M., et al. (2003). User's Guide, GPP and NPP (MOD17A2/A3) Products NASA MODIS Land Algorithm, Version 2.0. The University of Montana.

Heinsch, F.A., Zhao, M., Running, S.W., Kimball, J.S., Nemani, R.R., Davis, K.J., Bolstad, P.V., Cook, B.D., et al. (2006) Evaluation of remote sensing based terrestrial productivity from MODIS using regional tower eddy flux network observations. *IEEE Transactions on Geosciences and Remote Sensing*, **44**, 1908-1923.

Helton, J.C. & Davis, F.J. (2003) Latin hypercube sampling and the propagation of uncertainty in analyses of complex systems. *Reliability Engineering and System Safety*, **81**, 23-69.

Helton, J.C., Johnson, J.D., Sallaberry, C.J., & Storlie, C.B. (2006) Survey of sampling-based methods for uncertainty and sensitivity analysis. *Reliability Engineering and System Safety*, **91**, 1175-1209.

Kalnay, E., Kanamitsu, M., Kistler, R., Collins, W., Deaven, D., Gandin, L., Iredell, M., Saha, S., et al. (1996) The NCEP/NCAR 40-year reanalysis project. *Bulletin of the American Meteorological Society*, **77**, 437-471.

Kimball, J.S., Zhao, M., McDonald, K.C., & Running, S.W. (2006) Satellite remote sensing of terrestrial net primary production for the pan-Arctic basin and Alaska. *Mitigation and Adaptation Strategies for Global Change*, **11**, 782-804, doi:10.1007/s11027-005-9014-5.

Kistler, R., Kalnay, E., Collins, W., Saha, S., White, G., Woollen, J., Chelliah, M., Ebisuzaki, W., et al. (2001) The NCEP-NCAR 50-year reanalysis: Monthly means CD-ROM and documentation. *Bulletin of the American Meteorological Society*, **82**, 247-267.

Lucht, W., Prentice, I.C., Myneni, R.B., Sitch, S., Friedlingstein, P., Cramer, W., Bousquet, P., Buermann, W., et al. (2002) Climatic control of the High-latitude vegetation greening trend and Pinatubo effect. *Science*, **296**, 1687-1689.

Monteith, J.L. (1972) Solar radiation and productivity in tropical ecosystem. *Journal of Applied Ecology*, **9**, 747-766.

Myneni, R.B., Keeling, C.D., Tucker, C.J., Asrar, G., & Nemani, R.R. (1997a) Increased plant growth in the northern high latitudes from 1981 to 1991. *Nature*, **386**, 698-702.

Myneni, R.B., Nemani, R.R., & Running, S.W. (1997b) Estimation of global leaf area index and absorbed par using radiative transfer models. *IEEE Transactions on Geoscience and Remote Sensing*, **35**, 1380-1393.

Nemani, R.R., Keeling, C.D., Hashimoto, H., Jolly, W.M., Piper, S.C., Tucker, C.J., Myneni, R.B., & Running, S.W. (2003) Climate-driven increases in global terrestrial net primary production from 1982 to 1999. *Science*, **300**, 1560-1563.

Olson, R.J., Johnson, K.R., Zheng, D.L., & Scurlock, J.M.O. (2001). Global and regional ecosystem modeling: Databases of model drivers and validation measurement. ORNL Technical Memorandum TM-2001/196. Oak Ridge National Laboratory, Oak Ridge, Tennessee, USA.

Parrish, D.F. & Derber, J.C. (1992) The National-Meteorological-Centers Spectral Statistical-Interpolation Analysis System. *Monthly Weather Review*, **120**, 1747-1763.

Pinzon, J., Brown, M.E., & Tucker, C.J. (2005). Satellite time series correction of orbital drift artifacts using empirical mode decomposition. In *Hilbert-Huang Transform: Introduction and Applications* (eds N.E. Huang & S.S.P. Shen), pp. 167-186. World Scientific Publishing Co. Pte. Ltd., Singapore.

Ruess, R.W., Van Cleve, L., Yarie, J., & Viereck, L.A. (1996) Comparative estimates of fine root production in successional taiga forests of interior Alaska. *Canadian Journal of Forest Research*, **26**, 1326-1336.

Running, S.W. & Hunt, E.R. (1993). Generalization of a forest ecosystem process model for other biomes, BIOME-BGC, and an application for global-scale models. In *Scaling Physiological Process: Leaf to Globe* (eds J.R. Ehleringer & C.B. Field), pp. 141-158. Elsevier, New York.

Running, S.W., Nemani, R.R., Heinsch, F.A., Zhao, M., Reeves, M., & Hashimoto, H. (2004) A continuous satellite-derived measure of global terrestrial primary productivity: Future science and applications. *Bioscience*, **56**, 547-560.

Running, S.W., Thornton, P.E., Nemani, R.R., & Glassy, J.M. (2000). Global terrestrial gross and net primary productivity from the Earth Observing System. In *Methods in Ecosystem Science* (eds O.E. Sala, R.B. Jackson & H.A. Mooney), pp. 44-57. Springer, New York.

Saugier, B., Roy, J., & Mooney, H.A. (2001). Estimations of global terrestrial productivity: Converging toward a single number? In *Terrestrial Global Productivity* (eds J. Roy, B. Saugier & H.A. Mooney), pp. 543-557. Elsevier, New York.

Schulze, E.D., Lloyd, J., Kelliher, F.M., Wirth, C., Rebmann, C., Luhker, B., Mund, M., Knohl, A., et al. (1999) Productivity of forests in the Eurosiberian boreal region and their potential to act as a carbon sink - a synthesis. *Global Change Biology*, **5**, 703-722.

Shaver, G.R. & Jonasson, S. (2001). Productivity of arctic ecosystems. In *Terrestrial Global Productivity* (eds J. Roy, B. Saugier & H.A. Mooney), pp. 189-210. Elsevier, New York.

Simmons, A.J., Jones, P.D., Bechtold, V.D., Beljaars, A.C.M., Kallberg, P.W., Saarinen, S., Uppala, S.M., Viterbo, P., et al. (2004) Comparison of trends and low-frequency variability in CRU, ERA-40, and NCEP/NCAR analyses of surface air

temperature. *Journal of Geophysical Research-Atmospheres*, **109**, D24115, doi:10.1029/2004JD005306.

Thornton, P.E. & Running, S.W. (1999) An improved algorithm for estimating incident daily solar radiation from measurements of temperature, humidity, and precipitation. *Agricultural and Forest meteorology*, **93**, 211-228.

Tucker, C.J., Pinzon, J.E., Brown, M.E., Slayback, D., Pak, E.W., Mahoney, R., Vermote, E., & Saleous, N. (2005) An extended AVHRR 8-km NDVI data set compatible with MODIS and SPOT vegetation NDVI data. *International Journal of Remote Sensing*, **26**, 4485-4498.

Turner, D.P., Ritts, W.D., Cohen, W.B., Gower, S.T., Zhao, M.S., Running, S.W., Wofsy, S.C., Urbanski, S., et al. (2003) Scaling Gross Primary Production (GPP) over boreal and deciduous forest landscapes in support of MODIS GPP product validation. *Remote Sensing of Environment*, **88**, 256-270.

Turner, D.P., Ritts, W.D., Cohen, W.B., Maeirsperger, T.K., Gower, S.T., Kirschbaum, A.A., Running, S.W., Zhao, M.S., et al. (2005) Site-level evaluation of satellite-based global terrestrial gross primary production and net primary production monitoring. *Global Change Biology*, **11**, 666-684.

Uppala, S.M., Kallberg, P.W., Simmons, A.J., Andrae, U., Bechtold, V.D., Fiorino, M., Gibson, J.K., Haseler, J., et al. (2005) The ERA-40 re-analysis. *Quarterly journal of the Royal Meteorological Society*, **131**, 2961-3012.

White, M.A., Thornton, P.E., Running, S.W., & Nemani, R.R. (2000) Parameterization and sensitivity analysis of the BIOME-BGC terrestrial ecosystem model: Net primary production controls. *Earth Interactions*, **4**, 1-85.

Yang, S.K., Hou, Y.T., Miller, A.J., & Campana, K.A. (1999) Evaluation of the earth radiation budget in NCEP-NCAR reanalysis with ERBE. *Journal of Climate*, **12**, 477-493.

Zhang, K., Kimball, J.S., Zhao, M., Oechel, W.C., Cassano, J., & Running, S.W. (2007) Sensitivity of pan-Arctic terrestrial net primary productivity simulations to daily surface meteorology from NCEP-NCAR and ERA-40 reanalysis. *Journal of Geophysical Research*, **112**, G01011, doi:10.1029/2006JG000249.

Zhao, M., Heinsch, F.A., Nemani, R.R., & Running, S.W. (2005) Improvements of the MODIS terrestrial gross and net primary production data set. *Remote Sensing of Environment*, **95**, 164-176.

Zhao, M., Running, S.W., Heinsch, F.A., & Nemani, R.R. (2008). Terrestrial primary production from MODIS. In *Land Remote Sensing and Global Environmental*

Change: NASA's EOS and the Science of ASTER and MODIS (eds C. Justice & M. Abrams), pp. 423-444. Springer, New York.

Zhao, M., Running, S.W., & Nemani, R.R. (2006) Sensitivity of Moderate Resolution Imaging Spectroradiometer (MODIS) terrestrial primary production to the accuracy of meteorological reanalysis. *Journal of Geophysical Research*, **111**, G01002, doi:10.1029/2004JG000004.

CHAPTER 3: CLIMATE-DRIVEN CHANGES IN PAN-ARCTIC VEGETATION PRODUCTIVITY

3.1. Quantification of Climatic Constraints to PEM-based Vegetation Productivity

Low temperature, water stress and limited solar irradiance are the primary environmental constraints on vegetation activity and productivity in the pan-Arctic domain (Chapin III *et al.*, 1986; Jolly *et al.*, 2005; Nemani *et al.*, 2003; Running *et al.*, 2004). Figure 3-1 shows the geographic distribution of potential climatic constraints to vegetation productivity. Low temperature and water stress have experienced substantial changes in this region during the recent decades (see Section 1.2.2), while incoming solar radiation on the ground can be impacted by the changes in cloud cover and atmospheric aerosols.

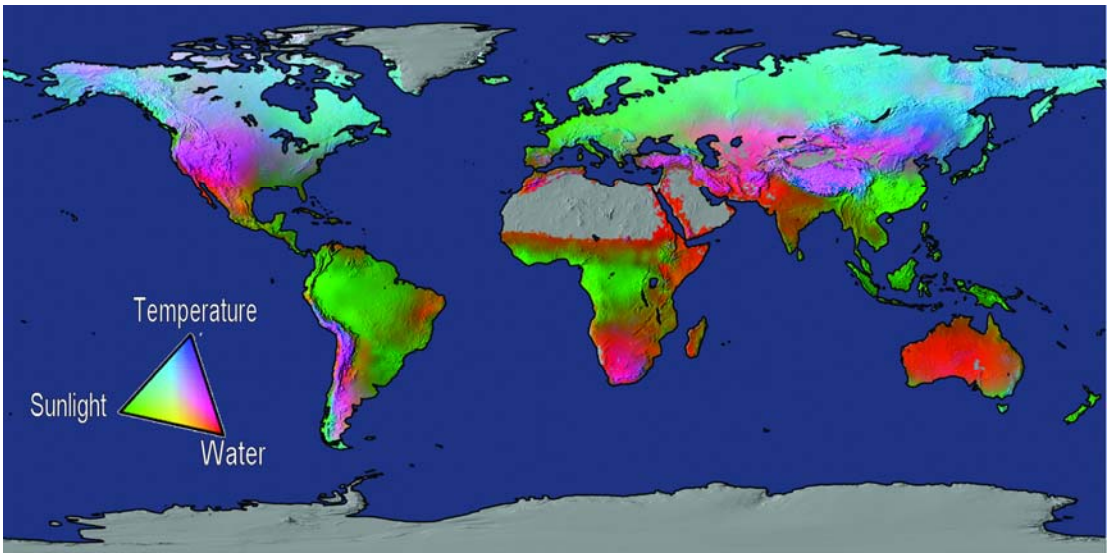

Figure 3-1: Geographic distribution of potential climatic constraints to vegetation productivity derived from long-term climate statistics. Data are from Nemani *et al.* (2003). This graph is provided by Running *et al.* (2004).

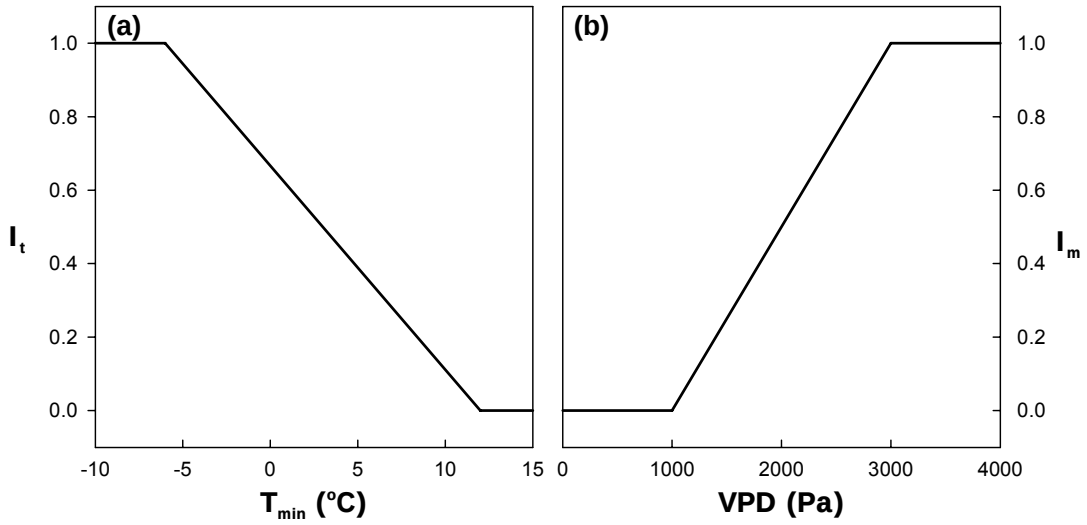

Figure 3-2: Graphic representation of low-temperature stress index (I_t) and a moisture stress index (I_m).

To quantify the effects of low-temperature and moisture constraints to NPP, I defined a low-temperature stress index (I_t), and a moisture stress index (I_m) based on the original MOD17A2/A3 algorithms (Heinsch *et al.*, 2003; Running *et al.*, 2004; Running *et al.*, 2000; Zhao *et al.*, 2008):

$$I_t = 1 - T_f \tag{3.1}$$

$$I_m = 1 - VPD_f \tag{3.2}$$

The I_t and I_m parameters are dimensionless, ranging from 0 to 1 with increasing low-temperature and moisture constraints to GPP and NPP (Figure 3-2). I calculated potential NPP ($NPP_{Potential}$) under non limiting atmospheric conditions by removing both low-temperature and moisture constraints to the PEM calculations. I then calculated NPP using only moisture (NPP_M) and low-temperature (NPP_T) constraints, respectively.

Finally, I determined the proportional (%) losses of potential NPP due to moisture ($\delta loss_M$) and low-temperature ($\delta loss_T$) constraints according to the following definitions:

$$\delta loss_M = \frac{NPP_{Potential} - NPP_M}{NPP_{Potential}} \times 100 \quad (3.3)$$

$$\delta loss_T = \frac{NPP_{Potential} - NPP_T}{NPP_{Potential}} \times 100 \quad (3.4)$$

The study period for analyzing climatic constraints and vegetation productivity are from 1983 to 2005 based on the availability of meteorology reanalysis, solar radiation data and satellite-derived vegetation attributes. To verify changes in moisture availability for the domain, a simple climate moisture index (CMI) (Hogg, 1997; Hogg *et al.*, 2005; Hogg *et al.*, 2008; Hogg & Wein, 2005) was computed as the difference between annual precipitation (P) and potential evapotranspiration (PET), where PET was calculated using a simplified Penman-Monteith approach (Hogg, 1997). The CMI was derived on a 12-month period basis ending on 31 July of each given year from 1974–2005 using regional weather station observations of daily air temperature and precipitation provided by the NCDC CSB Global Surface Summary of the Day. The total number of NCDC CSB stations used to compute the CMI varied annually and ranged from 2,053 to 2,924 stations per year for the domain.

To evaluate the potential effects of incoming solar radiation on vegetation productivity, I also analyzed the spatial change patterns and temporal trends of incoming solar radiation within the pan-Arctic region.

3.2. Satellite FPAR/LAI Inputs

In this study, I used satellite-derived vegetation properties including monthly FPAR and LAI from the NOAA AVHRR PAL (Pathfinder AVHRR Land) 16-km resolution data set (Myneni *et al.*, 1997b) and 8-day FPAR and LAI from the NASA MODIS MOD15 1-km resolution data set (Myneni *et al.*, 2002). The AVHRR PAL FPAR/LAI data are only available from 1982 to 2000, while the MODIS MOD15 FPAR/LAI data are ongoing and available since 2000. Because the NASA/GEWEX SRB shortwave solar radiation data were only available from 1983 to 2005 during this study, I chose 1983–2005 as the study period. A NASA Global Inventory Modeling and Mapping Studies (NASA GIMMS) NDVI product has made some improvements over the AVHRR PAL product and is currently available at 8-km resolution (Pinzon *et al.*, 2005). However, there is currently no alternative GIMMS FPAR/LAI product with similar spatial resolution to the 16-km PAL data set for the study period.

3.2.1. Integration of AVHRR-MODIS FPAR/LAI Time Series

To produce a continuous time series estimation of annual NPP from 1983 to 2005, I first employed a pixel-wise linear regression method to combine the two FPAR/LAI series into a single, continuous record, and then derived the long-term NPP record using the integrated AVHRR-MODIS FPAR/LAI series.

The AVHRR PAL FPAR/LAI data are based on a monthly maximum value compositing of AVHRR spectral reflectance data to mitigate cloud cover, smoke, and other atmospheric aerosol contamination effects. To be consistent with the spatial resolution of the AVHRR PAL FPAR/LAI data, the 8-day 1-km MODIS FPAR/LAI data

were first interpolated to a daily time step by removing cloud contamination and snow effects indicated by the MOD15A2 QC fields (Zhao *et al.*, 2005), followed by temporal linear interpolation of adjacent 8-day values to a daily time step, and spatial aggregation to a 16-km resolution by averaging the FPAR/LAI values of the dominant land cover class. The following procedures were then used to combine the two series: (1) derive monthly maximum values of MODIS FPAR/LAI for each pixel for 2000; (2) regress monthly MODIS FPAR/LAI on corresponding AVHRR FPAR/LAI for the overlapping period in 2000 using simple linear regression on a pixel-by-pixel basis; (3) use the resulting regression equations to adjust the AVHRR FPAR/LAI time series and compute an integrated AVHRR-MODIS FPAR/LAI monthly time series from 1983–2005. Although alternate regressions based on regional groupings by land cover type would increase the sample size for the linear regressions, this approach would not account for the considerable spatial variation in the relationships between AVHRR and MODIS FPAR/LAI series, limiting the accuracy and reliability of this approach. The corrected monthly AVHRR PAL FPAR/LAI data were then resampled to a daily time step by temporal linear interpolation of adjacent monthly values. The daily linear interpolation approach used for this investigation is a relatively simple, but effective means for producing a daily FPAR and LAI time-series for PEM simulations and has been used extensively for global vegetation analyses of the AVHRR Pathfinder series e.g. (Kimball *et al.*, 2006b; Zhang *et al.*, 2007b). Finally, the combined data were reprojected to the 25 km polar EASE-grid format using a nearest-neighbor resampling scheme.

There are three primary justifications for the above integration methods. First, the two products reflect quasi-simultaneous satellite observations of the same objects and

show strong, positive correlations for most pixels. Although the observations were acquired from different sensors, similar physical mechanisms and models (Myneni *et al.*, 2002; Myneni *et al.*, 1997b) were used to produce each FPAR/LAI series. Second, the simple linear regression method is a global unbiased method which guarantees a reasonable error distribution and simplifies the evaluation of errors. Finally, the simple linear regression only involves linear transformation of the AVHRR FPAR/LAI time series, which conserves the same general trend as the original data series.

3.2.2. Validation of the Integrated FPAR/LAI Time Series

To verify the consistency of our results, I compared the corrected monthly AVHRR FPAR/LAI series with corresponding MODIS FPAR/LAI values for 2000 by analyzing the error distribution and correlation results using the validation procedure in Section 2.2.1. In the validation procedure, I regarded the MODIS FPAR/LAI time series as "truth", while acknowledging that while MODIS has improved precision over AVHRR, there is no truly error free FPAR/LAI data set.

To evaluate the potential propagation of errors from integrated FPAR/LAI inputs on PEM based NPP calculations, I calculated 95% confidence intervals for estimated NPP before 2000. Due to the normal distributions of the errors for both LAI and FPAR, and the strong association between these variables, I assume that the errors for both LAI and FPAR have similar normal distributions. By adding and/or subtracting one standard error to LAI and FPAR inputs in combination and individually, I established 95% confidence intervals for the resulting PEM calculations.

To assess the role of the historical FPAR/LAI record in determining the observed interannual variation in NPP and associated sensitivity of PEM calculations to the AVHRR-MODIS integrated FPAR/LAI series, I conducted a sensitivity analysis by calculating NPP over the 23-year time series using a constant, average seasonal FPAR/LAI time series (i.e., the 23-year means) on a pixel-by-pixel basis. I then assessed differences between these results and the NPP series derived from the historical FPAR/LAI record.

3.3. Timings of Growing Season Onset and End

I used the daily NPP series in each year to derive annual growing season onset (T_{NPP_Onset}) and end (T_{NPP_End}) using a 7-day moving window method. To determine the annual timing of growing season onset, (1) I applied the 7-day moving window over the daily NPP time series on a year-by-year basis; (2) for each 7-day increment I checked whether there were five or more days with positive daily NPP values; (3) if not, the window progressed one day forward and step (2) was repeated; (4) if yes, the first day with positive daily NPP in the 7-day window was assigned as the start of the growing season. A similar method was used to determine the timing of growing season end, but with the moving window applied in reverse, finding the first 7-day period with five or more days of positive NPP and selecting the final positive NPP day as the growing season end date. A schematic representation of this search method is listed in Figure 3-3 (a).

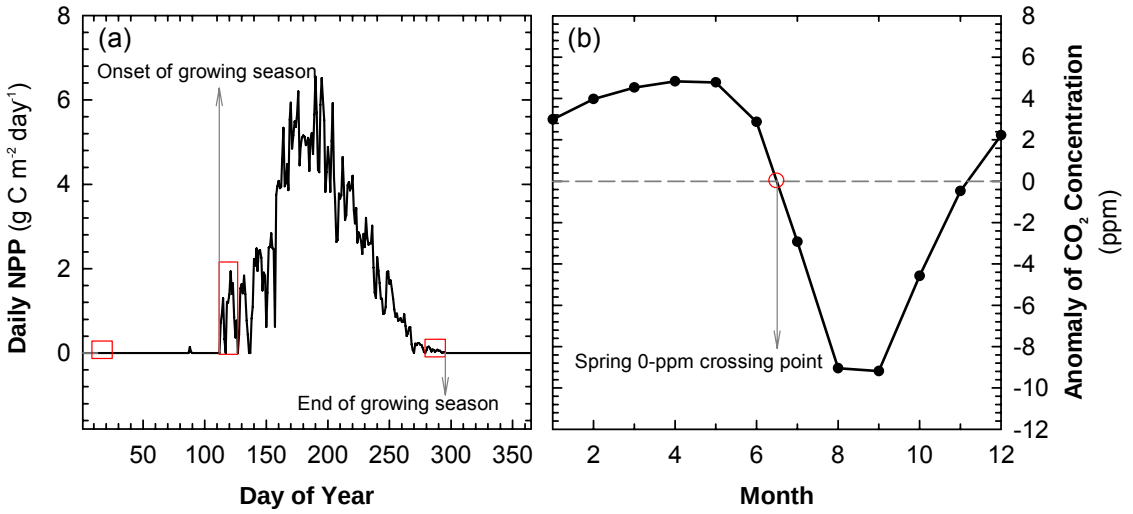

Figure 3-3: Schematic representations for deriving (a) the onset and end of growing season using 7-day moving window along the daily NPP time series and (b) the spring 0-ppm crossing point from the monthly anomalies of atmospheric CO_2 concentrations.

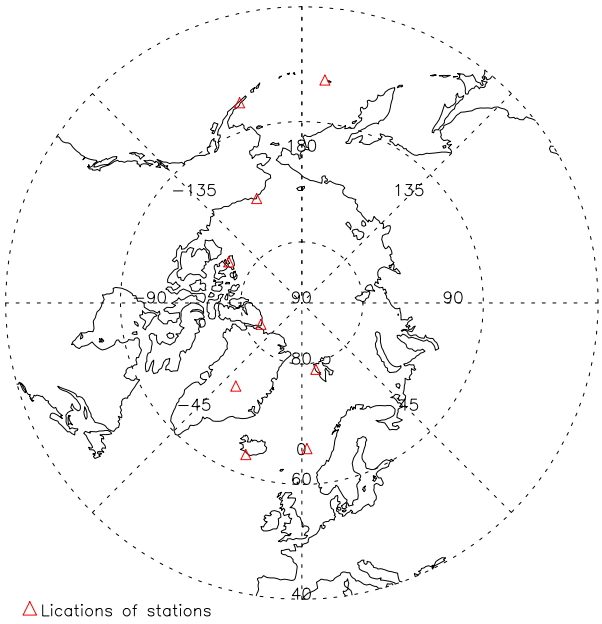

Figure 3-4: Locations of NOAA GMD atmospheric CO_2 monitoring stations across the pan-Arctic region (>50°N).

I compared the daily NPP-derived growing season onset results with the timing of spring drawdown of atmospheric CO_2 concentrations (T_{CO2_Spr}) (Zhang *et al.*, 2007a)

derived from NOAA GMD (Global Monitoring Division) monitoring stations across the pan-Arctic region (>50°N) (Figure 3-4), including BRW (71°N), ALT (82°N), MBC (76°N), STM (66°N), CBA (55°N), ICE (63°N), SHM(52°N), SUM (72°N), and ZEP (79°N) stations (GLOBALVIEW-CO_2, 2006), to assess relative agreement between the satellite record and atmospheric CO_2 concentrations regarding recent trends and annual anomalies in northern growing season dynamics with regional warming. The average of the nine stations' mean monthly records were normalized as the difference between monthly and mean annual CO_2 concentrations for each year. The timing of the spring 0-ppm crossing date represents the X-intercept of the normalized monthly CO_2 transition from positive (winter) to negative (summer) conditions (Figure 3-3 (b)) and is an indication of the seasonal timing of vegetation photosynthetic activity (Keeling *et al.*, 1996; Randerson *et al.*, 1997). Previous studies have shown that the seasonal atmospheric CO_2 cycle at high northern latitudes is dominated largely by northern terrestrial ecosystems, with minimal impacts from ocean exchange, fossil fuel emissions, and tropical biomass burning (Erickson *et al.*, 1996; Heimann *et al.*, 1998; Randerson *et al.*, 1997).

3.4. Remote Sensing of Vegetation Greenness

The Normalized Difference Vegetation Index (NDVI) is a widely used remote sensing metric of the vegetation greenness and is defined as (Tucker, 1979):

$$\mathrm{NDVI} = \frac{\rho_{\mathrm{NIR}} - \rho_{\mathrm{Red}}}{\rho_{\mathrm{NIR}} + \rho_{\mathrm{Red}}} \tag{3.5}$$

where ρ_{NIR} and ρ_{Red} are the spectral reflectance measurements acquired by sensors onboard satellites or other platforms in the red and near-infrared (NIR) bands, respectively. These spectral reflectance values are themselves ratios of reflected over the incoming radiation in each spectral band; hence they take on values between 0 and 1. By design, the NDVI varies between -1.0 and +1.0. The NDVI is built on the observation that chlorophylls a and b in green leaves strongly absorb light in the red, with maximum absorption at about 690 nm, while the cell walls strongly scatter (reflect and transmit) light in the NIR region (about 850 nm). Therefore, the value of NDVI is strongly sensitive to photosynthetic canopy cover (e.g. Tucker, 1979). As a result, dense vegetation has a high NDVI, while soil values are low but positive, and values over open water are negative due to strong absorption in the NIR.

The NOAA Advanced Very High Resolution Radiometer (AVHRR) Global Inventory Modeling and Mapping Studies (GIMMS) NDVI (Pinzon *et al.*, 2005; Tucker *et al.*, 2005) record extends from 1981 to present and provides the longest continuous record of vegetation greenness on a global scale. The AVHRR GIMMS NDVI record is available at 8-km spatial resolution and twice monthly temporal repeat.

3.5. Remote Sensing of Landscape Freeze-Thaw

Annual vegetation productivity and carbon cycle dynamics for pan-arctic ecosystems are strongly regulated by seasonal cold temperature constraints to photosynthesis and respiration such that annual growing seasons are limited to a

relatively brief period in spring and summer (Churkina & Running, 1998; Nemani *et al.*, 2003). However, a growing body of evidence indicates that growing seasons are shifting in response to global change-related warming and associated decreases in cold temperature constraints to plant growth (Euskirchen *et al.*, 2006; Myneni *et al.*, 1997a; Nemani *et al.*, 2003; Randerson *et al.*, 1999; Randerson *et al.*, 1997). Satellite microwave remote sensing based freeze-thaw algorithms utilize a temporal change classification approach, exploiting the large dynamic response of surface dielectric properties and related microwave emissions that occur as the landscape transitions between predominantly frozen and thawed conditions (McDonald & Kimball, 2005). These methods have been developed and validated using both active and passive microwave observations from a variety of satellite sensors including SSM/I (Special Sensor Microwave/Imager) (McDonald *et al.*, 2004), NSCAT (NASA Scatterometer) (Frolking *et al.*, 1999; Kimball *et al.*, 2004a; Kimball *et al.*, 2001) and SeaWinds (Kimball *et al.*, 2004b). These seasonal variations in landscape dielectric properties have been found to correspond closely with the onset and duration of annual growing seasons for subalpine, boreal, and tundra ecosystems (Frolking *et al.*, 1999; Kimball *et al.*, 2004b). These methods also provide a relatively precise and reliable approach for spatial and temporal mapping of annual growing seasons in boreal and arctic landscapes relative to satellite optical-IR based methods. This is because satellite optical-IR based approaches for monitoring northern phenology are strongly limited by the predominance of evergreen vegetation in boreal biomes. These biomes are not characterized by dynamic seasonal variability in canopy structure. Optical remote sensing at high latitudes is also constrained by reduced solar illumination and shadowing, and the coarse spatial and

temporal compositing necessary to mitigate frequent cloud cover, smoke and other atmospheric aerosol effects. In contrast, satellite microwave sensors can observe the land surface effectively day or night, regardless of solar illumination and most atmospheric effects.

To understand the effects of freeze-thaw processes and other underlying mechanisms on vegetation productivity, it is necessary to obtain longer and more recent records of the timing of thawing and the length of non-frozen season derived from the satellite microwave records. In this study, I used the records of spring thawing and fall freezing derived from SSM/I remote sensing brightness temperatures from 1988 to 2005 by McDonald *et al.* (2004) to analyze the changes in seasonal freeze-thaw and the corresponding constraints on vegetation productivity.

3.6. Trend Analysis

Linear trend analysis was used to analyze regional trends in the biophysical variables (y_t) in this dissertation. The linear model, $y_t = a_0 + a_1 t + \varepsilon_t$, is used to model y_t against time (t) where a_0 and a_1 are the Y-intercept and slope of the simple linear regression coefficients, respectively. The statistic $a_1 / SE(a_1)$ has a Student's t-distribution where $SE(a_1)$ is the standard error of estimate associated with the parameter a_1. The Student's t-test was used to analyze and classify trend significance into weak, moderate and strong categories. When $|a_1 / SE(a_1)| < 1.0$, i.e. a_1 is within one standard deviation, the trend is classified as weak; when $1.0 \le |a_1 / SE(a_1)| < t_{0.10}$ where $t_{0.10}$ is the 10% critical value of the Student's t-distribution, the trend is classified as moderate; when

$|a_1 / SE(a_1)| \geq t_{0.10}$, the trend is statistically significant and classified as strong. These categories were further stratified into six classes according to the slopes of the statistical trends: positive weak, positive moderate, positive strong, negative weak, negative moderate and negative strong.

3.7. Results

3.7.1. Changes of Vegetation Greenness

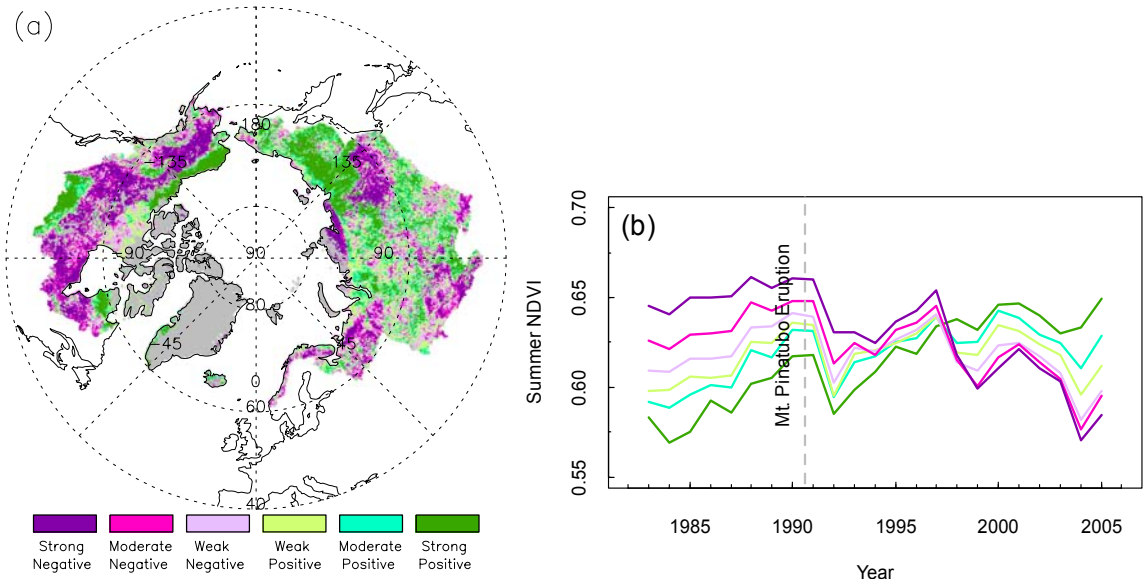

Figure 3-5: Spatial distribution of trends in summer (June-August) mean NDVI across the pan-Arctic region from 1983 to 2005 (a). The spatial averages of mean values for all areas identified as the same trend categories are shown in (b).

There is large spatial variability in the trends of summer mean NDVI across the pan-Arctic region from 1983 to 2005 (Figure 3-5 (a)). Summer NDVI shows moderate to strong negative trends in most regions of central Alaska, western, central and eastern Canada, northwestern and southwestern Eurasia, and eastern Siberia, while other areas show generally positive trends. For all six trend categories, the time series of spatial

Table 3-1. Percentages of the six trend types for summer mean NDVI in the three major biome types in the pan-Arctic region.

Trend Types		Tundra (10^4 km^2)	Boreal Forest (10^4 km^2)	Grassland (10^4 km^2)
Negative	Weak	184.7 (18.6%)	194.5 (23.6%)	60.6 (23.8%)
	Moderate	81.4 (8.2%)	122.0 (14.8%)	32.9 (12.9%)
	Strong	123.2 (12.4%)	219.2 (26.6%)	30.8 (12.1%)
	Subtotal	389.3 (39.2%)	535.7 (65.0%)	124.3 (48.8%)
Positive	Weak	227.5 (22.9%)	162.3 (19.7%)	51.7 (20.3%)
	Moderate	127.1 (12.8%)	73.3 (8.9%)	28.8 (11.3%)
	Strong	249.3 (25.1%)	52.7 (6.4%)	49.9 (19.6%)
	Subtotal	603.9 (60.8%)	288.3 (35%)	130.4 (51.2%)

averages show generally positive trends from 1983 to 1990, experience sudden drops in 1991 and 1992 caused by temporary global cooling induced by the volcanic eruption of Mount Pinatubo in June 1991 (Lucht *et al.*, 2002; Luhr, 1991), and continue increasing from 1992 to 1997 (Figure 3-5 (b)). For areas showing negative trends during the 23-year period, the time series of spatial averages experience large drops in 1998 and 1999. After 2000, most trend categories generally display decreasing trends until 2005. The areas showing negative trends in summer NDVI mainly occur in boreal forest regions (Table 3-1), while regions with positive trends mainly occur in tundra. Grasslands show mixed results with approximately half of the biome exhibiting negative trends and the other half showing positive trends (Table 3-1).

As a result, the tundra region shows a moderate greening trend (0.9% decade^{-1}; P = 0.31), whereas the boreal region displays a moderate browning trend (-1.07% decade^{-1}; P = 0.11) (Figure 3-6), and the grassland region shows a weak greening trend. Overall, the pan-Arctic region shows a small, but insignificant greening trend.

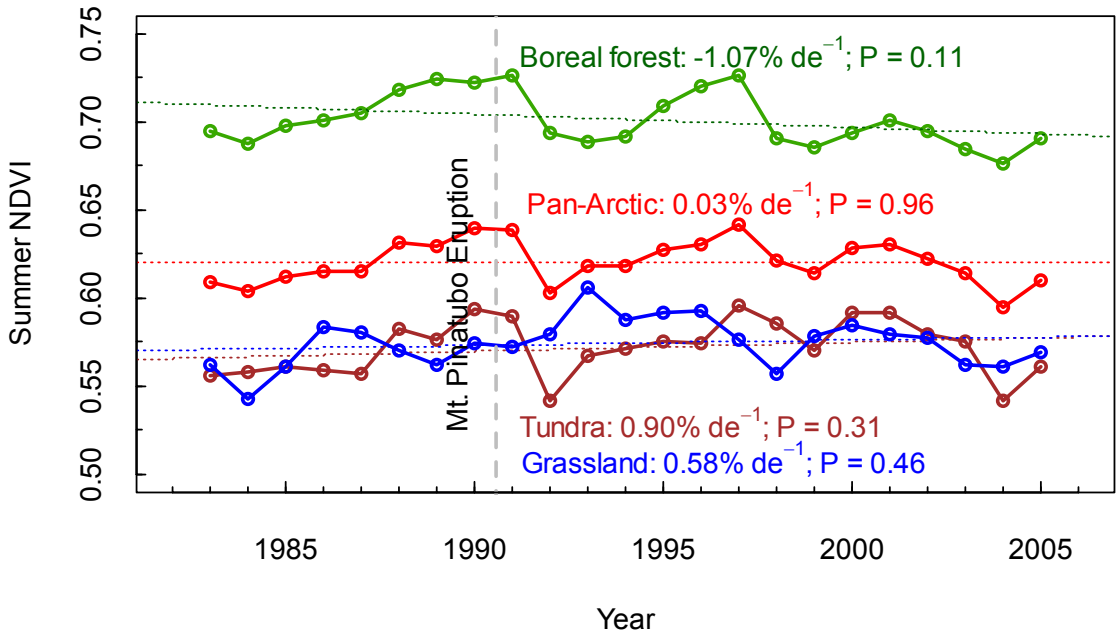

Figure 3-6: Time series of annual average summer NDVI values for the three major biome types and entire pan-Arctic region.

3.7.2. Assessment of Integrated FPAR/LAI Inputs

The error distributions of the combined AVHRR-MODIS FPAR/LAI series are shown in Table 3-2. Since the simple linear regression method is unbiased, the mean error of the adjusted AVHRR FPAR/LAI series is zero relative to the MODIS FPAR/LAI product and there is no bias in the combined AVHRR-MODIS FPAR/LAI time series.

Table 3-2. Comparison of accuracy in the integrated FPAR/LAI time series.

Variables	Error Distribution					Accuracy			
	$\bar{\varepsilon}$	s_ε	Q_{1st}	M_ε	Q_{3rd}	MAE	RMSE	δ_ε	[a]r
LAI (m^2 m^{-2})	0	0.59	-0.30	-0.02	0.22	0.40	0.59	0	0.91
FPAR	0	0.07	-0.04	-0.005	0.03	0.05	0.07	0	0.93

[a]All correlation coefficients are significant at the level of 0.001.

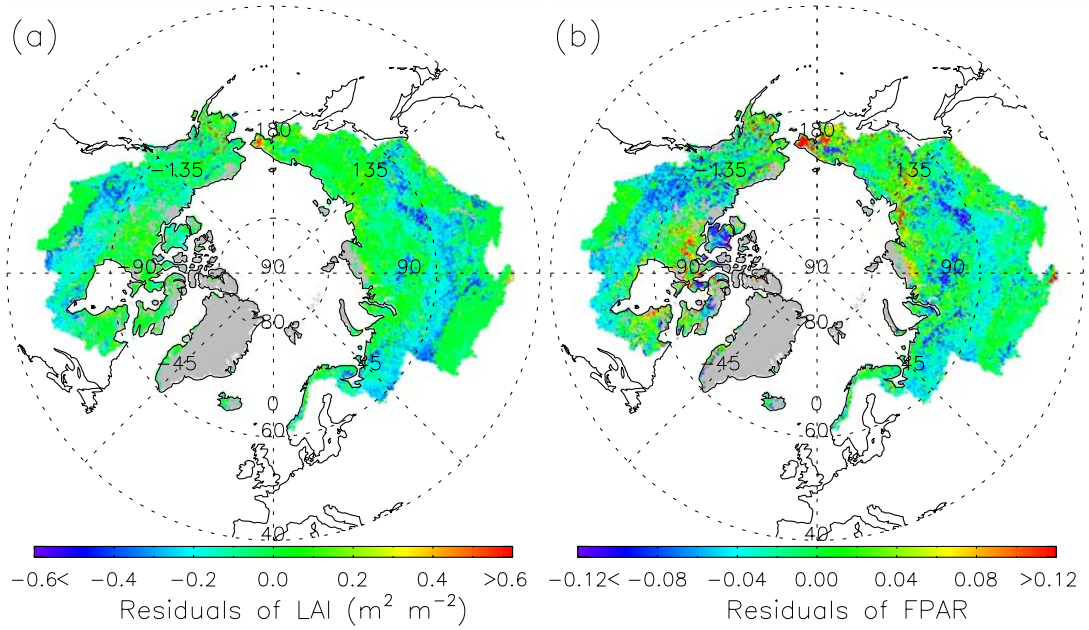

Figure 3-7: Maps of spatial mean residual distributions of integrated satellite LAI (a) and FPAR (b) in 2000. The non-vegetated areas are masked as grey.

The quartile and median statistics indicate that errors from the adjusted AVHRR FPAR/LAI series are normally distributed; standard error statistics show that the errors have a narrow spread; mean absolute error and root mean square error show that the adjusted AVHRR FPAR/LAI series is generally consistent with the corresponding MODIS data series. Correlation coefficients of 0.91 and 0.93 indicate strong correspondence between the adjusted AVHRR and MODIS FPAR/LAI series. Therefore, both error distribution and correlation analyses indicate that the approach for combining AVHRR and MODIS FPAR/LAI time series is reliable. Although errors from the adjusted AVHRR FPAR/LAI series show a slight spatial variation in 2000 (Figure 3-7), the errors are confined to a relatively small area and narrow intervals (± 0.4 m^2 m^{-2} for LAI; ± 0.06 for FPAR) over more than 90% of the vegetated domain.

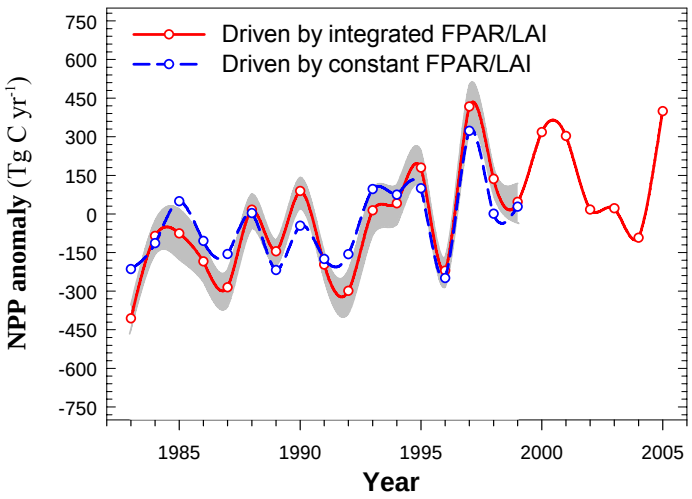

Figure 3-8: Comparison of annual NPP anomalies driven by integrated FPAR/LAI inputs and those driven by constant FPAR/LAI inputs. The 95% confidence intervals of estimated NPP before 2000 are also shown, and account for potential errors from the AVHRR-MODIS FPAR/LAI integration method.

The narrow 95% confidence intervals of estimated NPP before 2000 (Figure 3-8) indicate that the methods for combining the AVHRR and MODIS time series are reliable and robust, and that potential FPAR/LAI errors do not introduce significant uncertainty into NPP calculations for the domain. The NPP results derived using constant FPAR/LAI inputs accounted for 86.13% ($P < 0.001$) of the variability in NPP results derived from the historical FPAR/LAI record (Figure 3-8), indicating that the estimated pan-Arctic NPP trends are primarily climate driven rather than a response to changes in photosynthetic canopy cover. These results also indicate that uncertainties associated with the combined AVHRR-MODIS FPAR/LAI series have a relatively small impact on PEM based estimates of regional NPP trends and annual variability for the domain.

3.7.3. Changes in Climatic Factors of Vegetation Productivity

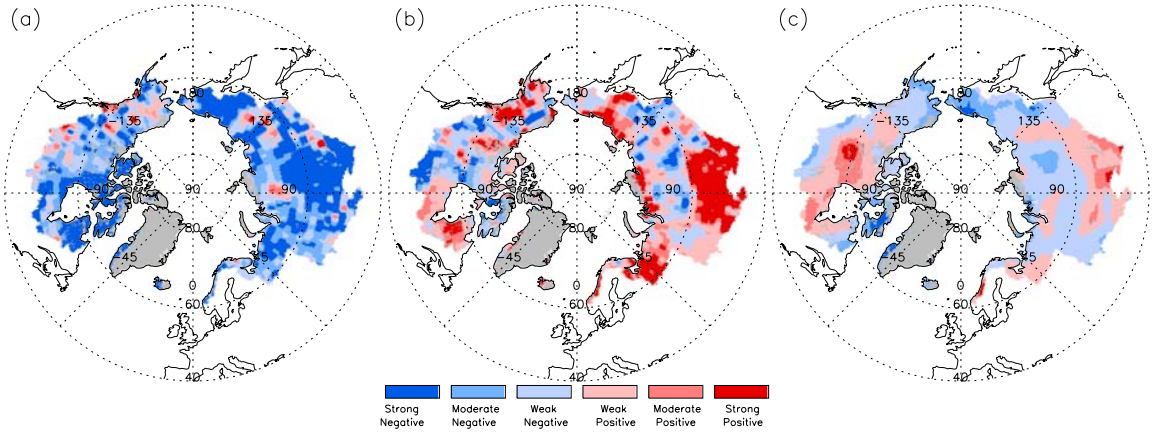

Figure 3-9: Spatial patterns of changes in growing season (GS, April to October) (a) I_t, (b) I_m, and (c) $SW_{\downarrow}$ across the pan-Arctic region from 1983 to 2005.

Since vegetation sequesters carbon mainly during the growing season (GS), I chose to analyze potential changes in climatic drivers of vegetation productivity during the GS. The general GS (April-October) in this region is defined as all months in which the 1983-2005 monthly average air temperature for the pan-Arctic domain is above 0.0°C. The GS I_t generally shows negative trends in approximately 89% of the pan-Arctic region, and has the strongest positive trends in the coastal regions around Hudson Bay, and central, southern and far-eastern Eurasia, while the GS I_m shows positive trends over approximately 61% of the region. These areas with strongest low-temperature stress reductions generally show the largest increases in moisture stress, because warming air temperatures can greatly increase the capacity of the atmosphere to hold water vapor, resulting in increased vapor pressure deficits (VPDs) without sufficient increases in precipitation and evaporation to meet the additional atmospheric moisture demand. Incoming solar radiation during the growing season showed insignificant changes over

approximately 97% of the domain, but with negative trends over 58% of the domain likely caused by recent increases in cloudiness (Wang & Key, 2003).

3.7.4. Changes in Seasonal Freeze-Thaw and Growing Season, and Connection to Vegetation Productivity

The satellite NPP record indicates that the pan-Arctic region is experiencing an advancing trend of 1.7 days per decade ($P = 0.23$) in regional average annual onset of the growing season (T_{NPP_Onset}), which is generally consistent with the atmospheric CO_2

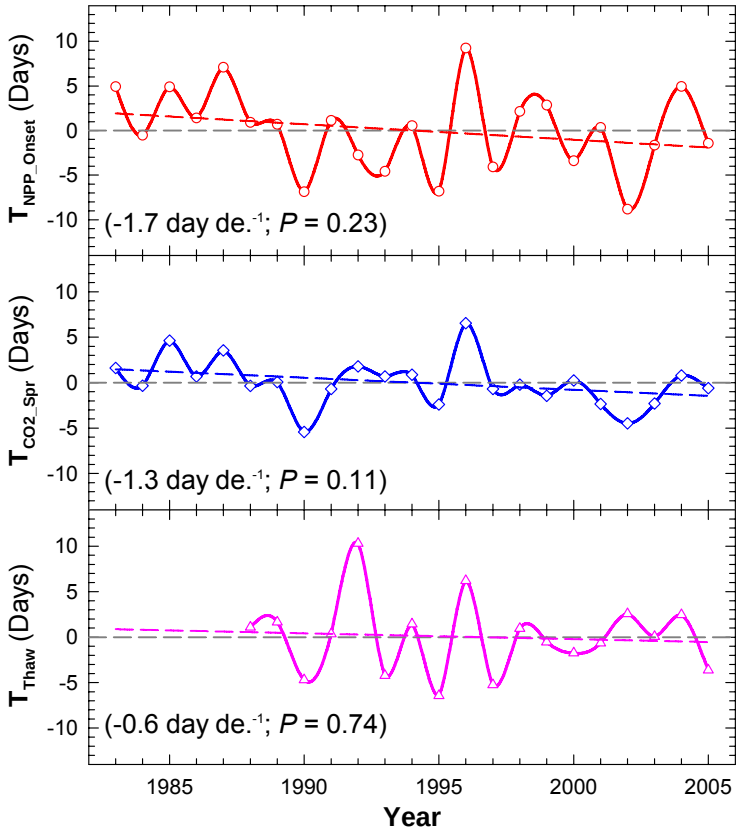

Figure 3-10: Correspondence among annual anomalies of regional average NPP-derived growing season onset (T_{NPP_Onset}), timing of the spring drawdown of atmospheric CO_2 from NOAA GMD high latitude (>50 °N) monitoring sites (T_{CO2_Spr}), and regional average timing of the spring thaw (T_{Thaw}) across the pan-Arctic region.

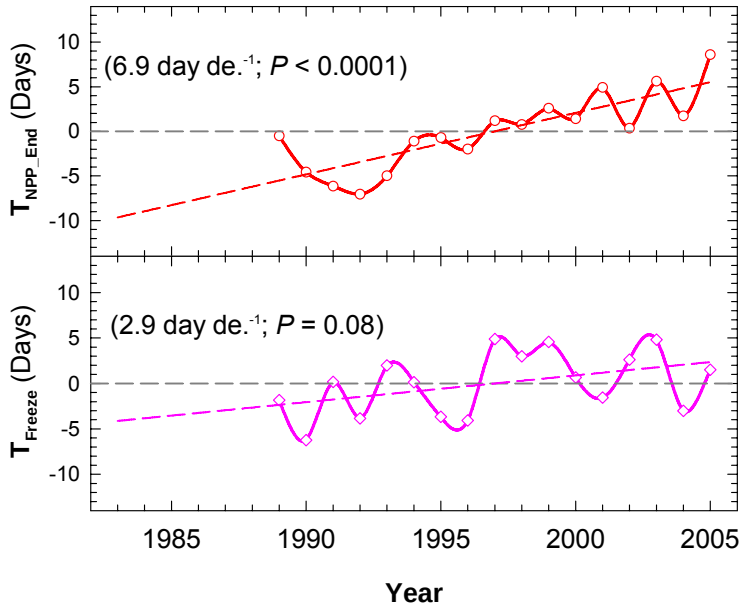

Figure 3-11: Correspondence between annual anomalies of regional average NPP-derived growing season end (T_{NPP_End}) and regional average timing of the fall freezing (T_{Freeze}) across the pan-Arctic region.

observation derived estimates of growing season onset (T_{CO2_Spr}) ($r = 0.78$; $P < 0.001$) and satellite microwave remote sensing derived measures of regional average timing of spring thaw (T_{Thaw}) ($r = 0.48$; $P = 0.05$) (Figure 3-10) . These results indicate that the PEM captures the annual timing and generally earlier arrival of the growing season with regional warming. The negative (earlier) trends of T_{CO2_Spr} and T_{Thaw} also reveal that the growing season and annual non-frozen period are advancing in the pan-Arctic as a response to regional warming.

The pan-Arctic region also shows a significant lengthening trend in regional average annual termination of the growing season (T_{NPP_End} **:** 6.9 days per decade; $P <$ 0.0001) and timing of fall freezing (T_{Freeze} **:** 2.9 days per decade; $P = 0.08$) (Figure 3-11). The favorable correspondence between T_{NPP_End} and T_{Freeze} ($r = 0.46$; $P = 0.07$) indicates

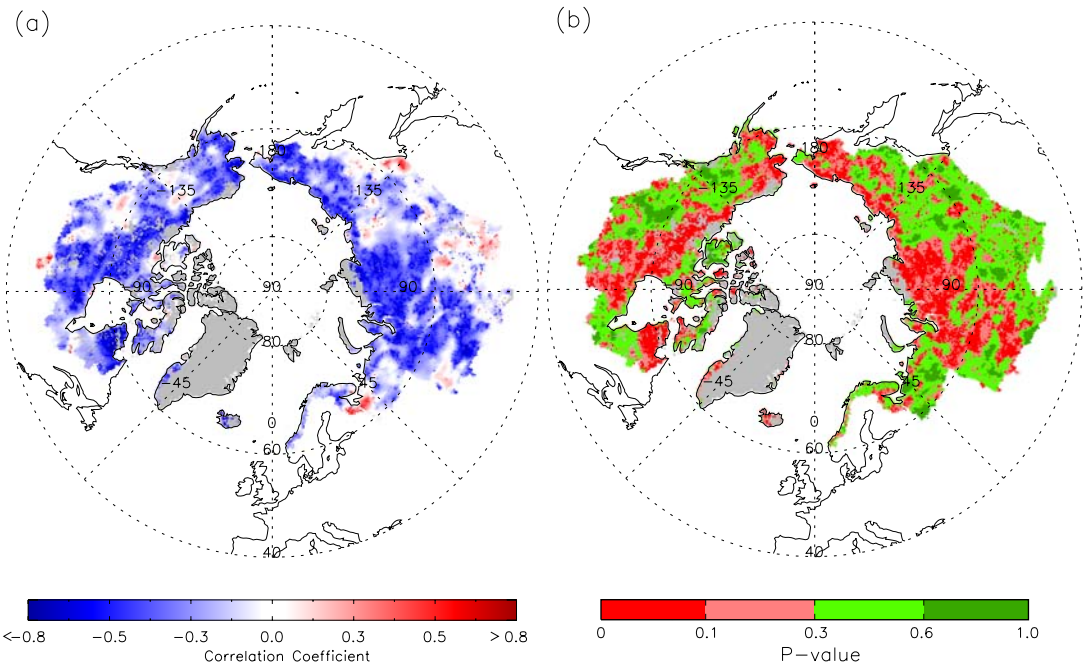

Figure 3-12: Maps of (a) correlation between T_{Thaw} and annual NPP from 1983 to 2005 and (b) the statistical *P*-value.

that the timing of growing season cessation and fall freezing are similar, though growing season cessation is influenced by additional environmental factors in the high latitudes including solar illumination and plant-available moisture (e.g. Kimball *et al.*, 2004b).

The general advance in growing season onset and spring thaw timing, and the significant delays in growing season cessation and fall freezing indicate that the growing season and annual non-frozen period are lengthening in the pan-Arctic as a result of warming; these results also confirm previous findings (Euskirchen *et al.*, 2006; Smith *et al.*, 2004). The favorable correlations between growing season timing and the non-frozen season that annual vegetation productivity and carbon cycle dynamics in the high latitudes are strongly regulated by seasonal freeze-thaw cycle. The correlation between T_{Thaw} and annual NPP is negative for approximately78% of this region (Figure 3-

12 (a)), while 31% of areas with negative correlations are statistically significant (Figure 3-12 (b)). The correlation map (Figure 3-12 (a)) also shows that this negative correlation becomes stronger at higher latitudes, indicating the increasing impact of the freeze-thaw cycle, i.e. low temperature constraints, on vegetation productivity at higher latitudes.

3.7.5. Vegetation Productivity Changes

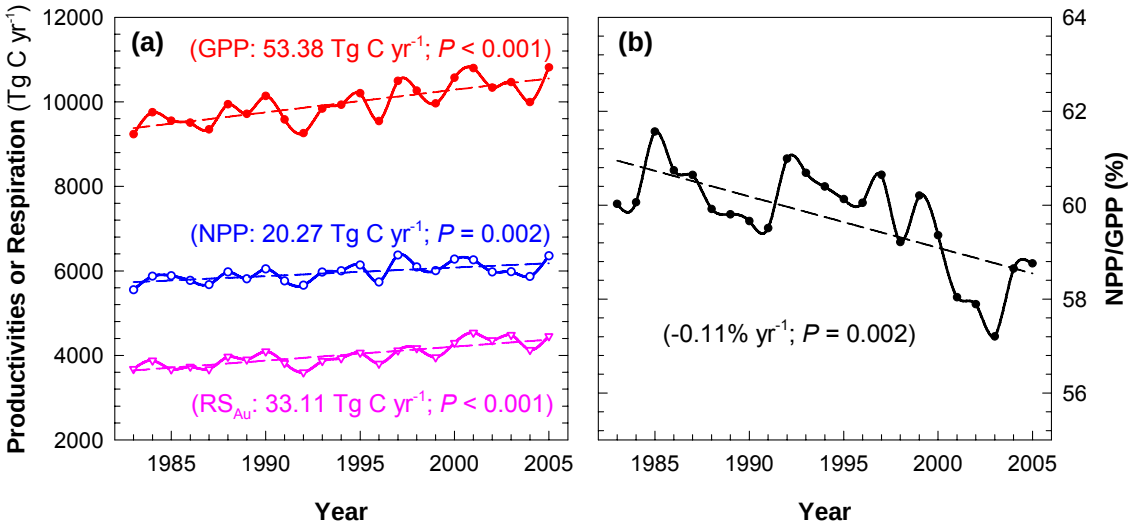

Figure 3-13: Time series of annual average GPP, NPP and autotrophic respiration (RS_{Au}) from 1983 to 2005 for the pan-Arctic region (a). The ratio of NPP to GPP (i.e. CUE) is also shown in (b).

To better understand the biophysical processes driving regional productivity trends I examined regional trends in the gross primary production (GPP) and autotrophic respiration (RS_{Au}) components of NPP. Mean annual GPP for the pan-Arctic domain shows a significant positive linear trend ($53.38\,TgC/yr$; $P < 0.001$) from 1983 to 2005 (Figure 3-13 (a)), while mean annual autotrophic respiration (RS_{Au}) also displays a significant positive linear trend ($33.11\,TgC/yr$; $P < 0.001$). The linear GPP tend during the 23-year period is larger than the RS_{Au} trend, resulting in a positive linear NPP trend

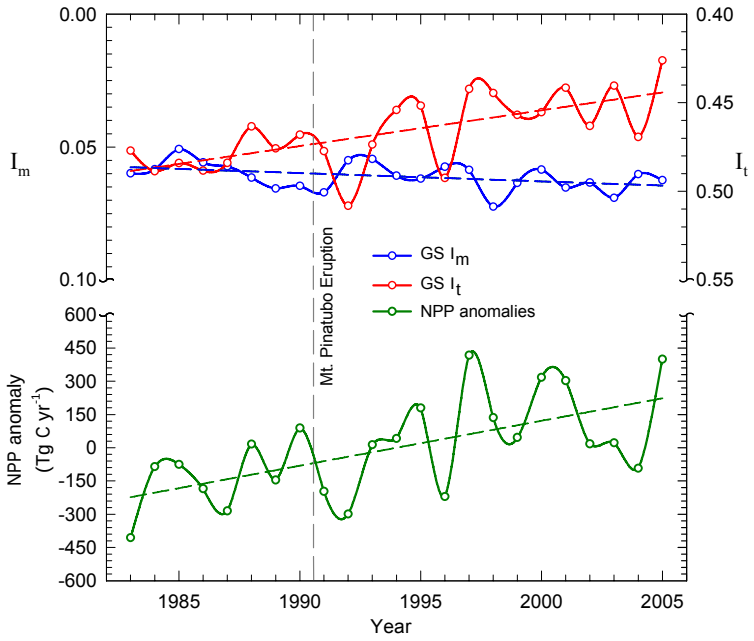

Figure 3-14: Annual NPP anomalies, mean growing season (GS, Apr.–Oct.) I_m and mean GS I_t from 1983 to 2005 for the pan-Arctic domain; the Y-axis for I_m and I_t increases from upper to lower portions of the graphic and corresponds to increasing environmental constraints on productivity. Linear trends for the three variables are shown as dotted lines.

of 0.34% per year ($20.27\,TgC/yr$; $P = 0.002$) from 1983 to 2005 (Figure 3-13 (a)). However, the increasing rate of RS_{Au} is larger than the increasing rate of GPP because the ratio of NPP to GPP (i.e. the carbon use efficiency, CUE) is significantly decreasing (-0.11% yr^{-1}; $P = 0.002$) during the 23-year period (Figure 3-13(b)).

The generally increasing NPP trend during the 23-year period is mainly driven by a declining trend (-0.43% per year; $P < 0.001$) in low-temperature stress (I_t) during the growing season (Apr.–Oct.) (Figure 3-14). However, a coincident and strong increasing trend (0.49% per year; $P = 0.04$) in growing season moisture stress (I_m) partially counteracts the positive effects of more favorable temperatures for photosynthesis. The larger magnitude of I_t relative to I_m (Figure 3-14) indicates that low temperature during

Table 3-3. Summary of annual NPP trend and growing season (Apr.–Oct.) atmospheric moisture stress (I_m) and low temperature stress (I_t) indices within the study domain for the three major biome types.

Land cover	NPP trend		I_m		I_t	
	Trend (% yr^{-1})	[a]Mean (Tg C)	Trend (% yr^{-1})	Mean	Trend (% yr^{-1})	Mean
Tundra	0.50***	2288.79	0.34	0.030	-0.41***	0.543
Boreal forests	0.20	3364.90	0.59*	0.085	-0.49**	0.405
Grassland	0.69***	297.90	1.18**	0.128	-0.46***	0.415

[a] Mean is the 23-year mean.
* $P < 0.05$, ** $P < 0.01$, *** $P < 0.001$

the growing-season is generally the dominant limiting factor for NPP in the pan-Arctic domain. The NPP series also captured large regional productivity declines in 1991 and 1992, which have been attributed to temporary global cooling following the Mount Pinatubo eruption in June, 1991 (Lucht *et al.*, 2002; Luhr, 1991). Earlier onset and lengthening of growing seasons with regional warming are also potential drivers of positive NPP trends (Kimball *et al.*, 2006a; McDonald *et al.*, 2004).

There was considerable spatial variability in NPP anomalies and trends (Figure 3-15), and associated moisture (I_m) and temperature (I_t) constraints to productivity (Table 3-3). For tundra, the PEM results showed a positive NPP trend (0.50% per year, $P < 0.001$) that was primarily driven by a declining trend in I_t (-0.41% per year, $P < 0.001$), indicating a relaxation of the low temperature constraint to productivity. The tundra biome showed positive, but insignificant trends in I_m, indicating that moisture limitations are increasing with regional warming but are not yet a major influence on tundra NPP trends. For the boreal forest biome, annual NPP showed a weak, positive trend (0.20% per year) over the long-term record. The I_t results for this region showed a

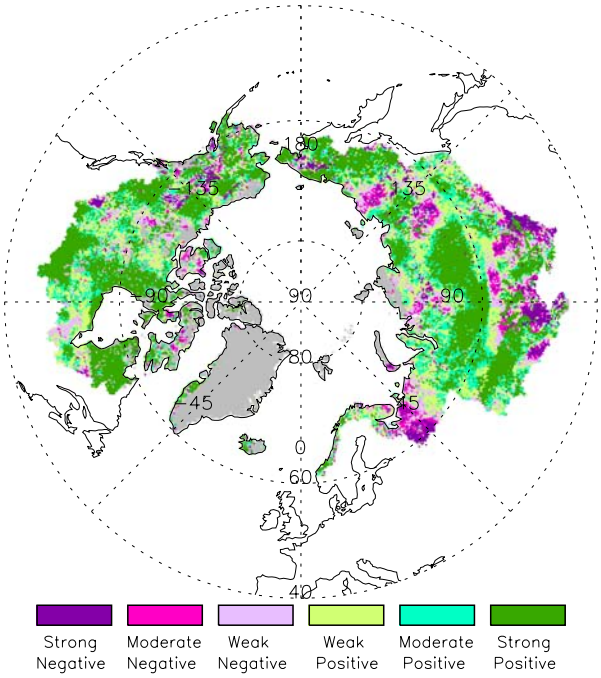

Figure 3-15: Map of annual NPP trends from 1983 to 2005 across the pan-Arctic region.

strong decreasing trend (-0.49% per year, $P < 0.01$) for the period, which coincided with a significant positive trend in the associated moisture constraint to NPP. For the grassland and cropland biomes, mean annual NPP showed a positive regional trend (0.69% per year, $P < 0.001$) coinciding with opposing trends in I_t and I_m of -0.46% ($P < 0.001$) and 1.18% ($P < 0.01$) per year, respectively.

The results summary in Figure 3-16 shows that the low-temperature constraint to productivity is relaxing over the 23-year period, leading to less potential NPP loss for the three biomes, whereas the moisture constraint is increasing and partially counteracting the potential benefits of warmer temperatures. Over the long-term record, moisture constraints reduce annual NPP by 10.11% relative to potential conditions for the pan-Arctic region. This relative annual NPP reduction increased from 9.51% in the 1980s to 11.16% after 2000. Annual productivity for tundra benefits most from the warming trend

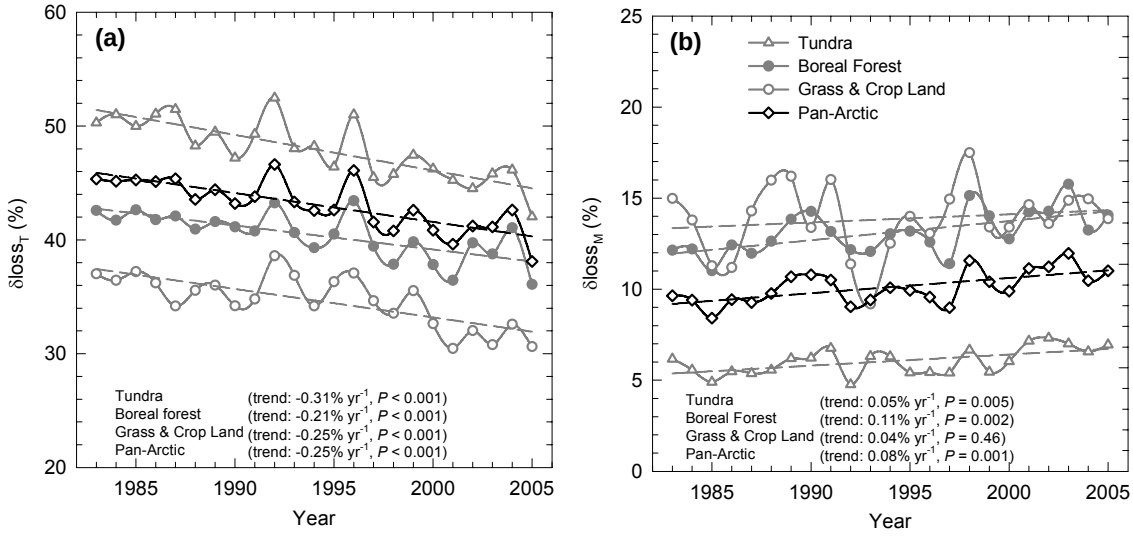

Figure 3-16: Proportional losses of potential NPP due to (a) low-temperature ($\delta loss_T$) and (b) moisture ($\delta loss_M$) constraints for the three major land cover types within the pan-Arctic domain. The dashed lines denote linear trends.

and suffers least from moisture limitations, since tundra is mainly temperature limited, with average 47.96% and 5.32% losses relative to potential conditions due to low-temperature and moisture constraints, respectively. The boreal forest biome shows a similar moisture constraint to productivity as the grassland and cropland biomes, but the increasing trend in NPP losses due to moisture limitations is much larger for boreal forest ($0.11\%\ yr^{-1},\ P = 0.002$) than for grassland and cropland biomes ($0.04\%\ yr^{-1},\ P = 0.46$). The warming trend brings comparable benefits for boreal forest and grassland and cropland biomes as indicated by similar respective decreasing trends in potential NPP losses of $-0.21\%\ yr^{-1}$ ($P = 0.0002$) and $-0.25\%\ yr^{-1}$ ($P < 0.0001$).

The Figure 3-16 summary also shows that relatively cool conditions in 1992, 1996 and 2004, and periodic dry conditions from 1989–1991, 1998–1999, and 2001–2003 coincided with large NPP declines for the pan-Arctic region, as shown in Figure 3-14. The results (Figure 3-16) indicate three major drought periods for the pan-Arctic

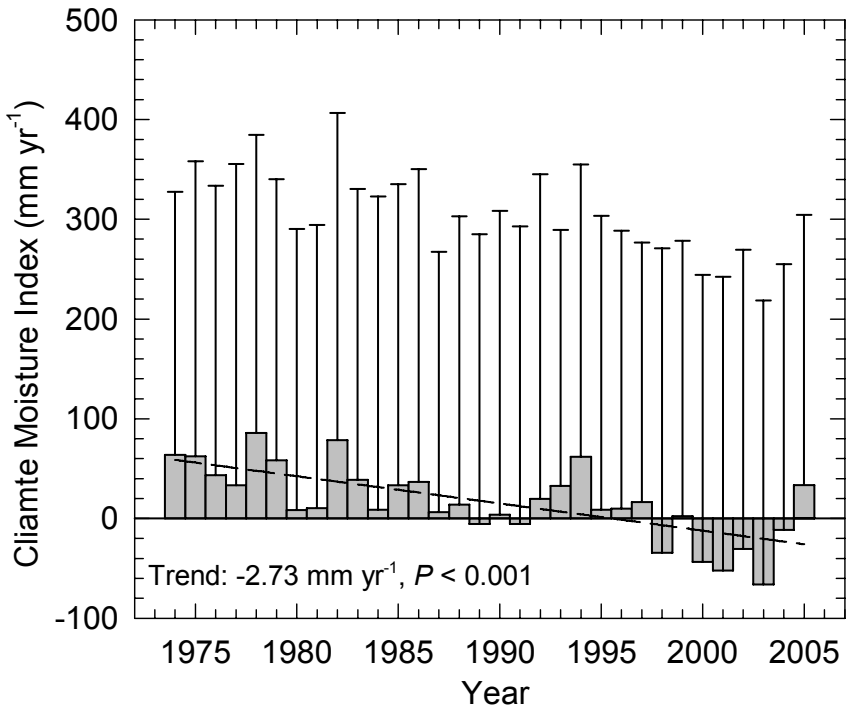

Figure 3-17: Mean annual climate moisture index (*P-PET*) for the pan-Arctic basin and Alaska domain and 1974–2005 period; error bars denote the standard deviation of annual observations for the domain. The total number of NCDC CSB stations used to compute the index ranged from 2053 to 2924 per year.

region from 2001–2003, 1998–1999, and 1989–1991, which are ranked in terms of highest to lowest relative severity of potential NPP losses due to moisture limitations. These drought events are confirmed by mean annual CMI anomalies derived from the regional surface weather station network (Figure 3-17). The CMI shows a drying trend of $-2.73\,mm/yr$ ($P < 0.001$) from 1974 to 2005 for the domain. The relative strength of the negative CMI anomalies and proportional losses of potential NPP from increasing I_m based constraints after 2000 indicates that the severity and persistence of the post-2000 drought is unprecedented for the 30+ year station record. These conditions also promoted a widespread NPP decline relative to potential conditions for the domain (Figure 3-14).

The spatial patterns of summer I_m and annual NPP anomalies for 1998, 2001, 2002, and 2003 are presented in Figure 3-18. These results indicate summer drought across much of the domain with corresponding decreases in annual NPP. Summer (June –August) drought, indicated by anomalous increases in I_m, contributed to reductions in PEM derived annual NPP for predominantly inland areas including western and central Canada and southern and central Eurasia. Model results for eastern Alaska also indicated widespread drought effects. These results are consistent with the timing and location of recent documented drought events. Waple *et al.*(2002) reported that Canada experienced one of its most serious and extensive droughts on record in 2001, while the most severely affected areas occurred in the Canadian Prairies where the 2001 drought followed two to three consecutive years of below-average rainfall. Waple and Lawrimore (2003) also reported that some areas of central Canada suffered the driest August on record and western Canada suffered the second consecutive year with the most severe drought on record in 2002. Alaska had the warmest recorded year to date in 2002, while Russia reported a substantial precipitation deficit in July and August of 2002, which led to meteorological and hydrological drought for most of the region. In 2003, drier-than-normal conditions continued in the western provinces despite relatively wet conditions in other regions of Canada (Levinson & Waple, 2004); during July, anomalously warm and dry conditions appeared in some regions of Eurasia.

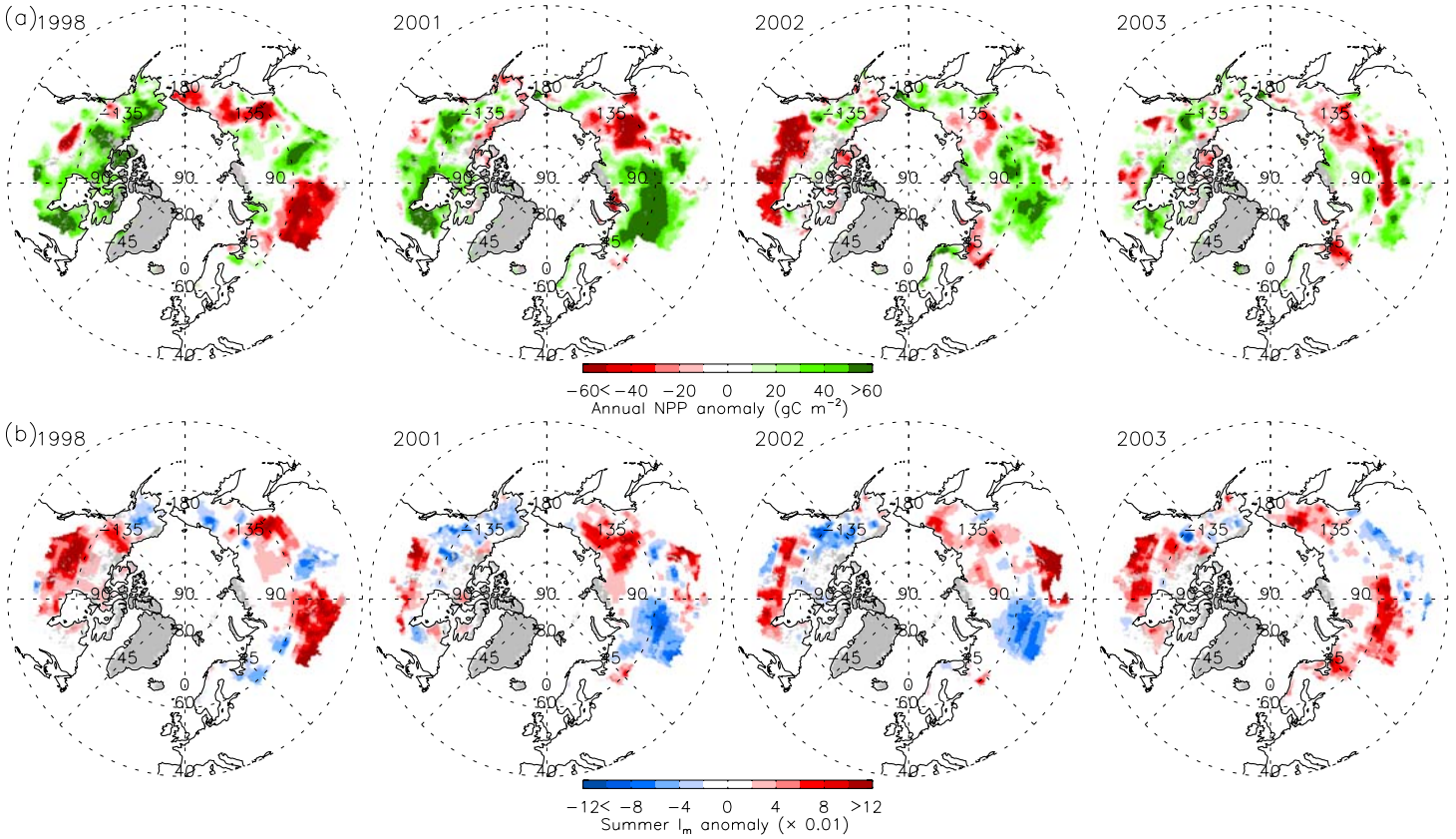

Figure 3-18: Maps of (a) annual NPP and (b) summer (Jun.–Aug.) I_m anomalies (relative to the 23-year mean) for 1998, 2001, 2002, and 2003. A positive anomaly for I_m corresponds to increasing moisture constraints on productivity relative to the long-term mean.

3.7.6. Comparison between PEM-based Vegetation Productivity and Stand Inventory Records

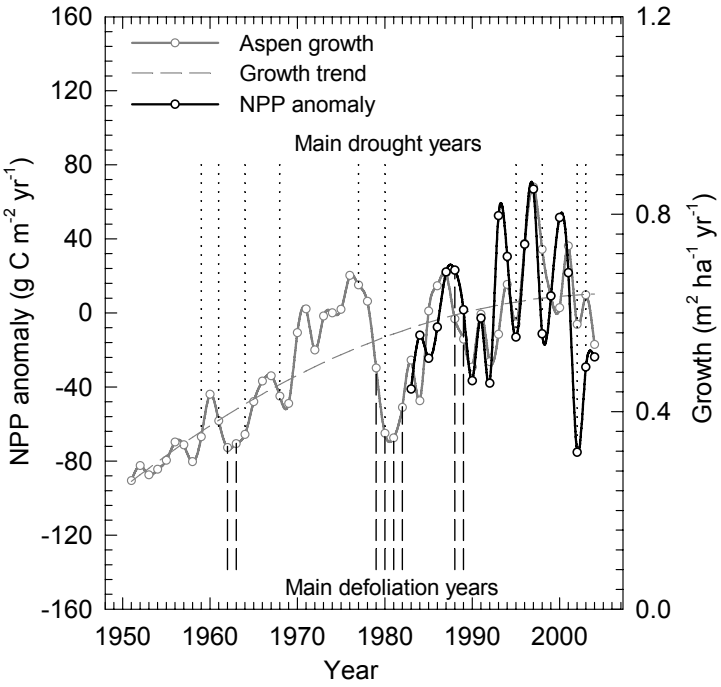

Figure 3-19: Comparison between PEM derived NPP anomalies and boreal aspen growth derived from tree-ring analyses for 72 CIPHA stands across western Canada. Vertical dotted lines and dashed lines denote major drought and insect defoliation years, respectively, as reported by (Hogg *et al.*, 2005).

Figure 3-19 shows the CIPHA stand inventory network derived mean boreal aspen growth observations from 1951 to 2004 and corresponding PEM based mean annual NPP anomalies from 1983 to 2004. Also shown are the major drought and defoliation years for the region as reported by Hogg *et al.* (2005). The trend line using a best-fit quadratic equation is also shown, indicating a general increasing growth trend with large annual variations due to the effects of periodic insect defoliations, drought, and vegetation re-growth. It should be noted that the tree ring based growth estimates also

reflect the normal process of stand development, e.g., age, mortality, and competition, though annual growth variations have been linked to the effects of climate and insects (Hogg *et al.*, 2005).

The PEM based annual NPP anomalies were positively correlated ($r = 0.56$; $P = 0.007$) with mean stand-level observations of boreal aspen growth for the 72 CIPHA sites. Both the PEM and CIPHA time series showed large decreases in plant growth in 1995, 1998, 2002, and 2003. These anomalous productivity declines have been attributed to severe regional drought conditions for these years (Hogg *et al.*, 2005). Both data series also confirm a generally positive vegetation growth trend for the 1980s and 1990s (1.65% per year, $P = 0.03$ for CIPHA Aspen growth; 0.67% per year, $P = 0.07$ for PEM derived NPP) and recent drought-induced NPP decreases after late-1990s.

3.8. Discussion and Summary

The PEM based NPP results may be negatively impacted by uncertainties in satellite remote sensing inputs including the PAL FPAR/LAI product, which incorporates uncertainties from dropped scan lines, navigation errors, data drop outs, edge-of-orbit composite discontinuities, and other artifacts of the AVHRR PAL NDVI series (Cihlar *et al.*, 1997; Tucker *et al.*, 2005). The NASA GIMMS NDVI product has attempted to correct most of the above problems and is currently available at 8-km resolution (Pinzon *et al.*, 2005; Tucker *et al.*, 2005). However, although the GIMMS LAI product is now available, there is no alternative GIMMS FPAR product. Though the SRB solar radiation product is of generally good quality, solar radiation has a larger uncertainty relative to the other PEM inputs for the domain. Therefore, the solar radiation inputs may introduce

uncertainty into the PEM calculations. However, the impact of these uncertainties on NPP calculations is partially mitigated by the relative importance of other surface meteorological inputs to the PEM.

Despite the potential negative effects of the above uncertainties, the generally consistent temporal patterns between PEM derived NPP and tree-ring based aspen growth observations (Figure 3-19) indicate that the NPP time series from relatively coarse resolution satellite remote sensing effectively captures the regional impacts of summer drought, along with the impacts of transient global cooling following a major volcanic eruption. Both stand inventory observations and satellite based PEM results also confirm a generally positive vegetation growth trend for the 1980s and 1990s across west-central Canada and recent drought-induced NPP decreases after the late 1990s.

The results show that increasing productivity trends generally occur in tundra regions while NPP reductions occur in boreal forest regions. These findings are consistent with previous AVHRR GIMMS based analyses of regional photosynthetic trends (Bunn & Goetz, 2006; Goetz *et al.*, 2005). The results also indicate that recent widespread NPP reductions in boreal forest regions were due to vegetation drought stress, which is also consistent with previous studies of AVHRR-based photosynthetic trends (Bunn & Goetz, 2006; Goetz *et al.*, 2007). The negative effects of recent drought on terrestrial productivity are widespread for boreal regions, impacting not only western and central Canada but also eastern Alaska and south-central Eurasia. These results are also supported by other published field observations. In Alaska, tree-ring studies showed a reduction in the growth of white spruce (Barber *et al.*, 2000; Barber *et al.*, 2004; Davi *et al.*, 2003), even at some upper tree-line sites (Lloyd & Fastie, 2003; Wilmking *et al.*,

2004), because of a recent increase in temperature-induced drought stress. Hogg and Wein (2005) also reported the negative impacts of recent drought on forest growth and regeneration in southwestern Yukon, Canada.

Over western and central Canada, most available moisture for precipitation comes from the Pacific Ocean in winter (November–March) and the Gulf of Mexico in summer (May–August) (Liu *et al.*, 2004). Thus regional precipitation has strong teleconnections to global sea surface temperature (SST) patterns (Shabbar & Skinner, 2004), especially variations in tropical and north Pacific SSTs (Seager *et al.*, 2005; Zhang *et al.*, 2007a), which may explain the relative persistence of recent drought in southern Alaska and south-western Eurasia. Goetz *et al.* (2007) reported the lagged correlation between spring climate fields (like temperature and precipitation) and spring boreal North America net carbon exchange and suggested teleconnections between carbon fluxes in the pan-arctic region and large-scale atmospheric/oceanic oscillations such as the Arctic Oscillation and ENSO. More explicit analyses of teleconnections between climate oscillations and pan-Arctic NPP patterns were also documented in Zhang *et al.* (2007a). The results of this study show that the largest negative NPP anomalies are predominantly located in relatively drought prone inland areas with greater annual extremes in temperature and precipitation. In addition, earlier spring thawing and corresponding earlier and longer growing seasons in this region (Kimball *et al.*, 2006a; Levinson & Waple, 2004; McDonald *et al.*, 2004; Waple & Lawrimore, 2003; Waple *et al.*, 2002) may be contributing to drought by enhancing vegetation growth and potential water loss. Bunn and Goetz (2006) reported that the recent boreal browning trends are more pronounced in more densely forested areas, as derived from MODIS tree cover products, which may

reflect a greater vegetation water use requirement and potential drought stress for these areas.

Future changes in terrestrial productivity will depend strongly on adequate supplies of plant-available moisture to support positive vegetation growth trends under a warming climate. Positive trends in regional warming and drying (Figure 3-14), and earlier onset of the growing season (Figure 3-10) are consistent with previous studies. Current and projected future warming of the region with a declining or negative water balance (i.e., the difference between precipitation and evaporation) will likely result in more frequent and severe drought, leading to further decreases in regional productivity and impairing the potential terrestrial sink strength for atmospheric CO_2. However, regional warming with commensurate increases in precipitation and a positive water balance (Cassano *et al.*, 2007) will likely support further increases in productivity. In addition, future warming likely surpasses the photosynthetic temperature optimum of many boreal tree species such as black spruce (Way & Sage, 2008), reducing forest carbon sequestration and altering associated species composition in this region. However, our results also indicate that in tundra biomes the relaxation of low-temperature constraints to photosynthesis is still the dominant environmental factor driving positive NPP trends despite concurrent increases in plant available moisture constraints. These results are consistent with AVHRR GIMMS based observations of positive photosynthetic trends for North American tundra (*Goetz et al*. 2005). The observed regional trajectory in I_m indicates that the negative effects of increasing moisture constraints on productivity are likely to become more severe and widespread under a warming climate, counteracting the positive effects of a lengthening growing season,

without sufficient increases in precipitation to offset increasing evapotranspiration demands. Improvements in the spatial resolution of regional climate reanalyses coupled with standardization and augmentation of solar radiation and precipitation monitoring networks, and enhanced resolution satellite remote sensing products would dramatically improve the regional assessment of NPP changes and associated linkages between the terrestrial water and carbon cycles.

3.9. References Cited

Barber, V.A., Juday, G.P., & Finney, B.P. (2000) Reduced growth of Alaskan white spruce in the twentieth century from temperature-induced drought stress. *Nature*, **405**, 668-673.

Barber, V.A., Juday, G.P., Finney, B.P., & Wilmking, M. (2004) Reconstruction of summer temperatures in interior Alaska from tree-ring proxies: Evidence for changing synoptic climate regimes. *Climatic Change*, **63**, 91-120.

Bunn, A.G. & Goetz, S.J. (2006) Trends in satellite-observed circumpolar photosynthetic activity from 1982 to 2003: The influence of seasonality, cover type, and vegetation density. *Earth Interactions*, **10**, 1-19.

Cassano, J.J., Uotila, P., Lynch, A.H., & Cassano, E.N. (2007) Predicted changes in synoptic forcing of net precipitation in large Arctic river basins during the 21st century. *Journal of Geophysical Research*, **112**, G04S49, doi:10.1029/2006JG000332.

Chapin III, F.S., Shaver, G.R., & Kedrowski, R.A. (1986) Environmental Controls over Carbon, Nitrogen and Phosphorus Fractions in Eriophorum-Vaginatum in Alaskan Tussock Tundra. *Journal of Ecology*, **74**, 167-195.

Churkina, G. & Running, S.W. (1998) Contrasting climatic controls on the estimated productivity of global terrestrial biomes. *Ecosystems*, **1**, 206-215.

Cihlar, J., Ly, H., Li, Z., Chen, J., Pokrant, H., & Huang, F. (1997) Multitemporal, multichannel AVHRR data sets for land biosphere studies-Artifacts and corrections. *Remote Sensing of Environment*, **60**, 35-57.

Davi, N.K., Jacoby, G.C., & Wiles, G.C. (2003) Boreal temperature variability inferred from maximum latewood density and tree-ring width data, Wrangell Mountain region, Alaska. *Quaternary Research*, **60**, 252-262.

Erickson, D.J., Rasch, P.J., Tans, P.P., Friedlingstein, P., Ciais, P., Maier-Reimer, E., Six, K., Fischer, C.A., et al. (1996) The seasonal cycle of atmospheric CO_2: A study based on the NCAR Community Climate Model (CCM2). *Journal of Geophysical Research*, **101**, 15079-15097.

Euskirchen, E.S., McGuire, A.D., Kicklighter, D.W., Zhuang, Q., Clein, J.S., Dargaville, R.J., Dye, D.G., Kimball, J.S., et al. (2006) Importance of recent shifts in soil thermal dynamics on growing season length, productivity, and carbon sequestration in terrestrial high-latitude ecosystems. *Global Change Biology*, **12**, 731-750.

Frolking, S., McDonald, K.C., Kimball, J.S., Way, J.B., Zimmermann, R., & Running, S.W. (1999) Using the space-borne NASA scatterometer (NSCAT) to determine the frozen and thawed seasons. *Journal of Geophysical Research-Atmospheres*, **104**, 27895-27907.

GLOBALVIEW-CO_2 (2006). Cooperative atmospheric data integration project - carbon dioxide. CD-ROM. NOAA GMD, Boulder, Colorado.

Goetz, S.J., Bunn, A.G., Fiske, G.J., & Houghton, R.A. (2005) Satellite-observed photosynthetic trends across boreal North America associated with climate and fire disturbance. *Proceedings of the National Academy of Sciences*, **102**, 13521-13525.

Goetz, S.J., Mack, M.C., Gurney, K.R., Randerson, J.T., & Houghton, R.A. (2007) Ecosystem responses to recent climate change and fire disturbance at northern high latitudes: observations and model results contrasting northern Eurasia and North America. *Environmental Research Letters*, **4**, 045031, doi:10.1088/1748-9326/2/4/045031.

Heimann, M., Esser, G., Haxeltine, A., Kaduk, J., Kicklighter, D.W., Knorr, W., Kohlmaier, G.H., McGuire, A.D., et al. (1998) Evaluation of terrestrial carbon

cycle models through simulations of the seasonal cycle of atmospheric CO_2: First results of a model intercomparison study. *Global Biogeochemical Cycles*, **12**, 1-24.

Heinsch, F.A., Reeves, M., Votava, P., Kang, S., Milesi, C., Zhao, M., Glassy, J., Jolly, W.M., et al. (2003). User's Guide, GPP and NPP (MOD17A2/A3) Products NASA MODIS Land Algorithm, Version 2.0. The University of Montana.

Hogg, E.H. (1997) Temporal scaling of moisture and the forest-grassland boundary in western Canada. *Agricultural and Forest meteorology*, **84**, 115-122.

Hogg, E.H., Brandt, J.P., & Kochtubajda, B. (2005) Factors affecting interannual variation in growth of western Canadian aspen forests during 1951-2000. *Canadian Journal of Forest Research*, **35**, 610-622.

Hogg, E.H., Brandt, J.P., & Michaelian, M. (2008) Impacts of a regional drought on the productivity, dieback and biomass of western Canadian aspen forests. *Canadian Journal of Forest Research*, **38**, 1373-1384.

Hogg, E.H. & Wein, R.W. (2005) Impacts of drought on forest growth and regeneration following fire in southwestern Yukon, Canada. *Canadian Journal of Forest Research*, **35**, 2141-2150.

Jolly, W.M., Nemani, R., & Running, S.W. (2005) A generalized, bioclimatic index to predict foliar phenology in response to climate. *Global Change Biology*, **11**, 619-632.

Keeling, C.D., Chin, J.F.S., & Whorf, T.P. (1996) Increased activity of northern vegetation inferred from atmospheric CO_2 measurements. *Nature*, **382**, 146-149.

Kimball, J.S., McDonald, K.C., Frolking, S., & Running, S.W. (2004a) Radar remote sensing of the spring thaw transition across a boreal landscape. *Remote Sensing of Environment*, **89**, 163-175.

Kimball, J.S., McDonald, K.C., Keyser, A.R., Frolking, S., & Running, S.W. (2001) Application of the NASA scatterometer (NSCAT) for determining the daily frozen and nonfrozen landscape of Alaska. *Remote Sensing of Environment*, **75**, 113-126.

Kimball, J.S., McDonald, K.C., Running, S.W., & Frolking, S.E. (2004b) Satellite radar remote sensing of seasonal growing seasons for boreal and subalpine evergreen forests. *Remote Sensing of Environment*, **90**, 243-258.

Kimball, J.S., McDonald, K.C., & Zhao, M. (2006a) Spring thaw and its effect on terrestrial vegetation productivity in the Western Arctic observed from satellite microwave and optical remote sensing. *Earth Interactions*, **10**, 1-22.

Kimball, J.S., Zhao, M., McDonald, K.C., & Running, S.W. (2006b) Satellite remote sensing of terrestrial net primary production for the pan-Arctic basin and Alaska. *Mitigation and Adaptation Strategies for Global Change*, **11**, 782-804, doi:10.1007/s11027-005-9014-5.

Levinson, D.H. & Waple, A.M. (2004) State of climate in 2003. *Bulletin of the American Meteorological Society*, **85**, S1-S72.

Liu, J.L., Stewart, R.E., & Szeto, K.K. (2004) Moisture transport and other hydrometeorological features associated with the severe 2000/01 drought over the western and central Canadian Prairies. *Journal of Climate*, **17**, 305-319.

Lloyd, A.H. & Fastie, C.L. (2003) Recent changes in treeline forest distribution and structure in interior Alaska. *Ecoscience*, **10**, 176-185.

Lucht, W., Prentice, I.C., Myneni, R.B., Sitch, S., Friedlingstein, P., Cramer, W., Bousquet, P., Buermann, W., et al. (2002) Climatic control of the high-latitude vegetation greening trend and Pinatubo effect. *Science*, **296**, 1687-1689.

Luhr, J.F. (1991) Mount-Pinatubo - Volcanic Shade Causes Cooling. *Nature*, **354**, 104-105.

McDonald, K.C. & Kimball, J.S. (2005). Hydrological application of remote sensing: freeze-thaw states using both active and passive microwave sensors. In *Encyclopedia of Hydrological Sciences. Part Five: Remote Sensing* (eds M.G. Anderson & J.J. McDonnell). Wiley & Sons Ltd.

McDonald, K.C., Kimball, J.S., Njoku, E., Zimmermann, R., & Zhao, M. (2004) Variability in springtime thaw in the terrestrial high latitudes: Monitoring a major control on the biospheric assimilation of atmospheric CO2 with spaceborne microwave remote sensing. *Earth Interactions*, **8**, 1-22.

Myneni, R.B., Hoffman, S., Knyazikhin, Y., Privette, J.L., Glassy, J., Tian, Y., Wang, Y., Song, X., et al. (2002) Global products of vegetation leaf area and fraction absorbed PAR from year one of MODIS data. *Remote Sensing of Environment*, **83**, 214-231.

Myneni, R.B., Keeling, C.D., Tucker, C.J., Asrar, G., & Nemani, R.R. (1997a) Increased plant growth in the northern high latitudes from 1981 to 1991. *Nature*, **386**, 698-702.

Myneni, R.B., Nemani, R.R., & Running, S.W. (1997b) Estimation of global leaf area index and absorbed par using radiative transfer models. *IEEE Transactions on Geoscience and Remote Sensing*, **35**, 1380-1393.

Nemani, R.R., Keeling, C.D., Hashimoto, H., Jolly, W.M., Piper, S.C., Tucker, C.J., Myneni, R.B., & Running, S.W. (2003) Climate-driven increases in global terrestrial net primary production from 1982 to 1999. *Science*, **300**, 1560-1563.

Pinzon, J., Brown, M.E., & Tucker, C.J. (2005). Satellite time series correction of orbital drift artifacts using empirical mode decomposition. In *Hilbert-Huang Transform: Introduction and Applications* (eds N.E. Huang & S.S.P. Shen), pp. 167-186. World Scientific Publishing Co. Pte. Ltd., Singapore.

Randerson, J.T., Field, C.B., Fung, I.Y., & Tans, P.P. (1999) Increases in early season ecosystem uptake explain recent changes in the seasonal cycle of atmospheric CO2 at high northern latitudes. *Geophysical Research Letters*, **26**, 2765-2768.

Randerson, J.T., Thompson, M.V., Conway, T.J., Fung, I.Y., & Field, C.B. (1997) The contribution of terrestrial sources and sinks to trends in the seasonal cycle of atmospheric CO_2 at high northern latitudes. *Geophysical Research Letters*, **26**, 2765-2768.

Running, S.W., Nemani, R.R., Heinsch, F.A., Zhao, M., Reeves, M., & Hashimoto, H. (2004) A continuous satellite-derived measure of global terrestrial primary productivity: Future science and applications. *Bioscience*, **56**, 547-560.

Running, S.W., Thornton, P.E., Nemani, R.R., & Glassy, J.M. (2000). Global terrestrial gross and net primary productivity from the Earth Observing System. In *Methods in Ecosystem Science* (eds O.E. Sala, R.B. Jackson & H.A. Mooney), pp. 44-57. Springer, New York.

Seager, R., Kushnir, Y., Herweijer, C., Naik, N., & Velez, J. (2005) Modeling of tropical forcing of persistent droughts and pluvials over western North America: 1856-2000. *Journal of Climate*, **18**, 4065-4088.

Shabbar, A. & Skinner, W. (2004) Summer drought patterns in Canada and the relationship to global sea surface temperatures. *Journal of Climate*, **17**, 2866-2880.

Smith, N.V., Saatchi, S.S., & Randerson, J.T. (2004) Trends in high northern latitude soil freeze and thaw cycles from 1988 to 2002. *Journal of Geophysical Research-Atmospheres*, **109**, D12101, doi:10.1029/2003JD004472.

Tucker, C.J. (1979) Red and photographic infrared linear combinations for monitoring vegetation. *Remote Sensing of Environment*, **8**, 127-150.

Tucker, C.J., Pinzon, J.E., Brown, M.E., Slayback, D., Pak, E.W., Mahoney, R., Vermote, E., & Saleous, N. (2005) An extended AVHRR 8-km NDVI data set compatible with MODIS and SPOT vegetation NDVI data. *International Journal of Remote Sensing*, **26**, 4485-4498.

Wang, X.J. & Key, J.R. (2003) Recent trends in arctic surface, cloud, and radiation properties from space. *Science*, **299**, 1725-1728.

Waple, A.M. & Lawrimore, J.H. (2003) State of the climate in 2002. *Bulletin of the American Meteorological Society*, **6**, S1-S68, doi:10.1175/BAMS-84-6-Waple.

Waple, A.M., Lawrimore, J.H., Halpert, M.S., Bell, G.D., Higgins, W., Lyon, B., Menne, M.J., Gleason, K.L., et al. (2002) Climate Assessment for 2001. *Bulletin of the American Meteorological Society*, **83**, S1-S62.

Way, D.A. & Sage, R.F. (2008) Elevated growth temperatures reduce the carbon gain of black spruce [Picea mariana (Mill.) BSP]. *Global Change Biology*, **14**, 624-636.

Wilmking, M., Juday, G.P., Barber, V.A., & Zald, H.S.J. (2004) Recent climate warming forces contrasting growth responses of white spruce at treeline in Alaska through temperature thresholds. *Global Change Biology*, **10**, 1724-1736.

Zhang, K., Kimball, J.S., McDonald, K.C., Cassano, J.J., & Running, S.W. (2007a) Impacts of large-scale oscillations on pan-Arctic terrestrial net primary production. *Geophysical Research Letters*, **34**, L21403, doi:10.1029/2007GL031605.

Zhang, K., Kimball, J.S., Zhao, M., Oechel, W.C., Cassano, J., & Running, S.W. (2007b) Sensitivity of pan-Arctic terrestrial net primary productivity simulations to daily surface meteorology from NCEP-NCAR and ERA-40 reanalysis. *Journal of Geophysical Research*, **112**, G01011, doi:10.1029/2006JG000249.

Zhao, M., Heinsch, F.A., Nemani, R.R., & Running, S.W. (2005) Improvements of the MODIS terrestrial gross and net primary production data set. *Remote Sensing of Environment*, **95**, 164-176.

Zhao, M., Running, S.W., Heinsch, F.A., & Nemani, R.R. (2008). Terrestrial primary production from MODIS. In *Land Remote Sensing and Global Environmental Change: NASA's EOS and the Science of ASTER and MODIS* (eds C. Justice & M. Abrams), pp. 423-444. Springer, New York.

CHAPTER 4: SATELLITE-BASED ANALYSIS OF EVAPOTRANSPIRATION AND ASSOCIATED CHANGES IN THE REGIONAL WATER BALANCE

4.1. Introduction

Hydrological and ecological processes are strongly coupled in northern high latitude boreal forest and Arctic tundra regions. Precipitation and snowmelt influence plant-available moisture during the growing season, which impacts water, energy and carbon cycles through vegetation canopy controls on transpiration, plant-atmosphere exchanges of water vapor and carbon dioxide, and the partitioning of net radiant energy into sensible and latent heat fluxes. Substantial changes in hydrological and ecological processes have been observed in the northern high latitudes with persistent climatic warming over the past century (Trenberth *et al.*, 2007), while further warming is projected to continue (Meehl *et al.*, 2007). Recent hydrological changes observed for boreal forest and tundra regions include changes in seasonality and magnitude of river discharge, thawing and degradation of permafrost and associated rapid gains/losses in lake area, increasing soil active layer depths, and receding glaciers (McClelland *et al.*, 2006; Oelke *et al.*, 2004; White *et al.*, 2007; Zhang *et al.*, 2005). Ecological responses to these changes include earlier onset and lengthening growing seasons, increased vegetation structure and growth, and alteration of land-atmosphere CO_2 exchange (McDonald *et al.*, 2004; Oechel *et al.*, 2000; Sturm *et al.*, 2001; Zhang *et al.*, 2007b). A growing body of evidence indicates that changes in the regional water cycle are impacting ecological processes in this domain. Recent, post-2000 occurrences of

widespread and persistent drought have occurred across the boreal high latitudes (Schindler & Donahue, 2006; Zhang *et al.*, 2008), resulting in a general decrease in vegetation productivity for boreal forest indicated by atmospheric CO_2 anomalies (Angert *et al.*, 2005), satellite NDVI and vegetation productivity records (Goetz *et al.*, 2005; Zhang *et al.*, 2008), and stand inventory data (Hogg *et al.*, 2008; Schindler & Donahue, 2006).

According to the well-known Clausius-Clapeyron relationship between air temperature and water vapor capacity of the atmosphere, warming is expected to promote increases in evapotranspiration and precipitation leading to a general intensification (i.e., acceleration) of the global water cycle (Held & Soden, 2000; Meehl *et al.*, 2007). Huntington (2006) reviewed the literature regarding historical trends in hydrologic variables and suggested an ongoing intensification of the global water cycle. Because the northern high-latitudes have experienced substantial warming during the last decades, the water cycle in these regions may also be intensifying. Serreze *et al.* (2006) and White *et al.* (2007) showed that the major components of the Arctic freshwater cycle including precipitation, runoff and precipitable water have generally experienced increasing trends consistent with an intensifying water cycle. However, the relative magnitudes and spatial heterogeneity of these trends are highly uncertain due to sparse measurement networks and large natural variability in seasonal to annual weather patterns for the region.

Better understanding of recent changes in the northern high latitude terrestrial water cycle requires improved documentation of spatial patterns and changes of its primary components including precipitation, evapotranspiration and river discharge. Precipitation and river discharge measurements are currently available from pan-Arctic

observation networks (McClelland *et al.*, 2006; Yang *et al.*, 2005). Evapotranspiration (ET) is highly heterogeneous both spatially and temporally due to strong vegetation canopy control on transpiration. However, there are very few direct measurements of ET over global land areas. The ET fields from GCM-based reanalyses such as ERA-40 and NNR are not considered reliable because they are not well constrained by precipitation and radiation (Betts *et al.*, 2003; Ruiz-Barradas & Nigam, 2005). ET plays an important role in linking the water, energy and carbon cycles and represents over 60% of precipitation on a global basis (L'vovich & White, 1990). Soil evaporation and plant transpiration are determined by surface meteorology and plant biophysics. Relatively sparse measurements of these variables for the northern high latitudes make accurate assessment of ET a challenge. Remotely sensed data, especially from polar-orbiting satellites, provide relatively frequent and spatially contiguous monitoring of surface biophysical variables affecting ET, including albedo, biome type and vegetation density. Satellite-based ET products have been produced at regional and global scales with varying accuracy (Bastiaanssen *et al.*, 1998a; Bastiaanssen *et al.*, 1998b; Cleugh *et al.*, 2007; Fisher *et al.*, 2008; Mu *et al.*, 2007). However, currently there is no continuous, long-term satellite based ET record for the northern high latitudes. The Normalized Difference Vegetation Index (NDVI) from the NOAA Advanced Very High Resolution Radiometer (AVHRR) record extends from 1981 to present and can be used to estimate regional patterns and trends in ET for the pan-Arctic domain since NDVI is sensitive to vegetation structure and photosynthetic canopy cover.

There are numerous methods to calculate or simulate surface ET, however the Penman-Monteith equation (Monteith, 1965) is arguably the most physically based,

advanced resistance model of evaporation used in hydrological practice today (Shuttleworth, 1992). Based on the Penman-Monteith equation, Priestley and Taylor (1972) defined equilibrium evaporation (E) or ET over large regions by replacing surface and aerodynamic resistance terms with an empirical multiplier to simulate E or ET under optimal conditions (Jones & Kiniry, 1986; Steiner *et al.*, 1991). The Priestley and Taylor method is simpler and requires less parameterization and inputs relative to the Penman-Monteith equation, while the Penman-Monteith equation is more theoretically accurate. Both methods have been applied to estimate ET on a regional or global basis by incorporating satellite remote sensing information (Cleugh et al., 2007; Mu et al., 2007; Fisher et al., 2008).

In this chapter, I developed a satellite-based algorithm by applying the Penman-Monteith equation, modified Penman-Monteith equation, and Priestley-Taylor method with AVHRR GIMMS NDVI (Pinzon *et al.*, 2005; Tucker *et al.*, 2005) based vegetation attributes and daily surface meteorology inputs from regionally corrected meteorology reanalysis to calculate canopy transpiration, soil evaporation and water body evaporation, respectively for the pan-Arctic basin and Alaska based. I then applied these results with available precipitation records, and river discharge measurements to assess recent changes in the pan-Arctic terrestrial water balance. I also compared these results to satellite based vegetation productivity records to determine whether observed changes in the water balance are consistent with recent trends in vegetation productivity for the region. The primary objectives of this chapter are to (1) assess spatial patterns and temporal trends in ET and precipitation over the northern high latitudes from 1983 to 2005; (2) determine whether these results and associated changes in the regional water

balance are consistent with an intensification (acceleration) of the terrestrial water cycle, and (3) assess whether the regional water balance changes are consistent with satellite based records of a greening arctic and recent drought-induced declines in boreal forest productivity.

4.2. Evapotranspiration Algorithm Logic

In the ET algorithm, I first identified water body and vegetated pixels using the remote sensing based land cover classification (Figure 4-1). For vegetated pixels, ET is partitioned into soil evaporation and canopy transpiration by partitioning available energy for evapotranspiration using the fractional vegetation cover (f_C) defined as:

$$f_C = \frac{\mathrm{NDVI} - \mathrm{NDVI}_{\min}}{\mathrm{NDVI}_{\max} - \mathrm{NDVI}_{\min}} \tag{4.1}$$

where $\mathrm{NDVI}_{\min}$ and $\mathrm{NDVI}_{\max}$ are the signals from bare soil and dense green vegetation, which are set as seasonally and geographically invariant constants 0.05 and 0.95, respectively; NDVI is the Normalized Difference Vegetation Index. Mu et al. (2007) used the MODIS enhanced vegetation index (EVI) instead of NDVI to calculate f_C because of saturation of the NDVI signal under high biomass conditions. However, the NDVI is generally below saturation for the northern high latitudes due to characteristically low biomass conditions. The MODIS EVI data are only available since 2000, while the AVHRR GIMMS NDVI is the only available vegetation index product covering the entire 1983-2005 study period.

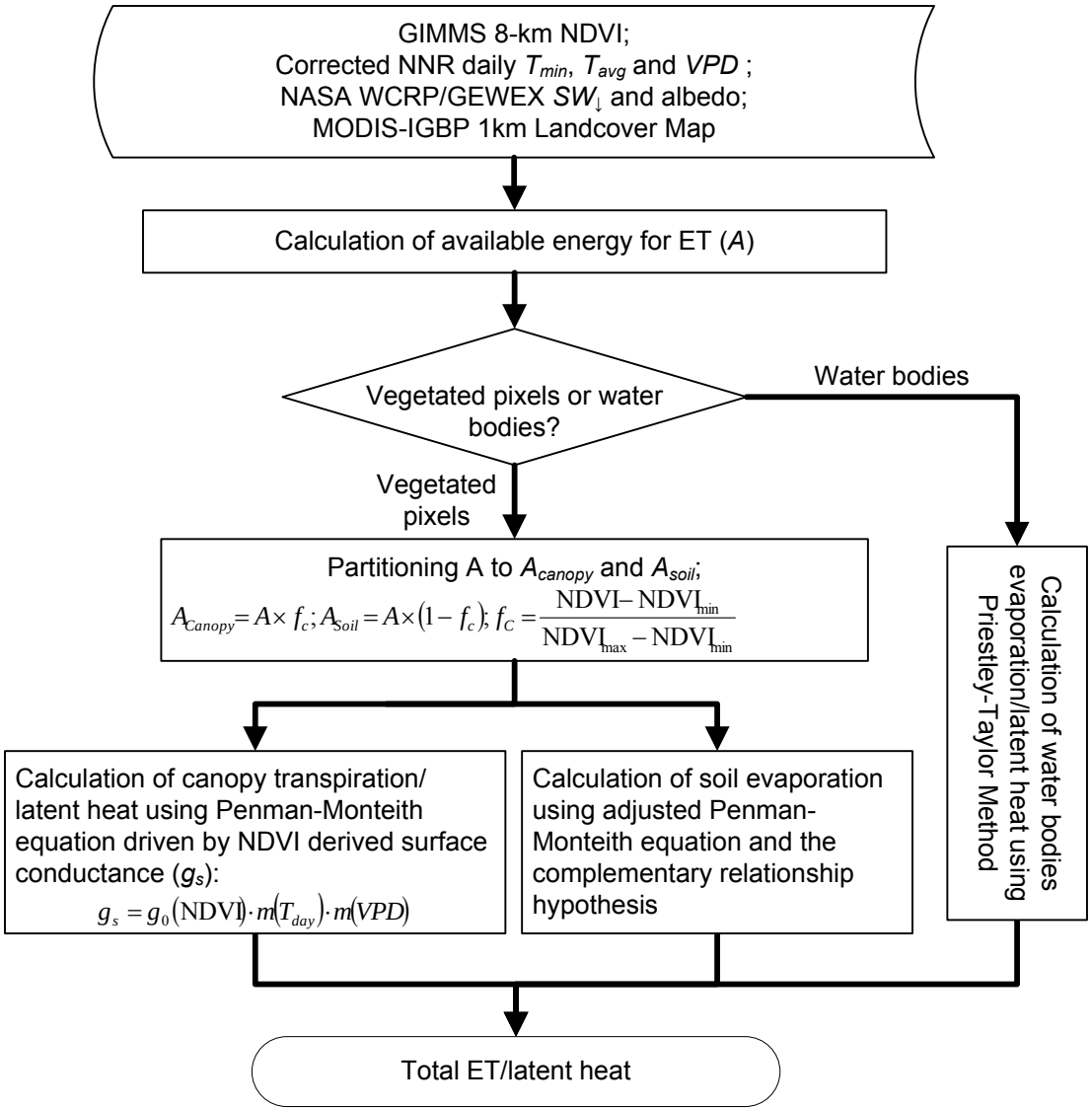

Figure 4-1: Flowchart of the satellite remote sensing based ET algorithm.

The available energy for evapotranspiration (A : W m^{-2}) is determined as the difference between net all-wave solar radiation (R_n : W m^{-2}) and soil heat flux (G : W m^{-2}) derived from daily average temperature (T_{avg} : K; T_{avg} is transferred to the Kelvin scale),

incoming short-wave solar radiation ($SW_{\downarrow}$: W m^{-2}) and albedo (α) using the energy formulas of Cleugh et al. (2007):

$$A = R_n - G \tag{4.2}$$

$$R_n = SW_{\downarrow}(1-\alpha) - (1-\varepsilon_a)\sigma T_{avg}^4 \tag{4.3}$$

$$G = c_G R_n \tag{4.4}$$

where σ is the Stefan-Boltzmann constant (=5.670400×10^{-8} W m^{-2} K^{-4}); c_G is the ratio of the soil heat flux G to the net radiation and set to 0.1 by the suggestion of Cleugh et al. (2007); ε_a is called atmospheric emissivity and calculated from air temperature using the formula of (Idso & Jackson, 1969):

$$\varepsilon_a = 1 - 0.261\exp\left[-7.77\times10^{-4}\times\left(273-T_{avg}\right)^2\right] \tag{4.5}$$

The A term is then linearly partitioned into available energy components for the canopy (A_{Canopy} : W m^{-2}) and soil surface (A_{Soil} : W m^{-2}) using f_C (Mu et al., 2007) such that:

$$A_{Canopy} = A\times f_c \tag{4.6}$$

$$A_{Soil} = A\times(1-f_c) \tag{4.7}$$

4.2.1. Vegetation Transpiration

The Penman-Monteith equation (Monteith, 1965) is used to calculate vegetation transpiration as:

$$\lambda E_{Canopy} = \frac{\Delta A_{Canopy} + \rho_{air} C_P (e_{sat} - e_a)/r_a}{\Delta + \gamma(1 + r_s/r_a)} \tag{4.8}$$

where λE_{Canopy} (W m^{-2}) is the latent heat flux of canopy (i.e., LE_{Canopy}) and λ (J kg^{-1}) is the latent heat of vaporization; $\Delta = d(e_{sat})/dT$ (Pa K^{-1}) and is the slope of the curve relating saturated water vapor pressure (e_{sat} : Pa) to air temperature (T : K); e_a (Pa) is the actual air water vapor pressure, so $e_{sat} - e_a = VPD$, where VPD (Pa) is the vapor pressure deficit; ρ_{air} (kg m^{-3}) is the air density; C_P (J kg^{-1} K^{-1}) is the specific heat capacity of air; r_a (s m^{-1}) is the aerodynamic resistance and its reciprocal, g_a (m s^{-1}), is the aerodynamic conductance. The psychrometric constant is given by $\gamma = (M_a / M_w)(C_P P_{air} / \lambda)$, where M_a (kg mol^{-1}), M_w (kg mol^{-1}) and P_{air} (Pa) are the molecular mass of dry air, the molecular mass of wet air, and the air pressure, respectively. The bulk surface resistance term (r_s : s m^{-1}) is the effective resistance to canopy transpiration.

The relative accuracy of the Penman-Monteith equation depends upon accurate estimation of r_s or its reciprocal – surface conductance (g_s : m s^{-1}). A common approach to simulate surface conductance is the so-called Jarvis-Stewart formula (Jarvis, 1976; Stewart, 1988), which can be expressed as:

$$g_s = g_0 \cdot m(\theta_1) \cdot \ldots \cdot m(\theta_n) \tag{4.9}$$

where g_0 is a biome-dependent (i.e. vegetation cover dependent) maximum value of g_s; $m(\theta_1),...,m(\theta_n)$ are a series of multiplicative factors (i.e. stress factors) representing one or more environmental constraints ($\theta_1,...,\theta_n$) such as sub-optimal conditions for water vapor, temperature, solar radiation and soil moisture. This general approach is effective and has been widely used (e.g. Dolman & van Den Burg, 1988; Granier & Loustau, 1994;

Granier *et al.*, 2000). Cleugh et al. (2007) determined canopy g_s by multiplying the mean surface conductance per unit leaf area index (c_L: m s^{-1}) using satellite derived leaf area index (LAI) inputs. Mu et al. (2007) then introduced the Jarvis-Stewart-type water stress and temperature multipliers into the Cleugh et al.'s surface conductance equation, as:

$$g_s = c_L \cdot m(T_{\min}) \cdot m(VPD) \cdot LAI \tag{4.10}$$

where $T_{\min}$ (°C) is the daily minimum temperature; $m(T_{\min})$ and $m(VPD)$ represent respective low-temperature and moisture constraints on potential plant transpiration (Mu et al., 2007).

Mu et al. (2007) then applied this method to calculate ET globally and assessed the model results over 19 AmeriFlux eddy covariance flux towers with generally favorable agreement with tower based ET. However, their results also showed large biases for some sites that were attributed to biased estimates for some model parameters and uncertainty in satellite derived LAI. Moreover, the application of Mu et al.'s method required LAI inputs. The empirical integration of AVHHR PAL and MODIS LAI series by Zhang et al. (2008) and the subsequent global LAI product derived from the AVHRR GIMMS NDVI (Ganguly *et al.*, 2008a; Ganguly *et al.*, 2008b) provides a long-term LAI record for the pan-Arctic domain. However, considering the uncertainties in these products and the fact that LAI is a derived product of NDVI, we chose NDVI instead of LAI to define vegetation canopy attributes and ET in this study. Therefore, we defined a NDVI-based Jarvis-Stewart-type surface conductance as:

$$g_s = g_0(\mathrm{NDVI}) \cdot m(T_{day}) \cdot m(VPD) \tag{4.11}$$

where $g_0(\text{NDVI})$ is the biome-dependent potential (i.e. maximum) value of g_s, which is a function of NDVI; T_{day} (°C) is the daylight average air temperature; $m(T_{day})$ is a temperature stress factor and function of T_{day}; $m(VPD)$ is a water/moisture stress factor and function of VPD. Based on general ecological principles and previous approaches from (June *et al.*, 2004) and Mu et al. (2007), we established a new expression for $m(T_{day})$:

$$m(T_{day}) = \begin{cases} 0.01 & T_{day} \le T_{close\_\min} \\ \exp\left(-\left(\dfrac{T_{day} - T_{opt}}{\beta}\right)\right) & T_{close\_\min} < T_{day} < T_{close\_\max} \\ 0.01 & T_{day} \ge T_{close\_\max} \end{cases} \quad (4.12)$$

where T_{opt} (^{o}C) is a biome-specific optimum air temperature for photosynthesis; $T_{close\_\min}$ (^{o}C) and $T_{close\_\max}$ (^{o}C) are the biome-specific minimum and maximum critical temperatures for stomatal closure and the effective cessation of plant photosynthesis; β (^{o}C) is a biome-specific empirical parameter. In this study, $m(VPD)$ is calculated using the same formula in Mu et al. (2007):

$$m(VPD) = \begin{cases} 1.0 & VPD \le VPD_{open} \\ \dfrac{VPD_{close} - VPD}{VPD_{close} - VPD_{open}} & VPD_{open} < VPD < VPD_{close} \\ 0.1 & VPD \ge VPD_{close} \end{cases} \quad (4.13)$$

where VPD_{open} (Pa) is the biome-specific critical value of VPD at which the canopy stomata are completely open; VPD_{close} (Pa) is the biome-specific critical value of VPD at which canopy stomata are completely closed.

4.2.2 Evaporation for Water Bodies and Soil

The evaporation over water bodies was calculated using the Priestley-Taylor equation (Priestley & Taylor, 1972):

$$\lambda E_{Water} = a\frac{\Delta A}{\Delta + \gamma} \tag{4.14}$$

where the constant a accounts for the evaporation arising from the humidity deficit in addition to the equilibrium term and is set to 1.26 following Priestley and Taylor (1972).

Soil evaporation is calculated using the soil evaporation equation used in Mu et al. (2007), which is a combination of an adjusted Penman-Monteith equation and the complementary relationship hypothesis (Bouchet, 1963; Fisher *et al.*, 2008). The details of these equations can be found in Mu et al. (2007) and are expressed in the context of this study as:

$$\lambda E_{Soil} = RH^{(VPD/k)}\frac{\Delta A_{Soil} + \rho C_P VPD / r_a}{\Delta + \gamma \cdot r_{totc} / r_a} \tag{4.15}$$

$$r_a = r_c r_r / \left(r_c + r_r\right) \tag{4.16}$$

$$r_r = \rho C_P / \left(4.0 \times \sigma \times T_{day}^3\right) \tag{4.17}$$

$$r_{totc} = r_{tot} \times R_{corr} \tag{4.18}$$

$$R_{corr} = \frac{1.0}{\left(\frac{273.15 + T_{day}}{293.15}\right) \times \frac{101300}{P_{air}}} \tag{4.19}$$

where RH is the relative humidity of air with values between 0 and 1; k (Pa) is a parameter to fit the complementary relationship (Fisher et al., 2008) and is set to 100 Pa by Mu et al. (2007); for this study k is adjusted for different vegetation types; r_r (s m^{-1})

is the resistance to radiative heat transfer and is calculated using Equation (4.17) (Choudhury & DiGirolamo, 1998); σ (= 5.670400×10^{-8} W m^{-2} K^{-4}) is the Stefan–Boltzmann constant. In Equation (4.17), the unit of T_{day} is in degrees Kelvin. The r_c (s m^{-1}) term is the resistance to convective heat transfer and is assumed to be equal to the boundary layer resistance (Thornton, 1998). General boundary layer resistance values were obtained for each land cover class from reported values for similar global biome types (White *et al.*, 2000). The r_{tot} (s m^{-1}) term is the total aerodynamic resistance to vapor transport and the sum of surface resistance and the aerodynamic resistance components. The r_{totc} (s m^{-1}) term is the corrected value of r_{tot} from the standard conditions for temperature and pressure (STP) using the correction coefficient (R_{corr}) (Jones, 1992). The value of r_{tot} is set to a constant 107 s m^{-1} for all vegetation types in Mu et al. (2007), while r_{tot} is adjusted by land cover class for this investigation. All of the above biome-specific parameters for the ET algorithm are given in Appendix A.

4.2.3. Fitting of Relationship between Potential Surface Conductance and NDVI

To establish the biome-specific relationship between g_0 and NDVI, I first removed the calculated latent heat flux from soil evaporation (LE_{Soil} , namely λE_{Soil}) driven by *in situ* tower meteorology coinciding with tower observed LE (see Section 4.3) to produce the latent heat flux from canopy transpiration (LE_{Canopy} or λE_{Canopy}). I then derived the surface conductance term (g_s) from LE_{Canopy} and measured meteorology from the six flux towers (section 4.3.2) using the rearranged Penman-Monteith equation:

$$g_s = \frac{g_a \gamma LE_{Canopy}}{\Delta A_{Canopy} + \rho_{air} C_P VPD g_a - LE_{Canopy}(\Delta + \gamma)} \tag{4.20}$$

Due to lack of available vertical wind profile measurements, I set values of g_a as biome-specific constants based on evidence that the range of g_a variability is generally conservative over low wind speeds (e.g. ≤ 5 m s^{-1}) and aerodynamically rough surfaces following (Monteith & Unsworth, 2008). The use of a constant g_a has been successfully applied for similar satellite based ET mapping studies (e.g. Mu et al., 2007). Substituting g_s in Equations (4.20) and (4.11) I define the derived potential surface conductance as:

$$g_0^* = \frac{g_a \gamma LE_{Canopy}}{\left[\Delta A_{Canopy} + \rho_{air} C_P VPD g_a - LE_{Canopy}(\Delta + \gamma)\right] \cdot m(T_{day}) \cdot m(VPD)} \tag{4.21}$$

I (1) calculated daily g_0^* for the four general biome types using daily surface meteorology and LE measurements from the six flux towers; (2) removed outliers falling below the 10th percentile and above the 90th percentile for g_0^*; (3) calculated the average daily values of g_0^* and NDVI (i.e., $\overline{g}_0^*$ and $\overline{\text{NDVI}}$) for each NDVI interval (the size of interval is 0.04) with sufficient samples (≥ 10), and (4) fitted the scatter plots of $\overline{g}_0^*$ vs. $\overline{\text{NDVI}}$ using sigmoid response functions for each biome type:

$$g_0(\text{NDVI}) = 1/[b_1 + b_2 \cdot \exp(-b_3 \cdot \text{NDVI})] + b_4 \tag{4.22}$$

where b_1 (mm s^{-1}), b_2 (mm s^{-1}), b_3 (dimensionless) and b_4 (mm s^{-1}) are empirical parameters, and $g_0(\text{NDVI} = 0) = 0$.

4.3. Data

4.3.1. Meteorological and Satellite Inputs to the ET Algorithm

I used the regional bias-corrected version of the NNR daily surface meteorology (Section 2.5) as the primary meteorological inputs to the ET model. The original and bias-corrected NNR products are provided in a global Gaussian grid (T62, 192×94 points) format with approximately $1.9°\text{latitude} \times 1.875°\text{longitude}$ resolution. The daily meteorological inputs from the bias-corrected NNR include daily minimum and average air temperatures ($T_{\min}$ and T_{avg}: ^{o}C) and daylight average vapor pressure deficit (VPD: Pa). The $T_{\min}$ and T_{avg} variables are also used to calculate the daylight average air temperature (T_{day}: ^{o}C). Daily incident shortwave solar radiation ($SW_{\downarrow}$: W m^{-2}) and albedo (α) inputs are derived from the NASA World Climate Research Programme/Global Energy and Water-Cycle Experiment (WCRP/GEWEX) Surface Radiation Budget (SRB) Project (http://eosweb.larc.nasa.gov/PRODOCS/srb/table_srb.html) data set with $1.0° \times 1.0°$ resolution. All of the above meteorological and climatic variables are interpolated to the study sites or pixels using the spatial interpolation method of Zhao *et al.* (2005).

In this study, I derived a daily NDVI series for each grid cell in the domain using temporal linear interpolation of adjacent semi-monthly values of the 8-km semi-monthly AVHRR GIMMS NDVI product. The daily linear interpolation approach is a relatively simple, but effective means for producing daily time series of satellite-observed vegetation state variables including fraction of photosynthetically active radiation (FPAR) and LAI and has been successfully applied for vegetation based analyses of the AVHRR series (e.g. Kimball *et al.*, 2006; Kimball *et al.*, 2007; Zhang *et al.*, 2007b).

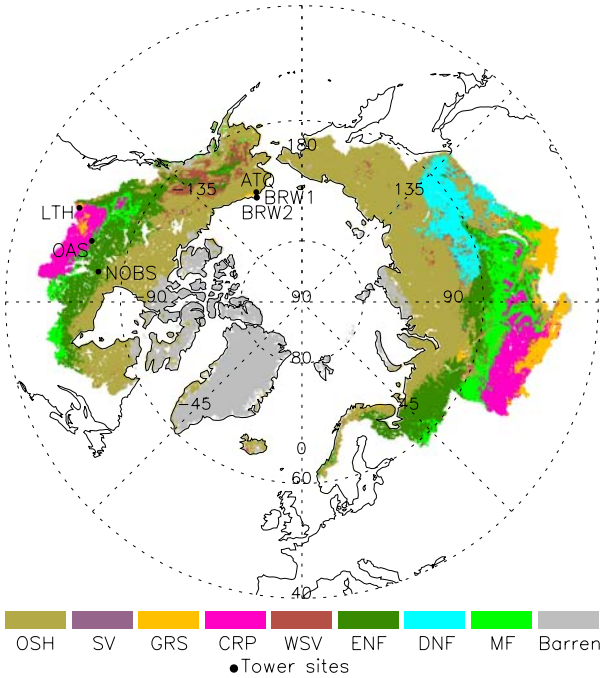

Figure 4-2: Locations of six flux towers and regional land cover derived from the NASA MODIS-IGBP global land cover classification (see Figure 1-1) within the pan-Arctic region.

4.3.2. Eddy Covariance Flux Towers

The model ET parameters and outputs for this study were calibrated and verified using daily meteorology and latent energy flux measurements from six eddy covariance flux tower sites representing dominant vegetation classes within the study domain (Figure 4-2). The six sites represent four distinct vegetation types (Table 4-1; Figure 4-2) including wet sedge and tussock tundra, boreal evergreen needleaf forest, boreal deciduous broadleaf forest, and northern temperate grassland. Coastal wet sedge tundra is represented by the Barrow sites (BRW1 and BRW2) and is characterized by low topography and a shallow water table with numerous thaw lakes, while the Atqasuk (ATQ) site represents tussock tundra. The wet sedge tundra is predominantly composed

Table 4-1. Site abbreviations, latitude (lat), longitude (lon), MODIS IGBP land cover (MODIS LC) (Friedl et al., 2002) and dominant vegetation community within each 1 km^2 tower footprint (Tower LC) for the six eddy covariance flux tower sites; OSH: open shrubland; GRS: grassland; ENF: evergreen needle forest; MF: mixed forest.

Site	Abbrev.	Lat (◦)	Lon(◦)	MODIS LC	Tower LC
Barrow 1, AK[a]	BRW_1	71.32	-156.62	OSH	Wet-sedge tundra
Barrow 2, AK[b]	BRW_2	71.32	-156.62	OSH	Wet-sedge tundra
Atqasuk, AK	ATQ	70.47	-157.41	OSH	Tussock tundra
NSA-OBS, Manitoba, CN	NOBS	55.88	-98.48	ENF	Boreal spruce forest
SSA-OAS, Sask, CN	OAS	53.63	-106.20	MF	Boreal aspen forest
Lethbridge, Alberta, CN	LTH	49.71	-112.94	GRS	Grassland

[a,b] BRW1 and BRW2 are about 2 km apart and represent contrasting moisture conditions (Engstrom *et al.*, 2006).

of low-growing sedges and mosses, interspersed with areas of shallow standing water. Soils are highly organic and consist of a shallow active layer that thaws each growing season and is underlain by continuous permafrost (Oechel *et al.*, 2000). The two flux towers at Barrow are approximately 2 km apart and represent relatively productive (BRW1) and less productive (BRW2) tundra, respectively. The BRW1 tower is located along the edge of a drained coastal lagoon with a greater proportion of standing water relative to the adjacent BRW2 tower footprint (Harazono *et al.*, 2003; Oechel *et al.*, 1998). The Northern Old Black Spruce (NOBS) tower site is dominated by mature black spruce (*Picea mariana*) forest with a canopy height of 10-13 m, low topographic relief, and understory composed of mosses (*Pleurozium* and *Sphagnum* spp.) overlying discontinuous permafrost (Dunn, 2006; Dunn & Wofsy, 2006). The Old Aspen (OAS) tower site is dominated by mature aspen (*Populus tremuloides*) forest with a mean

canopy height of 21 m, an understory composed of hazelnut (*Corylus cornuta* Marsh.) and low topographic relief (Griffis *et al.*, 2004). The Lethbridge (LTH) site is located in the northern Great Plains region with an average canopy height of 18.5 cm and orthic dark-brown chernozem soils (Carlson, 2000; Wever *et al.*, 2002). The LTH plant community is dominated by grasses *Agropyron dasystachyum* [(Hook.) Scrib.] and *A. smithii* (Rydb.) (Carlson, 2000; Wever *et al.*, 2002).

4.3.3. Precipitation and River Discharge

I selected two alternate precipitation data sources to assess changes in the pan-Arctic regional water balance over the 1983-2005 study period: the Global Precipitation Climatology Project (GPCP) Version 2 monthly precipitation (Alder *et al.*, 2003), and the Global Precipitation Climatology Centre (GPCC) monthly precipitation (Rudolf & Rubel, 2005; Rudolf & Schneider, 2005) products. The GPCP monthly precipitation data are provided at $2.5° \times 2.5°$ spatial resolution and produced by incorporating precipitation estimates from low-orbit satellite microwave data, geosynchronous-orbit satellite infrared data, and surface rain gauge observations. The GPCC monthly precipitation data are provided at $0.5° \times 0.5°$ spatial resolution and produced from surface gauge network observations.

Monthly gauge-observed river discharges were obtained from ArcticRIMS (http://rims.unh.edu/index.shtml), Water Survey of Canada HYDAT (version 2005-2.04) (http://www.wsc.ec.gc.ca/), and GRDC (The Global Runoff Data Centre, 56068 Koblenz, Germany) sources. I selected 22 sub-basins with relatively complete river discharge records at the outlet gauges to analyze recent water balance changes within the study

domain. These river discharge records were converted to runoff depth (Q: mm) to be comparable with precipitation and ET. The 22 sub-basins range in size from 0.03 to 2.9 million km^2 and include the Yukon (data missing from 1997 to 2000), Mackenzie, Back (data missing in 1997 and 1998), Thelon (data missing in 1997), Thlewiaza, Seal, Churchill, Nelson(data missing from 1983 to 1986), Hayes (data missing in 1998), Winisk (data missing from 1995 to 1998), Attawapiskat (data missing from 1995 to 1998), Albany (data missing from 1995 to 1998), Moose (data missing from 1998 to 2001), Onega(data missing in 1997), Northern Dvina, Mezen, Ob, Yenisei, Anabar (data missing from 2000 to 2005), Lena, Yana and Kolyma (data missing in 2001, 2004 and 2005) basins.

4.4. Results

4.4.1. Fitted Relationship between g_0 and NDVI

Figure 4-3 shows the scatter plot of g_0^* vs. NDVI for the four dominant boreal-Arctic biome types, as represented by LE and surface meteorological measurements from the six flux tower sites and satellite-observed NDVI of pixels overlapping the respective tower footprints. For all four biome types, g_0^* generally increases with increasing NDVI and gradually levels off at higher values of NDVI. The reduced slope of this relationship for higher NDVI levels reflects increasing shading of individual leaves and corresponding boundary layer adjustment with increasing canopy density. These effects provide a negative feedback for transpiration so that stomatal conductance has less effect on canopy water loss at higher NDVI and canopy density levels than would be

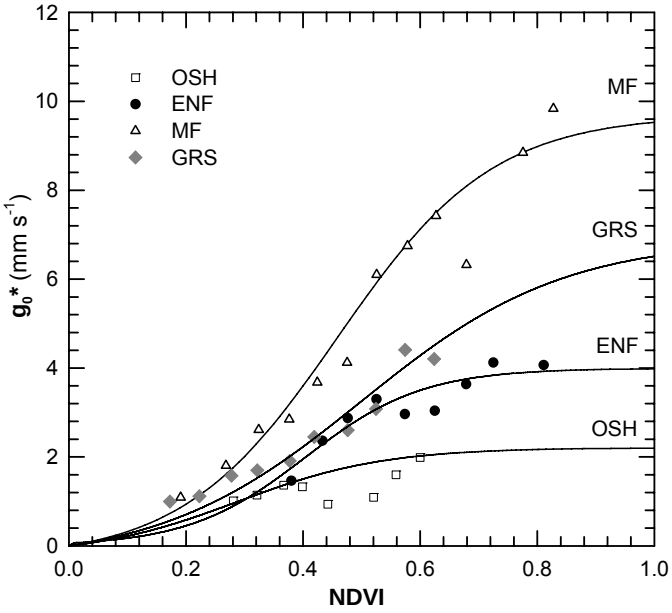

Figure 4-3: Scatter plot of the calculated potential surface conductance of vegetation (g_0^*) derived from tower measurements vs. AVHRR GIMMS derived NDVI and the empirical fitted relationship between g_0 and NDVI for OSH, ENF, GRS and MF vegetation types.

expected from an analysis of individual leaves (Jarvis & McNaughton, 1986). These derived surface conductance (i.e., canopy conductance) values are generally consistent with reported ranges from the literature for the major regional biome types. Jones (1992) reported a seasonal range of 1.7-10 mm s^{-1} in canopy conductance for grassland near Matador, Canada. Blanken and Black (2004) showed a seasonal range of 0.1-11 mm s^{-1} in canopy conductance for boreal Aspen forest in Prince Albert National Park, Canada; this area is classified as mixed forest by the MODIS Type 1 land cover classification. Measured canopy conductance values for black spruce forest around the NOBS site by Rayment *et al.* (2000) varied between 24 and 105 mmol m^{-2} s^{-1} (about 0.5-2.4 mm s^{-1}).

I applied a sigmoid function to describe the observed relationship between g_0 and NDVI in Figure 4-3. The fitted curves for the four biome types are also shown in Figure 4-3 and show favorable agreement with the observations. The fitted curves explain 94%,

92% and 86% of the variation in g_0 for the mixed forest (MF), grassland (GRS) and evergreen needleleaf forest (ENF) sites, respectively. The fitted curve for open shrubland (OSH) shows favorable agreement with some, but not all tower derived g_0 values; three outliers occur under moderate NDVI values, resulting in a fitted curve that only explains 20% of the variation in g_0. The relatively small sample size for OSH (Table 4-2) also contributes to the relatively large uncertainty in the observed relationship between g_0 and NDVI for OSH.

4.4.2. Comparison between ET Algorithm Results and Tower Observations

The daily time series of modeled LE fluxes derived from tower daily meteorological measurements and bias-corrected NNR meteorology are plotted in Figure 4-4 with corresponding tower LE measurements. Both sets of model results show generally favorable agreement with the tower observations and capture observed LE seasonality and associated differences among the major biomes represented (Table 4-2), although the model LE fluxes tend to underestimate tower observations in the spring for several sites, especially LTH. This LE underestimation is likely due to spring snowmelt and associated wet soil and vegetation conditions, resulting in greatly reduced surface resistance and enhanced evaporation. Moreover, the use of biome-specific constant aerodynamic conductance terms may contribute to these uncertainties. The ET algorithm from this study also produces comparable but slightly better results relative to the Mu et al. (2007) global ET algorithm for the three tundra sites and markedly improved results for the forest and grassland sites, especially for the LTH site. Overall, the NDVI-based

Table 4-2. Comparison of modeled and measured daily latent heat flux (W m^{-2}) for the six flux tower sites. The statistics include mean residual (Estimate – Observation) (MR), root mean squared error (RMSE) and correlation coefficient (r) between modeled and measured values. The modeled results include estimates derived from the NDVI-based ET algorithm using (1) bias-corrected NNR meteorology, (2) tower-measured meteorology, and (3) estimates derived from Mu et al.'s (2007) method using tower-measured meteorology. All correlation coefficients are significant at the 0.01 significance level.

Site	Sample Size	Modeling 1			Modeling 2			Modeling 3		
		$\overline{\varepsilon}$ (W m^{-2})	RMSE (W m^{-2})	r	$\overline{\varepsilon}$ (W m^{-2})	RMSE (W m^{-2})	r	$\overline{\varepsilon}$ (W m^{-2})	RMSE (W m^{-2})	r
ATQ	183	-2.75	13.42	0.51	0.46	10.57	0.69	7.56	13.95	0.66
BRW1	143	-7.48	11.93	0.73	-5.55	10.27	0.75	-2.97	10.93	0.70
BRW2	214	2.53	15.53	0.53	4.06	13.21	0.72	4.11	15.35	0.75
LTH	1008	11.47	31.52	0.87	7.27	25.00	0.91	27.83	50.91	0.77
NOBS	1513	0.48	17.95	0.83	-0.22	18.91	0.82	-10.92	28.96	0.79
OAS	1018	-2.53	23.67	0.88	-0.69	20.52	0.91	-4.32	24.41	0.88
[a]Overall	4079	2.13	23.03	0.84	1.58	20.25	0.88	2.20	33.55	0.67

[a] Sample includes all daily time series of the six flux tower sites.

ET algorithm reduced bias relative to the daily tower observations from 2.20 W m^{-2} using the Mu *et al.* (2007) method to 1.58 W m^{-2}; improved LE accuracy (i.e. RMSE) from 33.55 W m^{-2} to 20.25 W m^{-2}, and enhanced correlation with the measurements from 0.67 to 0.88 for the represented tower sites (Table 4-2). The biome-specific $g_0 \sim$ NDVI functions derived from the tower observations play a vital role in improving model performance. In addition, the use of biome-specific parameters (e.g. g_a, k, r_{tot}, etc.) instead of fixed values for all biomes and the adjusted temperature stress factor (i.e., $m(T)$) also contribute to improved model accuracy for the boreal-arctic vegetation types.

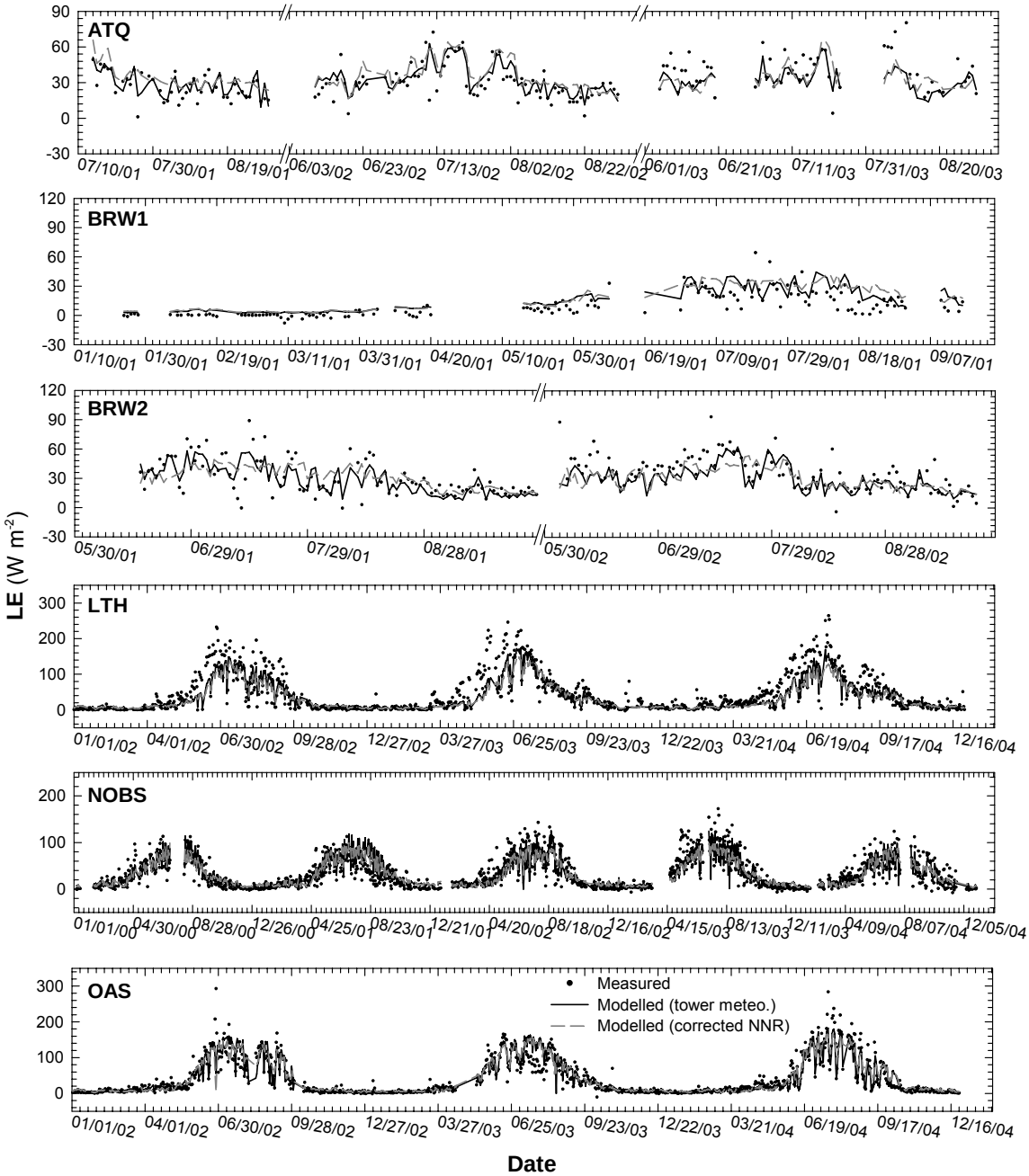

Figure 4-4: Time series of daily measured and modeled latent heat flux (LE: W m^{-2}). The two sets of modeled LE results derived from the NDVI-based ET algorithm are driven by tower-measured meteorology and bias-corrected NNR meteorology, respectively. The daily measured and modeled LE values are compared for days with complete records for both LE and surface meteorology.

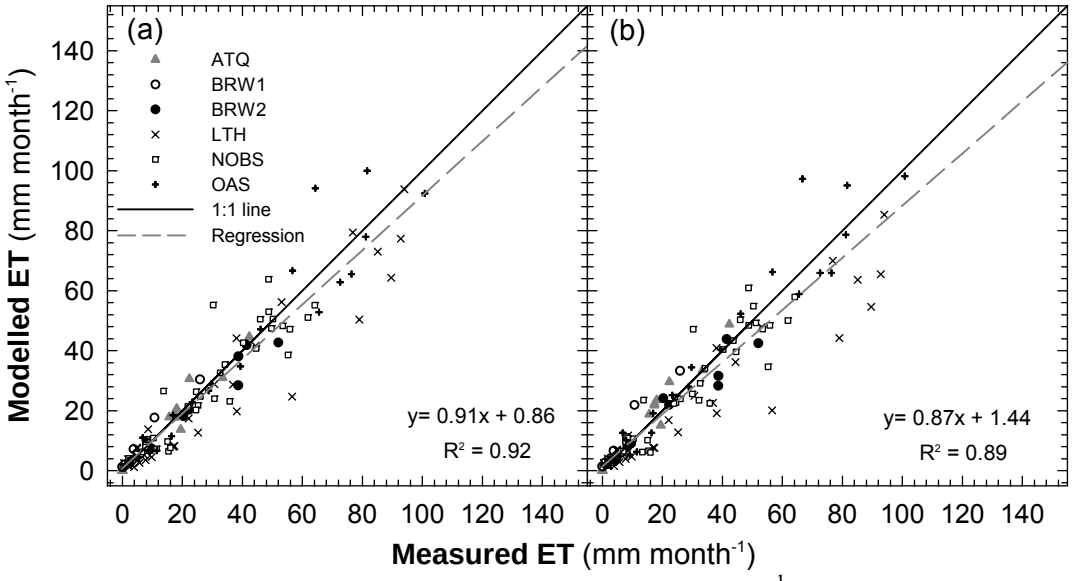

Figure 4-5: Scatterplots of monthly modeled ET (mm month^{-1}) derived from (a) tower-measured meteorology and (b) bias-corrected NNR meteorology against corresponding tower measurements for the six flux tower sites.

The NDVI-based ET algorithm results derived using bias-corrected NNR reanalysis surface meteorology show reduced accuracy relative to model runs driven by in situ meteorology measurements due to differences between regional weather conditions represented by the relatively coarse (at the $1.9° \times 1.875°$ resolution) NNR and local micrometeorology within the tower footprints. Nevertheless, model results derived from the bias-corrected NNR inputs are in general agreement with the tower derived results, with mean residual and accuracy (RMSE) values of 2.13 W m^{-2} and 23.03 W m^{-2}, respectively. The NNR based model results also show relatively strong correspondence ($r = 0.84$; $P < 0.001$) to observations and capture observed LE seasonality.

On a monthly basis, the model ET results derived from both local tower meteorology and bias-corrected NNR meteorology show good agreement with ET observations at the 6 tower sites (Figure 4-5). Model results derived from tower-

measured meteorology accounted for 92% of the variation in measured ET with a RMSE of 7.4 mm month^{-1} and mean residual difference of 1.20 mm month^{-1}, while similar results derived from bias-corrected NNR meteorology accounted for 89% of the variation in measured ET with a RMSE of 8.3 mm month^{-1} and mean residual difference of 1.50 mm month^{-1}. Although the model results slightly underestimate tower measured ET, the high coefficients of determination (i.e., R^2), low RMSE and small mean residuals for the two sets of monthly model ET results indicate that the model ET results generally capture observed seasonal patterns and site-to-site differences in ET.

4.4.3. Implementing the ET Algorithm for the Pan-Arctic

I applied the NDVI-based ET algorithm driven by bias-corrected NNR meteorology, NASA WCRP/GEWEX SRB solar radiation and albedo, and AVHRR GIMMS NDVI to estimate daily ET over the pan-Arctic basin and Alaska from 1983 through 2005. The ET results were then aggregated to monthly and annual fluxes and used with GPCP and GPCC derived precipitation (P) to evaluate recent changes in the regional water balance (P-ET). Figure 4-6 shows the spatial patterns of multi-year (1983-2005) mean annual ET derived from the model simulations, as well as regional precipitation patterns from both GPCP and GPCC sources. The model based annual ET patterns are spatially complex but show generally reduced ET with increasing latitude. The spatial pattern of ET also corresponds to distributions of the major biome types. Boreal forest regions have the highest annual ET (277.35 ± 68.89 mm yr^{-1}) among the three major biome types followed by grassland (248.40 ± 76.94 mm yr^{-1}) and arctic tundra (158.98 ± 37.61 mm yr^{-1}) biomes. Although open water bodies resolved by the 1-

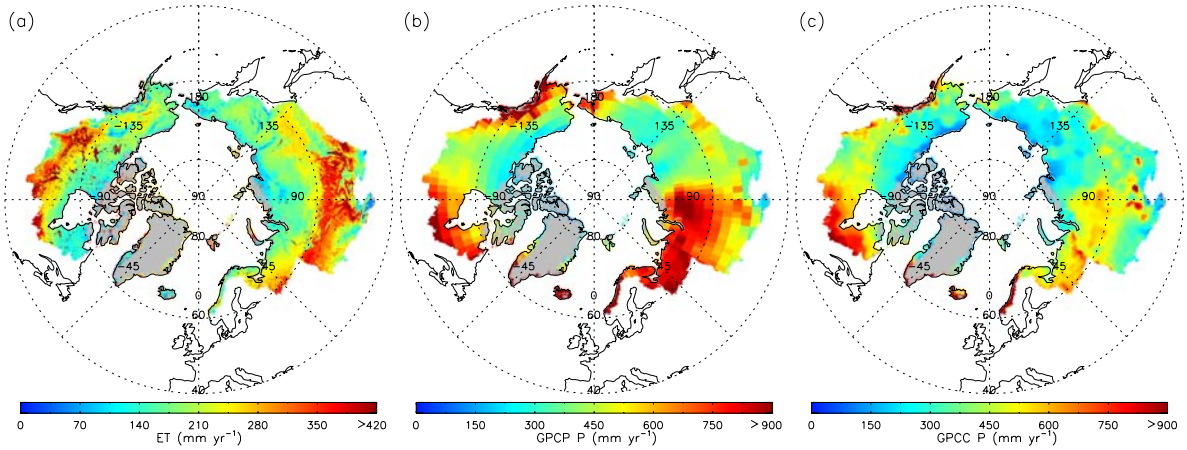

Figure 4-6: Maps of multi-year (1983-2005) mean annual calculated ET (a) and precipitation derived from (b) GPCP and (c) GPCC sources.

km resolution global land cover classification cover (Friedl *et al.*, 2002) only 6.4% (1.6×10^6 km^2) of the pan-Arctic domain, they are distributed across a wide geographic range, with relatively large magnitude and spatial variation in annual ET (410.35 ± 142.58 mm yr^{-1}) relative to vegetated land areas.

Both the GPCP and GPCC sources (Figure 4-6) show similar multi-year mean annual precipitation patterns, though the GPCP precipitation rates are much larger, averaging 1.31 (±0.38) times the GPCC precipitation rates. Both precipitation data sets show portions of Southern Alaska, Northeastern Canada near Hudson Bay and Western Eurasia having the largest precipitation, with relatively arid polar tundra areas showing the least precipitation. Since the GPCC data is produced from surface weather station network observations (Rudolf & Rubel, 2005; Rudolf & Schneider, 2005), it has lower bias and higher accuracy than the GPCP data relative to these observations (Table 4-3). However, due to the extremely sparse pan-Arctic station network density, space-time discontinuities of precipitation data and wind-related biases of gauge observations (Yang

et al., 2005), the gauge data likely underestimate actual precipitation for the region. Comparisons between GPCC precipitation and bias-corrected station observations indicate GPCC underestimation of precipitation by approximately 7.15 mm month^{-1}. The GPCP monthly precipitation data are produced from both gauge data and precipitation estimates from low-orbit satellite microwave data and geosynchronous-orbit satellite infrared data. These data show lower bias than GPCC precipitation (Table 4-3), but have coarser spatial resolution and larger error spread. Despite large discrepancies in spatial resolution and precipitation magnitudes, both datasets show similar spatial patterns (Figure 4-6) and are highly correlated (r = 0.91; $P < 0.001$) in terms of year-to-year variability (Figure 4-7).

Table 4-3. Comparison of accuracy in GPCP and GPCC monthly precipitation against gauge observations from pan-Arctic WMO weather stations and bias-corrected station observations from Yang et al. (2005).

Sources	$\bar{\varepsilon}$ (mm month^{-1})	MAE (mm month^{-1})	RMSE (mm month^{-1})	r
GPCP P vs. observation	-7.18	20.27	32.54	0.63
GPCP P vs. bias-corrected observation	-1.10	19.88	34.95	0.63
GPCC P vs. observation	1.07	11.05	25.15	0.79
GPCC P vs. bias-corrected observation	7.15	14.10	30.00	0.76

4.4.4. Changes in the Pan-Arctic Regional Water Balance

As a whole, the pan-Arctic region shows a small increasing trend in annual P for the 1983 to 2005 period, indicated by both GPCP (7.4 mm decade^{-1}; $P = 0.17$) and GPCC

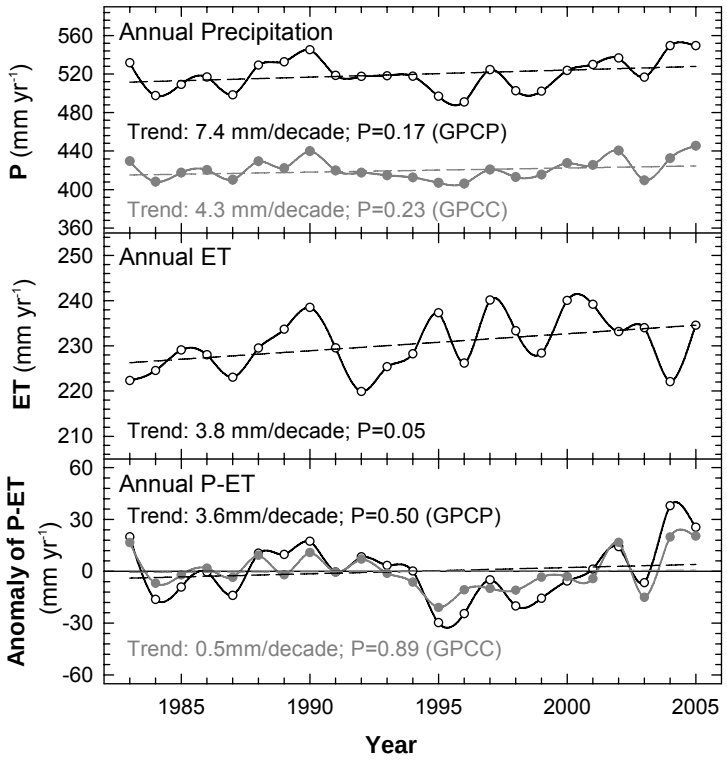

Figure 4-7: Annual time series of precipitation (P) derived from GPCP and GPCC data sources; ET derived from the NDVI-based ET algorithm, and corresponding annual P-ET anomalies from the long-term (23-year) mean. Dashed lines show linear trends for the time series. The two P series from GPCP and GPCC sources are highly correlated (r = 0.91; $P < 0.001$). The resulting P-ET anomalies are also highly correlated (r = 0.89; $P < 0.001$).

(4.3 mm decade^{-1}; $P = 0.23$) sources (Figure 4-7), while ET shows a significant increasing trend of 3.8 mm decade^{-1} ($P = 0.05$) for this period coinciding with regional warming (Trenberth et al., 2007) and vegetation greening trends (e.g. Goetz *et al.*, 2005; Zhang *et al.*, 2008). On average, ET represents 44.4 (±1.6) and 54.7 (±1.8) percent of P for the pan-Arctic domain relative to the GPCP and GPCC sources, respectively. Both P and ET show increasing trends so the net effect on P-ET is reduced and annual P-ET shows an insignificant wetting trend indicated by both GPCP and GPCC derived results (Figure 4-7). Both GPCP and GPCC derived results show P-ET interannual variability of approximately ±6% relative to the long-term mean. Time series plots of annual P-ET

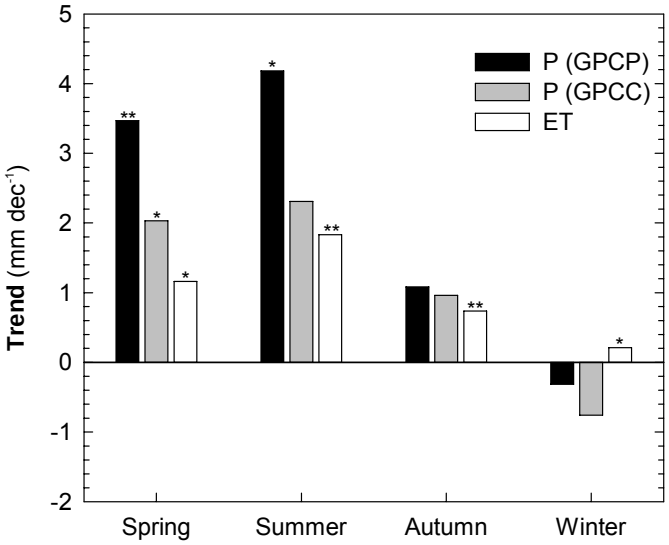

Figure 4-8: Seasonal trends of regional average precipitation derived from GPCP and GPCC sources and regional average ET from 1983 to 2005 for the pan-Arctic region. Asterisk denotes significant trends at the 0.1 significance level, while double asterisk denotes significant trends at the 0.05 significance level.

anomalies for the domain show that the years 1984-1985, 1995-1996, 1998-2001 and 2003 are dry relative to the long-term mean.

Both regional average P and ET show seasonal changes during the 23-year period (Figure 4-8). The GPCP and GPCC data show increasing regional P trends in spring, summer and autumn, with slightly decreasing P trends in winter. The ET results show significant ($P < 0.1$) positive trends for all four seasons, with the largest ET increases in spring and summer, similar to P. These results suggest that regional warming and associated lengthening of the seasonal non-frozen period are promoting increases in annual ET, while increasing P trends during this period (Figure 4-8) are counteracting these evaporative water losses and associated changes to the annual water balance. On a seasonal basis, larger positive trends in P relative to ET in spring, summer and autumn

(Figure 4-8) imply that the pan-Arctic domain is becoming wetter during the growing season. In contrast, decreasing P and slightly positive ET trends indicate that the pan-Arctic domain is becoming drier during the winter period.

There is considerable spatial variability in P, ET and P-ET trends for the domain (Figure 4-9). The two precipitation data sets show similar trends over 70% of the pan-Arctic domain, though large spatial discrepancies in P trends between GPCP and GPCC data occur over northern Arctic coastal tundra areas. The GPCP and GPCC sources show respective positive P trends for 59% and 51% of the domain, while moderate to strong negative precipitation trends occur over 17% and 21% of the region. Areas with negative precipitation trends primarily occur in southern Alaska, western and southeastern Canada (including western Yukon, northeastern British Columbia, Alberta and central Ontario), northeastern Russia, southern and northeastern Siberia, and northern Mongolia. Approximately 72% and 62% of areas with negative P trends occur in boreal forests and grasslands indicated by the GPCP and GPCC sources, respectively (Table 4-4).

The ET results show generally positive trends for 68% of the pan-Arctic domain (Figure 4-9). Approximately 62% of areas with moderate to strong negative ET trends occur over boreal forest, especially boreal regions of North America, while other biomes of North America and Eurasia show generally positive ET trends. Both GPCP and GPCC data sources also show predominantly negative P trends over North American boreal forests. These results are consistent with recent reports of widespread drought (e.g. Levinson & Waple, 2004; Schindler & Donahue, 2006; Waple *et al.*, 2002), vegetation browning (Goetz et al., 2005) and corresponding declines in vegetation productivity (Hogg *et al.*, 2008; Zhang *et al.*, 2008) for these regions.

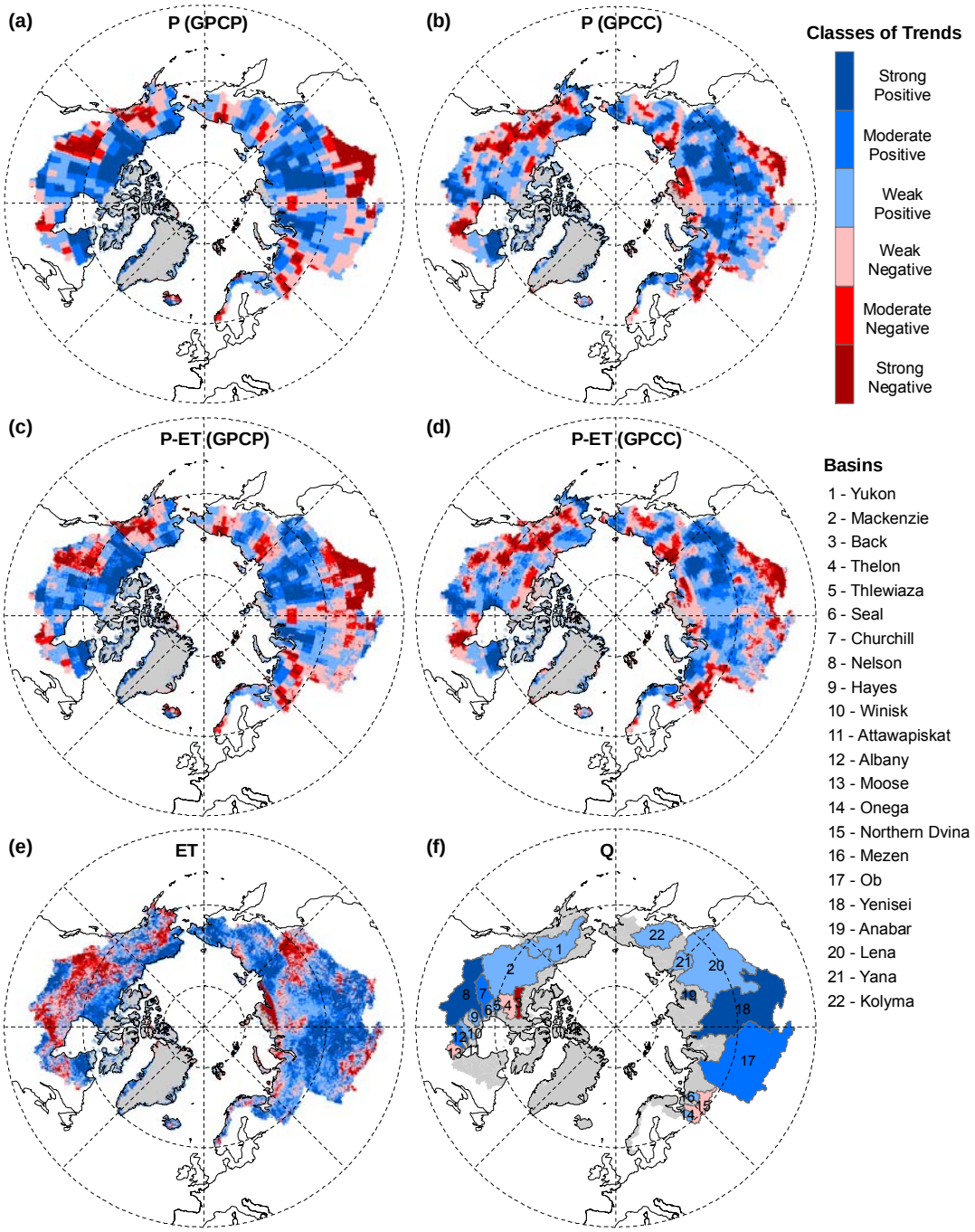

Figure 4-9: Spatial distributions of trends in annual P ((a) and (b)), P-ET ((c) and (d)) and ET (e), and annual runoff depths of 22 major sub-basins (f) within the pan-Arctic basin and Alaska from 1983 through 2005. There are two sets of P and P-ET that are derived from GPCP and GPCC precipitation sources, respectively. The trends are classified into six categories according statistical linear trend analysis.

Table 4-4. Trends of annual precipitation, ET and P-ET from 1983 to 2005 for the three primary regional biome types and North American and Eurasian portions of the pan-Arctic domain. Grey color denotes negative trends.

Continent	Biome Type	Area	P Trend (mm de^{-1})		ET Trend	P-ET Trend (mm de^{-1})	
		(10^6 km^2)	GPCP	GPCC	(mm de^{-1})	GPCP	GPCC
North American	Tundra	3.90	19.80**	8.77	2.81*	16.99*	5.97
	Forest	2.69	-7.97	-11.9*	-3.06	-4.90	-8.84
	Grassland	0.72	5.03	5.12	6.54*	-1.52	-1.42
Eurasia	Tundra	6.21	12.83**	8.70*	2.72	10.11*	5.98
	Forest	4.91	2.53	6.27	6.94**	-4.41	-0.68
	Grassland	1.96	-9.99	-6.05	4.71*	-14.70	-10.77

* $P < 0.10$, ** $P < 0.05$

The P-ET results show similar spatial patterns with respect to GPCP and GPCC precipitation sources (Figure 4-9). There are also large spatial discrepancies in the northern Arctic coastal areas between P-ET trends derived from GPCP and GPCC data sets. Areas showing moderate to strong negative P-ET trends primarily occur in southern Alaska, western and southeastern Canada, northeastern Russia, southern Siberia, northern Mongolia and northeastern Siberia. Positive P-ET trends generally occur over tundra, while negative trends occur within grassland and boreal forest regions of the domain (Table 4-4).

While the GPCP and GPCC sources show variable precipitation patterns over the domain, both products show predominantly positive trends for the major pan-Arctic sub-basins (Table 4-5). Both the GPCP and GPCC derived P-ET results show insignificant trends for most pan-Arctic sub-basins (Table 4-5). Nine sub-basins show positive water balance (i.e., P-ET) trends indicated by both the GPCP and GPCC sources, while eight

Table 4-5. Summaries of annual ET, runoff (Q) and P-ET trends from 1983 to 2005 for 22 drainage basins within the pan-Arctic domain having available long-term gauge measurements; grey color denotes negative trends.

Continent	Ocean	Names of Basins	Area (10^4 km^2)	P Trend (mm de^{-1})		ET Trend (mm de^{-1})	Q Trend (mm de^{-1})	P-ET Trend (mm de^{-1})	
				GPCP	GPCC			GPCP	GPCC
North America	Pacific Ocean	Yukon	83.50	-21.54	-10.61	-0.17	4.20	-21.36	-10.43
	Arctic Ocean	Mackenzie	176.20	3.39	-17.53*	-2.57	3.36	5.96	-14.96
		Back	14.23	34.84***	0.98	6.57*	-22.72**	28.27***	-5.59
	HJUBs	Thelon	24.03	22.34*	37.71	6.50**	-0.46	15.84	31.21
		Thlewiaza	6.48	25.25	80.17*	4.40	1.83	20.85	75.77
		Seal	5.37	32.44	53.69**	1.27	3.54	31.17	52.41**
		Churchill	30.00	23.00*	15.07	-4.20	12.16*	27.20*	19.27
		Nelson	111.36	9.47	7.20	1.79	20.21**	7.68	5.41
		Hayes	10.58	21.81*	20.82	-1.43	12.44	23.24*	22.25
		Winisk	10.69	14.09	0.48	-6.80**	30.37	20.90	7.28
		Attawapiskat	3.06	15.01	-19.14	-7.86**	64.80**	22.87	-11.28
		Albany	12.35	-11.43	-8.67	4.42	29.37	-15.85	-13.08
		Moose	10.60	-32.86**	-48.28***	3.62	-10.10	-36.48**	-51.90***
Eurasia	Arctic Ocean	Onega	6.63	8.52	-2.27	5.82*	10.42	2.70	-8.09
		Northern Dvina	32.55	-20.90	-26.65**	3.93	-12.15	-24.83	-30.58**
		Mezen	7.72	-6.94	-23.71	1.31	1.44	-8.24	-25.01*
		Ob	296.04	2.72	3.43	6.49*	7.88	-3.77	-3.06
		Yenisei	257.11	-7.35	3.14	9.71**	8.28**	-17.06**	-6.56
		Mezen	8.57	20.74**	-9.51	-0.92	67.54***	21.66*	-8.59
		Lena	243.94	12.31	17.88**	1.13	5.26	11.18	16.76*
		Mezen	23.51	-0.13	0.82	10.40***	1.29	-10.53	-9.58
		Kolyma	65.71	11.32	7.21	3.65	0.80	7.67	3.56

[a] HJUBs denotes Hudson/James/Ungava Bays; * $P < 0.10$, ** $P < 0.05$, *** $P < 0.01$.

sub-basins display negative water balance trends. For the remaining five basins examined, the GPCP and GPCC derived results show opposite trends. However, only the Moose basin has a significant (with 90% or more confidence) trend confirmed by both GPCP and GPCC sources. The ET results (Table 4-5) show negative trends for the Yukon, Mackenzie, Churchill, Hayes, Winisk, Attawapiskat and Anabar basins but positive trends for the other 15 basins, indicating that ET outputs for the pan-arctic domain are generally increasing during the 23-year period. The measured annual runoff depth (Q) from regional basin gauges show positive trends for 94.3% of total examined basin area, except the Back, Thelon, Moose and Northern Dvina basins. These results indicate that river discharge outputs for the pan-Arctic region are also generally increasing. The general increasing trends in regional river discharges have been attributed to one or more factors including increasing poleward moisture transport and associated precipitation, permafrost thaw, and changes in regional fire regimes (e.g. Berezovskaya *et al.*, 2004; Groves & Francis, 2002; McClelland *et al.*, 2004; Yang *et al.*, 2002). The generally positive trends in ET, precipitation and river discharge for most basins (Figure 4-9; Table 4-5) are consistent with an intensification of the pan-Arctic terrestrial water cycle during the 23-year period. However, some areas have experienced drying trends during this period, including portions of eastern Alaska, southern Yukon, British Columbia, Alberta, southern Siberia and Mongolia. These drying patterns may be due to one or more related factors associated with regional climate warming, including decreasing precipitation inputs; a lengthening growing season and associated increases in evaporative water losses; alteration of regional storages from earlier onset of seasonal snowmelt, permafrost

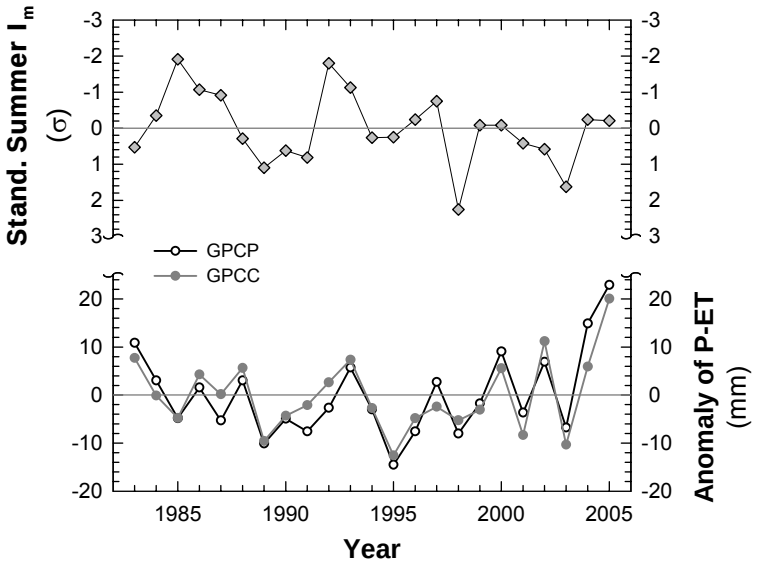

Figure 4-10: Time plots of standardized summer (Jun. - Aug.) vegetation moisture stress index (I_m) and corresponding summer P-ET anomalies derived from GPCP and GPCC precipitation sources, respectively; the y axis for standardized summer I_m increases from upper to lower portions of the graphic and corresponds to the changes from less-than-normal to more-than-normal moisture constraints on vegetation productivity.

thawing and increasing soil active layer depths (e.g. Berezovskaya *et al.*, 2004; McDonald *et al.*, 2004; Schindler & Donahue, 2006; Zhang *et al.*, 2005).

The standardized summer vegetation moisture stress index (I_m) and anomalies of summer P-ET were used to detect widespread summer droughts during the 23-year period for the pan-Arctic domain (Figure 4-10). The standardized summer I_m and summer P-ET anomalies (Figure 4-10) indicate that years 1989-1991, 1995, 1998, 2001 and 2003 had the driest summers over the 23-year period. The summer I_m and P-ET anomalies also show similar spatial patterns as illustrated in Figure 4-11 for years 1998, 2001, 2002 and 2003. Both variables indicate persistent, widespread dry conditions for these years, especially for eastern Alaska, Yukon, southern and central Canada, northeastern and

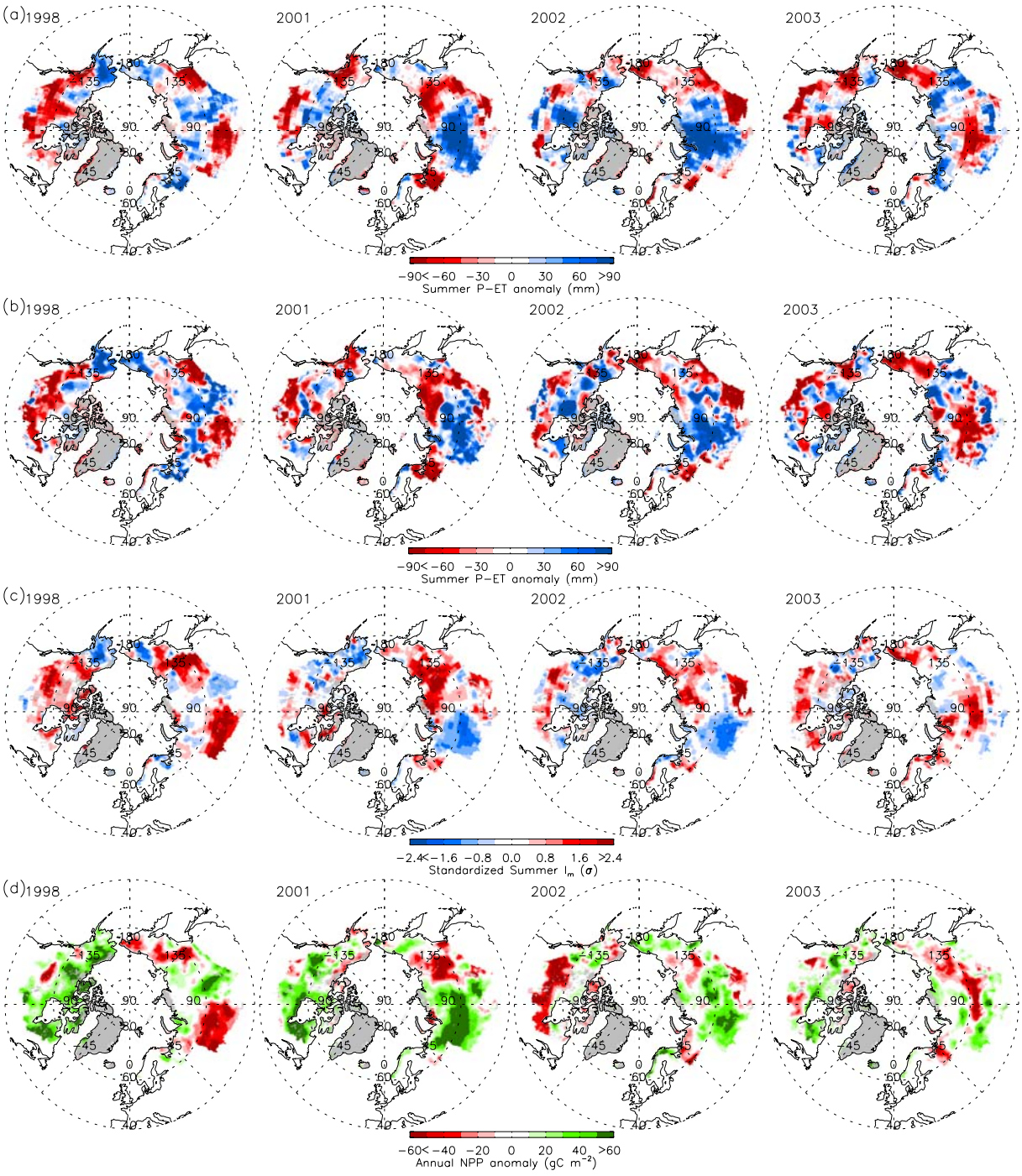

Figure 4-11: Maps of summer P-ET anomalies derived from (a) GPCP and (b) GPCC precipitation sources, (c) standardized summer I_m, and (d) annual NPP anomalies for years 1998, 2001, 2002 and 2003. Negative values of I_m denote less-than-normal moisture constraints on vegetation productivity and are indicated by the blue colors, while positive values indicate more-than-normal moisture constraints on vegetation productivity and are indicated by the red colors.

southeastern Siberia, and northern Mongolia. The North American portion of the domain shows more persistent drought in recent years than the Eurasian portion of the domain. These results are also consistent with the timing and locations of recent documented drought events (e.g. Waple et al., 2002; Waple et al., 2003; Levinson et al., 2004). Previous studies for the region (Kimball et al., 2006; Zhang et al., 2007a; Zhang et al., 2008) show generally positive trends in NPP for the domain, with large drought induced NPP decreases for boreal regions in recent years (Goetz et al., 2005; Zhang et al., 2008). The results from this study show generally consistent declines in P-ET and NPP for major drought years despite generally positive trends over the 23-year period. The relatively close correspondence between the summer regional water balance and NPP (Figure 4-11) reflects the strong impact of summer water balance on CO_2 exchange.

4.5. Discussion and Conclusions

I developed a satellite-based ET algorithm and used this information with regional precipitation data and available river discharge measurements to analyze spatial patterns, annual variability and recent (1983 through 2005) trends in P, ET and the terrestrial water balance (P-ET) for the pan-Arctic basin and Alaska. The pan-Arctic domain as a whole shows a small increasing trend in annual P, a significant increasing trend in annual ET and generally positive trends in measured annual runoff for most of the sub-basins examined. These results imply an intensification of the pan-Arctic terrestrial water cycle during the 23-year period. Both regional average P and ET show significant seasonal trends for the pan-Arctic domain. The ET results display significant positive trends in all four seasons with larger trends in spring and summer. The P results show larger positive

trends in spring, summer and autumn than ET but a small negative trend in winter, indicating that the pan-Arctic region as a whole is becoming wetter during the growing season. However, both P and ET trends show large spatial variability. Some areas have experienced drying trends during this period, including boreal forest and grassland regions of eastern Alaska, southern Yukon, British Columbia, Alberta, southern Siberia and Mongolia. These areas generally experienced recent (post-2000) summer droughts indicated by the spatial maps of summer P-ET decreases and a standardized summer vegetation moisture stress index (I_m), coinciding with anomalous decreases in satellite-detected annual vegetation productivity.

The water balance results may be negatively impacted by large uncertainties in both GPCP (MR = 1.10 mm month^{-1}; RMSE = 34.95 mm month^{-1}) and GPCC (MR = -7.15 mm month^{-1}; RMSE = 30.00 mm month^{-1}) precipitation sources, indicated by sparse station observations and associated uncertainties from coarse meteorology reanalysis inputs for model simulations. Open water bodies accounted for 6.4 percent of the pan-Arctic domain, while ET from these water bodies represented approximately 13.0 (±0.4) percent of total mean annual ET for the domain; however, ET from open water bodies are likely underestimated due to the characteristic abundance of small open water bodies in tundra regions that may not be adequately resolved by relatively coarse resolution (1 km) MODIS land cover information. Also some 1-km water body pixels may be lost when aggregated to an 8-km resolution by dominant land cover. Other uncertainties in our results reflect limitations of the ET algorithms and incomplete river discharge records for some sub-basins within the pan-Arctic domain. Despite these limitations, the GPCP and GPCC sources generally showed similar spatial patterns of annual P over 70% of the pan-

Arctic domain and high temporal correlation during the 23-year period, while the model ET results showed favorable agreement with tower derived ET (e.g. MR = -1.50 mm month^{-1}; RMSE = 8.3 mm month^{-1}; R^2= 0.89) over dominant regional land cover types.

Our findings of a general wetting trend for the pan-Arctic region are generally consistent with previous modeling and observational studies. Both precipitation observations and simulations from 22 coupled climate models showed generally increasing trends over high-latitude land areas above 55°N from 1950 to 2000 (Min *et al.*, 2008). Satellite remote sensing based observations also show generally increased poleward moisture transport to the Arctic from 1980 to 1998 (Groves and Francis 2002). A regional synthesis of recent changes in precipitation, runoff and precipitable water also show predominantly positive trends in recent decades for these major components of the Arctic freshwater cycle (Serreze et al. 2006, White et al. 2007). Together, these results provide broad-based evidence in support of a general intensification of the pan-Arctic terrestrial water cycle in response to a warming climate.

Our findings of a general pan-Arctic wetting trend coincide with regional warming (Trenberth et al., 2007) and vegetation greening trends (e.g. Goetz et al., 2005; Zhang et al., 2008). However, the regional water balance changes also show large spatial and temporal variability in the various water cycle components. Boreal forest and grassland areas of the domain show widespread drying trends for the 1983 to 2005 period, with recent (post-2000) large summer drought events coinciding with anomalous decreases in summer water balance and annual vegetation productivity. The impacts of recent droughts on boreal vegetation are also documented in other studies (Bunn & Goetz, 2006; Verbyla, 2008). In Alaska, tree-ring studies show a reduction in the growth of

white spruce (Barber *et al.*, 2004; Davi *et al.*, 2003), even at some upper tree-line sites (Lloyd & Fastie, 2003; Wilmking *et al.*, 2004), because of a recent increase in temperature-induced drought stress. Hogg and Wein (2005) also reported recent drought-induced reductions in forest growth and regeneration in southwestern Yukon, Canada, while Schindler and Donahue (2006) reported widespread and persistent post-2000 droughts in Canada's western Prairie Provinces. Together these results indicate strong coupling between regional water, energy and carbon cycles. A changing water balance is impacting regional vegetation productivity and associated sequestration of atmospheric CO_2 by altering the supply of plant-available moisture, while vegetation is influencing regional water and energy cycles through strong canopy controls to LE and ET. Northern boreal forest and tundra regions are considered to be an important global carbon sink for anthropogenic CO_2 emissions (Dargaville *et al.*, 2005). However, the stability of this northern carbon sink will likely depend on the continuing supply of adequate moisture and a positive water balance to offset increased evaporative demands of a warming climate.

Precipitation in the pan-Arctic region has strong teleconnections to global sea surface temperature (SST) patterns (Shabbar & Skinner, 2004), especially variations in tropical and north Pacific SSTs (Seager *et al.*, 2005; Zhang *et al.*, 2007a). Zhang et al. (2007a) showed that moisture availability in many areas of the pan-Arctic region has high correlation with the Pacific Decadal Oscillation (PDO) during the growing season. Groves and Francis (2002) showed that the net precipitable water flux across 70°N in winter is 6 times larger than on negative-index days, suggesting that poleward moisture transport is strongly tied to the NAO/AO. Goetz *et al.* (2007) reported the lagged

correlation between spring climate fields (like temperature and precipitation) and spring boreal North America net carbon exchange and suggested teleconnections between carbon fluxes in the pan-arctic region and large-scale atmospheric/oceanic oscillations such as the AO and ENSO.

The regional water balance trends from this investigation likely reflect both natural climate variability from ocean-atmosphere climate oscillations, and human-induced climate warming. The relative impacts of natural and human induced climate variability on regional water budget calculations are difficult to attribute due to the large natural variability of the Arctic system, and the relatively short record of satellite based observations. However, the continued growth of satellite observational records coupled with improvements in regional climate models will likely lead to improved diagnosis and attribution of global climate change impacts to the pan-Arctic water cycle. The results of this study show that ET and associated water balance changes are spatially complex, with large uncertainties in precipitation inputs due to sparse northern gauge networks and relatively coarse resolution reanalysis data sources. Longer and better precipitation reanalysis products should lead to better understanding of water cycle changes in this region, while improvements in precipitation monitoring networks and river discharge observations would dramatically improve the regional assessment of the terrestrial water balance and associated linkages between the terrestrial water and carbon cycles.

4.6. References Cited

Alder, R.F., Huffman, G.J., Chang, A., Ferraro, R., Xie, P.-P., Janowiak, J., Rudolf, B., Schneider, U., et al. (2003) The version-2 global precipitation climatology project

(GPCP) monthly precipitation analysis (1979-present). *Journal of Hydrometeorology*, **4**, 1147-1167.

Angert, A., Biraud, S., Bonfils, C., Henning, C.C., Buermann, W., Pinzon, J., Tucker, C.J., & Fung, I. (2005) Drier summers cancel out the CO_2 uptake enhancement induced by warmer springs. *Proceedings of the National Academy of Sciences*, **102**, 10823-10827.

Barber, V.A., Juday, G.P., Finney, B.P., & Wilmking, M. (2004) Reconstruction of summer temperatures in interior Alaska from tree-ring proxies: Evidence for changing synoptic climate regimes. *Climatic Change*, **63**, 91-120.

Bastiaanssen, W.G.M., Menenti, M., Feddes, R.A., & Holtslag, A.A.M. (1998a) A remote sensing surface energy balance algorithm for land (SEBAL): 1. Formulation. *Journal of Hydrology*, **212-213**, 198-212.

Bastiaanssen, W.G.M., Pelgrum, H., Wang, J., Ma, Y., Moreno, J.F., Roerink, G.J., & van der Wal, T. (1998b) A remote sensing surface energy balance algorithm for land (SEBAL): 2. Validation. *Journal of Hydrology*, **212-213**, 213-229.

Berezovskaya, S., Yang, D.Q., & Kane, D.L. (2004) Compatibility analysis of precipitation and runoff trends over the large Siberian watersheds. *Geophysical Research Letters*, **21**, L21502, doi:10.1029/2004GL021277.

Betts, A.K., Ball, J.H., & Viterbo, P. (2003) Evaluation of the ERA-40 surface water budget and surface temperature for the Mackenzie River basin. *Journal of Hydrometeorology*, **4**, 1194-1211.

Blanken, P.D. & Black, T.A. (2004) The canopy conductance of a boreal aspen forest, Prince Albert National Park, Canada. *Hydrological Processes*, **18**, 1561-1578.

Bouchet, R.J. (1963). Evapotranspiration réelle evapotranspiration potentielle, signification climatique. In *International Association of Scientific Hydrology. General Assembly of Berkeley, Transactions, vol.2, Evaporation*, pp. 134-142, Berkeley, California.

Bunn, A.G. & Goetz, S.J. (2006) Trends in satellite-observed circumpolar photosynthetic activity from 1982 to 2003: The influence of seasonality, cover type, and vegetation density. *Earth Interactions*, **10**, 1-19.

Carlson, P.J. (2000) Seasonal and iner-annual variation in carbon dioxide exchange and carbon balance in a mixed grassland, University of Lethbridge, Lethbridge, Alta., Canada.

Choudhury, B.J. & DiGirolamo, N.E. (1998) A biophysical process-based estimate of global land surface evaporation using satellite and ancillary data I. Model description and comparison with observations. *Journal of Hydrology*, **205**, 164-185.

Cleugh, H.A., Leuning, R., Mu, Q., & Running, S.W. (2007) Regional evaporation estimates from flux tower and MODIS satellite data. *Remote Sensing of Environment*, **106**, 285-304.

Dargaville, R., Baker, D., Rödenbeck, C., Rayner, P., & Ciais, P. (2005) Estimating high latitude carbon fluxes with inversions of atmospheric CO_2. *Mitigation and Adaptation Strategies for Global Change*, **11**, 769-782, doi:10.1007/s11027-005-9018-1.

Davi, N.K., Jacoby, G.C., & Wiles, G.C. (2003) Boreal temperature variability inferred from maximum latewood density and tree-ring width data, Wrangell Mountain region, Alaska. *Quaternary Research*, **60**, 252-262.

Dolman, A.J. & van Den Burg, G.J. (1988) Stomatal behavior in an oak canopy. *Agricultural and Forest meteorology*, 99-108.

Dunn, A.L. (2006) Carbon fluxes and the boreal forest mosaic. Ph.D. Dissertation, Harvard University, Cambridge, MA.

Dunn, A.L. & Wofsy, S.C. (2006). Boreal forest CO_2 flux, soil temperature, and meteorological data. Department of Earth & Planetary Sciences, Cambridge, MA.

Engstrom, R., Hope, A., Kwon, H., Harazono, Y., Mano, M., & Oechel, W. (2006) Modeling evapotranspiration in Arctic coastal plain ecosystems using a modified BIOME-BGC model. *Journal of Geophysical Research-Biogeosciences*, **111**, G02021, doi:10.1029/2005JG000102.

Fisher, J.B., To, K.P., & Baldocchi, D.D. (2008) Global estimates of the land-atmosphere water flux based on monthly AVHRR and ISLSCP-II data, validated at 16 FLUXNET sites. *Remote Sensing of Environment*, **112**, 901-919.

Friedl, M.A., McIver, D.K., Hodges, J.C.F., Zhang, X.Y., Mahoney, D., Staler, A.H., Woodcock, C.E., Goal, S., et al. (2002) Global land cover mapping from MODIS: algorithms and early results. *Remote Sensing of Environment*, **83**, 287-302.

Ganguly, S., Samantha, A., Scholl, M.A., Shawano, N.V., Milesi, C., Nemani, R.R., Knyazikhin, Y., & Myneni, R.B. (2008a) Generating vegetation leaf area index Earth system data record from multiple sensors. Part 2: Implementation, analysis and validation. *Remote Sensing of Environment*, **112**, 4318-4332.

Ganguly, S., Scholl, M.A., Samantha, A., Shawano, N.V., Milesi, C., Nemani, R.R., Knyazikhin, Y., & Myneni, R.B. (2008b) Generating vegetation leaf area index earth system data record form multiple sensors. Part 1: Theory. *Remote Sensing of Environment*, **112**, 4333-4343.

Goetz, S.J., Bunn, A.G., Fiske, G.J., & Houghton, R.A. (2005) Satellite-observed photosynthetic trends across boreal North America associated with climate and fire disturbance. *Proceedings of the National Academy of Sciences*, **102**, 13521-13525.

Goetz, S.J., Mack, M.C., Gurney, K.R., Randerson, J.T., & Houghton, R.A. (2007) Ecosystem responses to recent climate change and fire disturbance at northern high latitudes: observations and model results contrasting northern Eurasia and North America. *Environmental Research Letters*, **4**, 045031, doi:10.1088/1748-9326/2/4/045031.

Granier, A. & Loustau, D. (1994) Measuring and modelling the transpiration of a maritime pine canopy from sap-flow data. *Agricultural and Forest meteorology*, **71**, 61-81.

Granier, A., Loustau, D., & Bréda, N. (2000) A generic model of forest canopy conductance dependent o climate, soil water availability and leaf area index. *Annals of Forest Science*, **57**, 755-765.

Griffis, J., Black, T.A., Gaumont-Guay, D., Drewitt, G.B., Nesic, Z., Barr, A.G., Morgenstem, K., & Kljun, N. (2004) Seasonal variation and partitioning of ecosystem respiration in a southern Boreal aspen forest. *Agricultural and Forest meteorology*, **125**, 207-223.

Groves, D.G. & Francis, J.A. (2002) Variability of the Arctic atmospheric moisture budget from TOVS satellite data. *Journal of Geophysical Research-Atmospheres*, **D24**, 4785, doi:10.1029/2002JD002285.

Harazono, Y., Mano, M., Miyata, A., Zulueta, R.C., & Oechel, W.C. (2003) Inter-annual carbon dioxide uptake of a wet sedge tundra ecosystem in the Arctic. *Tellus*, **55B**, 215-231.

Held, I.M. & Soden, B.J. (2000) Water vapor feedback and global warming. *Annual Review of Energy and the Environment*, **25**, 441-475.

Hogg, E.H., Brandt, J.P., & Michaelian, M. (2008) Impacts of a regional drought on the productivity, dieback and biomass of western Canadian aspen forests. *Canadian Journal of Forest Research*, **38**, 1373-1384.

Hogg, E.H. & Wein, R.W. (2005) Impacts of drought on forest growth and regeneration following fire in southwestern Yukon, Canada. *Canadian Journal of Forest Research*, **35**, 2141-2150.

Huntington, T.G. (2006) Evidence for intensification of the global water cycle: Review and synthesis. *Journal of Hydrology*, **319**, 83-95.

Idso, S.B. & Jackson, R.D. (1969) Thermal radiation from the atmosphere. *Journal of Geophysical Research*, **74**, 5397-5403.

Jarvis, P.G. (1976) The interpretation of the variations in leaf water potential and stomatal conductance found in canopies in the field. *Philosophical Transactions of the Royal Society B*, **273**, 593-610.

Jarvis, P.G. & McNaughton, K.G. (1986) Stomatal control of transpiration: Scaling up from leaf to region. *Advances In Ecological Research*, **15**, 1-49.

Jones, C.A. & Kiniry, J.R. (1986) *CERES-Maize: A simulation model of maize growth and development*. A&M University Press, College Station.

Jones, H.G. (1992) *Plants and microclimate: a quantitative approach to environmental plant physiology*, 2nd ed. Cambridge University Press, Cambridge.

June, T., Evans, J.R., & Farquhar, G.D. (2004) A simple new equation for the reversible temperature dependence of photosynthetic electron transport: A study on soybean leaf. *Functional Plant Biology*, **31**, 275-283.

Kimball, J.S., Zhao, M., McDonald, K.C., & Running, S.W. (2006) Satellite remote sensing of terrestrial net primary production for the pan-Arctic basin and Alaska. *Mitigation and Adaptation Strategies for Global Change*, **11**, 782-804, doi:10.1007/s11027-005-9014-5.

Kimball, J.S., Zhao, M., McGuire, A.D., Heinsch, F.A., Glein, J., Calef, M., Jolly, W.M., Kang, S., et al. (2007) Recent climate-driven increases in vegetation productivity for the western Arctic: Evidence for an acceleration of the northern terrestrial carbon cycle. *Earth Interactions*, **11**, 1-30.

L'vovich, M.I. & White, G.F. (1990). Use and transformation of terrestrial water systems. In *The Earth as transformed by human action: global and regional changes in the biosphere over the past 300 years* (eds B.L. Turner II, W.C. Clark, R.W. Kates, J.F. Richards, J.T. Mathews & W.B. Meyer), pp. 235-252. Cambridge University Press, New York.

Levinson, D.H. & Waple, A.M. (2004) State of climate in 2003. *Bulletin of the American Meteorological Society*, **85**, S1-S72.

Lloyd, A.H. & Fastie, C.L. (2003) Recent changes in treeline forest distribution and structure in interior Alaska. *Ecoscience*, **10**, 176-185.

McClelland, J.W., Déry, S.J., Peterson, B.J., Holmes, R.M., & Wood, E.F. (2006) A pan-arctic evaluation of changes in river discharge during the latter half of the 20th century. *Geophysical Research Letters*, **33**, L06715, doi:10.1029/2006GL025753.

McClelland, J.W., Holmes, R.M., Peterson, B.J., & Stieglitz, M. (2004) Increasing river discharge in the Eurasian Arctic: Consideration of dams, permafrost thaw, and fires as potential agents of change. *Journal of Geophysical Research*, **109**, D18102, doi:10.1029/2004JD004583.

McDonald, K.C., Kimball, J.S., Njoku, E., Zimmermann, R., & Zhao, M. (2004) Variability in springtime thaw in the terrestrial high latitudes: Monitoring a major control on the biospheric assimilation of atmospheric CO2 with spaceborne microwave remote sensing. *Earth Interactions*, **8**, 1-22.

Meehl, G.A., Stocker, T.F., Collins, W.D., Friedlingstein, P., Gaye, A.T., Gregory, J.M., Kitoh, A., Knutti, R., et al. (2007). Global climate projections. In *Climate Change 2007: The Physical Science Basis* (eds S. Solomon, D. Qin, M. Manning, Z. Chen, M. Marquis, K.B. Averyt, M. Tignor & H.L. Miller). Cambridge University Press, Cambridge, United Kingdom and New York, NY, USA.

Min, S.K., Zhang, X.B., & Zwiers, F. (2008) Human-induced arctic moistening. *Science*, **320**, 518-520.

Monteith, J. & Unsworth, M. (2008) *Principles of environmental physics*. Academic Press, San Diego, California, USA.

Monteith, J.L. (1965) Evaporation and environment. The State and movement of water in living organisms. In Symposium of the society of experimental biology, Vol. 19, pp. 205-234. Cambridge University Press, Cambridge.

Mu, Q., Heinsch, F.A., Zhao, M., & Running, S.W. (2007) Development of a global evapotranspiration algorithm based on MODIS and global meteorology data. *Remote Sensing of Environment*, **111**, 519-536.

Oechel, W.C., Vourlities, G.L., Hastings, S.J., Zulueta, R.M., Hinzman, L.D., & Kane, D.L. (2000) Acclimation of ecosystem CO_2 exchange in the Alaskan Arctic in response to decadal climatic warming. *Nature*, **406**, 978-981.

Oechel, W.C., Vourlitis, G.L., Hastings, S.J., Ault Jr., R.P., & Bryant, P. (1998) The effects of water table manipulation and elevated temperature on the net CO_2 flux of wet sedge tundra ecosystems. *Global Change Biology*, **4**, 77-90.

Oelke, C., Zhang, T., & Serreze, M.C. (2004) Modeling evidence for recent warming of the Arctic soil thermal regime. *Geophysical Research Letters*, **31**, L07208, doi:10.1029/2003GL019300.

Pinzon, J., Brown, M.E., & Tucker, C.J. (2005). Satellite time series correction of orbital drift artifacts using empirical mode decomposition. In *Hilbert-Huang Transform: Introduction and Applications* (eds N.E. Huang & S.S.P. Shen), pp. 167-186. World Scientific Publishing Co. Pte. Ltd., Singapore.

Priestley, C.H.B. & Taylor, R.J. (1972) On the assessment of surface heat flux and evaporation using large-scale parameters. *Monthly Weather Review*, **100**, 81-92.

Rayment, M.B., Loustau, D., & Jarvis, P.G. (2000) Measuring and modeling conductances of black spruce at three organizational scales: shoot, branch and canopy. *Tree Physiology*, **20**, 713-723.

Rudolf, B. & Rubel, F. (2005). Global precipitation. In *Observed global climate, Landolt-Börnstein (Numerical Data and Functional Relationships)* (ed M. Hantel), Vol. 6. Springer, Berlin, Heidelberg and New York.

Rudolf, B. & Schneider, U. (2005) Calculation of gridded precipitation data for the global land-surface using in-situ gauge observations. In Proceedings of the 2nd Workshop of the International Precipitation Working Group IPWG, Monterey.

Ruiz-Barradas, A. & Nigam, S. (2005) Warm season rainfall variability over the US great plains in observations, NCEP and ERA-40 reanalyses, and NCAR and NASA atmospheric model simulations. *Journal of Climate*, **18**, 1808-1830.

Schindler, D.W. & Donahue, W.F. (2006) An impending water crisis in Canada's western prairie provinces. *Proceedings of the National Academy of Sciences*, **103**, 7210-7216.

Seager, R., Kushnir, Y., Herweijer, C., Naik, N., & Velez, J. (2005) Modeling of tropical forcing of persistent droughts and pluvials over western North America: 1856-2000. *Journal of Climate*, **18**, 4065-4088.

Serreze, M.C., Barrett, A.P., Slater, A.G., Woodgate, R.A., Aagaard, K., Lammers, R.B., Steele, M., Moritz, R., et al. (2006) The large-scale freshwater cycle of the Arctic. *Journal of Geophysical Research-Oceans*, **C11**, C11010, doi:10.1029/2005JC003424.

Shabbar, A. & Skinner, W. (2004) Summer drought patterns in Canada and the relationship to global sea surface temperatures. *Journal of Climate*, **17**, 2866-2880.

Shuttleworth, W.J. (1992). Evaporation. In *Handbook of hydrology* (ed D.R. Maidment), pp. 4.1-4.53. McGraw Hill, New York.

Steiner, J.L., Howell, T.A., & Schneider, A.D. (1991) Lysimetric Evaluation of Daily Potential Evapotranspiration Models for Grain-Sorghum. *Agronomy Journal*, **83**, 240-247.

Stewart, J.B. (1988) Modelling surface conductance of pine forest. *Agricultural and Forest meteorology*, **43**, 19-35.

Sturm, M., Racine, C., & Tape, K. (2001) Increasing shrub abundance in the Arctic. *Nature*, **411**, 546-547.

Thornton, P.E. (1998) Regional ecosystem simulation: combining surface- and satellite-based observations to study linkages between terrestrial energy and mass budgets. Ph.D. Dissertation, The University of Montana, Missoula, MT.

Trenberth, K.E., Jones, P.D., Ambenje, P., Bojariu, R., Easterling, D., Klein Tank, A., Parker, D., Rahimzadeh, et al. (2007). Observations: surface and atmospheric climate change. In *Climate Change 2007: The Physical Science Basis* (eds S. Solomon, D. Qin, M. Manning, Z. Chen, M. Marquis, K.B. Averyt, M. Tignor & H.L. Miller). Cambridge University Press, Cambridge, United Kingdom and New York, NY, USA.

Tucker, C.J., Pinzon, J.E., Brown, M.E., Slayback, D., Pak, E.W., Mahoney, R., Vermote, E., & Saleous, N. (2005) An extended AVHRR 8-km NDVI data set compatible with MODIS and SPOT vegetation NDVI data. *International Journal of Remote Sensing*, **26**, 4485-4498.

Verbyla, D. (2008) The greening and browning of Alaska based on 1982-2003 satellite data. *Global Ecology and Biogeography*, **17**, 547-555.

Waple, A.M., Mann, M.E., & Bradley, R.S. (2002) Long-term patterns of solar irradiance forcing in model experiments and proxy based surface temperature reconstructions. *Climate Dynamics*, **18**, 563-578.

Wever, L.A., Flanagan, L.B., & Carlson, P.J. (2002) Seasonal and interannual variation in evapotranspiration, energy balance and surface conductance in a northern temperate grassland. *Agricultural and Forest meteorology*, **112**, 31-49.

White, D., Hinzman, L., Alessa, L., Cassano, J., Chambers, M., Falkner, K., Francis, J., Gutowski Jr., W.J., et al. (2007) The arctic freshwater system: Changes and impacts. *Journal of Geophysical Research*, **112**, G04S54, doi:10.1029/2006JG000353.

White, M.A., Thornton, P.E., Running, S.W., & Nemani, R.R. (2000) Parameterization and sensitivity analysis of the BIOME-BGC terrestrial ecosystem model: Net primary production controls. *Earth Interactions*, **4**, 1-85.

Wilmking, M., Juday, G.P., Barber, V.A., & Zald, H.S.J. (2004) Recent climate warming forces contrasting growth responses of white spruce at treeline in Alaska through temperature thresholds. *Global Change Biology*, **10**, 1724-1736.

Yang, D., Kane, D., Zhang, Z., Legates, D., & Goodison, B. (2005) Bias corrections of long-term (1973-2004) daily precipitation data over the northern regions. *Geophysical Research Letters*, **32**, L19501, doi:10.1029/2005GL024057.

Yang, D.Q., Kane, D.L., Hinzman, L.D., Zhang, X.B., Zhang, T.J., & Ye, H.C. (2002) Siberian Lena River hydrologic regime and recent change. *Journal of Geophysical Research*, **D23**, 4694, doi:10.1029/2002JD002542.

Zhang, K., Kimball, J.S., Hogg, E.H., Zhao, M., Oechel, W.C., Cassano, J.J., & Running, S.W. (2008) Satellite-based model detection of recent climate-driven changes in northern high-latitude vegetation productivity. *Journal of Geophysical Research*, **113**, G03033, doi:10.1029/2007JG000621.

Zhang, K., Kimball, J.S., McDonald, K.C., Cassano, J.J., & Running, S.W. (2007a) Impacts of large-scale oscillations on pan-Arctic terrestrial net primary production. *Geophysical Research Letters*, **34**, L21403, doi:10.1029/2007GL031605.

Zhang, K., Kimball, J.S., Zhao, M., Oechel, W.C., Cassano, J., & Running, S.W. (2007b) Sensitivity of pan-Arctic terrestrial net primary productivity simulations to daily surface meteorology from NCEP-NCAR and ERA-40 reanalysis. *Journal of Geophysical Research*, **112**, G01011, doi:10.1029/2006JG000249.

Zhang, T.J., Frauenfeld, O.W., Serreze, M.C., Etringer, A., Oelke, C., McCreight, J., Barry, R.G., Gilichinsky, D., et al. (2005) Spatial and temporal variability in active layer thickness over the Russian Arctic drainage basin. *Journal of Geophysical Research*, **110**, D16101, doi:10.1029/2004JD005642.

Zhao, M., Heinsch, F.A., Nemani, R.R., & Running, S.W. (2005) Improvements of the MODIS terrestrial gross and net primary production data set. *Remote Sensing of Environment*, **95**, 164-176.

CHAPTER 5: IMPACTS OF LARGE-SCALE OSCILLATIONS ON PAN-ARCTIC VEGETATION PRODUCTIVITY AND THE REGIONAL WATER BALANCE

5.1. Climate Oscillations

Any phenomenon that tends to vary above or below a mean value in some sort of periodic way is properly designated as an oscillation (Oliver, 2005). The large-scale atmospheric circulation patterns (Wallace & Thompson, 2002) and ocean circulation patterns (Siedler *et al.*, 2001) showing quasi-periodic behaviors are generally called climate oscillations. Teleconnections in atmospheric science refer to climate anomalies being related to each other at large distances, typically thousands of kilometers (Glantz *et al.*, 1991). Climate oscillations can generally show be described by their teleconnections and quantified by their respective oscillation indices.

The major oscillations of the planetary atmospheric pressure fields were proposed by Sir Gilbert Walker, who first described and named the seesaw pressure readings of the southern oceans as the Southern Oscillation (Oliver, 2005). Walker's work went relatively unnoticed until recent decades. In a 1966 paper Bjerknes recognized the contributions of Walker and identified the Walker Circulation (Bjerknes, 1966). Increased research on teleconnections has identified other oscillations. The major global oscillations include El Niño-Southern Oscillation (ENSO) (Rasmusson & Carpenter, 1982), the North Atlantic Oscillation (NAO) (Hurrell & van Loon, 1997), the Pacific Decadal Oscillation (PDO) (Mantua *et al.*, 1997), the Pacific North American Oscillation

(PNA) (Wallace & Gutzler, 1981), the Arctic Oscillation (AO) (Thompson & Wallace, 1998), the Antarctic Oscillation (AAO) (Gong & Wang, 1998) , and the Quasibiennial Oscillation (QBO) (Maruyama, 1997).

The ENSO is a pressure anomaly over the Indian and South Pacific Oceans with a slightly variable periodicity averaging 2.33 years. The NAO reflects the atmospheric stability of the Icelandic low-pressure cell and the Azores – Bermuda high-pressure cell and has a marked influence on the climate of Western Europe. The PDO is a relatively long-lived (20-30 year cycle) phenomenon defined by ocean surface temperatures in the northeast and tropical Pacific; the PDO has a long-term influence on the climate of North America. The PNA is an alternating pattern between pressures in the central Pacific Ocean and centers of action over western Canada and the southeastern United States; it is expressed as an index that is both ocean- and land-based. The AO is an oscillation in which atmospheric pressure anomalies, at polar and mid-latitude locations, fluctuate between distinct positive and negative phases. The AAO is represented by an oscillation in values of mid- and high-latitude surface pressure systems in the southern hemisphere. The Quasibiennial Oscillation (QBO) is a low-latitude oscillation that is longer than the dominant annual cycle and whose identification rests with sophisticated computer modeling.

Most oscillations are involved with the strength and location of the major planetary highs and lows (centers of action) and sea surface temperatures, and are derived statistically from long-range atmospheric pressure observation series. For some, and to a lesser extent, rainfall and temperature data series can also be employed.

In this study, I mainly focus on the primary oscillations that may strongly affect regional climate in pan-arctic region. These oscillations include the NAO, AO and PDO. The NAO and the AO are different representations and conceptual interpretations of the same phenomenon (Kerr, 1999; Wallace, 2000). Moreover, the AO correlates strongly (85-95%) with the NAO (e.g. Deser, 2000; Dickson *et al.*, 2000; Hurrell, 1995). The AO captures more hemispheric variability than the NAO because many of the recent changes associated with the AO have occurred in the Laptev, East Siberian, Chukchi and Beaufort Seas – a long way from the NAO's center of action (Thompson & Wallace, 1998). Therefore, the AO is examined instead of the NAO, and the AO and PDO are the two major climate oscillations addressed in this study.

5.1.1. The Arctic Oscillation

The AO is defined as the leading principal component of sea level pressure (SLP) variability in the Northern Hemisphere, is a robust surface manifestation of the strength of the polar vortex and explains much of the variance both of the surface pressure and of the geopotential height in the troposphere (Thompson & Wallace, 1998). It is the dominant pattern of non-seasonal SLP variations north of 20° N and is characterized by SLP anomalies of one sign in the Arctic and anomalies of opposite sign centered about 37-45° N (Figure 5-1).

The AO exhibits a "positive phase" or "warm phase" with relatively low pressure over the polar region and high pressure at mid-latitudes (about 45 degrees North), and a "negative phase" or "cold phase" in which the pattern is reversed (Figure 5-1). In the

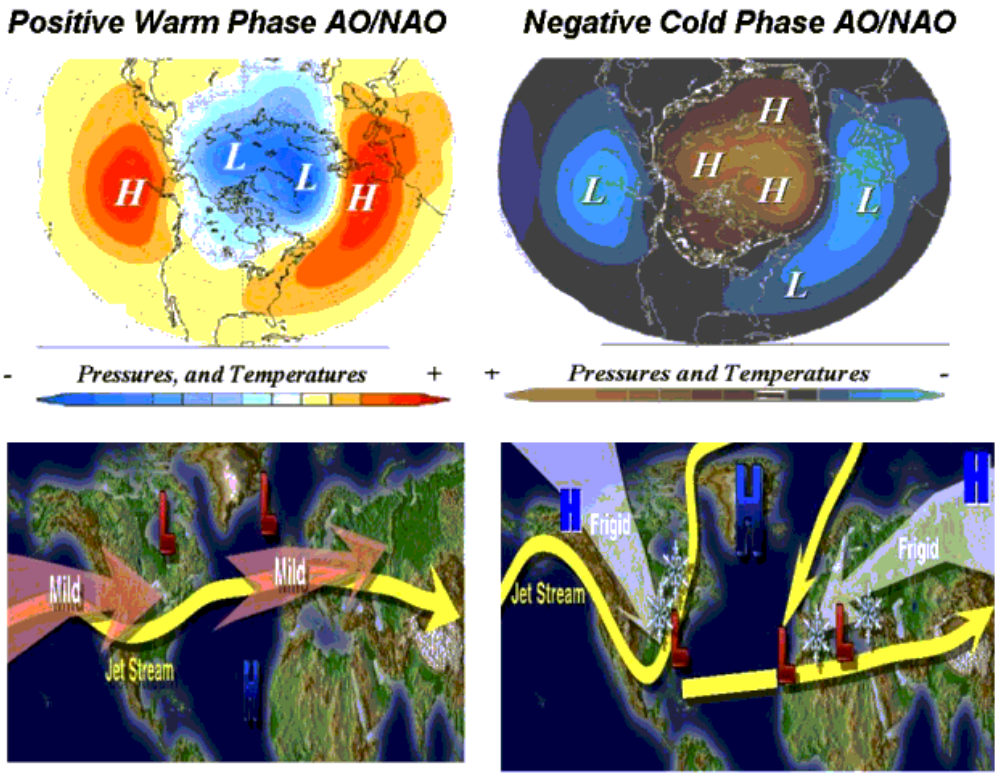

Figure 5-1: General pressure and temperature patterns in the Northern Hemisphere during positive (warm) phase (upper left) and negative (cold) phase (upper right) of the AO/NAO, and corresponding effects on mid-high latitude wind fields by positive (lower left) and negative (lower right) phases of the AO/NAO (graphs are from http://www.newx-forecasts.com/ao_2.html).

positive phase, higher pressure at mid-latitudes drives ocean storms farther north, and changes in the circulation pattern bring wetter weather to Alaska, Scotland and Scandinavia, as well as drier conditions to the western United States and the Mediterranean. The pressure patterns favor the Jet streams and create strong westerlies that keep cold Arctic air to the north and push warmth and precipitation toward northern Europe. In the negative phase, the pressure patterns disturb the Jet Steams and weaken the westerlies (Figure 5-1). As a result, frigid Arctic air reaches more southerly latitudes. The Northern Europe and Asia get hit with cold Arctic air (Figure 5-1).

The AO is reported to influence winter Eurasian snow cover (Gong *et al.*, 2003), Hudson Bay river discharge (Déry & Wood, 2004), freshwater-ice break/freeze-up dates over Canada (Bonsal *et al.*, 2006) and interannual forest fire variability in Central Siberia (Balzter *et al.*, 2005).

5.1.2. The Pacific Decadal Oscillation

The PDO is the leading principal component of North Pacific sea surface temperature (SST) variability and shifts phases over inter-decadal time scales of approximately 20 to 30 years (Mantua *et al.*, 1997). The PDO is detected as anomalous warm or cool surface waters of the Pacific Ocean, north of 20° N (Figure 5-2). During a "warm" or "positive" PDO phase, western Pacific SST becomes cool and portion of the eastern Pacific warm; during a "cool" or "negative" PDO phase, the opposite pattern occurs (Figure 5-2). The specific drivers of have not been identified, but may involve a response to intrinsic variability in atmospheric conditions of the North Pacific, remote

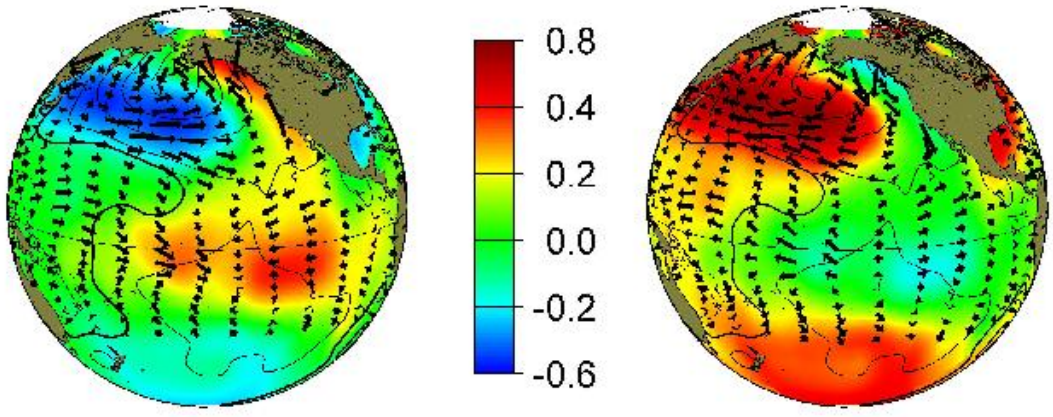

Figure 5-2: Typical winter time SST (colors), SLP (contours) and surface windstress (arrows) anomaly patterns during warm (left) and cool (right) PDO phases (graphs are from University of Washington, http://jisao.washington.edu/pdo/).

forcing by ENSO, and ocean wave processes associated with ENSO and corresponding adjustment of the North Pacific Ocean by Rossby waves (Schneider & Cornuelle, 2005).

Major changes in northeast Pacific marine ecosystems have been correlated with phase changes in the PDO; warm phases have coincided with enhanced coastal ocean biological productivity in Alaska and inhibited productivity off the west coast of the contiguous United States, while cold PDO phases have coincided with the opposite north-south pattern of marine ecosystem productivity. The PDO has also been correlated with North American precipitation and stream flow patterns (Dettinger et al., 1998), and northeast Asia surface air temperature fluctuations (Minobe, 2000).

5.2. Data and Methodology

Teleconnections between the climate oscillations and vegetation productivity and atmospheric CO_2 anomalies with teleconnections were analyzed on a monthly basis since the effects of teleconnections don't last the whole year, e.g. the AO/NAO contribute significantly to Northern Europe annual surface atmosphere temperatures mainly in winter and early spring (Kryjov, 2004).

I hypothesized that the AO and PDO influence pan-Arctic terrestrial production by regulating the timing of annual growing season onset and the supply of plant-available moisture.

5.2.1. PEM NPP Series and Moisture Stress Index

Daily NPP series were derived from 1983-2005 on a grid cell-by-cell basis with 16km×16km resolution using the MOD17A2/A3 production efficiency model (PEM)

driven by satellite remote sensing based monthly leaf area index (LAI) and fraction of photosynthetically active radiation (FPAR) developed from NOAA Advanced Very High-Resolution Radiometer (AVHRR) Pathfinder and NASA MODerate resolution Imaging Spectroradiometer (MODIS) records, and a gridded daily surface meteorological dataset developed from a regional correction of the NCEP/NCAR reanalysis and NASA Solar Radiation Budget daily shortwave solar radiation inputs (see Chapter 3).

To quantify the moisture constraints to NPP, I used the simple moisture stress index (I_m) based on the PEM algorithms introduced in Section 3.1. The I_m parameter is dimensionless, ranging from 0 to 1 with increasing VPD constraints to NPP. I calculated a potential annual NPP rate ($NPP_{\_M}$) by eliminating the VPD based moisture constraint in the PEM calculations. I then determined the proportional difference between annual NPP calculations under non-moisture-stressed and actual conditions as a simple NPP loss index: $\delta_{NPP\_Loss} = \frac{NPP_{\_M} - NPP_{actual}}{NPP_{\_M}} \times 100\%$. The δ_{NPP_Loss} values were then standardized using estimated means and standard deviations of the 1983-2005 time series. The standardized value of δ_{NPP_Loss} (SI_{NPP_Loss}) represents a direct measure of drought-induced NPP losses, whereas the I_m parameter describes the relative strength of the VPD defined moisture constraint on NPP calculations.

5.2.2. Timing of growing season onset

The timing (day of year) of growing season onset was derived from two different approaches, including: the seasonal onset of terrestrial NPP (T_{NPP_Onset}) derived from the

PEM, and timing of the spring drawdown of atmospheric CO_2 concentrations (T_{CO2_Spr}) from NOAA CMDL arctic and sub-arctic monitoring stations (>50°N) (see Section 3.3).

5.2.3. AO and PDO Indices

The monthly AO indices were obtained from the US National Weather Service Climate Prediction Center (http://www.cdc.noaa. gov/Correlation/ao.data), while the monthly PDO indices were provided by the University of Washington (ftp://ftp.atmos.washington.edu/mantua/pnw_impacts /INDICES/PDO.latest) .

To analyze the relationship between oscillations and the timing of growing season onset in the region, I first calculated early-spring (February- April) mean values of the monthly oscillation indices, and then standardized the values using the means and standard deviations. I then conducted a pixel-wise correlation analysis between the oscillation indices and T_{NPP_Onset} time series to examine the spatio-temporal correlations. The same procedures were applied to evaluate linkages between mean oscillation indices during the growing season, I_m and SI_{NPP_Loss}. The growing season (GS, April-October) is defined as all months in which the 1983-2005 monthly average air temperature for the pan-Arctic domain is above 0.0°C.

5.3. Results

5.3.1. Connection of AO Spring Patterns to Growing Season Onset

The spring AO index (AO_{spr}) showed a strong systematic correlation with T_{NPP_Onset} (Figure 5-3). The correlations between AO_{spr} and T_{NPP_Onset} were

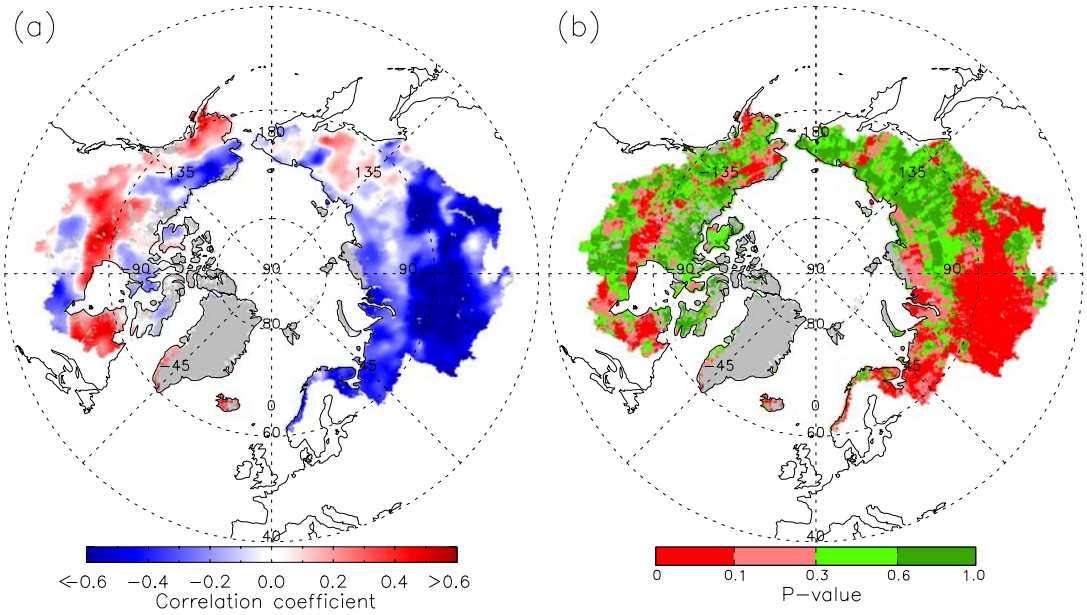

Figure 5-3: Maps of (a) pixel-wise correlation between AO_{spr} and the timing of growing season onset derived from PEM calculations and (b) the corresponding statistical *P*-values for the pan-Arctic region.

predominantly negative for the Eurasian portion of the domain, but positive for Central and Northeastern Canada (Figure 5-3). This is because a positive AO_{spr} reflects stronger-than-normal pressure patterns, resulting in stronger-than-normal westerly winds across the North Atlantic Ocean in the 40-60°N latitude belt, warmer-than-normal conditions and earlier growing season onset over Eurasia, and colder-than-normal conditions and later growing season onset over the eastern Canadian Arctic (Hurrell, 1996). The pan-Arctic regional average T_{NPP_Onset} was negatively correlated with AO_{spr} ($r = -0.653$; $P = 0.001$) (Figure 5-4). The relatively strong correlation ($r = 0.777$; $P < 0.001$) between T_{CO2_Spr} and regional average T_{NPP_Onset} (Figure 5-4) also indicates that northern terrestrial ecosystems dominate the seasonal atmospheric CO_2 cycle at high northern latitudes and that the PEM captures the annual timing of the growing season onset.

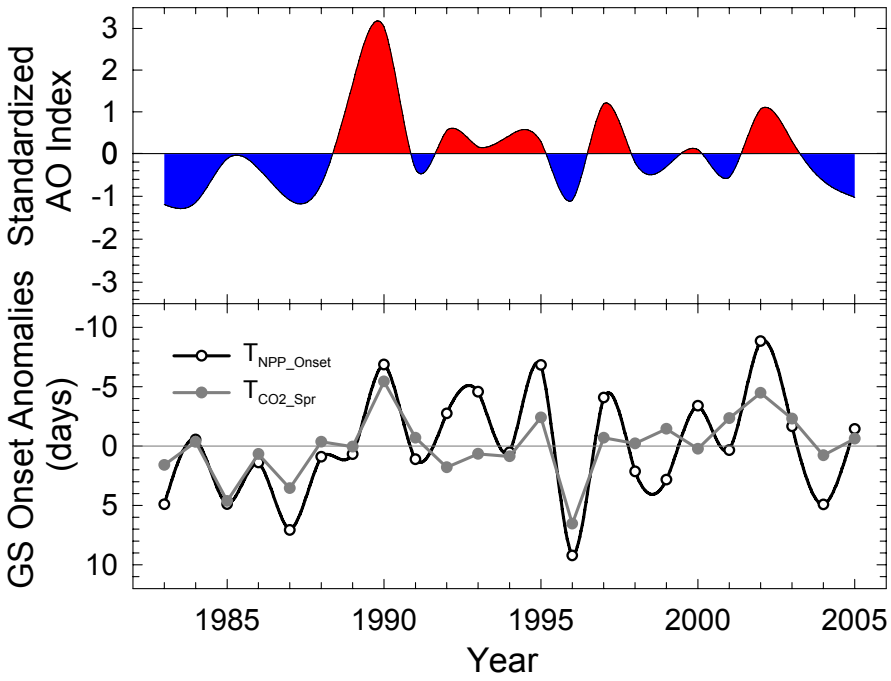

Figure 5-4: Temporal trajectories of the AO_{spr} and annual anomalies of regional average growing season onset derived from PEM calculations (T_{NPP_Onset}), and the seasonal pattern of atmospheric CO_2 concentrations (T_{CO2_Spr}); negative anomalies denote earlier onset of the growing season, while positive values denote the opposite response relative to the 23-year record.

Positive AO_{spr} phases coincided with generally earlier growing season onset, while negative AO_{spr} phases are concurrent with later growing season onset. These results indicate that regional oscillations captured by the AO_{spr} influence annual NPP by affecting the timing of growing season onset. Previous studies indicate that approximately 1% of annual NPP is gained or lost for each additional day advance or delay in the annual onset of the growing season (Baldocchi *et al.*, 2001; Kimball *et al.*, 2004; Kimball *et al.*, 2006). Within the pan-Arctic domain, 86.6% of the vegetated area showed a negative correlation between the timing of growing season onset and annual NPP for the 1983-2005 period, while 59.3% of this area showed a significant correlation with at least 90% confidence (Figure 5-3). A temporal advance in growing season onset

promotes vegetation growth by increasing the potential annual duration of photosynthesis, but may not necessary lead to greater annual vegetation production because of other influences on NPP including plant-available moisture constraints to photosynthesis, fire and related disturbance impacts during the growing season.

5.3.2. Connection of Growing Season PDO Patterns to Plant Moisture Stress and Water Balance

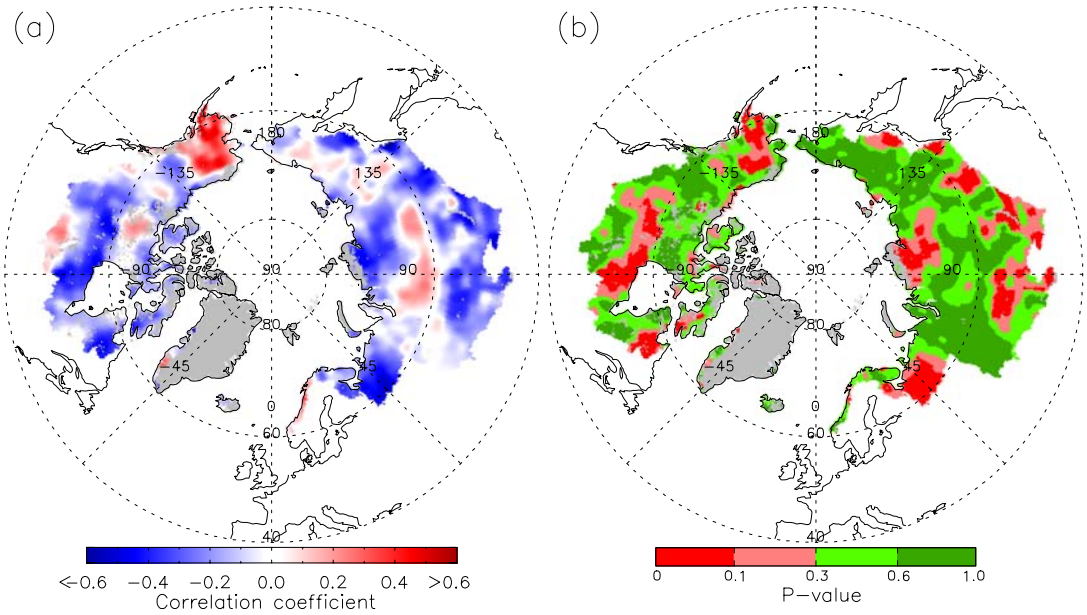

Figure 5-5: Maps of (a) pixel-wise correlation between PDO_{GS} and GS I_m values and (b) the corresponding statistical *P*-values for the pan-Arctic region.

The spatial patterns of correlations between PDO_{GS} and GS I_m indicate that the PDO_{GS} shows strong systematic association with GS I_m (Figure 5-5). The PDO_{GS} and GS I_m relationship (Figure 5-5) is predominantly negative for Southern, Central and Northeastern Canada, and Northwestern and Southern Eurasia indicating a reduced VPD constraint to NPP for positive PDO conditions, but positive for Western and Southern

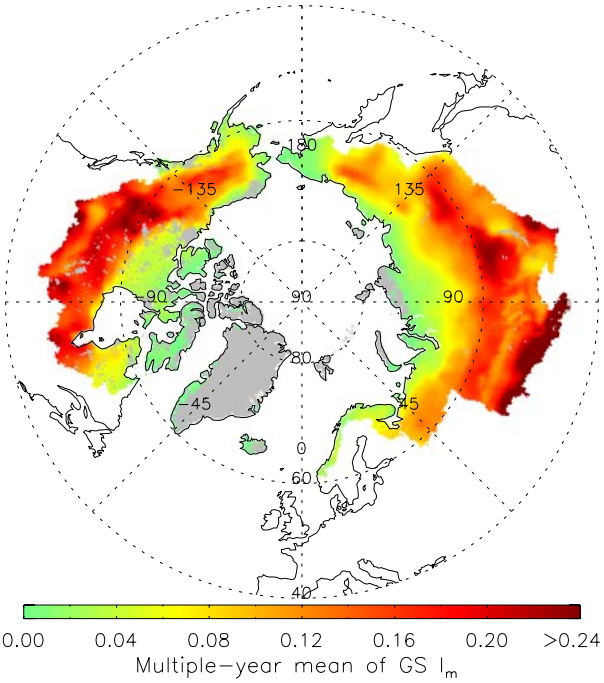

Figure 5-6: Map of mean (23-year) GS I_m values for the pan-Arctic domain.

Alaska. Overall, approximately 75.7% of the domain showed a negative correlation between PDO_{GS} and GS I_m for the 23-year period, 29.6% of which showed a significant correlation with at least 90% confidence. Approximately 50.7% of this area showed above-average moisture stress (i.e. greater than average moisture stress relative to the 23-year pan-Arctic regional mean) that was predominantly located in boreal forest and grassland/cropland biomes, rather than tundra (Figure 5-6).

The PDO_{GS} index also shows spatial correlations with the growing season water balance (P-ET) on a pixel-by-pixel basis (Figure 5-7), but the correlations are generally weaker than correspondence between PDO_{GS} and GS I_m. Uncertainties in the precipitation data may reduce the correlations between PDO_{GS} and GS P-ET. However, the results using the GPCP and GPCC sources (Figure 5-7) generally show the similar

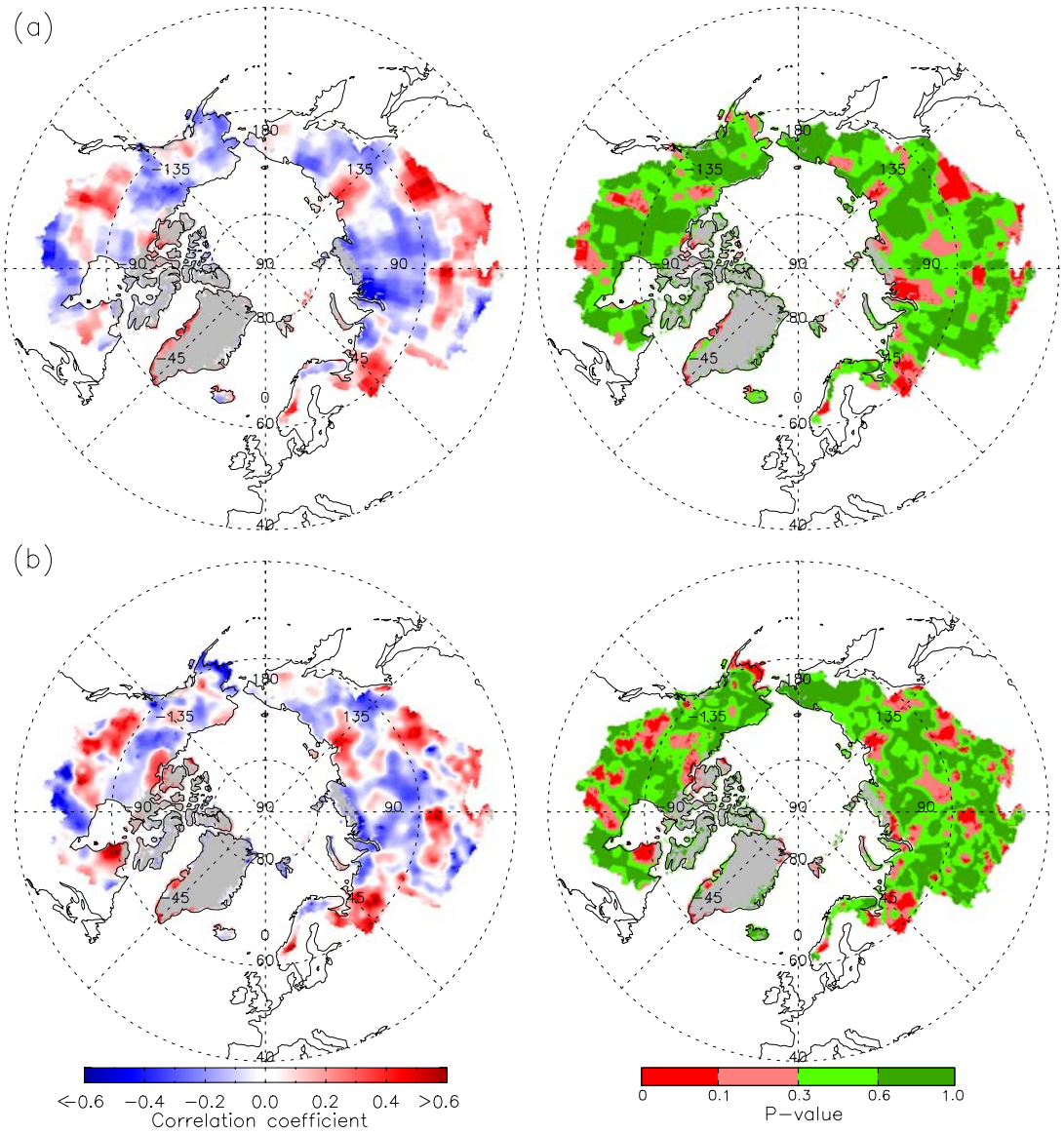

Figure 5-7: Maps of correlations between PDO_{GS} and GS P-ET and corresponding *P*-values; the top graphs are derived using GPCP precipitation while the bottom graphs are derived using GPCC precipitation.

spatial patterns. The results indicate that the growing season water balance is positively correlated with the PDO_{GS} in Southern, Central and Northeastern Canada, and Northwestern and Southern Eurasia indicating increased net water inputs under positive PDO conditions.

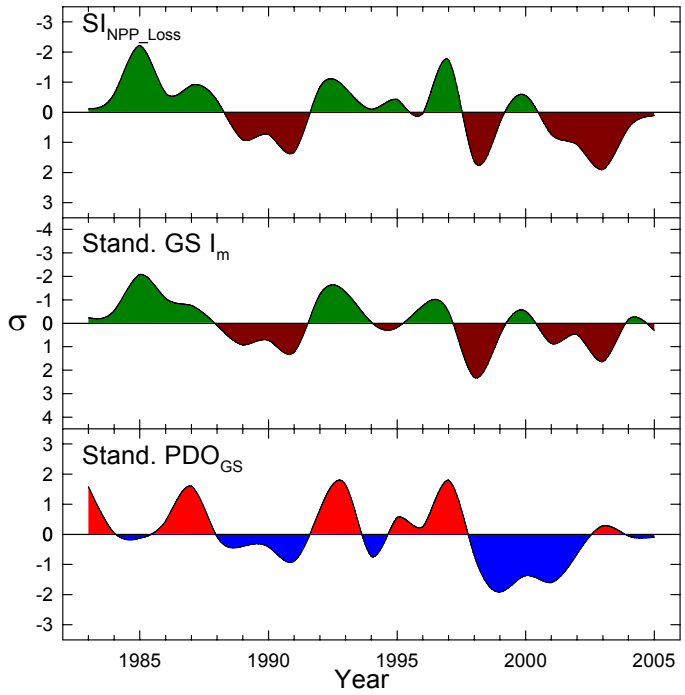

Figure 5-8: Time plots of SI_{NPP_Loss}, and standardized GS I_m and PDO_{GS} anomalies for the pan-Arctic domain. SI_{NPP_Loss} represents drought-induced NPP losses relative to potential conditions, where less-than-normal (green) and larger-than-normal (brown) NPP losses are standardized relative to 23-year mean conditions. Positive PDO_{GS} phases (red) generally corresponded to wetter-than-normal conditions (green), whereas negative PDO_{GS} phases (blue) were generally related to drier-than-normal conditions (brown).

The PDO_{GS} index was correlated to regional average GS I_m ($r = -0.471$; $P = 0.023$) (Figure 5-8), indicating that North Pacific SST patterns during the growing season impact atmospheric moisture inputs to the pan-Arctic land mass, especially for boreal forest and grassland/cropland biomes. Positive phases of the PDO_{GS} generally correspond to wetter-than-normal conditions, while the negative PDO_{GS} phases were concurrent with drier-than-normal conditions for the region. The PDO_{GS} index was also significantly correlated with SI_{NPP_Loss} ($r = -0.485$; $P = 0.019$). The relative influence of PDO_{GS} on GS I_m also showed substantial spatial (Figure 5-5) and temporal variability

(Figure 5-8). Both GS I_m and SI_{NPP_Loss} indicated two widespread and prolonged droughts that resulted in substantial NPP declines from 1988-1991 and 1998-2003. The most recent drought resulted in particularly large NPP losses relative to the 23-year record. Drought-induced NPP losses in 1998, 2002, and 2003 were 1.63, 1.07 and 1.90 standard deviations from mean (23-year) conditions. Both of these droughts corresponded to negative PDO_{GS} phases. The most severe (1998-2003) regional drought coincided with a particularly strong negative PDO_{GS} phase. A previous study (MacDonald & Case, 2005) also reported that a prolonged and strongly negative PDO phase between AD 993 and 1300 is contemporaneous with a severe medieval mega-drought that is apparent in many proxy hydrologic records for the western United States and Canada. Although the PDO_{GS} didn't show strong correspondence with SI_{NPP_Loss} in 2000 and 2003, the relatively weak correlation between PDO_{GS} and SI_{NPP_Loss} within less drought prone tundra regions may be partially responsible for this. Since the oceans are the major atmospheric moisture source for the pan-Arctic land mass, the correspondence between PDO_{GS} and SI_{NPP_Loss} indicates that large-scale oscillations characterized by the PDO have a major impact on northern terrestrial NPP by regulating the supply of plant-available moisture during the growing season. However, the effect of the PDO on NPP shows strong spatial and temporal variability depending on the sign and relative strength of the PDO phase, and the potential vulnerability of vegetation to drought. The effect of PDO_{GS} on NPP appears to be larger within continental interior regions and southern margins of the boreal forest and grassland/cropland biomes where warmer air temperatures, longer potential growing seasons and a limited summer moisture supply result in larger potential moisture

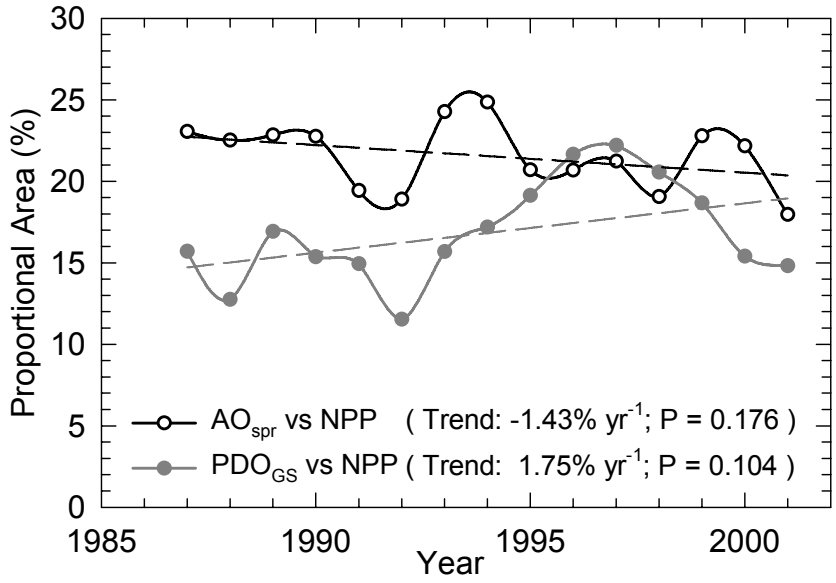

Figure 5-9: Time series of the proportional area of the pan-Arctic domain showing significant correlation between AO_{spr} and annual NPP and the proportional area of drought prone regions having significant correlations between PDO_{GS} and annual NPP, where the 23-year mean GS I_m exceeds regional mean conditions. The time series represents a nine-year moving correlation analysis, while dashed lines show the linear trends for the time series.

constraints to regional production. The recent increasing trend in GS I_m has been attributed to decreasing plant-available water supply and increasing air temperature, rather than changes in solar irradiance (see Chapter 3). The relative impact of the oscillations on regional productivity may also be changing as warming trends increase potential growing seasons and GS air temperatures.

To assess temporal trends in the relations between AO_{spr} and PDO_{GS} patterns, and annual NPP, I calculated time series of the proportional areas (%) of the pan-Arctic domain showing significant correlations between annual NPP and AO_{spr}, and between annual NPP and PDO_{GS} using a nine-year moving correlation analysis. The NPP-PDO_{GS} relationship was only assessed for drought prone areas where the 23-year mean GS I_m value exceeded pan-Arctic regional mean conditions, because the drought prone areas

covered 50.4% of the total vegetated area, and PDO_{GS} generally showed insignificant ($P > 0.1$) correspondence to GS I_m for other areas. The proportional area showing a significant correlation between AO_{spr} and annual NPP decreased by 1.43% per year ($P = 0.176$) from 1983 to 2005 (Figure 5-9), indicating that the AO_{spr} influenced timing of growing season onset became less important to annual NPP as low-temperature constraints to photosynthesis relaxed under an observed (0.5°C per decade; $P = 0.002$) positive trend in GS air temperature for the period of record (see Section 3.7.3). Coincidently, the proportional area of drought prone regions showing significant correlations between PDO_{GS} and annual NPP increased by 1.75% per year ($P = 0.104$), indicating that the PDO_{GS} influenced supply of plant-available moisture became an increasing constraint on annual productivity with regional warming. However, the significance of these trends is limited by the relatively short duration of the satellite record.

5.4. Conclusions

Synchronous ocean-atmosphere oscillations of the North Pacific, North Atlantic, and Arctic regions have a strong impact on the seasonal cycle and magnitude of pan-Arctic vegetation productivity and the regional uptake and sequestration of atmospheric CO_2 by vegetation biomass. These oscillations affect NPP by influencing the seasonal pattern of low temperature and moisture constraints to photosynthesis. The early-spring pattern of the AO influences the timing of growing season onset within the pan-Arctic domain, while growing season PDO patterns correspond with the supply of plant-available moisture. As potential growing seasons become longer under a warming climate,

negative phases of the PDO may have increasingly widespread and negative impacts on northern terrestrial uptake and sequestration of atmospheric CO_2, as plant-available moisture becomes more limiting to NPP. The two largest observed drought-induced reductions in regional productivity occurred during the latter half of the 23-year satellite record and coincided with particularly strong, negative PDO_{GS} phases. The influence of the springtime AO on terrestrial production is likely to decline under current warming trends as low temperature constraints to vegetation growth relax and NPP becomes increasingly constrained by the available supply of moisture during the growing season.

5.5. References Cited

Baldocchi, D.D., Falge, E., Gu, L., Olson, R., Hollinger, D., Running, S.W., Anthoni, P., Bernhofer, C., et al. (2001) FLUXNET: A new tool to study the temporal and spatial variability of ecosystem-scale carbon dioxide, water vapor, and energy flux densities. *Bulletin of the American Meteorological Society*, **82**, 2415-2443.

Balzter, H., Gerard, F.F., George, C.T., Rowland, C.S., Jupp, T.E., McCallum, I., Shvidenko, A., Nilsson, S., et al. (2005) Impact of the Arctic Oscillation pattern on interannual forest fire variability in Central Siberia. *Geophysical Research Letters*, **32**, L14709, doi:10.1029/2005GL022526.

Bjerknes, J. (1966) A possible response of the atmospheric Hadley circulation, to equatorial anomalies of ocean temperature. *Tellus*, **8**, 820-829.

Bonsal, B.R., Prowse, T.D., Duguay, C.R., & Lacroix, M.P. (2006) Impacts of large-scale teleconnections on freshwater-ice break/freeze-up dates over Canada. *Journal of Hydrology*, **330**, 340-353.

Déry, S.J. & Wood, E.F. (2004) Teleconnection between the Arctic Oscillation and Hudson Bay river discharge. *Geophysical Research Letters*, **31**, L18205, doi:10.1029/2004GL029729.

Deser, C. (2000) On the teleconnectivity of the "Arctic Oscillation". *Geophysical Research Letters*, **27**, 779-782.

Dettinger, M.D., Cayan, D.R., Diaz, H.F., & Meko, D.M. (1998) North-south precipitation patterns in western North America on interannual-to-decadal timescales. *Journal of Climate*, **11**, 3095-3111.

Dickson, R.R., Osborn, T.J., Hurrell, J.W., Meincke, J., Blindheim, J., Adlandsvik, B., Vinje, T., Alekseev, G., et al. (2000) The Arctic Ocean response to the North Atlantic oscillation. *Journal of Climate*, **13**, 2671-2696.

Glantz, M.H., Katz, R.W., & Nicholls, N. (1991) *Teleconnections linking worldwide climate anomalies: scientific basis and societal impact*. Cambridge University Press, Cambridge.

Gong, D.Y. & Wang, S.W. (1998) Antarctic oscillation: concept and applications. *Chinese Science Bulletin*, **43**, 734-738.

Gong, G., Entekhabi, D., & Cohen, J. (2003) Relative impacts of Siberian and North American snow anomalies on the winter Arctic Oscillation. *Geophysical Research Letters*, **30**, 1848, doi:10.1029/2003GL017749.

Hurrell, J.W. (1995) Decadal Trends in the North-Atlantic Oscillation - Regional Temperatures and Precipitation. *Science*, **269**, 676-679.

Hurrell, J.W. (1996) Influence of variations in extratropical winter-time teleconnections on Northern Hemisphere temperature. *Geophysical Research Letters*, **23**, 665-668.

Hurrell, J.W. & van Loon, H. (1997) Decadal variations in climate associated with the North Atlantic Oscillation. *Climatic Change*, **36**, 301-326.

Kerr, R.A. (1999) A new force in high-latitude climate. *Science*, **284**, 241-242.

Kimball, J.S., McDonald, K.C., Frolking, S., & Running, S.W. (2004) Radar remote sensing of the spring thaw transition across a boreal landscape. *Remote Sensing of Environment*, **89**, 163-175.

Kimball, J.S., Zhao, M., McDonald, K.C., & Running, S.W. (2006) Satellite remote sensing of terrestrial net primary production for the pan-Arctic basin and Alaska.

Mitigation and Adaptation Strategies for Global Change, **11**, 782-804, doi:10.1007/s11027-005-9014-5.

Kryjov, V.N. (2004) Searching for circulation patterns affecting North Europe annual temperature. *Atmospheric Science Letters*, **5**, 23-34.

MacDonald, G.M. & Case, R.A. (2005) Variations in the Pacific Decadal Oscillation over the past millennium. *Geophysical Research Letters*, **32**, L08703, doi:10.1029/2005GL022478.

Mantua, N.J., Hare, S.R., Zhang, Y., Wallace, J.M., & Francis, R.C. (1997) A Pacific interdecadal climate oscillation with impacts on salmon production. *Bulletin of the American Meteorological Society*, **78**, 1069-1079.

Maruyama, T. (1997) The Quasi-Biennial Oscillation (QBO) and equatorial waves - A historical review. *Meteorology and Geophysics*, **48**, 1-17.

Minobe, S. (2000) Spatio-temporal structure of the pentadecadal variability over the North Pacific. *Progress in Oceanography*, **47**, 382-408.

Oliver, J.E. (2005). Oscillations. In *Encyclopedia of World Climatology* (ed J.E. Oliver), pp. 555-556. Springer, New York.

Rasmusson, E.M. & Carpenter, T.H. (1982) Variations in Tropical Sea-Surface Temperature and Surface Wind Fields Associated with the Southern Oscillation El-Nino. *Monthly Weather Review*, **110**, 354-384.

Schneider, N. & Cornuelle, B.D. (2005) The forcing of the Pacific decadal oscillation. *Journal of Climate*, **18**, 4355-4373.

Siedler, G., Church, J., & Gould, J. (2001) *Ocean circulation and climate: Observing and modelling the global ocean*. Academic Press, London.

Thompson, D.W.J. & Wallace, J.M. (1998) The Arctic Oscillation signature in the wintertime geopotential height and temperature fields. *Geophysical Research Letters*, **25**, 1297-1300.

Wallace, J.M. (2000) North Atlantic Oscillation/Annular Mode: Two paradigms-One phenomenon. *Quarterly journal of the Royal Meteorological Society*, **126**, 791-806.

Wallace, J.M. & Gutzler, D.S. (1981) Teleconnections in the geopotential height field during the Northern Hemisphere winter. *Monthly Weather Review*, **109**, 784-812.

Wallace, J.M. & Thompson, D.W.J. (2002) Annular modes and climate prediction. *Physics Today*, **55**, 28-33.

CHAPTER 6: CONCLUSIONS AND FUTURE STUDIES

6.1. Key Findings

6.1.1. Uncertainties in Meteorology Reanalyses

There are considerable uncertainties associated with surface meteorology reanalyses products that are used to assess global and regional climate changes and as primary environmental drivers of ecological and hydrological modeling systems in the northern high latitudes.

I developed a mathematical regional correction method to effectively reduce the biases and uncertainties in the meteorology reanalyses using the ground observations. Improved availability and density of northern ground observation networks would be helpful to further improve the quality of meteorology reanalyses.

6.1.2. Changes of Climatic Constraints to Vegetation Productivity

The climate of the pan-Arctic region has undergone rapid and dramatic changes in the past and there is no reason that it could not experience similar changes in the future. Low-temperature, plant-available moisture and solar irradiance are the major climatic constraints to vegetation productivity in this region. The temperature in this region shows the most significant change of these three major climatic factors and corresponds with global warming. As a result, low temperature constraints on pan-Arctic vegetation productivity are significantly decreasing over the 23-year study period and strongly favor additional plant growth. However, vegetation moisture stress also shows strong

increasing trends in response to regional warming, changes in the hydrological cycle and variability in land-ocean moisture exchanges, that are offsetting the potential benefits of longer growing seasons and contributing to recent disturbances in vegetation productivity.

Climate change and human activities are also impacting regional clouds and aerosol properties, and incoming solar radiation. However, changes in incoming solar radiation are generally insignificant over the observed period of record, and appear to have a much smaller impact on pan-Arctic vegetation productivity than the other two environmental constraints.

6.1.3. Changes of Vegetation Phenology, Greenness and Productivity

The satellite remote sensing based retrievals of seasonal freeze-thaw and vegetation productivity indicate that the timings of growing season onset and cessation coincide with the timings of major thaw and freezing events in the pan-Arctic region. Satellite observations of a generally earlier growing season onset are also confirmed by an earlier spring drawdown of atmospheric CO_2 concentrations by plant photosynthesis as observed from the regional air CO_2 measurement network. These results indicate that timing of seasonal thawing and growing season onset are advancing, while onset of seasonal freezing and growing season cessation are retreating and extending the length of the vegetation growing season with regional warming.

The satellite optical-infrared remote sensing record shows that past evidence for ubiquitous “greening” trends have not remained consistent through time or uniform in space. Some areas, mainly located in the boreal forest region, are experiencing recent declines in vegetation greenness and productivity. These “browning” trends generally

occur after the late 1990's and are largely the result of recent, widespread drought events and generally increasing moisture stress.

Estimated regional average annual GPP, autotrophic respiration and NPP all show significant positive linear trends mainly driven by a significant decreasing trend in low-temperature constraints to vegetation productivity and associated earlier and longer growing seasons. However, vegetation autotrophic respiration shows a stronger rate of increase with regional warming than GPP, resulting in a significant decreasing trend in carbon use efficiency (i.e. the ratio of NPP to GPP). The NPP trends show large spatial variability with generally increasing trends in the tundra region, whereas some boreal forest regions show large NPP decreases in recent years corresponding with widespread summer drought.

6.1.4. Changes of Hydrological Cycle and Water Balance

The developed satellite remote sensing based ET algorithms show high accuracy (RMSE = 7.4-8.3 mm $month^{-1}$; R^2 = 0.89-0.92) by comparing the simulated results with measured tower fluxes from regionally dominant land cover types, provide an effective means to estimate actual ET, and have potential for the global application.

The satellite remote sensing based ET results show generally positive trends over most of the pan-Arctic domain, though negative ET trends occurred over 32% of the region, primarily in boreal forests of southern and central Canada. Generally positive trends in ET, precipitation and available long-term river discharge measurements imply that the pan-Arctic terrestrial water cycle is intensifying, though uncertainty in regional precipitation and associated water balance estimates is large. Increasing water deficits

occurred in some boreal and temperate grassland regions including eastern Alaska, the Canadian Yukon and western Prairie Provinces, and Northern Mongolia, which agree with regional drought records and recent satellite observations of vegetation browning and productivity decreases. The results also show that the pan-Arctic water balance is changing in complex ways in response to global warming, with direct linkages to terrestrial carbon and energy cycles.

6.1.5. Impacts of Climate Oscillations

Large-scale atmospheric and ocean oscillations, i.e. climate oscillations, represent the natural variability of the climate system, but may also be influenced by human-induced climate change. Although the underlying mechanisms behind many climate oscillations aren't well understood, many studies have shown that climate oscillations have strong impacts on land surface processes.

Analyses of regional climate oscillation indices in relation to satellite remote sensing derived NPP and growing season dynamics for the pan-Arctic region indicate that the oscillations influence NPP by regulating seasonal patterns of low temperature and moisture constraints to photosynthesis. Early-spring (February-April) patterns of the Arctic Oscillation (AO) are proportional to growing season onset ($r = -0.653$; $P = 0.001$), while growing season patterns of the Pacific Decadal Oscillation (PDO) are proportional to plant-available moisture constraints to NPP (I_m) ($r = -0.471$; $P = 0.023$). Relatively strong, negative PDO phases from 1988-1991 and 1998-2002 coincided with prolonged regional droughts indicated by a standardized moisture stress index. These severe droughts resulted in widespread reductions in NPP, especially for relatively drought

prone boreal forest and grassland/cropland ecosystems. The influence of AO and PDO patterns on northern vegetation productivity appears to be decreasing and increasing, respectively, as low temperature constraints to plant growth relax and NPP becomes increasingly limited by available water supply under a warming climate.

6.2. Suggested Future Research

My study results in Chapters 2, 3 and 4 show that the ground observation network for meteorology and hydrology are relatively sparse and that there are considerable uncertainties in the current meteorology reanalyses. Improvements in the spatial resolution of regional climate reanalyses coupled with standardization and augmentation of solar radiation and precipitation monitoring networks, and enhanced resolution satellite remote sensing products would dramatically improve the regional assessment of NPP changes and associated linkages between the terrestrial water and carbon cycles.

Secondly, it is important to obtain longer ecological and hydrological data records with fine spatial resolution and high quality for assessing climate change and understanding the responses and feedbacks of ecosystems. It is necessary to create and extend a series of science-quality time-series data records, i.e. Land Earth System Data Records, by using the current scientific research satellite observations, refining current satellite-based retrieval algorithms for the land surface processes, and developing model assimilation systems by coupling model simulations with all kinds of observations or measurements. The used satellite-based Productivity Efficiency Model and the developed satellite-based ET algorithms in this study provide potential tools to produce the Land Earth System Data Records.

Thirdly, net ecosystem exchange (NEE) is the residual difference between GPP and ecosystem respiration and the net exchange of CO_2 between the atmosphere and terrestrial ecosystems. Improved regional quantification of NEE spatial patterns and temporal dynamics is needed to identify terrestrial carbon sinks and sources and their response to landscape complexity and environmental perturbations. In this study, I have improved the estimation quality of GPP and NPP by reducing uncertainties in meteorology reanalysis. The next step to accurately quantify NEE is to accurately estimate ecosystem respiration. To accurately estimate terrestrial carbon sources and sinks (i.e. net biome productivity), it is necessary to incorporate satellite remote sensing based retrievals of soil moisture and temperature into process-based ecological modeling to quantify ecosystem respiration. It is also vital to develop improved disturbance modules to quantify the effects of disturbances such as fires, insects, crop harvest, and deforestation on NEE by incorporating remotely sensed data and ground measurements with modeling framework based on ecological and biological knowledge of ecosystem succession. A data assimilation system for estimate of net CO_2 exchange is also imperative to combine simulations and measurements at all spatial levels. For example, measurements from tall towers are representative of an area governed by the integrating effect of boundary layer transport and turbulence, while eddy covariance flux towers provide plot-level measurements.

Lastly, additional studies on the physical mechanisms driving climate oscillations would be helpful to better understand the natural variability of boreal-Arctic climate system to enable improved prediction of future ecosystem responses. Coupled land-ocean-atmosphere model simulations and coordinated interdisciplinary efforts are needed

to better assess physical linkages and feedbacks of the sub-systems of global climate system.

LIST OF ACRONYMS AND ABBREVIATIONS

ACIA	Arctic Climate Impact Assessment
AAO	Antarctic Oscillation
AO	Arctic Oscillation
ARCSS	ARCtic System Science
AMSR-E	Advanced Microwave Scanning Radiometer for EOS
ATLAS	Arctic Transition in the Land Atmosphere System
AVHRR	Advanced Very High Resolution Radiometer
BIOME-BGC	BIOME BioGeochemical Cycles
BOREAS	BOReal Ecosystem-Atmosphere Study
BPLUT	Biome Properties Look-Up Table
CDAS	Climate Data Assimilation System
CDF	Cumulative Distribution Function
CMI	Climate Moisture Index (mm yr^{-1})
CRP	Cropland
CRU	Climatic Research Unit
CSB	Climate Services Branch
DNF	Deciduous Needleleaf Forest
ECMWF	European Centre for Medium-range Weather Forecasts
ENF	Evergreen Needleleaf Forest
ENSO	El Niño-Southern Oscillation
EOS	Earth Observing System
ERA-15	15-year ECMWF Re-Analysis
ERA-40	45-year ECMWF Re-Analysis
ESH	Earth System History
ET	Evapotranspiration
EVI	Enhanced Vegetation Index
FPAR	Fractional Photosynthetically Active Radiation
GCM	General Circulation Model
GDAS	Global Data Assimilation System

GEWEX	Global Energy and Water-cycle EXperiment
GHCN	Global Historical Climatology Network
GIMMS	Global Inventory Modeling and Mapping Studies
GMD	Global Monitoring Division
GPP	Gross Primary Productivity
GRS	Grassland
GS	Growing Season
IASC	International Arctic Science Committee
ICSU	International Council for Science
IGBP	International Geosphere-Biosphere Programme
IPCC	Intergovernmental Panel on Climate Change
IPY	International Polar Year
LAI	Leaf Area Index
LAII	Land-Atmosphere-Ice Interactions
LE	Latent heat
LSI	Land-Shelf Interaction
LTER	Long Term Ecological Research
MAE	Mean Absolute Error
MF	Mixed Forest
MODIS	MODerate resolution Imaging Spectroradiometer
NAO	North Atlantic Oscillation
NASA	National Aeronautics and Space Administration
NCAR	National Center for Atmospheric Research
NCDC	National Climatic Data Center
NCEP	National Centers for Environmental Prediction
NDVI	Normalized Difference Vegetation Index
NIR	Near Infrared
NNR	NCEP-NCAR Reanalysis
NOAA	National Oceanic and Atmospheric Administration
NPP	Net Primary Productivity
NSCAT	NASA Scatterometer

NSF	National Science Foundation
NSRDB	National Solar Radiation Data Base
OSH	Open Shrubland
PAL	Pathfinder AVHRR Land
PARCS	Paleoenvironmental ARCtic Sciences
PDO	Pacific Decadal Oscillation
PEM	Production Efficiency Model
PET	Potential Evapotranspiration
PNA	Pacific North American Oscillation
QBO	Quasibiennial Oscillation
RMSE	Root Mean Square Error
SASS	Synthesis of Arctic System Science
SI	Statistical Independence
SLP	Sea Level Pressure
SMMR	Scanning Multichannel Microwave Radiometer
SNACS	Study of the Northern Alaskan Coastal System
SRB	Surface Radiation Budget
SSM/I	Special Sensor Microwave/Imager
SST	Sea Surface Temperature
SV	Savanna
WALE	Western Arctic Linkage Experiment
WMO	World Meteorological Organization
WSV	Woody Savanna

LIST OF SYMBOLS

Symbol	Meaning
a	a constant which is set to 1.26 in the Priestley-Taylor equation
a_0, a_1	the Y-intercept and slope of the simple linear regression coefficients, respectively
A	available energy for evapotranspiration (W m^{-2})
A_{Canopy}	available energy for canopy transpiration (W m^{-2})
A_{Soil}	available energy for soil evaporation (W m^{-2})
AO_{spr}	early-spring (February-April) mean value of monthly AO indices
b_1, b_2, b_3, b_4	fitted empirical parameters for the mathematical functions of g_0 vs. NDVI ($g_0(\mathrm{NDVI}) = 1/[b_1 + b_2 \cdot \exp(-b_3 \cdot \mathrm{NDVI})] + b_4$)
c	column number
c_G	ratio of the soil heat flux G to the net radiation
c_L	mean surface conductance per unit leaf area index (m s^{-1})
C_P	specific heat capacity of air (J kg^{-1} K^{-1})
$d_{SW_\downarrow}$	ratios of observed $SW_\downarrow$ to reanalysis $SW_\downarrow$
$\widetilde{d}_{SW_\downarrow}$	samples of $d_{SW_\downarrow}$
e_a	daily air water vapor pressure (Pa)
$e_{a,Obs}$	observed e_a (Pa)
$e_{a,Res}$	reanalysis e_a (Pa)
e_{sat}	daytime air saturated water vapor pressure (Pa)
E_{Canopy}	canopy transpiration (m)
E_{Soil}	soil evaporation (m)
E_{Water}	evaporation over water bodies (m)
f_C	fractional vegetation cover
$FPAR$	fractional Photosynthetical Active Radiation
g_a	aerodynamic conductance (m s^{-1})

g_s	surface conductance (m s^{-1})
g_0	biome-dependent maximum value of surface conductance (m s^{-1})
g_0^*	derived value of g_0 using the rearranged Penman-Monteith equation from the measurements
G	Soil heat flux (W m^{-2})
GPP	gross primary productivity (g C m^{-2} d^{-1})
$H(x)$	estimate of the entropy associated with x
$H(y)$	estimate of the entropy associated with y
LAI	leaf area index (m^{-2} m^2)
I_m	moisture stress index
I_t	low-temperature stress index
LE_{Canopy}	latent heat flux of canopy (W m^{-2})
LE_{Soil}	latent heat flux of soil (W m^{-2})
LE_{Water}	latent heat flux of water bodies (W m^{-2})
$m(\theta_1),...,m(\theta_n)$	a series of multiplicative factors (i.e. stress factors)
M_a	the molecular mass of dry air (kg mol^{-1})
M_w	the molecular mass of wet air (kg mol^{-1})
M_ε	median of error distribution
nE_{rc}	expected number of points falling in the cell (r,c)
nO_{rc}	the number of points falling in the cell (r,c)
nS	sample size
n_x	intervals in the x-axis direction
n_{x_c}	the number of points in column c
n_y	intervals in the y-axis direction
n_{y_r}	the number of points in row r
NDVI	normalized difference vegetation Index
$NDVI_{min}$	the value of NDVI for bare soil and set to 0.05
$NDVI_{max}$	the value of NDVI for dense green vegetation and set to 0.95

NPP_{actual}	actual calculated NPP under actual environmental conditions
NPP_{M}	NPP only with moisture constraints
NPP_{-M}	NPP without moisture constraints
$NPP_{Potential}$	potential NPP under non limiting atmospheric conditions
NPP_{T}	NPP only with low-temperature constraints
P_{air}	the air pressure (Pa)
PAR	photosynthetical active radiation (MJ m^{-2} d^{-1})
PDO_{GS}	growing season (April-October) mean value of monthly PDO indices
Q_1	first quartile of error distribution
Q_3	third quartile of error distribution
r	simple linear correlation coefficient
r_a	aerodynamic resistance (s m^{-1})
r_c	resistance to convective heat transfer (s m^{-1})
r_r	resistance to radiative heat transfer (s m^{-1})
r_s	surface resistance (s m^{-1})
r_{tot}	total aerodynamic resistance to vapor transport , i.e., the sum of surface resistance and the aerodynamic resistance components (s m^{-1})
r_{totc}	corrected value of r_{tot} from the standard conditions for temperature and pressure (STP) using the correction coefficient (R_{corr})
R_{corr}	correction coefficient for R_{corr}
R_g	annual growth respiration (g C m^{-2} yr^{-1})
R_{m_lr}	daily maintenance respiration of leaves and fine roots (g C m^{-2} d^{-1})
R_{m_w}	annual maintenance respiration from live wood (g C m^{-2} yr^{-1})
R_n	net all-wave solar radiation (W m^{-2})
RH	relative humidity of air
RS_{Au}	autotrophic respiration (g C m^{-2} yr^{-1})
r	row number
s_ε	standard error

$SE(a_1)$	standard error of estimate associated with the parameter
SI_{NPP_Loss}	standardized value of δ_{NPP_Loss}
$SW_{\downarrow}$	daily downward solar shortwave radiation (MJ m^{-2} d^{-1} or W m^{-2})
$SW_{\downarrow,\mathrm{Obs}}$	observed $SW_{\downarrow}$ (MJ m^{-2} d^{-1})
$SW_{\downarrow,\mathrm{Res}}$	reanalysis $SW_{\downarrow}$ (MJ m^{-2} d^{-1})
t	time
T	statistic of the statistical independence test or air temperature (°C)
T_{avg}	daily average surface air temperature (°C)
$T_{\mathrm{avg,Obs}}$	observed T_{avg} (°C)
$T_{\mathrm{avg,Res}}$	reanalysis T_{avg} (°C)
$T_{close\_\max}$	biome-specific maximum critical temperatures for stomatal closure and the effective cessation of plant photosynthesis (°C)
$T_{close\_\min}$	biome-specific minimum critical temperatures for stomatal closure and the effective cessation of plant photosynthesis (°C)
T_{CO2_Spr}	timing of spring drawdown of atmospheric CO_2 concentration
T_{day}	daylight average air temperature (°C)
T_{dew}	daily dew point temperature (°C)
T_f	daily minimum temperature scalar (°C)
T_{Freeze}	timing of fall freezing
$T_{\max}$	daily maximum surface air temperature (°C)
$T_{\min}$	daily minimum surface air temperature (°C)
$T_{\mathrm{min,Obs}}$	observed $T_{\min}$ (°C)
$T_{\mathrm{min,Res}}$	reanalysis $T_{\min}$ (°C)
T_{NPP_End}	growing season end derived from daily NPP time series
T_{NPP_Onset}	growing season onset derived from daily NPP time series
T_{opt}	biome-specific optimum air temperature for photosynthesis (°C)
T_{Thaw}	timing of spring thaw
$U(y,x)$	entropy-based measure of the strength of the association between

	x and y
VPD	daytime air vapor pressure deficit (Pa)
VPD_f	vapor pressure deficit scalar
VPD_{close}	biome-specific critical value of VPD at which canopy stomata are completely closed (Pa)
VPD_{open}	biome-specific critical value of VPD at which the canopy stomata are completely open (Pa)
x	vector of observed/measured values, random variable or x axis
$\hat{x}$	vector of estimated values
y_t	biophysical variables
α	albedo or reflectivity
β	a biome-specific empirical parameter for the calculation of the temperature stress factor for plant transpiration ($m(T_{day})$) (°C)
γ	psychrometric constant
$\delta loss_M$	proportional loss of potential NPP due to moisture constraints (%)
$\delta loss_T$	proportional loss of potential NPP due to low-temperature constraints (%)
δ_{NPP_Loss}	a simple NPP loss index by comparing actual NPP with the potential NPP without moisture constraints (%)
δ_ε	relative error
Δ	the slope of the curve relating saturated water vapor pressure to air temperature
ε	residual defined as the observed value minus the estimated value
$\bar{\varepsilon}$	mean residual
ε_{a}	atmospheric emissivity
$\varepsilon_{\mathrm{e_a}}$	residuals of e_a
$\tilde{\varepsilon}_{\mathrm{e_a}}$	samples of $\varepsilon_{\mathrm{e_a}}$
$\varepsilon_{\mathrm{T_{avg}}}$	residuals of T_{avg}

$\widetilde{\varepsilon}_{T_{avg}}$	samples of $\varepsilon_{T_{avg}}$
$\varepsilon_{T_{min}}$	residuals of T_{min}
$\widetilde{\varepsilon}_{T_{min}}$	samples of $\varepsilon_{T_{min}}$
$\theta_1,...,\theta_n$	a series of environmental constraint variables on plants
k	a parameter to fit the complementary relationship (Pa)
λ	the latent heat of vaporization (J kg^{-1})
ξ	light use efficiency
ξ_{max}	maximum light use efficiency
ρ_{air}	air density (kg m^{-3})
ρ_{NIR}	spectral reflectance in the near-infrared band
ρ_{Red}	spectral reflectance in the red band
σ	Stefan-Boltzmann constant ($=5.670400\times10^{-8}$ W m^{-2} K^{-4})

APPENDIX A

The Biome Properties Look-Up Table (BPLUT) for the NDVI-based ET

Parameter	OSH	SV	GRS	CRP	WSV	ENF	DNF	MF
T_{close_min} (^{o}C)	-8.00	-8.00	-8.00	-8.00	-8.00	-8.00	-8.00	-7.00
T_{close_max} (^{o}C)	38	38	45	45	40	40	40	45
VPD_{close} (Pa)	3700	3600	3900	3800	3300	2500	3500	2700
VPD_{open} (Pa)	650	650	650	650	650	650	650	650
T_{opt} (^{o}C)	10	10	20	20	15	15	15	20
β (^{o}C)	30	30	30	30	25	25	25	30
k (Pa)	50	50	250	250	105	105	105	100
r_a (s m^{-1})	100	100	90	90	20	20	20	15
r_{tot} (s m^{-1})	111	111	500	500	100	100	100	167
b_1 (mm s^{-1})	0.412	0.412	0.138	0.138	0.25	0.25	0.25	0.10
b_2 (mm s^{-1})	4.118	4.118	2.5	2.5	14.19	14.19	14.19	3.172
b_3	8	8	5.8	5.8	10	10	10	7.53
b_4 (10^{-3} mm s^{-1})	220.78	220.78	379.15	379.15	6.923	6.923	6.923	305.65